

https://dspace.org/

Study of the influence of gust fronts and topographical features in the development of severe thunderstorms across South Africa

Mofokeng, Puseletso Samuel

2024

University of the Witwatersrand, Johannesburg

https://hdl.handle.net/10539/44980

Mofokeng, Puseletso Samuel. (2024). Study of the influence of gust fronts and topographical features in the development of severe thunderstorms across South Africa [Master's dissertation, University of the Witwatersrand, Johannesburg]. WIReDSpace. https://hdl.handle.net/10539/44980

Downloaded from a DSpace repository. https://dspace.org/

STUDY OF THE INFLUENCE OF GUST FRONTS AND TOPOGRAPHICAL FEATURES IN THE DEVELOPMENT OF SEVERE THUNDERSTORMS ACROSS SOUTH AFRICA

by

Puseletso Samuel Mofokeng

(Student Number: 2235939)

Submitted to the Faculty of Science at the University of the Witwatersrand

in partial fulfilment of

Master of Science degree in Meteorology

Supervisor: Prof. Stefan W. Grab (Wits GAES)

Co-supervisors: Prof. Francois A. Engelbrecht (Wits GCI; Wits GAES) and Dr Mary-Jane M. Bopape (SAEON)

September 2024

“There is a great solution buried in every assignment” – George Lois

DECLARATION

I declare that this dissertation, titled the STUDY OF THE INFLUENCE OF GUST FRONTS AND TOPOGRAPHICAL FEATURES IN THE DEVELOPMENT OF SEVERE THUNDERSTORMS ACROSS SOUTH AFRICA, reflects my own efforts. Further, citations of the work of other authors were acknowledged in literature review and in support of my own work.

Signature



……

Puseletso Samuel Mofokeng

DEDICATION

I dedicate this dissertation to

God Almighty for keeping me creative and resilient to complete this task;

my family unit: Nomasonto, Lesedi, Katleho, Mamello and Bophelo;

the community of Protea Glen, Soweto

[Exceptional gratitude to Ms Dineo Maja for sharing the call log, which showed the call on the first tornado touchdown on 30 December 2017, and to Mr. Tshokolo Lamola for leading me to other community members who video-recorded the event.];

and

Naledi Peter Mofokeng and Susan Chauke for their moral support.

ACKNOWLEDGEMENTS

Acknowledgements are in order, for the following pillars:

Professor Stefan Grab for unassailable interest and belief in my project through and through. Thank you for prompt evaluation of my efforts and for all the advice to improve academic writing, starting from when you read my proposal and the technical hurdles you helped me to overcome for the period predating my registration at Wits University through to the very last moment. It will remain memorable that you checked on my health when COVID-19 pandemic impacted humankind. Thank you for showing me the correct protocol to hold my studies in abeyance so I could recover from the illness I suffered in 2021.

Professor Francois Engelbrecht for using your subject prowess to keep me on my toes and pushing me to the limit. I would not have realised and known some of the trickiest meteorological concepts had it not been for you. You developed a better problem solver in me.

Dr Marry-Jane Bopape for first introducing me to the current university environment and players. It was very thoughtful of you to rope in Mr Robert Maisha to introduce me to writing scripts and creating my own images from the numerical prediction model. Thank you for directing me to present these images.

Mr Victor Mafata and the South African Police Services for leading me around Protea Glen two days later after a partial tornado destruction on 30 December 2017.

Ms Elelwani Phaduli for encouragement and making model data available, as per my request.

Ms Patience Mulovhedzi for introducing me to the management of references. Your two examples produced a long list of references.

Mr Wetsi Moloi for assisting with intermittent programming challenges during my study.

Mr Jerry Figlan of the SABC Graphic Department for the techniques of reducing the image sizes while maintaining their quality.

My son, Katleho, for the fast and effective use of Bluetooth technology.

Ms Ruth Moeti for creating a generalised topographic map of South Africa.

Colleagues in weather research and forecasting who engaged (and keep engaging) in weather discussions, particularly Messrs. Lesetja Lekoloane, Edward Engelbrecht, Luthando Masimini, Ms Vanetia Phakula and Dipuo Tawana.

Helpful librarians at the South African Weather Service (Ms Karin Oxley and Anastasia Demertzis). Thank you, Karin, for the moment you worked beyond your normal hours translating a Beeld article into English.

Librarians at Tshwane University of Technology (TUT) for going the extra mile to assist me with books dealing with research methods and Fortran.

My nephew, Tahleho Mofokeng, for confirming the identified severe thunderstorms using the set criteria in Section 3.4.1.

The South African Weather Service for being the main financial supporter of my studies.

My niece, Malefu Mokubung, for additional financial support, especially for the last registration.

Nomasonto Mofokeng, Mamello Mofokeng and Samukelisiwe Thwala for mentioning the names of the colours on colour scales so I could find their digital representation quicker.

Table of Contents

List of Figures x
List of Tables xvi
Units xvi
Direction xvi
Symbols xvii
Abbreviations xviiii
Acronyms xviiii
Abstract xvii
Chapter 1: Introduction 1
1.1 Study overview 1
1.2 Location and topography of South Africa 1
1.3 Climate of South Africa 3
1.4 Thunderstorm classes 5
1.5 Rationale 6
1.6 Aim and objectives 7
1.6.1 Aim 7
1.6.2 Objectives 8
1.7 Research questions 9
Chapter 2: Literature Review 10
2.1 Definitions 10
2.2 Moisture sources 11
2.3 Some triggers of severe thunderstorms 11
2.4 Localised inducement of low-level wind shear 13
2.4.1 Involving more than one 13
2.4.2 Involving topographical features 15
2.5 Synergy of surface and middle level vorticities 17
2.5.1 Up-down synergy of vorticities 17
2.5.2 Down-up synergy of vorticities 19
2.5.3 Storm-relative helicity (SRH) 22
2.6 Indicators of potential severe events 23
2.6.1 Tornadoes 23

2.6.2 Hail and lightning 27
2.7 Severe thunderstorms in El-Niño Southern Oscillation 28
2.7.1 Severe thunderstorms related to El-Niño phase 28
2.7.2 Severe thunderstorms related to the La-Niña phase 29
Chapter 3: Data and methodologies 30
3.1 Background 30
3.2. Data sources 30
3.2.1 Meteorological satellite data 30
3.2.2 Meteorological RADAR data 31
3.2.3 Severe weather log and social media 31
3.2.4 Measurements of temperature, humidity, rain and wind 32
3.2.5 Regional weather forecasts and Tweets 32
3.2.6 Coordinate system and high-resolution topographical maps 33
3.2.7 Numerical weather prediction and reanalysis data 33
3.2.8 The ERA5 Reanalysis 34
3.2.9 Historic oceanic Niño indices 34
3.3 Scope limitation of the study 34
3.4. Data processing 35
3.4.1 Criteria used for the identification of severe thunderstorms 35
3.4.1.1 Severe storms produced from gust front of another storm……37
3.4.1.2 Severe storms related to topographic features…….……37
3.4.1.3 Production of landspouts and tornadoes……38
3.4.1.4 Severe storms relating to 500 hPa vorticity advection…….……43
3.5 Tornadic storms in relation to El-Niño Southern Oscillation 43
Chapter 4: Severe thunderstorms across South Africa 45
4.1 Overview of severe storms across South Africa 45
4.1.1 Forecast decision-making in association with MTS circulations 46
4.2 Effect of topography and gust fronts on severe thunderstorms 49
4.2.1 Case studies: isolated severe storms under weak MTS ridge 49
4.2.1.1 Case A: Flash floods and small hail at Sun City on 15 December 2018……...49
4.3 Severe thunderstorms related to MTS cyclonic flows……55
4.3.1 Case studies on short-wave MTS troughs 56

4.3.2 Strong MTS waves 56
4.3.2.1 Well-developed MTS troughs……56
4.3.2.1.a Case B: Organised storm over central South Africa - 24 January 2020……...57
4.3.2.2 Cut-off low pressure systems……..……..61
4.3.2.2a Case C: Severe storms ageostrophic to MTS winds - 13 February 2018……63
4.3.2.2b Case D: Downburst at New Bethesda - 2 September 2020…..70
Chapter 5: Tornadoes across South Africa 79
5.1 Introduction 79
5.2 Systematic analysis of tornadoes in South Africa 79
5.2.1 Summer season tornadoes 79
5.2.2 Autumn season tornadoes 82
5.2.3 Spring season tornadoes 83
5.2.4 Winter season tornadoes 84
5.2.5 Landspouts across South Africa 85
5.2.6 Summary of overall South African tornadoes 86
5.3 Tornadogenesis in South Africa 87
5.3.1 Tornadogenesis effected after thunderstorm deviation 88
5.3.1.1 The Richmond tornado – 17 March 2020……88
5.3.1.2 The Vaal Marina tornado – 11 December 2017……90
5.3.2 Tornadogenesis due to topography-enhanced gust front 93
5.3.2.1 The Protea Glen tornado – 30 December 2017……93
5.3.2.2 The Mthatha tornado – 7 October 2019……96
5.3.2.3 The Ulundi tornado – 23 November 2019……99
5.3.3 Simplified representation of tornadoes and landspouts 104
5.3.3.1 Schematic model of tornadogenesis in South Africa……...104
5.3.3.2 Schematic model of landspout development in South Africa…….106
5.4 Longevity of tornadoes in South Africa 108
5.4.1 Short-lived tornadic storms 108
5.4.2 Long-lasting tornadic storms 109
5.5 Distribution of tornadoes across South Africa 110
5.5.1 Tornado distribution by region 110

5.5.1.1 Distribution of tornadic supercell storms……112
5.5.2 Tornado distribution by seasons 113
5.5.3 Distribution of anticyclone tornadoes 115
5.6 Spread of tornadoes relative to El-Niño/Southern Oscillation 117
5.6.1 Frequencies of tornadic storms 117
5.6.2 Indirect causal effects for high frequencies of tornadic storms..... 118
Chapter 6: Conclusions and recommendations 123
6.1 Overview summary 123
6.2 Effect of topographic features to gust fronts and severe storms..... 124
6.3 Effect of gust fronts of upwind storms on severe storms 126
6.4 Synergy of storms with large 500 hPa vorticity advection..... 126
6.5 Development of landspouts and tornadoes 127
6.6 Recommendations 130
Appendix……142
References 147

List of Figures

Figure 1.1: The topography of South Africa as created from station heights (Source: SAWS, 2020). 3

Figure 1.2: The generalised rainfall distributions according to seasons (Source: Botai *et al.*, 2018). 4

Figure 1.3: The Thunderstorm Spectrum (Source: learnweather.com)..... 6

Figure 2.1: Schematic profile with multiple hazards associated with supercell storms (Source: Schratz, 2016), as adapted from Bluestein and Parks (1983) and cited in Puskeiler (2013). 10

Figure 2.2: Supercell storm at Klein Kariba, about 5 km north of Bela-Bela, South Africa, at 18:30 on 10 November 2013 (Labels adopted and modified from Marquis *et al.* (2012); Photo source: Des Erasmus). 14

Figure 2.3: Schematic presentation of mountain-generated wind with thunderstorm development on the lee side (Source: WMO, 1978). 17

Figure 2.4: Observed cyclonical vorticity advection (Photo source: Lucky Mthombeni)..... 19

Figure 2.5: Rapid developing thunderstorm is shown in Figure 2.5a taken at 17:40 SAST on 19 April 2019 (Photo source: Mr Tumo Xaba). Satellite image at 17:45 in Figure 2.5b was supplied by the EUMETSAT and shows the distribution of the CCTs over and around Bethlehem in the Free State province. The middle dash of the arc to the south-west of this city shows the coldest section of the convective clouds and is linked with red oval circle in Figure 2.5c and the picture in Figure 2.5a. 20

Figure 2.6: Structure of a tornado observed at several stages of its life cycle. Sketches show a funnel cloud with resultant debris (Source: Klemp, 1987)..... 23

Figure 2.7: Latitudinal and longitudinal differences between the USA and South Africa (Modified from Satsig, 2011)..... 24

Figure 2.8: Idealised plan view of supercell thunderstorms on satellite and low-level precipitation by horizontally scanning RADAR (Source: Houze, 2014)..... 25

Figure 2.9: Idealised frequency of lightning leading to additional severe thunderstorms (Source: Williams *et al.*, 1999). 28

Figure 3.1: The Cartesian plane in black solid lines depicting unit vectors i, j and k with respective x-, y-, and z-directions, as modified from Holtan (1972). Idealised thunderstorms (downwind storm (S_1) along the red vector and upwind storm (S_2) along the green vector) first move in parallel in x-direction for a given time (t_n). The grey shapes underneath the intensified $S_1(t_{n2})$ represent significant topography that has the tendency to deform near surface low with occurrence of strong convection and

storm intensification. On some occasions, S_1 deviates onto y-direction such that its increasing gust front initiates and increase localized rotational tendency with respect to height (z-direction) when it interacts with the increasing gust front of the S_2 40

Figure 3.2: Interaction of the gust fronts of S_1 and S_2 from time t_{n5} as expanded from location P(x,y,0) and its vicinity in Figure 3.1c. Figure 3.2a represent the horizontal view of gust fronts as cold fronts shown in Figures 2.1 and 2.8. Marked difference in the velocities of the gust fronts of S_1 (in blue colour) and S_2 (in red colour) together with their directional effect typically initiate strong wind shear and vorticity (the rotational flow of fluids). Figure 3.2b is the vertical cross-section at P(x,y,0) and shows the colder and denser gust front of S_1 rapidly undercuts the gust front of S_2, with lifting of rotational flow into S_1. Gravity of heavier and denser air usually drops the base of the S_1 with potential for tornadogenesis.

Figure 4.1: Summary of MTS weather circulations associated with severe thunderstorms for the period June 2016 to June 2021. (Source: author after the analysis of data in the Appendix). 46

Figure 4.2: Rate of decision-making in reference to MTS circulations over South Africa for the duration June 2016 to June 2021. (Source: author after the analysis of data in the Appendix)..... 48

Figure 4.3: Comparison of surface circulations and wind flow (barbs) at 13:00 UTC on 15 December 2018. The UM and ERA5 model outputs are respectively shown in 4.3a and 4.3b with more focus in the subregion highlighted in red. 50

Figure 4.4: Comparison of MTS circulations and wind flow (barbs) at 13:00 UTC on 15 December 2018. The UM and ERA5 model outputs are respectively shown in 4.4a and 4.4b with more focus in the subregion highlighted in red. 51

Figure 4.5: Thunderstorm movements between 13:00 UTC and 14:00 on 15 December 2018. The general northward movement of storms along the Magaliesberg mountain range in 4.5a to 4.5c are demonstrated with blue arrows in 4.5d. Small-scale stationary storm to the north of Ga-Luka (at Sun City) persisted for nearly an hour as the times on 4.5a and 4.5e show. The ultimate merger took place a few minutes leading 14:00 UTC. (Sources: 4.5a to 4.5c – EUMETSAT; 4.5e and 4.5f – SAWS). 54

Figure 4.6: Storm impacts at Sun City Resort. Large quantity of small-sized hailstones with flash-flooding underneath is shown in 4.6a. Flooded resort is shown in part in 4.6b. 55

Figure 4.7: The 500 hPa comparison of circulations and winds at 12:00 UTC on 24 Jan 2020. Outputs of UM and ERA5 models are respectively shown in 4.7a and 4.7b. The dashed lines represent the trough axis. 59

Figure 4.8: The 850 hPa comparison of circulations and winds at 12:00 UTC on 24 Jan 2020. Outputs of UM and ERA5 models are respectively shown in 4.8a and 4.8b with deep surface trough on the west-central region of South Africa..... 60

Figure 4.9: Convective cloud pattern linked with a baroclinic well-defined MTS trough in Figure 4.7a. Storms were still developing in Figure 4.9a, intensifying in 4.9b and 4.9c. (Source of images: EUMETSAT). 61

Figure 4.10: Increase of CAPE amounts related to solar heating as shown by the ERA5 reanalysis model between 06:00 UTC and 12:00 UTC on 13 February 2018 in 4.10a and 4.10b respectively. 64

Figure 4.11: The 500 hPa pressure pattern (black contours) and the winds (barbs) at 13:00 UTC on 13 February 2018. Outputs of the UM and ERA5 models are respectively shown in 4.11a and 4.11b. The subregion of interest is highlighted in a red circle..... 66

Figure 4.12: The 850 hPa pressure pattern (black contours) and the winds (barbs) at 13:00 UTC on 13 February 2018. Outputs of the UM and ERA5 models are respectively shown in 4.12a and 4.12b. The subregion of interest is highlighted in a red circle..... 67

Figure 4.13: Thunderstorm initiation, movement and intensification. 4.13a and 4.13b represent the initiation of thunderstorms in the valley, shows the south-eastward movement to the curved mountain to the north of Calvinia where it intensified. Figures 4.13c and 4.13d show the unusual northwards movement in the afternoon and evening hours of 13 February 2018. (Source of images: 4.13a to 4.13c – EUMETSAT; 4.13d - author output topography data on GrADS)..... 68

Figure 4.14: Aftermath of severe thunderstorms occurring during the early evening of 13 February 2018 at Brandvlei. Island-like surfaces, which were reported to have resulted from heavy rain and flooding with remnants of hailstones on a photo taken on the morning of 14 February 2018. (Photo source: Beeld newspaper) 69

Figure 4.15: Comparison pressure analysis (black contours) and wind (barbs)s at 500 hPa at 0600 UTC on 01 September 2020 using UM and ERA 5 models in 4.15a and 4.15b, respectively. 71

Figure 4.16: Comparison pressure analysis (black contours) and wind (barbs)s at 850 hPa at 0600 UTC on 01 September 2020 using UM and ERA5 models in 4.16a and 4.16b, respectively. 73

Figure 4.17: Positions of 500 hPa low with associated winds at 18:00 UTC on 02 September 2020. Outputs of the UM and ERA5 models are shown in 4.17a and 4.17b . Area of interest is indicated in red..... 74

Figure 4.18: Positions of 850 hPa low with associated winds at 18:00 UTC on 01 September 2020. Outputs of the UM and ERA5 models are shown in 4.18a and 4.18b, respectively. Area of interest is circled in red..... 75

Figure 4.19: Comparison of 500 hPa pressure analysis and amounts of vorticity advection (VORT. ADV.) (shaded) at 00:00 UTC on 1 and 2 September 2020. The Vort. Adv. is calculated at x 10^{-5} s^{-1}. Amounts of VORT. ADV. are shown in 4.19a with significant increase of these amounts in 4.19b. 76

Figure 4.20: Isolated cold convective clouds associated with steep COL and cloud thinning on 2 September 2020. Shallow convective cloud that moved over Niewe Bethesda (in the red circle) are shown in 4.20a, 4.20b and 4.20c. (Source of images: EUMETSAT) 77

Figure 4.21: Impacts of strong gusty winds at Niue Bethesda on the early morning of 2 September 2020. Uprooted tree and broken stem in 4.21a and 4.21b are respectively shown as a sample of other storm-impacted trees..... 78

Figure 5.1: Tornado occurrences in association with MTS circulations in the idealised LSHC and HSLC environments. (Source: author after analysis of data from Caelum). 87

Figure 5.2: Trajectories and partial deflection of thunderstorms with the development of new downwind cell between 11:30 and 12:00 UTC on 17 March 2020. The gust front of the storm near Kurland in the north-west probably led to the development of the storm near Richmond in 5.2a. These storms are respectively labelled Storm A and Storm C in 5.2d. The storm to the south-west of Richmond in 5.2a intensified, deviated to the left and directed its gust front to the east in 5.2b. This storm is labelled Storm B in Figure 5.2d. These slow-moving storms continued to intensify in 5.2c. Optimally strong gust front and localised low-level wind shear could be inferred in the storm near Richmond (red circle in 5.2b) to the effect that the tornadogenesis occurred in Figure 5.2e..... 89

Figure 5.3: The tornadic storm on 11 December 2017 at 15:15 UTC. The ordinary storm (5.3a) typically intensifies into supercell storm (5.3b) on an encounter with curved ELEV (5.3c). The likelihood of tornadogenesis (5.3d) improves due to the gust front of the storm in the upwind. The ERA5 on 5.3e showed no localised vertical wind shearing near the ground surface with a possibility of ordinary storms. (Sources: 5.3a to 5.3c – EUMETSAT; 5.3e – SAWS)..... 91

Figure 5.4: Cross-sectional analysis of winds and relative vorticity. Tropospheric conditions are shown at 11:00 UTC on 17 March 2020 for Richmond in the Northern Cape in Figure 5.4a and at 15:00 UTC on 11 December 2017 for Vaal Marina in the Gauteng province in Figure 5.4b..... 92

Figure 5.5: Thunderstorm analysis by meteorological tools on 30 December 2017 with consideration of topographic features. Meteological satellite images in 5.5a to 5.5c

show storm intensification with cooling of CTTs. RADAR refectivities with hook echoe featurein 5.5d shows bottom-view scan at 3 km, the event that occurred soon after the storm in 5.5b. Storms propagated towards the from the north-west of Vereeniging into the City of Johannesburg Metropolitan Municipality. The intensification of these storms is related to the topograpgical features in 38e. (Sources: 5.5a to 5.5c – EUMETSAT; 5.5d – SAWS). 94

Figure 5.6: Communication that follwed the analysis of meteorological images in Figure 5.6 and subsequent events. A post on X account in Figure 5.6a shows a landmark tornado nowcast. Figure 5.6b is call log of the resident at Protea Glen which coincides with first tornado touchdown and confirm it was about 5 minutes after the tornado warning was issued. Figure 5.6c shows flash-flooding at Trade Route Mall, Lenasia on a photo posted at 17:58 UTC on 30 December 2017. A short summary of extreme events and acknowledgement of the receipt of weather warning was made by the South African politician in Figure 5.6d. 95

Figure 5.7: A band of thunderstorms along the leading edge of the steep COL. The intense thunderstorm cell that moved over Matyeba mountain (i.e. red circle on parts of 5.7b and 5.7c, led to the tornado strength of 252 km/h and the shaking of well-anchored, solid buildings in Mthatha. 97

Figure 5.8: Cross-sectional analysis of winds and relative vorticity. Tropospheric conditions are shown for Protea Glen in Gauteng at 14:00 UTC on 30 December 2017 in Figure 5.8a and for Mthatha in the Eastern Cape province at 12:00 UTC on 7 October 2019 in Figure 5.8b. 98

Figure 5.9: Analysis of meteorological conditions. CAPE amounts at 06:00 UTC as calculated by the UM (5.9a) and ERA5 (5.9b). 850 hPa Pressure (contours) and wind (barbs) at 14:00 UTC as calculated by the UM (5.9c) and ERA5 (5.9d). 500 hPa Pressure (contours) and wind (barbs) at 14:00 UTC as calculated by the UM (5.9e) and ERA5 (5.9f). 101

Figure 5.10: CAPE amounts at 14:00 UTC as calculated by the UM (5.10a) and ERA5 (5.10b) 102

Figure 5.11: Multicell thunderstorms that rapidly intensified to the north of Ulundi on the afternoon of 23 November 2019. Rapid cooling of CTTs just to the west of Ulundi in Figure 5.11b could be inferred to signal potential for large hailstones and very strong downslope on the lee side of the Nkonjeni mountain in Figure 5.11d. Topography-enhanced strong gust front could have rebounded near and forming a new cell at eDlebe where tornado in Figure 5.11e resulted 103

Figure 5.12: Tornadogenesis in the main thunderstorms due to the interaction of its inflow sector with the strong gust front of the upwind thunderstorms. Type A1 in 5.12a shows the tornadogenesis typically occurs in a storm after its deflection and interacts with the gust front of the intensifying upwind storm which is steered by the

mean wind flow. Type A2 in 5.12b tornadogenesis after the deflection strong gust front effected from the Bernoulli effect and wind channelling. Type A3 in 5.12c shows the tornadogenesis after the deflection of the rapidly developed storm forming cross wind with the strong gust front generated by the Bernoulli effect. Type A4 in 5.12d shows the tornadogenesis after the deflection of the storm generated from strong multicell gust front forming cross wind with the strong gust front of the dissipating storm. (Mountain drawings and background modified: www.fantasticmaps.com; valley in 45b was taken from www.freepik.com). 105

Figure 5.13: Tornadogenesis on the lee thunderstorms generated from the strong gust front enhanced by the Bernoulli effect on the significant concave topography. Type B1 in 5.13a shows the additional effect from the strong gust front of the secondary upwind thunderstorm. Type B2 in 5.13b shows the additional rotational effect from strong negative vorticity advection, which is related to the steep MTS troughs or COLs. (Mountain drawings and background modified: www.fantasticmaps.com). . 106

Figure 5.14: Sudden development of the landspout due to the influence of the non-precipitating convective clouds. Landspout development near pyramidal or tabletop peak showing Type A1 and Type A2 in 5.14a and 5.14b due to the strong gust front enhanced in the vortex line between two aretes. Landspout development Type A3 shown in 5.14c due to the interaction of the inflow sector of the deflected storm with the strong gust front of the organised non-precipitating thunderstorms and the Bernoulli effect. Landspout development Type A4 in 5.14d due to the sudden lift of the enhanced strong gust front channelling and rapid dissipation of the organised convective clouds. (Mountain drawings and background modified: www.fantasticmaps.com)..... 107

Figure 5.15: The vertical profile of variables at Bloemfontein airport on 7 September 2005 at 12:00 UTC. (Source: University of Wyoming with data from the SAWS).. 109

Figure 5.16: The distribution of tornadoes (triangles and squares) and landspouts (diamond shape) across South Africa. 111

Figure 5.17: Distribution of tornadic supercell storms across South Africa (June 2016 to June 2021). Matured tornadic supercell storms in interaction with the gust front of adjacent upwind storm (open triangle), with typical semi-stationary tornadic supercell rapidly developing due to the enhanced downburst of the intense upwind storms on the significant topography..... 112

Figure 5.18: Seasonal distribution of tornadoes across South Africa. 114

Figure 5.19: Seasonal distribution of CAPE across South Africa. 114

Figure 5.20: Analysis of storm features using images of meteorological RADAR at Irene (Pretoria) as at 14:16 UTC on 8 January 2018. Red oval in 5.20a highlights the reduced reflectivity (hook echo) in response to the cold gust front of a larger thunderstorm moving in opposite direction. Lime yellow in 5.20b highlights weak

circulating radial winds (i.e. inbound-outbound maxima) where a pink colour shows low-level wind moving away from the RADAR while light green colour shows low-level wind moving towards the RADAR. (Source of image: SAWS). 115

Figure 5.21: Relationship of ENSO phases with tornado frequencies. 119

Figure 5.21: Relationship of ENSO phases with tornado frequencies (continued). .. 120

Figure 5.21: Relationship of ENSO phases with tornado frequencies (continued). .. 121

List of Tables

Table 1: Enhanced Fujita scale following the relatively consistent marginal bias between the radial winds estimated by the Doppler RADAR and actual wind observations. The update was first used from February 2007 (Source: NWS, 2024). 26

Table 2: Influence of temperature on humid environment on 13 February 2018. **Error! Bookmark not defined.**131

Table 3: Tornadic supercell with upwind thunderstorm 133

Table 4: Tornadic storm influenced by intense storm across significant topography 135

Table 5: Tornadic multicell with enhanced gust front from upwind multicell..... 139

Table 6: Landspouts (Weak EF0 and EF1) Tornadoes 141

Units

s^{-1}	measure of rotation per second
^{O}C	degrees Celsius
gpm	geopotential height in metres
hPa	hectoPascal
$J.kg^{-1}$	Joules per kilogram
km	kilometres
m	metre
$m.s^{-1}$	metres per second
$m^{-2}.s^{-2}$	per metre squared per second squared
dBZ	decibel relative to Z (RADAR reflectivity)

Direction

E	East

N	North
S	South
W	West

Symbols

%	percent
θ_e	equivalent potential temperature
$\int$	integral

Abbreviations

AGL	above ground level
AMSL	above mean sea level
CTT	Cloud-top temperature
ECMWF	European Centre for Medium-range Weather Forecasts
e.g.	exempli gratia (for example)
HSHC	High Shear - High CAPE
HSLC	High Shear - Low CAPE
i.e.	id est (that is)
IOD	Indian Ocean Dipole
KZN	KwaZulu-Natal
LI	Lifted index
LLM	Low-level Mesoscale
LSHC	Low Shear - High CAPE
LSLC	Low Shear - Low CAPE
MTS	mid-tropospheric
NWP	Numerical Weather Prediction
SRH	storm-relative helicity
TTT	tropical-temperate trough
UKMO	United Kingdom Met Office
UM	Unified Model
USA	United States of America
UTC	Coordinated Universal Time
WMO	World Meteorological Organization
WRC	Water Research Commission
X	a social media platform formerly known as Twitter

Acronyms

CAPE	Convective Available Potential Energy
COL	Cut-off low
ELEV	Elevation
ENSO	El-Niño Southern Oscillation

ERA5	fifth generation ECMWF reanalysis
EUMETSAT	European Organisation for the Exploitation of Meteorological Satellites
EW4ALL	Early Warning for All
GrADS	Grid Analysis And Display System
RADAR	radio detection and ranging
SAST	South African Standard Time

Abstract

South Africa experiences a variety of severe thunderstorms which occasionally leads to a large quantity of small-sized or large-sized hailstones, heavy rain and flash flooding, strong damaging straight-line winds, and/or even tornadoes. For the base period, June 2016 to June 2021, a significant percentage of these severe storms was triggered by topographic features. The Unified Model (UM) at 4 km horizontal grid resolution was used and found to be unable to predict topography-generated vertical wind shear and the associated severe thunderstorms. This inability of the model necessitated the development of a conceptual model by relating the rapid cooling of the cloud-top temperatures with high resolution topographic maps. This means, satellite images were used to deduce the connection of atmospheric fluids (gust fronts) with near linear, concave and/or downslope topographical features. Severe thunderstorms included those connected to the large amounts of vorticity advection (e.g. 500 hPa level), development of low-level mesoscale circulations within the synoptic settings and the resultant vertical wind shear in the lower tropospheric levels. Large amounts of negative vorticity advection are typical with strong horizontal shear and curvature; they are often correlated with trough axes that lean from the south-west to north-east. The usage of large amounts of negative vorticity advection transcends to whether discrete severe thunderstorms will be characterised by heavy rain and flash-flooding or hail with damaging winds. Moreover, the interaction of topography with gust fronts of the upwind thunderstorms linked with large amounts of negative vorticity advection is also investigated. The impacts of storms studied in this dissertation posed a major threat to property, livelihood, agriculture, human and animal lives or even immediate to residual economic loss. This research is aimed at improving the service level for the benefit of disaster management agencies and the public at large. An in-depth study of microscale events such as tornadoes and landspouts was also conducted to improve lead-time for their nowcasting.

Chapter 1: Introduction

1.1 Study overview

The development of severe thunderstorms across South Africa is associated with topography, apart from other triggers (Garstang *et al.*, 1987; Steyn and Bruintjes, 1990; Simpson and Dyson, 2018; Liesker *et al.*, 2024). Authors such as Evans (1992), Barnes (2001) and more recently Alfahmi *et al.* (2019), also noted topography as an instigator of severe thunderstorms in other parts of the World. Van Heerden and Taljaard (1998) confirmed this finding but also broadened the domain to include southern Africa as a whole (i.e. 5°S and 35°S). An earlier study by Jury (1984) noted that the movements of thunderstorms are often controlled by the interaction of cyclonic fluids and mountain ranges. In some cases, severe thunderstorms developed due to the interaction with the gust front of the upwind (up-shear) thunderstorms (Terblanche *et al.*, 2000; Huang *et al.*, 2017). This dissertation studies and expands on discrete severe thunderstorm occurrences which were connected to the interaction of topographic features with inferred gust fronts. Other severe events of interest developed in the downwind (down-shear) thunderstorms when they connect with the respective gust fronts of the upwind thunderstorms. Still other severe events occurred during the merger of upwind and downwind thunderstorms. Discrete severe thunderstorms were also studied in relation to the middle and mid-tropospheric (*hereafter*, MTS) circulations to differentiate the influence of topographic features to the development of severe thunderstorms from the influence of the amounts of negative vorticity advection (e.g. at 500 hPa level). A theoretical framework could be developed from the interaction of topographic features and inferred optimally strong gust fronts is necessary to nowcast tornadoes and landspouts.

1.2 Location and topography of South Africa

Severe thunderstorms, which occurred across South Africa from June 2016 to June 2021, are investigated in Chapters 4 and 5. South Africa lies between the 22^{o} to 35° South (S) and 16^{o} to 33° East (E) (Benhin, 2006; Engelbrecht *et al.*, 2011; Landman *et*

al., 2012). The country is located largely in the subtropical latitudes (a zone between ±23.40° and ±30.00°). The investigation focussed on the influence of the topographical features and gust fronts of the upwind thunderstorms in the development of severe thunderstorms. In some cases, the synergistic effects of the 500 hPa vorticity advection are also considered. The composite topography of South Africa is shown in Figure 1.1. This map is composed of three primary regions: the central plateau (i.e. interior), nearly continuous escarpment (i.e. regions of steep orography) and a narrow strip of low-lying land near the coast (Benhin, 2006). Low-lying land (i.e. the coastal belt) is generally elevated at heights from sea level to 200 m but the low-lying land gently widens on the extreme north-eastern KwaZulu-Natal side (*hereafter*, KZN) (Botes, 2014). The land is elevated at 200 to 500 m further northwards towards the Lowveld of Mpumalanga and Limpopo. The topography of South Africa is rather complex along the escarpment where various mesoscale features develop (Pretorius, 2013; Maisha, 2014). Steep elevations (ELEVs) act as obstacles to the surface wind flow in the region and typically contribute to deep convection and tight rainfall gradients (Engelbrecht *et al.*, 2002; Anders *et al.*, 2006; Tshehla, 2008; Nel and Sumner, 2008; Dedekind *et al.*, 2016). The escarpment in the eastern areas of South Africa has ELEVs between 700 and 1 400 gpm above mean sea level (AMSL) in Limpopo (Mukheli, 2018), about 1 900 to 2 400 gpm AMSL in Mpumalanga (Pretorius, 2013). KZN has two additional topographical zones: the central zone (i.e. the midlands, found between 200 and 1 400 m) and escarpment (found between 1 400 to 3 500 m) on the western part of the province (Engelbrecht *et al.*, 2002; Botes, 2014). The interior covers a little over two thirds of South Africa and comprises the Highveld areas, the heights of which are about 1 500 gpm (Estie, 1984; Tennant and Van Heerden, 1994; Zunckel *et al*., 1996). The interior of South Africa drops gently to about 1 000 m in the western region of the country (Blamey and Reason, 2009). The averaging effect in the development of the composite topographical map in Figure 1.1 made a host of surface features invisible. To mitigate this challenge, high-resolution topographical maps were utilised in case studies in Chapters 4 and 5. High-resolution topographical maps were used to show the effect of surface features on severe thunderstorm development.

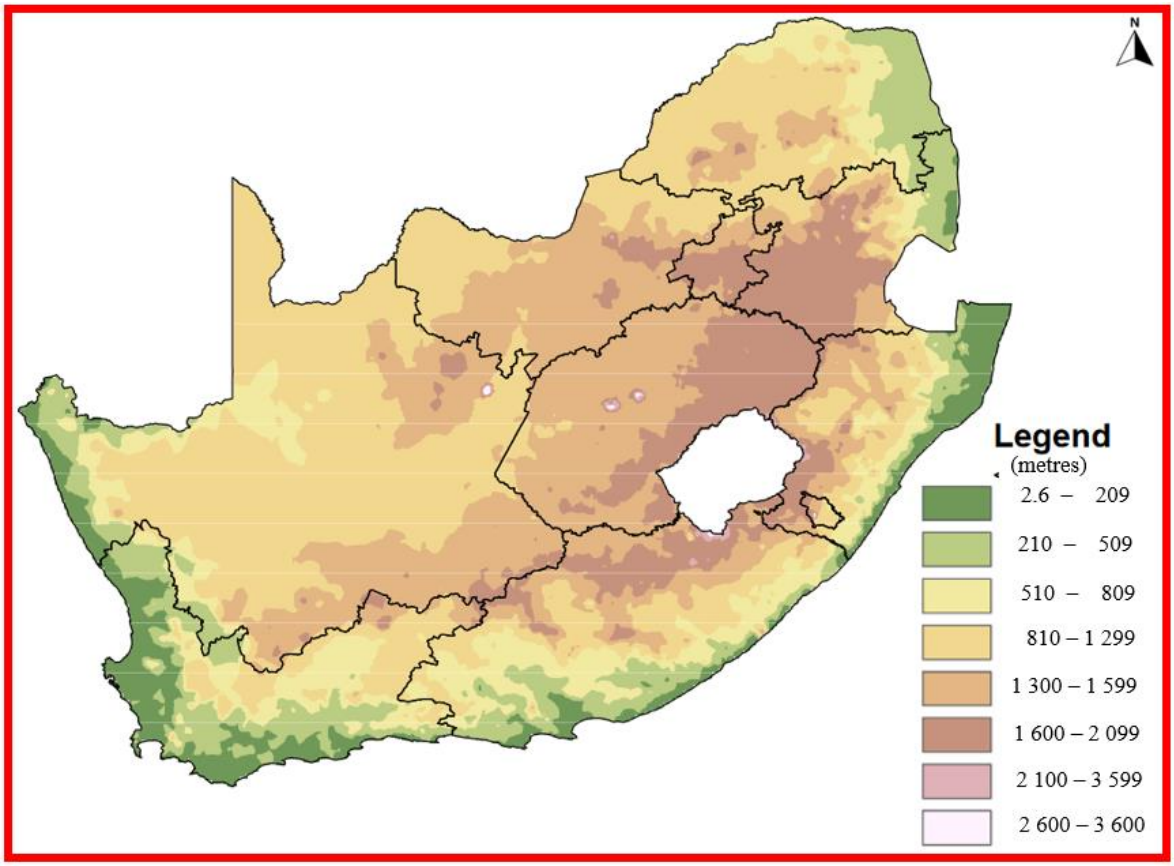


Figure 1.2 : The topography of South Africa as created from station heights (Source: SAWS, 2020).

Important factors of the surface features included their positions, shapes, sizes, orientations and ELEV (Adamson, 1981). The rate of wind uplift depends on the wind direction, including the height and shape of significant topographic (e.g. mountain network) ELEV (Spellman, 2013). The potential for the development of severe thunderstorms owing to mesoscale features are discussed at length in Sections 2.4, 2.5 and 2.6 as well as in the case studies in Chapters 4 and 5.

1.3 Climate of South Africa

Severe thunderstorms, as listed in the Appendix, were used in relation to the circulations in the MTS level (500 hPa). This effort was aimed at establishing whether severe thunderstorms are biased to MTS cyclonic (i.e. clockwise) or anticyclonic (i.e. counter-clockwise) circulations. Therefore, the alignment of severe thunderstorms was tested against the South African climate. Tropical atmospheric circulations become dominant across South Africa during the peak summer months, December, January and February

(D'Abreton and Lindesay, 1993; Landman and Tennant, 2000; Dyson *et al.*, 2015; Chikoore *et al.*, 2021). As illustrated in Figure 1.2, there is pronounced rainfall seasonality over the central and eastern regions of South Africa (Ratnam *et al.*, 2013; Engelbrecht, 2015; Dedekind *et al.*, 2016; Blamey *et al.*, 2016; Botai *et al.*, 2018).

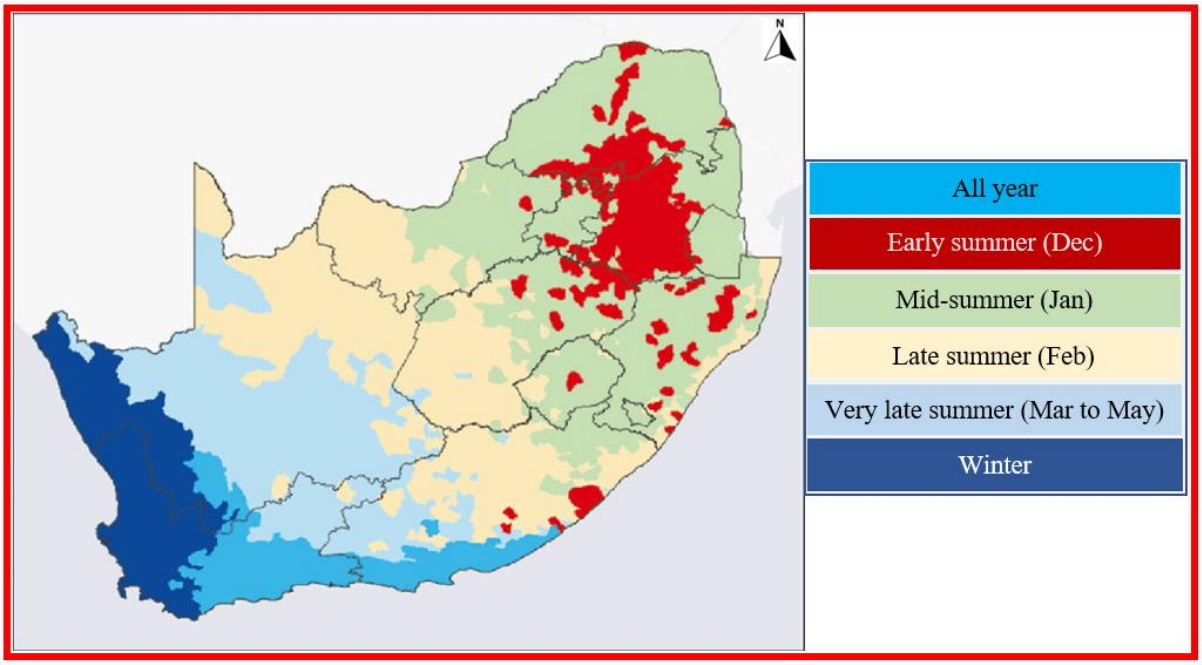


Figure 3.4: The generalised rainfall distributions according to seasons (Source: Botai *et al.*, 2018).

Climatic zones (i.e. Koppen-Geiger climate classification) may be used to study severe thunderstorms (Schulze, 1986; Tyson and Preston-Whyte, 2000; Bhavika, 2007; Joubert, 2008). South Africa is on average situated underneath the descending component of the Hadley cell circulation (Dube and Jury, 2000; Corlett, 2013). The country is positioned along the path of a high-pressure belt and the anticyclonic (i.e. counter-clockwise) circulations in the middle to upper (i.e. 600 to 200 hPa) levels are dominant (Taljaard, 1958; Zunckel *et al.*, 1996; Ndarana and Waugh, 2010). Anticyclonic flow is typically associated with strong zonality and subsidence with a consequential 80% of days representing a combination of cloud-free conditions with a few clouds (Van Loon, 1972; Harrison, 1984; Freiman and Tyson, 2000). Latitudinal position to the south of 30°S (e.g. parts of the Western Cape, Eastern Cape and KZN provinces) are likely to cause moderate to strong baroclinicity, which promote the development of severe storms (Barry and Carleton, 2001; Favre *et al.*, 2013).

Topography and proximity to the warm moisture source (e.g. the warm Indian Ocean) generally maintain humid climate in the east (Engelbrecht and Landman, 2010; Apaydin *et al.*, 2011). Additionally, the Agulhas Current, which is approximately 20 km away from the coastal line of KZN province, influences the high frequency of severe thunderstorms across this province (White, 2000; De Boer *et al.*, 2013; Morris *et al.*, 2017). Heat troughs have a tendency to develop in the lower troposphere (i.e. 850 and 700 hPa) in the austral summer months (Taljaard, 1996). The south-western region and to a lesser extent most of the western half of South Africa, receives the majority of its rainfall from cold fronts and associated synoptic scale wave troughs (Blamey and Reason, 2007). Precipitation to these western regions is sometimes associated with cut-off lows (COLs) (Engelbrecht *et al*., 2015). Additionally, Engelbrecht (2015) found that 28% of precipitation was contributed by tropical-temperate troughs (TTTs) with high variability in November, 46% by the ridging low-level high pressure, and 16% by COLs associated with ridging highs. But countrywide, most of the annual rainfall (about 60%) is thought to occur from TTT systems that control a band of convective storms (Harrison, 1984; Gill, 2008; Gijben, 2012; Ratna *et al.*, 2013; Hart *et al.*, 2013). TTTs are activated when steep MTS troughs or COLs develop at least to the east of 15° longitude and extend equatorward to between 30° and 10°S and often lead to substantial precipitation (Ndarana and Waugh, 2010; Reboita *et al.*, 2010; Favre *et al.*, 2013).

1.4 Thunderstorm classes

Previous studies of thunderstorms (i.e. convective storms) across various regions of the globe suggest three main classes in a thunderstorm spectrum, as summarised in Figure 1.3. These are single cell thunderstorms, multicell thunderstorms and supercell thunderstorms (Feldman *et al.*, 2022).

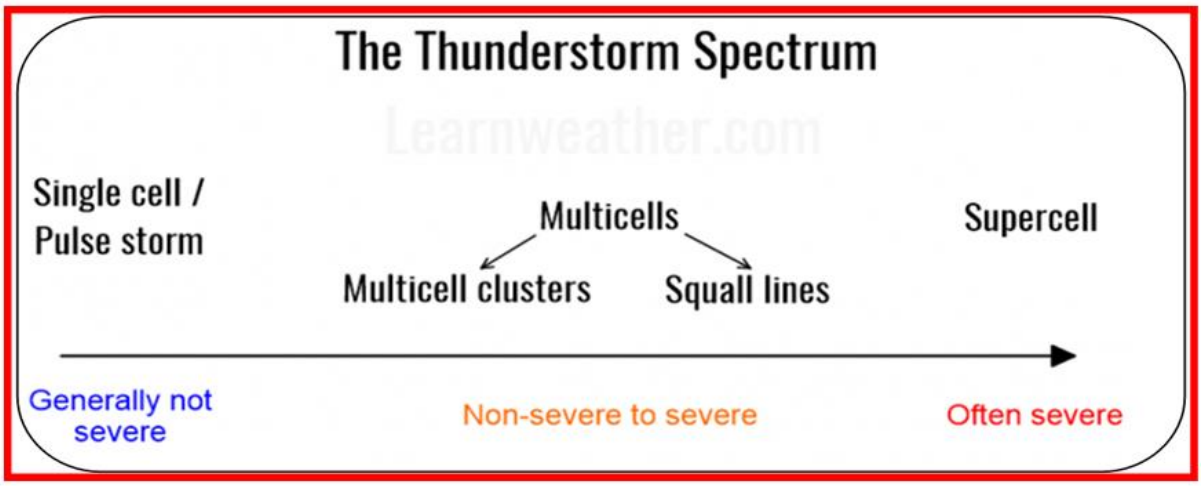


Figure 1.5: The Thunderstorm Spectrum (Source: learnweather.com).

The effects of these classes on the development of severe thunderstorms are reviewed in Chapter 2 and further discussed in the case studies mentioned in Chapters 4 and 5. In Section 3.4.1, cloud-top temperatures (hereafter, CTTs) of thunderstorms in these classes were utilised to determine their severity. Moreover, CTTs were used to assume the relative coldness of the gust front of the upwind thunderstorm relative to the inflow sector of the primary thunderstorm.

1.5 Rationale

The numerical weather prediction (NWP) model with a horizontal grid resolution of 4 km (e.g. the UM) is unable to resolve topography-generated vertical wind shear that occur within this grid. The UM at 4 km will be referred to as the UM in this dissertation. Consequentially, this presents a greater challenge on operational forecasting in that the timely prediction (of at least 2 to 36 hours) of the associated severe thunderstorms is significantly reduced. This challenge necessitates the need to develop conceptual models to study localised discrete severe thunderstorms. Conceptual models could be used for microscale events to the effect that nowcasting could be extended from a few minutes to more than an hour. Longer lead-times often serve as valuable input to the disaster management centres, to ensure preparedness and provide protection of the public and livelihoods. Further, economic losses such as in agricultural, construction, aviation and insurance industries, and other climate sensitive sectors could be reduced. An improved lead-time means early warnings will be communicated earlier using

different platforms such as social media, websites, mainstream media and disaster management agency networks.

This dissertation explores the severe thunderstorms that occurred across South Africa during the base period, June 2016 to June 2021. Storms that became severe when their trajectory encountered regions of pronounced near linear and/or concave topographies are considered. The rapid cooling of the CTTs was used in conjunction with high resolution topographic maps to deduce the connection between atmospheric fluids (gust fronts with cyclonic clouds) and the said topographical features. This means, satellite images were utilised because of the full coverage of South Africa and near complete data availability. On the other hand, the ground-based remote sensing tools (RADAR network) do not cover all regions of South Africa. Moreover, data from the RADAR network are typically reduced in cases of reactive maintenance but more so during electricity blackouts. The dissertation also considers the strength of the mean steering wind in the middle level layer (from 700 to 500 hPa) to anticipate whether the storm could be deviated (deflected) or be forced to move over during the encounter with the topographical features.

These efforts are in part the endeavour to achieve Early Warning for All (EW4ALL). EW4ALL is an initiative of the United Nations seeking to protect everyone on Earth, therefore also South Africa, from hazardous weather, water and climate events through lifesaving early warning systems (Gialletti and Alvar-Beltrán, 2023). Part of this initiative is run by the World Meteorology Organization (WMO).

1.6 Aim and objectives

1.6.1 Aim

The aim of this dissertation is to study a variety of severe thunderstorms over South Africa from June 2016 to June 2021 in order to understand the interaction of discrete thunderstorm gust fronts with topographic features. Understanding of this interaction is important for issuing warnings which could save lives and reduce socio-economic impacts. Particularly, low (e.g. 850 hPa) and middle (700 to 500 hPa) layers of

troposphere were used. Mesoscale circulations (e.g. MTS short waves) were considered within the synoptic circulations to reduce the region for which the potential for extreme thunderstorms existed. The influence of topography on the strengthening of the gust front and the development of severe thunderstorms (e.g. straight damaging winds and tornadoes) were delved into through a few case studies. Uprooted trees, hail damage and destruction of property were used as evidence for storms with damaging winds. Other cases, however, used heavy flash-flooding as an indicator of recent heavy rain. Gust fronts that contribute to the development of severe thunderstorms without much of topographic influence are also dealt with. Calculations of the 500 hPa vorticity advection were used to test their synergy with surface features in producing severe thunderstorms. However, to deepen the understanding, schematic thunderstorm models for severe thunderstorms, which occurred in similar fashion, were used to develop conceptual models that could be used to lengthen the lead-time. The development of algorithm and the subsequent automation of principles (i.e. developed for conceptual model) into the NWP models are beyond the scope of this dissertation.

1.6.2 Objectives

Objective 1: To study the development of severe thunderstorms across South Africa in terms of the topographical features and gust fronts of the upwind thunderstorms

Satellite images were used to identify severe thunderstorms, their seasonal and spatial spread over South Africa over a 5-year period (June 2016 to June 2021). Case studies of a few of these severe convective storms were used to determine the extent of topographic features, synoptic and mesoscale circulations (i.e. MTS zonal flow and MTS ridges, early development of MTS troughs, well-developed and steep MTS troughs or COLs) and/or a combination thereof. Such circulations may be associated with either low-shear and high convective available potential energy (CAPE) or high-shear and low CAPE environments. This dissertation envisages the improvement of the current forecasting processes.

Objective 2: To assess the storm events in terms of the synergy of the low-level circulations with the negative vorticity advection at 500 hPa at different orientations of a COL (or MTS troughs)

Characteristics and occurrence of events of the discrete severe thunderstorm were tested against the synergy of the low-level circulations with negative vorticity advection at 500 hPa at different orientations of a COL (or MTS troughs). Discrete storm of interest was studied by using a case study and is a prototype of such storms, which often occur behind the cloud band associated with COLs.

Objective 3: To formulate a theoretical basis for nowcasting the potential for tornadoes over South Africa

Reported tornadoes and landspouts were investigated using the meteorological satellite images to distinguish and group similar features. These features could be used to improve aspects of the NWP model simulations for nowcasting of the potential for the development of tornadoes (refer to Section 3.4.1.3 under methodology below).

1.7 Research questions

The following research questions are set for this study:

- What is the influence of synoptic MTS circulations in the formation of severe thunderstorms over South Africa?
- How do severe thunderstorms develop in relation to wind speed and direction in interaction with shapes and heights of the topography?
- Which additional factors are to be observed during severe thunderstorms for the development of tornadoes over South Africa?

Chapter 2: Literature Review

2.1 Definitions

Severe thunderstorms are storms that produce large hailstones or large quantities of small hailstones, flash-flooding, frequent rate of lightning flashes, damaging straight winds, tornadoes or a combination thereof (Letsie and Grab, 2015; Nielsen, 2015; Park and Jung, 2016; Özdemírm *et al*. 2019). The worst events of severe storms arise from supercell storms, which are characterised by deep, persistent rotating updrafts with storm widths ranging from 2 to 20 km (Moller *et al.*, 1994; Arnold, 2008; Simpson and Dyson, 2018; Wilson, 2019). Structure, dynamics and associated severe events are depicted in Figure 2.1**.** Severe thunderstorm events are studied individually in Section 2.6.

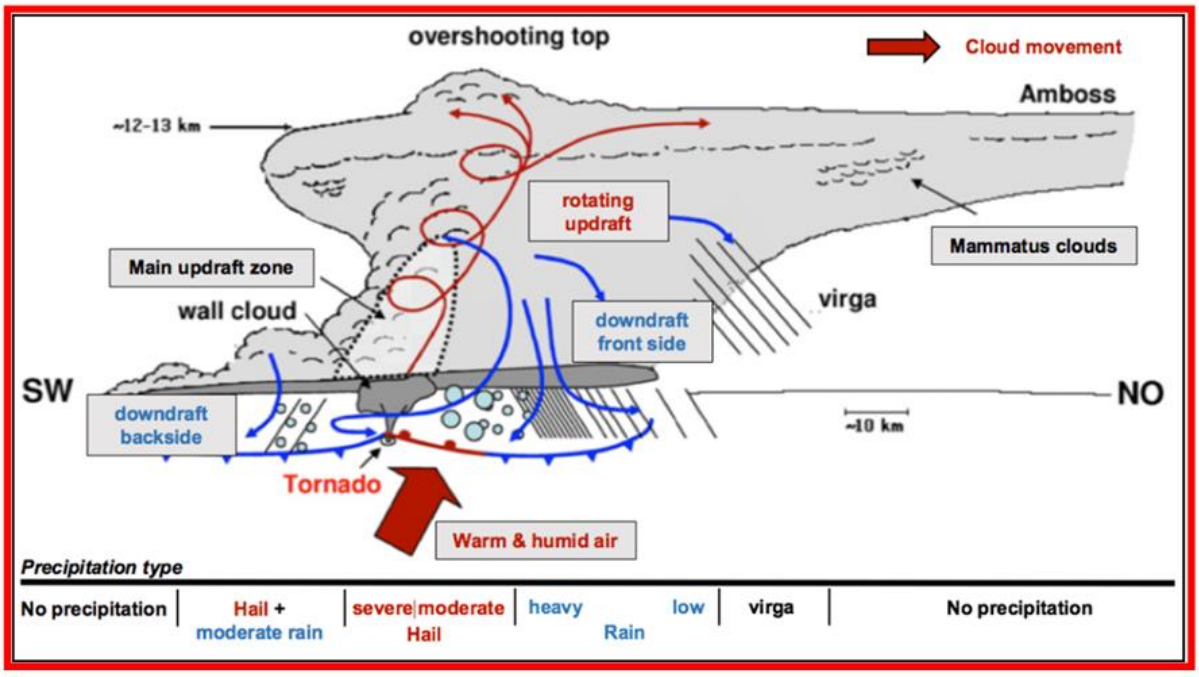


Figure 1.2: Schematic profile with multiple hazards associated with supercell storms (Source: Schratz, 2016), as adapted from Bluestein and Parks (1983) and cited in Puskeiler (2013).

Some supercell storms are possible under MTS circulations, which are characterised by baroclinic synoptic-scale or short-wave troughs resulting in strong tropospheric winds and large potential instabilities (Brady and Szoke, 1989). However, severe thunderstorms and other supercell storms occur in environments with weak or moderate

deep-layer shear in the lower to middle troposphere (Caruso and Davies, 2006; Simpson and Dyson, 2018). Low-level vertical wind shear is discussed in detail in Section 2.4 below.

2.2 Moisture sources

Forecasting severe thunderstorms requires identification of adequate moisture, extreme instability, lifting mechanism and vertical wind shear (Markowski and Richardson, 2010). South Africa experiences continual advection of cold maritime air from the south and warm continental air from the north (Singleton and Reason, 2006, 2007). Wind flows often cause the advection of unstable maritime air (e.g. from the warm Indian Ocean) onto the adjacent land (e.g. South Africa) (e.g. Durán-Quesada *et al*., 2012). Further, low-level moisture from the Agulhas Current is usually linked with a high frequency of thunderstorms occurring on the adjacent landmass (White, 2000; De Boer *et al.*, 2013). The warm Agulhas Current lies about 20 km off the east coast of South Africa (Morris *et al.*, 2017). Surface moisture with pronounced effect to the development of severe thunderstorms could also originate from the anomalously warm Indian Ocean (e.g. Mozambique Channel) (Simpson and Dyson, 2018). In some cases, unstable warm moisture is often transported to South Africa from tropical or temperate regions through patterns such as TTTs or tropical continental lows (van den Heever *et al.*, 1997; Jacobs, 2017; Webster, 2019). Significant influx of moisture over South Africa is typical during late spring and early autumn but particularly during peak austral summers (WRC, 2016).

2.3 Some triggers of severe thunderstorms

Low-level vertical wind shear was found to be one of the critical products required for the initiation and discrimination of thunderstorm severity (Markowski and Richardson, 2010; Barretta *et al.*, 2020). Vertical wind shear is discussed at length in Section 2.4. Further, Mathaba *et al.* (2012) associate diurnal heating with the development of low-level wind directional shear, with increased wind speed in increasing altitude. Simulations conducted by Chavas and Dawson II (2020) propose that there should be a steady thermodynamic and kinematic profile for severe convective storms to develop,

particularly in a well-moistened and unstable environment. Severe storms often require mesoscale features, which typically cause thermal heating, dryline and short-wave perturbations (Bluestein and Parker, 1993; Dedekind *et al.*, 2016). Diurnal effects in an environment with high-energy air (e.g. wet-bulb potential temperature of 20℃ or more) often lead to a substantial increase in the amounts of CAPE (Williams and Renno, 1993; Jayaratne and Ramachadran, 1998; Jayaratne and Keleshov, 2006). Low-level vertical shear linked with the increased quantities of CAPE may be used to differentiate between non-supercell and supercell events, rather than between tornadic and non-tornadic episodes (Moller, 2001). Such discrimination of severe thunderstorms requires the hodograph to detect straight lines (i.e. the environmental wind shear that does not turn with height) or curved lines (i.e. the environmental wind that turns with height). Triggers for (severe) thunderstorms should be in association with proportionally less the amount of convective inhibition in comparison with the CAPE amount (Woodhams *et al.*, 2019). Such triggers typically include any of the three known broad environments. One environment was found to have numerically less wind speed with large magnitudes of the CAPE. Such a conducive environment for the development of severe thunderstorm is discussed as the LSHC environment by Schultz *et al.* (2013) and King *et al.* (2017). The second conducive environment for severe thunderstorm development typically comprises numerically stronger wind speed with modest CAPE. This environment is described by Sherburn and Parker (2014) as High Shear - Low CAPE (HSLC) environment. The third, but rare environment, constitutes a combination of numerically stronger wind speeds with large magnitudes of CAPE (i.e. HSHC) (Brown *et al*., 2021). Dryline is another trigger along which relative warm moist low-level air meets cool arid air, leading to the optimal relationship between buoyancy (e.g. extreme surface-based instabilities) and vertical wind shear (Mitra *et al.*, 2012; Dyson *et al.*, 2015; Simpson and Dyson, 2018). In conditions favourable for thunderstorm development, the potential for severe storm events is accepted to be higher when low-level vertical wind shear exists (Craven and Brooks, 2004; Houston and Niyogi, 2007; Takemi, 2014). In the context of southern Africa (e.g. South Africa), Mulugeta and Simelani (2016) describe that the usefulness of vertical directional shear in the lower troposphere is dependent on the associated strength of the wind speed shear. These

authors describe the modest (pronounced) low-level wind speed shear as favourable for severe thunderstorms (destructive for thunderstorm development). Pronounced low-level wind speed shear diverts the unstable rising air from the surface, thus preventing the vertical development of thunderclouds. Speed and directional wind shear often result (or intensify) from a variety of meteorological conditions such as temperature inversions, land-sea breezes, frontal systems and/or strong surface winds due to adjacent thunderstorms (Jay, 2009). Low-level wind flow from the warm moisture source occurring simultaneously with mid-level winds flowing from dry source usually creates the horizontal vorticity (Hyndman and Hyndman, 2014). Horizontal vorticity is a product of directional wind shear with increasing wind speeds in increasing altitude (Schimid *et al.*, 1997; Mathaba *et al.*, 2012). Figure 2.2 shows that horizontal vorticity tilts into vertical vorticity when in contact with an active thunderstorm. Such small-sized severe thunderstorms are discussed in Section 2.4.

2.4 Localised inducement of low-level wind shear

2.4.1 Involving more than one storm

Secondary to severe thunderstorm forecasts, recognising the eminent development of such storms is required (Johns and Doswell III, 1992). A thunderstorm could affect the internal dynamics of the adjacent storm even without merging with it (Cox, 2000; Sano and Tsuboki, 2006; Tladi, 2018). An optimum degree of shear is necessary for the release of CAPE in the development of convective systems (e.g. towering cumulus or thunderstorms), otherwise shear that is too intense often leads to the demise of such convective systems (Takeda, 1966; Moncrieff and Green, 1972). Newly developed thunderstorm cells also have a tendency to cause variations in the general movement of larger storms (e.g. supercells) (AIC, 2000). The downdraft sector of a thunderstorm often causes straight-line wind gusts, which sometimes reach or exceed 50 knots (i.e. 25.7 metres per second or 92.6 km per hour) (Kruger *et al.*, 2016). Such gust fronts, including those linked with the rapidly developing cumulonimbus, augment low-level vertical wind shear, and is required for the inflow sector (updraft region) of the severe thunderstorm (Terblanche *et al.*, 2000; Doswell, 2001; Huang *et al.*, 2017). Terblanche

et al. (2000) further added that the area occupied by such downwind storm increases during natural evolution. The thunderstorm gust front that is supplied from evaporatively cold and spiralling downdraft usually leads to the baroclinic generation of near-surface horizontal vorticity (Trapp, 2018). Figure 2.2 shows that this near-surface horizontal vorticity is typically tilted vertically on interaction with the updraft sector of the downwind thunderstorms. In effect, rapid intensification of this vertical vorticity typically occurs (Lee *et al.*, 2006; Rogers and Weiss, 2008; Van Leer, 2013).

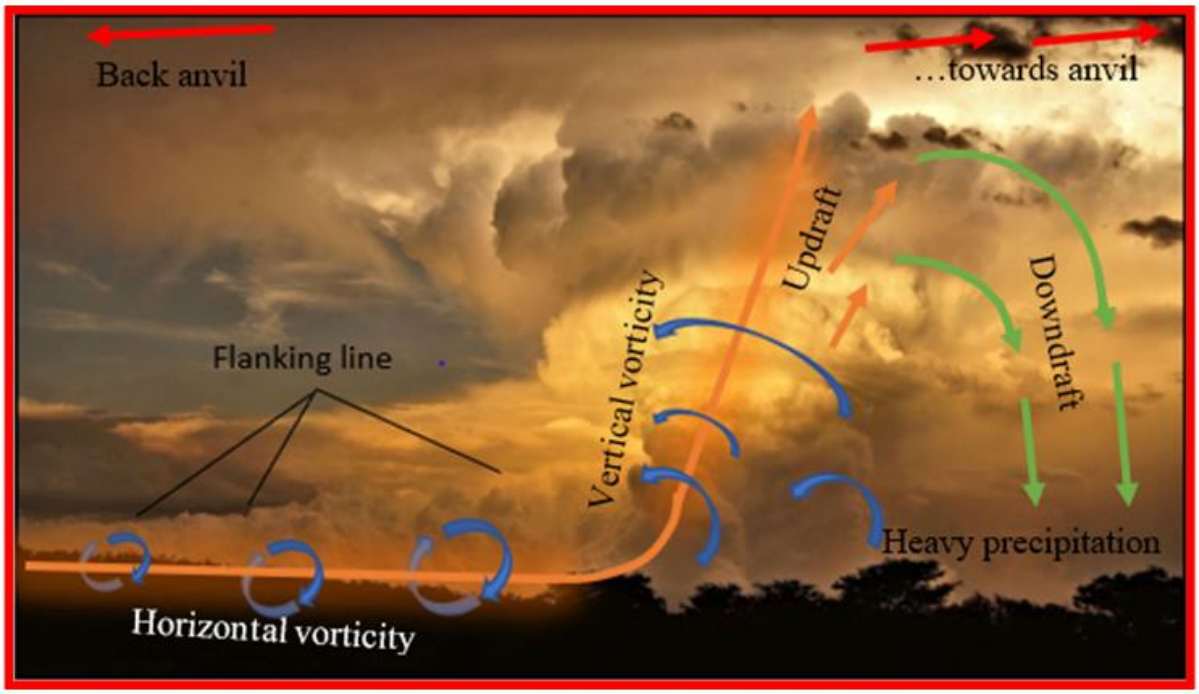


Figure 3.4: Supercell storm at Klein Kariba, about 5 km north of Bela-Bela, South Africa, at 18:30 on 10 November 2013 (Labels adopted and modified from Marquis *et al.* (2012); Photo source: Des Erasmus).

The temperature modification in the updraft with the resulting denser air may probably develop at a low-level mesoscale (LLM) below the cloud base within 1 km above ground level (AGL) (Trapp, 2018; Doswell III, 2001). LLM boundaries (or tornado cyclones) can provide lifting mechanism that help to initiate or intensify convective thunderstorms and the potential onset of tornadogenesis (Byers and Rodebush, 1948; Rotunno, 1979; Alexander *et al.*, 2018). Whether simultaneously or otherwise, thunderstorm outflows (i.e. gust fronts leading to LLMs) often remain separated from the updraft shear region vorticity (Betten *et al.*, 2018). As a result, over 50% of LLMs

do not produce tornadoes (Eastlund and Jenskins, 2000; Trapp *et al.*, 2005). Thunderstorms often move in the direction of mid-level (e.g. between 700 to 500 hPa) wind and light steering winds usually lead to slow-moving storms (AIC, 2000; Dyson, 2011). Mergers more often lead to the demise of the thunderstorms instead of a single strong updraft-downdraft separated pair (Bunkers *et al.*, 2006). The latter scenario occasionally occurs when the gust front of the upwind thunderstorms connects with the inflow (updraft) sector of the downwind thunderstorms, producing severe events (Bluestein and Parker, 1993; Bluestein and Weisman, 2000; Wurman *et al.*, 2012; Schultz *et al.*, 2013). The merging of supercell thunderstorms that effect a single updraft is very rare (Schultz *et al.*, 2013). Gust fronts from the intensified storms typically uproot trees and cause damage to property (NWS, 2004; Dean and Schneider, 2008; Hlalele, 2015; Seeley and Romps, 2015). Therefore, the development of severe convective storms is governed by a series of processes in the atmosphere, like a cascade rather than by isolated or random events (Martín *et al.*, 1997; Huang *et al.*, 2017).

2.4.2 Involving topographical features

Topography plays a major role in the circulations and weather systems of the landmass over southern Africa (e.g. South Africa) (Van Heerden and Taljaard, 1998). This might be because long-lived synoptic scale systems govern the development of mesoscale systems (Mass *et al.*, 2002; Maisha, 2014). Some of these mesoscale (or even microscale) systems with localised wind circulations are generated by topographical features (e.g. Lengoasa *et al.*, 1993; Alfahmi *et al.*, 2019). These features generate thermally and dynamically driven wind flows (Lennard, 2014; Koletsis *et al.*, 2016). Near-surface winds usually strengthen and converge as a consequence of the deepening of the surface low pressure, leading to localised vertical wind shear in the lower troposphere (Gray, 1968; Keshishian and Bosart, 1987; Alfahmi *et al.*, 2019). Low-level accelerations along with the vertical distribution of CAPE are favourable for the extremely rapid initiation of vorticity anomaly and tornadic supercells (Rasmussen and Blanchard, 1998; McCaul, 1991; Redelsperger *et al.*, 2002). The strength of localised wind circulations is typically stronger in the acute concave topographies, to the effect

that forced convection results in the rapid development of severe thunderstorms independent of organised rain-bearing (i.e. large-scale) circulations (Tennant and Hewitson, 2002). Such storms often become semi-stationary when moving into the network of valleys (e.g. concave significant topography) which often maintain steady localised vertical wind shear and vertical vorticity (WMO, 1969; Garstang *et al.*, 1987). Localised wind circulations appear to decrease with concave topographies at an obtuse angle. An obtuse angle, which forms between the near-linear significant topography and the original path of the storm, also increases the strengths of localised wind circulations. Quasi-steady deep rotating updraft from the inviscid fluids plays a vital role in producing the specific motion of the thunderstorm (e.g. supercell) (Schimid *et al.*, 1997; Duba, 2015; Spiridonov and Ćurić, 2019). Storms have a tendency to deviate to the left over the southern hemisphere region (e.g. South Africa), resulting in the cyclonic flow of fluids (clouds) in interaction with major topography in the region (Jury, 1984). Deviant storm motion is often referenced with the mean wind direction (Houze *et al.*, 1993; Johnson, 2002; Rae and Dyson, 2015). Some supercell storms do not veer off (Johnson, 2002) while others (Gao *et al.*, 2013) may be embedded in a cluster of clouds. These topographical arrangements appear to play a significant role in the development, sizes, distribution and frequency of storms such as supercells. Wind flows (e.g. gust fronts) that are channelled through topographical features converge and strengthen, and the interaction of such flows with the updraft corridor of the downwind thunderstorms intensify the vertical shear (Esau and Repina, 2012). Tropospheric conditions for such severe storms are more important in the short-term (i.e. 0 to 6 hours) range (Steyn, 1988; Olivier, 1990). Microscale features have sub-kilometre resolution, and most often occur within grids of the NWP models and are typically inferred to for triggering severe thunderstorms (Martín *et al.*, 1997; Engelbrecht *et al.*, 2011; Keat *et al.*, 2019). The area occupied by the storm increases during the natural evolution, reaching a peak within at least 20 minutes (Terblanche *et al.*, 2000). The topography-generated severe thunderstorms may be undetectable when they occur within the UM 4 km grid resolution, unless such storms move across such grids. Such severe thunderstorms are discussed in Chapters 4 and 5 of this dissertation. An air parcel that originates at a low level at the inflow region (e.g. thunderstorm gust front), climbs adiabatically over a

mountain with increased velocity and then descends on the lee side to form strong downslope wind-processes which are summarily referred to as the Bernoulli effect (Sun and Sun, 2015). The Bernoulli effect is graphically depicted in Figure 2.3.

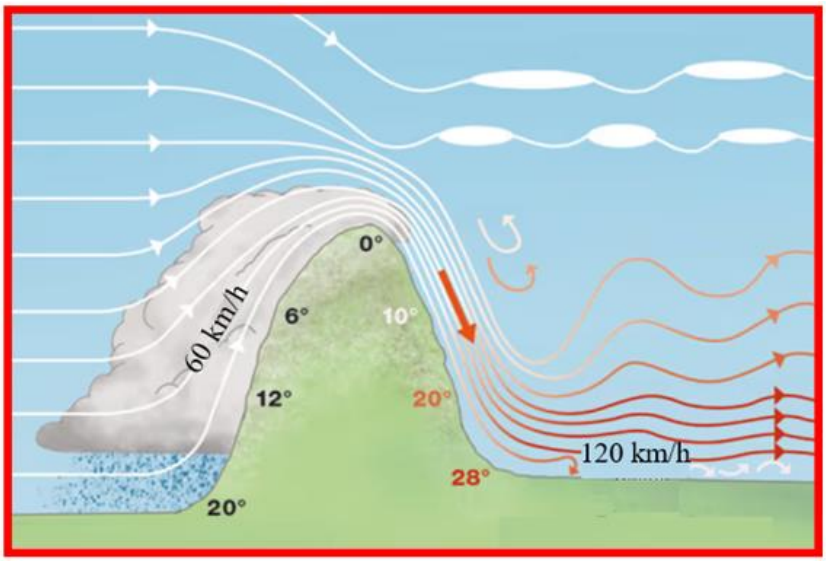


Figure 5.6: Schematic presentation of mountain-generated wind with thunderstorm development on the lee side (Source: Modified from WMO, 1978).

Strong downslope wind (e.g. gale force wind) sometimes lead to explosive lee cyclones and tornadogenesis (Chuang *et al.*, 2008; Xue *et al.*, 2019; Wang *et al.*, 2020; Figure 2.3). Such tornadogenesis may develop because windblown (e.g. gust front) over the mountain can result in vertical wind shear on the lee side (Starr, 2010; Marquis *et al.*, 2012). Other requirements for severe thunderstorms (e.g. tornado) include low-level moisture with optimum to extreme instabilities (Johns *et al.*, 1993; Edwards and Thompson, 2000).

2.5 Synergy of surface and middle level vorticities

2.5.1 Up-down synergy of vorticities

Mid-latitude atmosphere is often dynamically driven from the MTS level to the surface (Holton, 1979). Such latitudes (i.e. to the south or north of 30 °) are typically dominated by the well-defined MTS troughs and COLs. Composite or discrete values of vorticity advection (e.g. at 500 hPa) are typically found on the leading edge of the COLs (or MTS

troughs) where vorticities are often coupled with dropping heights (Röhner, 2016; Rammopo and Ndarana, 2019). In the southern hemisphere, geostrophic vorticity advection is typically negative and at a minimum at the inflection point or line east of the axis of the COL (Ndabambi, 2002; Ndarana *et al*., 2020). A significant proportion of the tornadic supercell thunderstorms in the USA were found to develop along the eastern or south-eastern edge of the 500 hPa COLs (Davies and Guyer, 2004). Such sections of COLs (well-defined MTS troughs) are probably linked with the pronounced vorticity advection (e.g. at 500 hPa) together with the eastward surge of the equatorward sector ahead of the poleward sector. A comparison of the orientations of COLs (or well-defined MTS troughs) and their associated vorticity advections in the South African context will be discussed in Section 4.3.2.2b and alluded to in the last paragraph of Section 5.3.2. Godoy *et al*. (2011) approximate the dynamic processes in free (frictionless) atmosphere by using the vorticity advection equation with the Equation 1 below:

$$\underbrace{\frac{\partial \zeta}{\partial t}}_{\text{LCV}} = \underbrace{-\delta(\zeta + f)}_{\text{DT}} \underbrace{- V_H \,.\, \nabla_p \zeta}_{\text{HVA}} \underbrace{- \nu\beta - \omega \frac{\partial \zeta}{\partial p} - \nabla . \omega \frac{\partial V_H}{\partial p}}_{\text{LOT}} \quad \ldots \text{Equation 1}$$

where ζ is the vertical component of the relative vorticity, V_H is the horizontal wind, ∇_p is the differential nabla operator at constant pressure, ω is the vertical velocity of the isobaric system, δ is the divergence of horizontal wind, f is the Coriolis parameter, β Rossby parameter, v meridional wind component. LCV stands for the local change of vorticity, DT for the divergence term, HVA for the horizontal vorticity advection and LOT for the lower order terms. These terms represent the sum of terrestrial vorticity advection, vertical vorticity advection and tilting. Some COLs are more intense in the upper and middle troposphere but weaker or absent in the lower troposphere (Reboita *et al.*, 2010). But other COLs (or MTS troughs), potentially those with large values of 500 hPa vorticity advection (e.g. -5 x 10^{-3} s^{-1}), were found to extend to the surface with rapid cyclogenesis development (Ndabambi, 2002; Barnes *et al*., 2021). Intensity and the position of the MTS-level jet with baroclinicity and mid-level vorticity typically lead to the merger of discrete vortices with rapid intensification and explosive

cyclogenesis (Zhang *et al.*, 2017). Typically, this synergy leads to the development of low-level directional wind shear with increasing wind speeds with increasing altitude (Mathaba *et al.*, 2012). The effectiveness of vertical wind shear in the development of severe thunderstorms is usually linked with warm air advection in the lower troposphere (Röhner, 2016).

2.5.2 Down-up synergy of vorticities

A host of severe thunderstorms in the subtropical atmosphere occur independently of mid-latitude rain-producing (e.g. MTS troughs and COLs) circulations (Barry, 1992; Barnes, 2001; Tennant and Hewitson, 2002). In such latitudes (e.g. between 5 and 30°S), processes that produce uplift and severe thunderstorms (e.g. heavy precipitation and flash- flooding) include topographic uplift (Van Heerden and Taljaard, 1998; Hart, 2012). Moreover, an increase in the middle level vorticities, reflected with cyclonic cloud circulation in Figure 2.4a, most probably occurred due to convection and uplift generated by the topographical features in Figure 2.4b. The photograph in Figure 2.4a is of a late afternoon thunderstorm on 28 March 2019, when it was moving north-eastwards along the south-eastern periphery of the middle-upper high pressure. The small-scale mountain of less than 50 km in length is highlighted with a red oval in Figure 2.4b.

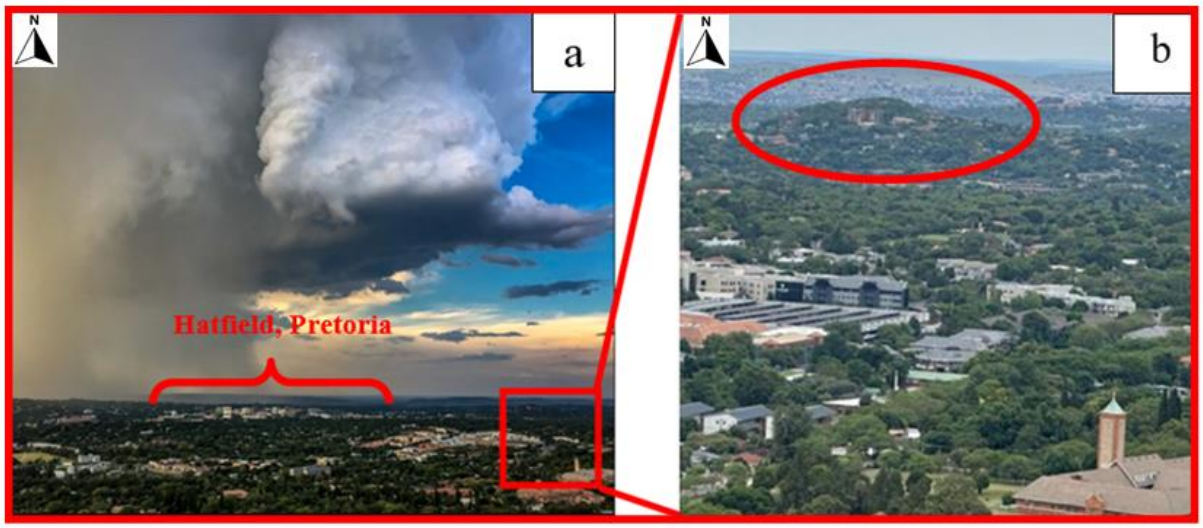


Figure 7.2: Observed cyclonical vorticity advection (Photo source: Lucky Mthombeni).

Surface features, circled in Figure 2.5c, reinforce the effect of topography in the development of thunderstorms, as shown in Figures 8a and 8b. In alignment with Peng *et al*. (1995), Coriolis force and its leftward deflection on the upstream side of the significant topography (e.g. small-scale mountains) creates a stagnation point. In effect, the Coriolis force acts to modify or diminish trough development on the lee side and so its effect cannot be neglected for the wind flow. As Mulovhedzi *et al*. (2021) noted, the numerical representation of microscale events, shown in Figures 7a and 8a, may not be calculable with wind components at the minimum of 4 km grid (e.g. UM 4 km) and one-hour time scale.

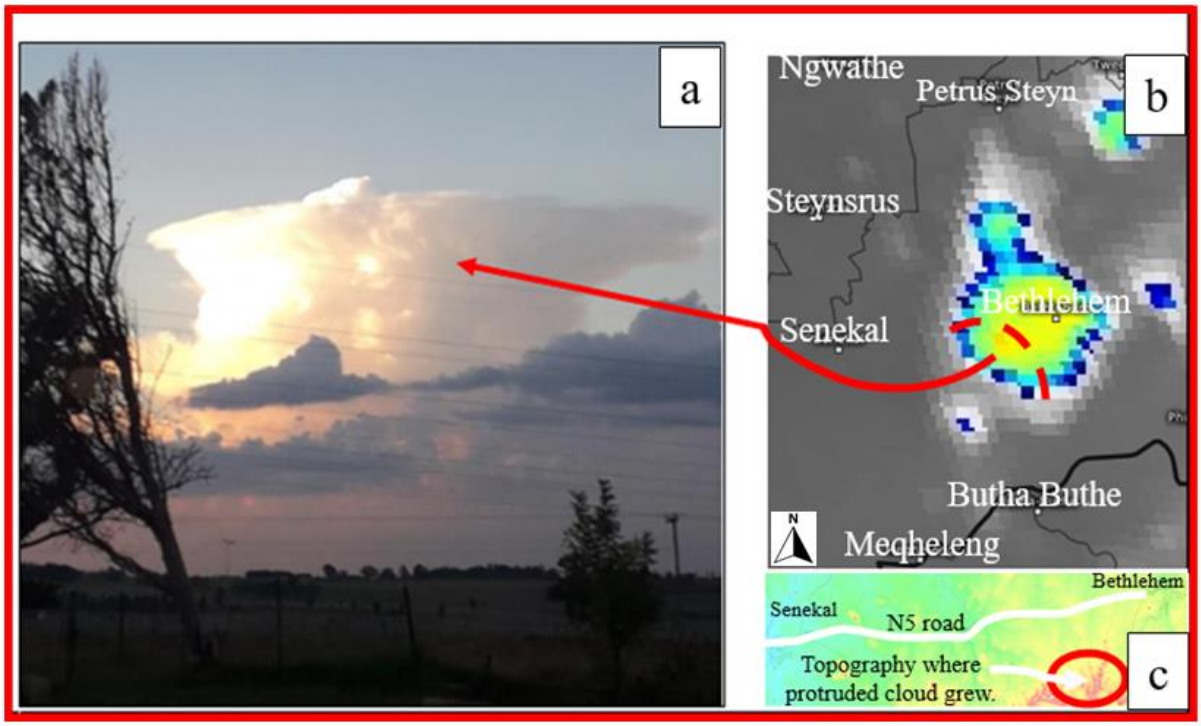


Figure 8.3: Rapid developing thunderstorm is shown in Figure 2.5a taken at 17:40 SAST on 19 April 2019 (Photo source: Mr Tumo Xaba). Satellite image at 17:45 in Figure 2.5b was supplied by the EUMETSAT and shows the distribution of the CCTs over and around Bethlehem in the Free State province. The middle dash of the arc to the south-west of this city shows the coldest section of the convective clouds and is linked with red oval circle in Figure 2.5c and the picture in Figure 2.5a.

Simulations of horizontal vorticity are shown to tilt vertically (i.e. vorticity advection) on interaction with the windward side of significant topographical (e.g. bell- shaped mountain) features (Wu and Arakawa, 2011). Similar tilting typically occurs when the horizontal vorticity interacts with the updraft of the downwind thunderstorm (Trapp,

2018; Figures 5, 7a and 8a). Boyer and Dahl (2020) calculate the approximations of the increase (decrease) in the rate of change of the vorticity advection with the Equation 2 below:

$$\frac{D\zeta}{Dt} = \underbrace{-\zeta\left(\frac{\partial u}{\partial x}+\frac{\partial v}{\partial y}\right)}_{\text{A}} + \underbrace{\left(\xi\frac{\partial \omega}{\partial x}+\eta\frac{\partial \omega}{\partial y}\right)}_{\text{B}} - \underbrace{\left(\left(\frac{\partial \alpha}{\partial x}\frac{\partial p}{\partial y}-\frac{\partial \alpha}{\partial y}\frac{\partial p}{\partial x}\right)\right)}_{\text{C}} + \underbrace{\left(\frac{\partial F_y}{\partial x}+\frac{\partial F_x}{\partial y}\right)}_{\text{D}} \quad \ldots \text{Equation 2}$$

In this equation ξ, η and ζ are the x, y, and z components of vorticity, respectively. Components u, υ, and ω are the x, y, and z components of velocity, respectively. The α is the specific volume of the air; p is the air pressure; and the vector F includes the diffusion and subgrid-scale mixing (turbulence) terms. Term A on the right-hand side represents the stretching term that acts to increase (decrease) the magnitude of vorticity advection which occasional change its polarity (Biggerstaff and Houze Jr., 1991; Boyer and Dahl, 2020). Term B represents the tilting of horizontal vorticity into the vertical by nonuniform vertical motion field and can change the polarity of the vorticity advection (Biggerstaff and Houze Jr., 1991; Boyer and Dahl, 2020). Negative vorticities were found to be correlated with cyclonic circulations in the southern hemisphere (Holton, 1979, 2004; De Coning and Adam, 2000). Tilting of horizontal vorticity has the tendency to originate or amplify the rotation on the flank of the updraft (Rotunno, 1981; Clark, 1988; Figures 5 and 7a). The pressure-volume solenoid term represents the baroclinic processes within the storm and is given by term C. Term D includes subgrid-scale turbulence and implicit diffusion. These terms are integrated to identify the mechanism that maintains the vortices. Significant amplification of vorticity advection usually occurs for thunderclouds of even moderate (or shallow) vertical extent, among other backgrounds (Wissmeier and Smith, 2011). Moderate heights of thunderstorms may be the result of cold air advection (e.g. associated with polar vortices of the cold front) (Lengoasa, 1988; Barry and Carleton, 2001). Localised amplification of vorticity advection may be achieved by the merger of the discrete vorticity advection in the middle level troposphere (Wu and Arakawa, 2011). Mergers of this kind usually occur as a result of the irregular acceleration of the gust front of the approaching thunderstorms, as discussed in Section 2.4.2.

2.5.3 Storm-relative helicity (SRH)

The storm-relative helicity (SRH henceforth) is a measurement of how much low-level rotation may be ingested into the thunderstorm (Tijssen, 2015). The SRH is integrated in the formula below and expresses helical changes as a quantity proportional to streamwise vorticity and storm-relative winds (e.g., Rasmussen and Blanchard, 1998; Davies-Jones *et al.*, 1990):

$$SRH = -\int_{0}^{h} k.(V - c) \times \frac{\partial V}{\partial z} dz \quad \ldots \text{Equation 3}$$

where V is horizontal velocity, c is the storm motion vector, and h is the depth over which the integration is performed. The values of SRH could either be negative for cyclonic (clockwise) motion or positive for anticyclonic (counter-clockwise) motion in the southern hemisphere; a concentration of numerically large values with negative sign are considered as proxies for rotational thunderstorms (e.g., supercell storms) (Barretta *et al.*, 2020). In contrast, the signs are the opposite for northern hemisphere cases. It has been observed that the NWP (e.g., UM) values of SRH may be set off spatially or temporally or both, particularly during the deviation of supercell storms and/or the shift of orientation of COLs; the SRH estimates are good when storm motions are predicted well (Zeitler and Bunkers, 2005). At worst, the SRH may not show or indicate the potential of a supercell developing (e.g., SRH showed no potential that a tornadic supercell would develop on the Highveld areas of South Africa on 11 December 2017). The SRH could be calculated within the boundary layer of 0 to 3 km AGL (Johnson, 2002) (as in the case of the UM used in South Africa) or within 0 to 1 km AGL (Rasmussen and Blanchard, 1998). However, several studies argue that SRH calculated in shallower layers (i.e. 0 to 500 m) might be a better proxy for rotational storms (e.g., supercell storms) if used with the proximity sounding of sufficient vertical resolution (Markowski *et al.*, 1998; Coffer *et al.*, 2019). Generally, the effective-layer SRH has by far the greatest forecast skill among significant tornado parameter components (Coffer *et al.*, 2019).

2.6 Indicators of potential severe events

2.6.1 Tornadoes

A tornado is defined as a violent rotating column of air that extends from an extreme thundercloud, nearing or reaching the ground at diameters averaging about 100 m (Smith, 2013). Tornado diameters could be as large as 1 km (Bluestein, 2013; 2017). Tornadoes are usually evidenced by blowing dust and debris near the surface of the Earth when there is no touchdown (Schmidlin, 2010; Figure 2.6). This dissertation draws parallels and differences from climatic studies on tornadic storms in the United States of America (*hereafter*, USA), including their details in some case studies. Tornadoes that develop in other regions across the globe were also considered but to a far lesser extent. Earlier, Heydenrych (1987) and Singleton and Reason (2006) identified several different mechanisms for severe thunderstorm development in the USA and South Africa; these include positions of warm moisture sources, flows associated with synoptic and mesoscale, and polarity of dynamic analysis. These mechanisms make it inappropriate or difficult to directly transfer the USA findings to South Africa.

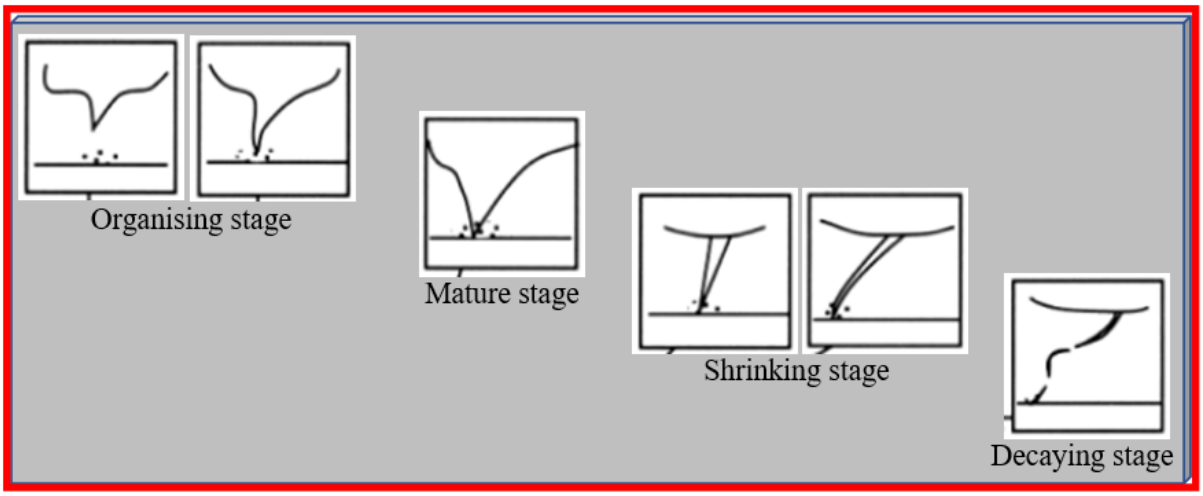


Figure 9.4: Structure of a tornado observed at several stages of its life cycle. Sketches show a funnel cloud with resultant debris (Source: Klemp, 1987).

The USA has a latitude-longitude domain of 24° to 50° N and 86° to 112° W, covering the landmass of about 26° in latitudinal range (Schlef *et al.*, 2019; Figure 2.7). Thus, the domain is largely in the mid-latitude zone (i.e. between 30° and 60°) (Swann *et al.*, 2012;

Moon *et al.*, 2017). The USA has an annual average of at least 1000 tornadoes (Ahrens and Henson, 2018). This average is markedly higher than any other region across the globe (Ahrens and Henson, 2018; Lepore *et al.*, 2017). The occurrence of severe thunderstorms is relatively more frequent in the USA than anywhere else in the World (Gao *et al.*, 2013; Cintineo *et al.*, 2014). Broadly, severe thunderstorms that develop in this region are often generated from events such as surface synoptic fronts, drylines, outflow boundaries, sea breeze boundaries or intense surface heating (Cintineo *et al.*, 2014). The peak occurrence in severe thunderstorms typically starts in the south-eastern part of the USA in late winter–early spring and moves north-west over time to the northern plains by midsummer (Schaefer *et al.*, 1980; McNulty, 1995). Supercell storms are associated with most tornadoes with the highest frequency during the transitional months of autumn and spring (Davies and Guyer, 2004; Bosart *et al.*, 2006). Because the USA is mainly in the mid-latitude zone, most of the severe thunderstorms (e.g. close to 75% of hailstorms) are associated with frontal activity (Olivier, 1990).

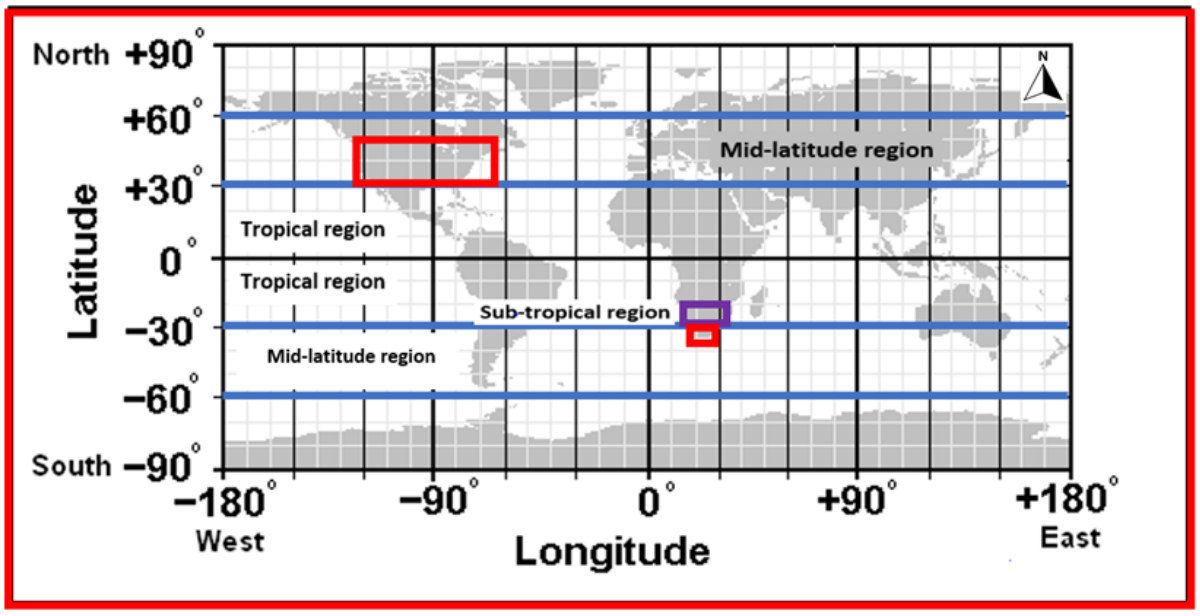


Figure 10.5: Latitudinal and longitudinal differences between the USA and South Africa (Modified from Satsig, 2011).

The tendency for tornadic supercell storms in association with occlusion may be because the front rotating about the parent low imparts an extra velocity component to the front (Hunter, 1987). The effect of occlusion on supercell tornadoes (labelled T)

also occur over the mid-western USA (Cotton *et al.*, 2011; Figure 2.8). Other synoptic environments associated with tornadic supercell storms are described and summarised by Miller (1959) and Barnes and Newton (1982). In a study focussing on a short five-year period from 1999 to 2003, Davies and Guyer (2004) found that tornadic supercell storms in central and eastern USA develop to the east or south-east of the 500 hPa COL, during the transitional months of autumn and spring in an environment of marginal weak instability (e.g., CAPE of 1 000 $J.kg^{-1}$ or less). Tornado damage and estimated wind strengths are summarised in an Enhanced Fujita (EF) scale (Wurman *et al.*, 2012; Table 1). Damage of tornadic supercell storms are often rated EF2 or greater in intensity (Brady and Szoke, 1989). However, South Africa is in the subtropical region (i.e. a zone between $\pm 23.40^{O}$ and $\pm 30.00^{O}$) with very rare cases of occluded fronts (Corlett, 2013). In Figure 2.7, South Africa is positioned within the purple rectangle and adjacent to the red one. Coordinates of South Africa are specified in Section 1.1.

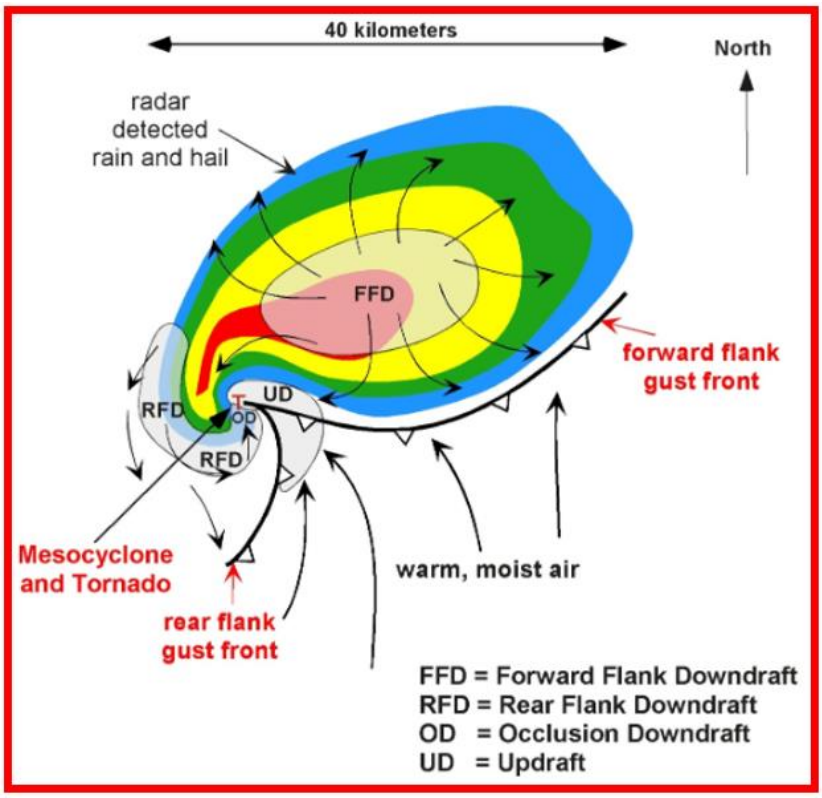


Figure 11.6: Idealised plan view of supercell thunderstorms on satellite and low-level precipitation by horizontally scanning RADAR (Source: Houze, 2014).

Occluded fronts are a rarity to the north of 35°S (Taljaard *et al.*, 1961; Tucker, 1971; Hunter, 1987; Van Heerden, 1987; White, 2000). A high degree of the development of severe thunderstorms (e.g. hailstorm) in South Africa is possible through mechanisms other than the frontal influence (Olivier, 1990). Tornadoes in the subtropical region (e.g. Australia) often occur without obvious support of circulations aloft (Barry, 1992**;** Barnes, 2001). Distinct physical properties such as very cold cloud tops (Zinner *et al.*, 2013) could sometimes be associated with overshooting tops (Reimel, 2017). Ludlam (1963) further presents that there are differences in structure between cumulonimbus clouds in the mid-latitudes and those in the tropics. In temperate latitudes (e.g. South Africa), intense thunderstorms often develop and evolve as a result of moisture discontinuity or sporadic airmass exchange, local effects (i.e. mesoscale features) and/or intense surface heating (Preston-Whyte, 1988; AIC, 2000; Keat *et al.*, 2019; Washington and Hodges, 2019).

Enhanced Fujita Scale (Implemented: February 2007)		
Rating	Winds	Expected Damage
EF0	104.61 to 136.79 km/h	**Minor damage.** Shingles or parts of roof peeled off; damage to gutters/sidings; branches broken off; shallow-rooted threes toppled.
EF1	138.4 to 177.03 km/h	**Moderate damage.** More significant roof damage; windows broken; exterior doors damaged or lost; mobile homes badly damaged or overturned.
EF2	178.64 to 217.26 km/h	**Considerable damage**. Roof torn off well-constructed homes; homes shifted off their foundations; mobile homes completely destroyed; large trees snapped or uprooted; cars may be tossed.
EF3	218.87 to 265.54 km/h	**Severe damage.** Entire stories of well-constructed homes destroyed; significnt damage to large buildings; homes with weak foundations may be blown away; trees begin to lose bark.
EF4	267.15 to 321.87 km/h	**Extreme damage.** Well-constructed homes leveled; cars thrown significant distances; top story exterior walls of masonry buildings likely collapse
EF5	> 321.87 km/h	**Incredible damage.** Well-constructed homes swept away; steel-reinforced concrete structures critically damaged; high-rise buildings sustain severe structural damage; trees usually completely debarked, stripped of branches and snapped.

Table 1: Enhanced Fujita scale following the relatively consistent marginal bias between the radial winds estimated by the Doppler RADAR and actual wind observations. The update was first used from February 2007 (Source: NWS, 2024).

Weaker low-level vertical wind shear may account for significantly fewer supercell storms across South Africa in comparison with supercell storms in the USA. Some details of South African tornadoes were studied by D'Abreton (1991), Goliger *et al.* (1997), De Coning and Adam (2000), Kimambo (2018), and Lekoloane *et al*. (2021). Further details of tornadic storms over South Africa are discussed in Chapter 5. Topographical features are discussed together with gust fronts of the upwind thunderstorms used in Chapter 5 to infer their contribution to tornadic supercell storms over South Africa.

2.6.2 Hail and lightning

Hail-producing storms in temperate climates (e.g. South Africa) are usually without strong vertical wind shear (Sansom, 1966; Hand and Cappellut, 2011). The microphysical process of graupel growth within the thundercloud usually begins when water vapour nucleates around minute centres of dust, clay minerals, black carbon and biological material (Kaufmann *et al.*, 2016). A strong rotating updraft is often consequential to collision and coalescence of large quantities of graupel into large hailstones (Tessendorf, 2009; Gultepe *et al.*, 2017; Witt *et al.*, 2018; Gutierrez, 2019). Hail growth also requires the inflow of dry cold air in the middle of the storm (Pienaar *et al.*, 2015). The effect of the rotating updraft leads to the formation of large hailstones (e.g. 1.9 cm or greater in size) with the associated high frequency of lightning strikes (Brimelow, 2018; Figure 12). Lightning rate significantly increases during a mature stage of the slow-moving thunderstorms (Bhavika, 2007). An increase in lightning rate is far more likely during periods of pressure fall and cyclonic intensification (Williams, 1995). Convective cloud typically grows its vertical extent to at least 3 km when associated with strong updraft (Rakov and Uman, 2006). Cloud tops in the region of 10 km or with RADAR reflectivities of at least 60 dBZ are suggestive of potential large hailstones (Borque *et al.*, 2020; Haberlie *et al.*, 2022). Further, RADAR scans may display storm-scale structures during a mature stage, which may suggest an imminent tornado occurrence (de Oliveira *et al.*, 2016). As demonstrated in Figure 2.9, a peak of cloud-to-ground lightning usually precedes tornadogenesis by about 10 to 15 minutes (Knapp, 1994; Perez *et al.*, 1997, Mahomed, 2020).

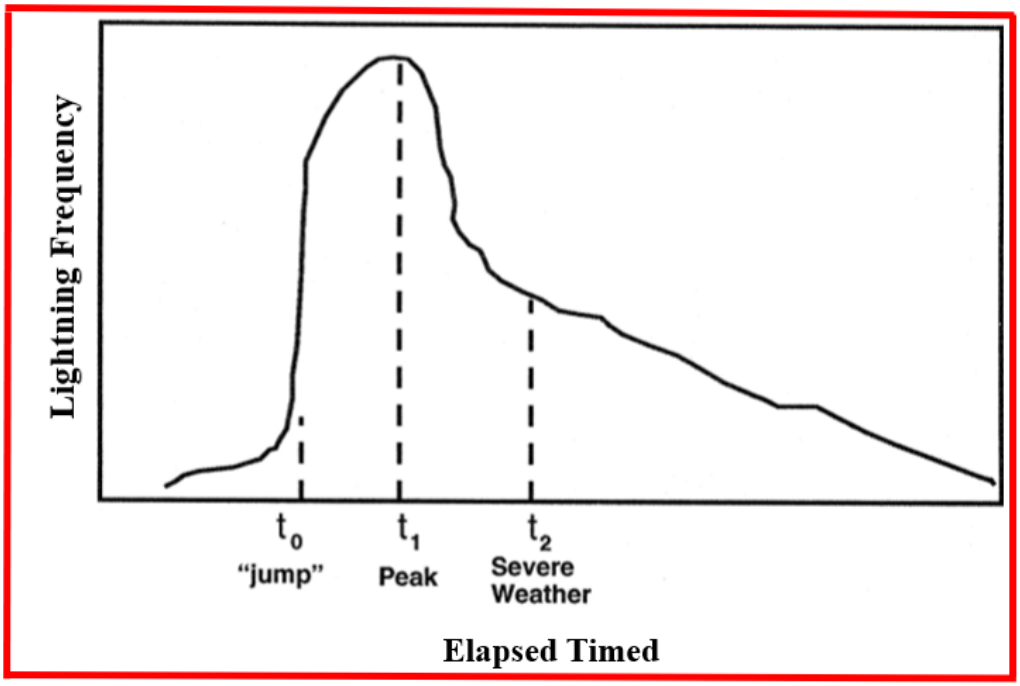


Figure 12.7: Idealised frequency of lightning leading to additional severe thunderstorms (Source: Williams *et al.*, 1999).

Often, hail growth within the thundercloud results in the upsurge of thunderstorm lightning, which is often used as a proxy for the onset of a severe thunderstorm (e.g. large hailstones, strong gusty winds and/or a tornado) events (Williams *et al.*, 1999; Reimel, 2017; Alexander *et al.*, 2018). However, lightning jumps may not result in severe storm events in some cases.

2.7 Severe thunderstorms in El-Niño Southern Oscillation

2.7.1 Severe thunderstorms related to El-Niño phase

Walker circulation is largely responsible for suppressing convective systems over the southern African region during El-Niño – the positive phase of El-Niño Southern Oscillation (ENSO) (Quagraine *et al.*, 2019; Dieppois *et al.*, 2015). Related factors include an expansion of the Hadley cell and a subsequent displacement of the subtropical jet stream (Dube and Jury, 2000; Kossin *et al.*, 2014). Subtropical jet streams are often associated with increased low-level vertical wind shear (Fitchett,

2018). In the southern African region, the El-Niño, which co-occurs with a positive Indian Ocean Dipole (IOD), typically leads to droughts (Chikoore *et al.*, 2021). In effect, the reduction in the supply of soil moisture leads to the loosening of the soil and the fragmentation of leaves of the drought-sensitive vegetation into minute particles (Chivangulula *et al.*, 2023). Earlier, Trenberth (1997) argued that the period after 1979 has been dominated by El-Niño events.

2.7.2 Severe thunderstorms related to the La-Niña phase

Sea-surface temperatures (SSTs) in the south-western Indian Ocean were observed to notably increase at least three months after the peak of El-Niño (Klein *et al.*, 1999; Trenberth *et al.*, 2002). Often, such SSTs are correlated with the La-Niña – the negative phase of ENSO (Moeletsi *et al*., 2011). A WRC (2019) report noted that the surface airflow in La-Niña seasons may be between 1.5 to 3.0 times higher than during El-Niño years. In addition, light to moderate vertical wind shear in the lower troposphere is promoted with the potential for severe thunderstorms in austral La-Niña, favouring thunderstorm development over southern Africa (Caruso and Davies, 2006; Adedoyin and Mphale, 2014; Mulugeta and Simelani, 2016). Recent studies in Israel (e.g. Yair *et al.*, 2022) have linked high concentration of dust (and other minute particles) to a longer thunderstorm lifespan. These findings seem to support Olivier (1990), who reported about the high frequency of severe thunderstorms over South Africa after drought. De Villiers and Van Heerden *et al*. (2007) noted that dust particles are lifted by the updraft into the thunderstorm. Dust lifting is also possible during the thunderstorm gust front (De Villiers and Van Heerden, 2007). This means, gust-front-lifted dust has an additional effect on the downwind thunderstorm, particularly during the interaction with its inflow sector. Agreeably, the concentration of dust in South Africa is proportionally far less when compared with the Middle East. The interaction of global-scale circulations (e.g. ENSO) with the synoptic scale and mesoscale circulations seem to control the trends of (severe) thunderstorm occurrences (Martín *et al.*, 1997; Changnon, 1999; Majodina, 2002; Mass *et al.*, 2002; Riphagen *et al.*, 2002; Lepore *et al.*, 2017).

Chapter 3: Data and methodologies

3.1 Background

This chapter introduces a variety of data sources used in Chapters 4 and 5 of this dissertation. The chapter also presents the methods used to identify the severe thunderstorms that occurred over 234 days during the base period, June 2016 to June 2021. Such storms were identified by employing a qualitative approach (i.e. interpretation of meteorological satellite images) as discussed in Section 3.4.1. A complement analysis of a few of these storms was done through the use of RADAR reflectivity data (see Section 3.2.2). As far as possible, the validity of these identified severe thunderstorms was confirmed with events recorded in the severe weather log. The collection of the severe weather events is explained in Section 3.2.3. Satellite images were relied on to analyse the case studies chosen from the identified severe thunderstorms in Chapters 4 and 5. To a lesser extent, other integral analysis tools were used. These included the effect of topography and meteorological RADAR images. Synergy of severe thunderstorms with the 500 hPa vorticity advection (part of dynamical analyses), low-level circulations and topographic features was explored using two case studies.

3.2. Data sources

3.2.1 Meteorological satellite data

Meteorological satellite data (i.e. combination of enhanced infrared [IR 10.8 µm] and high-resolution visible [HRV] window channel) was obtained from the European Organization for the Exploitation of Meteorological Satellites (i.e. EUMETSAT). Satellite images provided by the EUMESAT were ordered from www.eumetsat.int or retrieved from https://meteologix.com/za/satellite/top-alert-15min.html. IR and HRV have resolutions of 3 km x 3 km and 1 km x 1 km (Nilo *et al.*, 2018). Satellite images used were georeferenced over South Africa and were extensively used to identify severe thunderstorms that occurred over South Africa during 61 consecutive months from June 2016 to June 2021. Criteria for the identification of severe thunderstorms are laid out in

Section 3.4.1. EUMETSAT makes the Spinning Enhanced Visible and Infrared Imager (i.e. SEVERI) on-board the Meteosat Second Generation (i.e. MSG) available on request and usually at no cost (Nilo *et al.*, 2018). As used by De Coning *et al.* (2015) and Malala (2007, unpublished), satellite imagery at a grid resolution of 3 km x 3 km updates every 15 minutes. As in Section 3.2.1a, the bulk of severe thunderstorms as interpreted from satellite images, were confirmed with impacts that have been recorded in the severe weather log of the South African Weather Service (i.e. SAWS Caelum). Researchers continually use the SAWS Caelum as reference for information on extreme weather events in South Africa. It contains reports from historical journals and letters, as well as newspaper reports (e.g. Lynch, 2004; Alcock, 2013; McBride *et al.*, 2022). Updates of the SAWS Caelum includes electronic weather reports from over three decades ago and social media reports from over a decade ago (SAWS, 2003). Since more than six decades ago these reports are verified using remote sensing tools (i.e. satellite and RADAR images and where possible with in situ stations).

3.2.2 Meteorological RADAR data

Weather RADAR data were used in this dissertation for two cases of tornado occurrence in Gauteng province, South Africa, with the foci on the hook echo and reflectivity. The SAWS uses such data operationally at near-real time (i.e. with a lag of 5 minutes) from a RADAR network over South Africa. Data in the SAWS archive are obtainable on request for research purposes.

3.2.3 Severe weather log and social media

A total of 34 tornadoes and nine landspouts were selected from the severe weather log (i.e. Caelum) of the South African Weather Service (i.e. SAWS) during the 5-year period. The SAWS Caelum is continually updated to record extreme weather events (e.g. severe thunderstorms) reported in the print media, and also includes the accounts of weather professionals and members of the public. Such reports largely concentrate on urban and peri-urban areas. Thresholds that have to be met before reporting impacts of extreme weather obscure the full diversity of hazard landscape in South Africa

(Pharoah *et al.*, 2013). However, a sizable number of storm impacts that occur over rural or farming regions have most likely been recorded inadequately. Accounts given by the general public are accepted and used to update SAWS Caelum after verification by satellite images (and RADAR images where applicable) and/or site observations by professional meteorologists. The publication provides information on the days of occurrence of the weather events, locations, types and the associated impacts. To establish possible relationships between tornado frequencies and ENSO phases, information on additional tornadoes recorded in the SAWS Caelum from 1958 to 2021 were obtained.

3.2.4 Measurements of temperature, humidity, rain and wind

Temperature, humidity and rain recorded over several locations across the south-western region of South Africa were requested from the SAWS, particularly to study the severe thunderstorm of 13 February 2018. The observations for 00:00, 06:00, 12:00 and 18:00 Coordinated Universal Time (UTC henceforth) were used in Table 2 to establish the delivery of moisture and the effect of solar heating to these regions.

3.2.5 Regional weather forecasts and Tweets

Regional weather forecasts, which were issued on a daily basis (i.e. traditionally issued before 03:00 and 14:00 UTC), were requested from the SAWS. These forecasts are internally referred to as FPZA40 and are available electronically on request since the year 2002. Forecasts were used to track whether the severe thunderstorms over South Africa were issued at least 8 hours before storm initiation on the identified 234 days during the study period, June 2016 to June 2021. A complementary analysis of thunderstorm warnings that were posted on the X account (@saweatherservic) was conducted for the same period. The X is a social media platform formerly known as Twitter. Analyses of storm warnings focussed on the lead-times between 2 and 36 hours. These severe storms were studied in relation to the MTS weather circulations in Sections 4.1 and 5.2.6 to improve the lead-time. Alerts issued within 2 hours to the development of severe thunderstorms were excluded from the study.

3.2.6 Coordinate system and high-resolution topographical maps

A fine coordinate system was superimposed over the South African domain with satellite cloud patterns for the approximate positioning of the reported tornadic storms. These approximate positions were also used to read the times of the short temporal occurrences of these tornadic storms. Moreover, the positions of these tornadic storms were also used along with zoomable maps found at: https://en-za.topographic-map.com. These high-resolution maps were used to zoom in on the surface features, which were made invisible in Figure 1.1: the composite topographical map of South Africa. This means, the high-resolution topographical maps were used to detect the influence of topography on the development of tornadoes. These maps were also used extensively to show the extent of the contribution of non-tornadic severe thunderstorms in the case studies in Chapter 4 and 5.

3.2.7 Numerical weather prediction and reanalysis data

Forecast data of the UM were requested from the SAWS for the association of the 500 hPa circulations with the severe thunderstorms listed in the Appendix. The UM was developed by the United Kingdom Meteorological Office (UKMO) who continually upgrades the UM used for operational forecasting at the SAWS. The UM forecast is generated every 6 hours (i.e. four times a day) and provides the forecasts at a lead-time of three days with grid resolution of 4.4 km over the South African domain. Severe thunderstorms were identified after satisfying the criteria set out in Section 3.4.1. Output variables of the UM were also used to analyse the severe thunderstorms chosen for the few case studies in Chapters 4 and 5. Some of the UM variables were compared with the reanalysis model: the European Centre for Medium-range Weather Forecasting (i.e. ECMWF) – reanalysis version 5 (ERA5). Both the UM and ERA5 data were used to determine the synoptic and mesoscale circulations and to identify features such as the near-surface vertical wind shear and mid-level temperature perturbations.

3.2.8 The ERA5 Reanalysis

ERA5 reanalysis data blend available observational data with model simulations to derive at what is regarded as the most realistic description of historical weather patterns currently available for assessment. ERA5 generates reanalysis data sets at a grid resolution of 25 km in the horizontal, with a time-resolution of one hour (Hersbach *et al.*, 2020). Its levels in the vertical range from 1000 to 100 hPa. ERA5 was also useful for dynamic analyses, such as the vorticity dipole and 500 m vorticity advection. Development of some of these features could be attributed to surface features (e.g. complex topography and large vegetation) and steep MTS troughs (or COLs). These models were also used to test variables/features that are important in the development of tornadoes.

3.2.9 Historic oceanic Niño indices

Oceanic Niño Indices between 1957 and 2022 were used to track phases of ENSO from the data of the National Oceanic and Atmospheric Administration (NOAA), as updated and archived on https://ggweather.com/enso/oni.htm. Such phases were cross-checked with phases between 1957 and 1995, as compiled by Trenberth (1997). The phases were used to test correlations and tendencies with tornado frequencies over South Africa from 229 tornadic events that occurred over a period of 63 years, from 1958 to 2021. The tornadic events were read from the severe weather log of the South African Weather Service (i.e. unpublished SAWS Caelum).

3.3 Scope limitation of the study

Clusters of persistent non-severe thunderstorms with or without severe ones among them were excluded from this study due to the difficulty to track their gust fronts. The chosen thunderstorms include those associated with tropical cyclones (e.g. Dineo and Eloise), COL- or MTS trough-associated cloud bands. For example, the heavy Durban floods of October 2017 and the widespread heavy floods along the coastal regions of the Eastern Cape and KZN in April 2019 were excluded from severe thunderstorms listed in the Appendix. TTT-associated cloud bands were also excluded. Studies of

severe snowstorms in cold environments as studied by Stander *et al.* (2016) and Grab *et al.* (2017), among others, were also left out. Case studies of severe thunderstorms, which were attributed to the abundant moisture and extreme instabilities in the middle-level (i.e. temperature lapse rates of at least 7°C/km), were noted but not explored. However, relevant insights for such elevated severe thunderstorms could be found in the Forecaster Handbook of 1984. Ordinary thunderstorms were excluded from the study along with individual successive thunderstorm cells from which flooding occurred. Relative to tornadogenesis, the limitation of this study includes the absence of wind data from the NWP and reanalysis models. As in Figure 3.1, these wind data should represent the strength of gust fronts (vectors) each moving along the x- and y-directions towards a common location. Additionally, deriving the u and v components from velocities of gust fronts from each of the storms (i.e. S_1 and S_2 in Figure 3.1) is beyond the scope of this dissertation. Therefore, the mathematical quantification for fluid rotation at the intersection point (e.g. at P(x,y,0) coordinate in Figure 3.1) could not be done.

3.4. Data processing

3.4.1 Criteria used for the identification of severe thunderstorms

Satellite-derived CTTs of severe events of thunderstorms, which were recorded in the severe weather log, were used to develop the criteria for identifying severe thunderstorms. Thunderstorm characteristics from the previous findings and proposals included the sizes, leading edges of the squall-line and overshooting tops and were also used in the identification process of the thunderstorms. These criteria were used to minimise the subjectivity in the identification of the severe thunderstorms for the base period stated in Section 3.1. The criteria are discussed in subsequent subsections. The identification of severe thunderstorms was performed by using the meteorological satellite images introduced in Section 3.2.1. At CTTs of -40°C to -50°C, hights of thunderstorms were regarded to be low. The onset of severe thunderstorms was regarded as eminent when CTTs dropped to an average of -5°C or colder within successive 15-minute intervals. Alternatively, severe storms were regarded eminent when CTTs

increased to an average of 5℃ or warmer within successive 15-minute intervals. Such a drop (increase) is referred to as rapid drop (increase) in CTTs in this dissertation. The rapid drop in CTTs signifies the strengthening of the updraft and the potential for severe thunderstorms (De Coning et *al*., 2015). Indication for prolonged severe thunderstorms was interpreted from the CTTs that experienced a rapid drop in consecutive 15-minute intervals. Heavy rain and flooding were found to be linked with CTTs colder than -54℃ (Rouault et. al, 2002). These CTTs may include light hail. However, large hailstorms were associated with CTTs that were colder than -65℃. Marginal changes of the CTTs colder than -65℃ in consecutive 15-minute intervals were also interpreted as an indicator for prolonged severe thunderstorms. The rapid decline of the high frequency lightning with the eminent severe events of thunderstorms (e.g. eminent tornadogenesis) are discussed in Section 2.5.2 and revisited for more detail in Section 5.3.3. Times and dates on which severe thunderstorms occurred are listed in the Appendix. A significant proportion of these storms were linked with the rapid drops in CTT, which became colder than -50℃ and lasted for a short time (i.e. less than 60 minutes). A series of individual small-sized severe thunderstorms with CTTs in the region of -50 and -60℃ passed over the same area and produced heavy localised flooding once in the base period. Rapid drops in CTTs, which were colder than -60℃, was observed in close association with strong gusty winds and hail. These thunderstorms included those that exhibited overshooting tops. Squall-line thunderstorms, which developed to bow echo, produced strong damaging winds around the leading edge. Multiple mechanisms by which severe thunderstorms are produced were observed in some single days. Details of severe convective storms over South Africa, such as approximate location and appropriate events, were synthesised with MTS circulations (e.g. between 700 to 500 hPa) to improve the decision-making and lead-time. That is, there was an effort to migrate severe thunderstorms which are dealt with at the nowcasting time scale (i.e. within 2 hours) to a longer lead-time. MTS weather circulations were used for each day of severe thunderstorm occurrence to determine the dominant circulation. Thunderstorm gust fronts that were sampled and tested were found to accelerate downwind in response to the rapid drop (increase) in CTTs. Supporting the previous findings, gust fronts of the upwind thunderstorms were deduced to have the effect on

the development of severe thunderstorms. Dissipation of the upwind thunderstorms was closely associated with the decelerating gust fronts.

3.4.1.1 Severe storms produced from gust front of another storm

Satisfying the criteria set in Subsection 3.4.1, near-surface strong winds (i.e. gust fronts) from 30 automatic weather systems (AWS) were selected for the events over the period June 2016 to June 2021. Several authors have confirmed that satellite images are a valuable source for tracking the lifespan and dynamics (i.e. growth, movements and dissipation) of thunderstorms (e.g. Ernest and Matson, 1983; Van Heerden, 1995; De Coning *et al.,* 2015 and Gijben and De Coning, 2017). Tests of near-surface strong winds against the approaching thunderstorms have shown that gust fronts accelerate with rapid drop (increase) in CTTs. Such acceleration seems to be promoted with stronger downdrafts (Caplan *et al.,* 1990; Houze Jr., 1993). Gust fronts of the upwind thunderstorm were assumed to accelerate, as shown in case studies used in Chapters 4 and 5 to show their influence in the development of severe thunderstorms. Their relative coldness is used together with the inflow sector of the primary thunderstorms to illustrate the potential for tornadogenesis (see Section 3.4.1.3 and Chapter 5). Other rapid drops of CTTs were linked with storm mergers that led to severe thunderstorms. Severe storms resulting from storm mergers were investigated by Bluestein and Weisman (2000) period preceding the base period of this dissertation.

3.4.1.2 Severe storms related to topographic features

The composite topographical map was introduced in Figure 1.1, although the averaging effect in its production eliminated critical surface features. This challenge was mitigated by using the high-resolution topographical maps where rapid drops in CTTs occurred. A rapid drop in CTTs was considered when the criteria set in Section 3.4.1 were met. Geographical positions of the thunderstorms and their intensity were used in reference to the high-resolution topographical maps to test the effect of topography. Rapid drop in CTTs with severe thunderstorms were observed to develop in association with significant concave topography in some cases. But in other cases, thunderstorms were deflected to align with the orientation of the short, but significant, near linear

topography, the angle of which was obtuse relative to the original storm path. The dynamics and lifespan of thunderstorms were tracked with satellite image updates, as discussed in Section 3.4.1. The existence of topography-induced severe thunderstorms has similarly been supported by several authors (e.g. Steyn and Bruintjes, 1990; Van Heerden, 1995 and Alfahmi *et al*., 2019). Some topography-deflected thunderstorms were supercells, the characteristics of which included a significant drop in CTTs and duration in excess of 60 minutes (i.e. four consecutive 15-minute intervals). Some supercell thunderstorms occurred among the cumulus clouds but were isolated from a similar cohort of CTTs. Other rapid drops in CTTs and subsequent severe thunderstorms were found on the lee side of significant topography. Such severe thunderstorms result from near-surface moist and unstable conditions, which are undercut by the strong gust front of the thunderstorm on the windward side of significant topography. This is in agreement with the WMO (1978) and Sun and Sun (2015). Tornadic supercell thunderstorms are discussed in Section 5.3.2 and the complexity brought on by topography in severe thunderstorm development is highlighted. To this effect, fine topographic map and meteorological RADAR reflectivity data were used in Figures 5.5c and 5.5d to discuss key details of storm build-up. This image was used within a critical single 15-minute interval, in accordance with satellite image update. Similar case studies are re-examined in Figures 4.13a to 4.13d (Chapter 4) and in Figures 5.4b to 5.4d and 5.7c to 5.7e (Chapter 5). However, comparatively slower drops in CTTs were identified in association with some thunderstorms that moved along the nearly linear, significant topography. These storms were also accepted to have become severe. The movement of such storms, including those affected by concave topography, is supported by previous work (e.g. Jury, 1984; Lengoasa *et al*., 1988 and Lekoloane *et al*., 2021). Other thunderstorms, which intensified along a range of significant topography, are studied and discussed in Figures 4.5, 4.9 and 4.20 (Chapter 4).

3.4.1.3 Production of landspouts and tornadoes

A total of 34 reported tornadic storms in South Africa were captured from the severe weather log over the base period June 2016 to June 2021. Of these tornadic storms, 26

(i.e. about 76%) were produced from topography-deflected supercells, while the remaining 8 (i.e. about 24%) were linked with multicell storms. The CTTs of the storms which produced these tornadoes were colder than -50°C. Additionally, there were ten landspouts reported in the stated base period. The storms which produced these landspouts were much weaker with CTTs in the region of -35°C and -50°C, but only some of them caused localised wind damage. Reports with photographic evidence of funnel cloud were considered in the analysis of these landspouts. The reports of both landspouts and tornadoes were extracted from severe thunderstorms that occurred over the 234 days, as discussed in Section 3.1. Extended from Subsection 3.3.1.2, the geographic locations of these tornadic storms are explored with reference to the fine-scale topographic maps to highlight the link of their development with topographic features. Approximate positions of tornadoes were determined by using the fine-scale coordinate system. Times of occurrences of reported tornadoes across a particular location were read off as times when satellite images displayed the passage of severe storms across such locations. Preliminary criteria were developed in this section to objectively and consistently separate landspouts from tornadoes.

One of the attempts to understand tornadic developments was made by D'Abreton (1991). This effort used a computation of divergence and relative vorticity advection at each conventional level from 850 hPa to 300 hPa. To this end, basic trigonometric functions were used for resolving the u and v components from wind data recorded at radiosonde stations. However, this solution potentially presents at least two major challenges: (1) large distance from radiosonde stations to the location of tornadogenesis, and (2) significant lapse of time from 00:00 and 12:00 UTC. The bi-daily data that profile the troposphere within 200 km radius from the radiosonde stations are made available to weather forecasters soon after the weather balloon burst with cessation of data transmission by radiosonde. A case study conducted by Mpanza (2016) suggests that the tracking and assessment of the dynamical characteristics of tornadic storms is possible. Although the mathematical limitation of tornadic studies is stated in Section 3.3, the formation of bottom-up fluid rotation may be understood by considering the three-dimensional Cartesian plane, as shown in Figure 3.1a with usage in Figure 3.1c.

The figure scaled down the composite thunderstorm activities to two storms (*hereafter*, S_1 and S_2) critical for tornadogenesis. The movement of downwind S_1 is assumed in x-direction along the elongated red vector and that of upwind S_2 is in parallel x-direction along the elongated green vector, as steered by the average MTS winds.

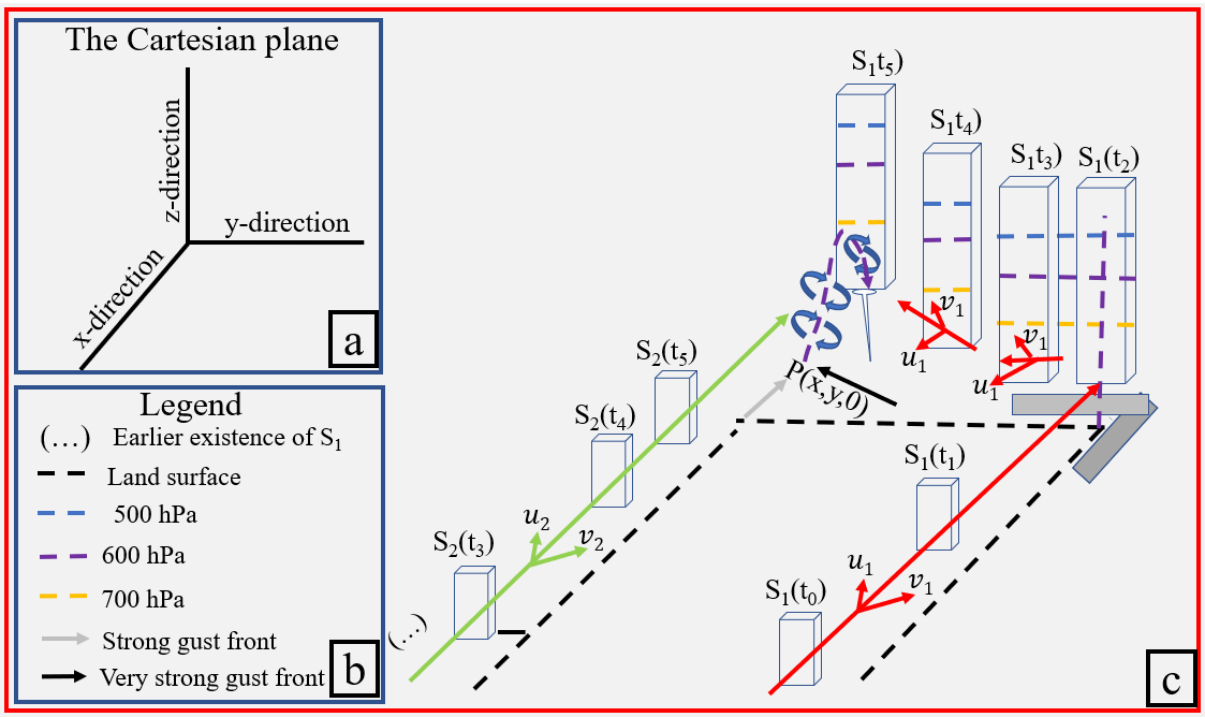


Figure 13.14: The Cartesian plane showing x-, y- and z-directions in solid black lines in Figure 3.1a, as from Holtan (1972). Figure 3.1b represent the legend for critical marks in Figure 3.1c. Idealised thunderstorms (downwind S_1 storm associated with elongated red vector and upwind S_2 storm along the elongated green vector) are shown at a given time t in Figure 3.1c. The grey shapes underneath the intensified S_1 at time (t_2) represent significant topography that has the tendency to deform near surface low with occurrence of strong convection and storm intensification. On some occasions, S_1 deviates onto y-direction but later moves diagonally from time t_4 in response to the initial MTS steering wind. The interaction and unequal strengthening of the gust fronts of S_1 and S_2 at P(x,y,0) at time t_5 initiate and increase localized rotational tendency with respect to height (z-direction). Sustained lifting of rotational flow with heavier density of air often at time t_5 drops the base of S_1 with potential for tornadogenesis.

Sometime later, the S_1 is assumed to encounter significant topography (see grey shapes near the end of elongated red vector in Figure 3.1c). As integrated from Saff and Snider (2003), the topography obstruction potentially causes the deformation of this mesoscale, near-surface low pressure. The associated local topographically induced pressure effects typically deepen the near-surface low pressure, leading to the reversal of surface wind flow and increase of surface convergence and convection (Tyson, 1999; Gbambie

and Steyn, 2012). Storm intensification near significant topography (e.g. initiation of supercell storm) is often evidenced by rapid cooling of CTTs with a link to stronger gust front. The deformed, near-surface low pressure that governs the S_1 at time t_3 has the tendency to defy MTS steering winds by deviating onto y-direction. It is probably the angular shape of significant topography and the application of Coriolis force that cause the storm deviation. Harrison (1986) suggest that Coriolis torque (i.e. directional deflection by the Coriolis force) occur when such mesoscale low pressure interacts with significant topography. The S_1 at times t_4 and t_5 is demonstrated to assume partial differentiation in both x- and y-directions due the deflection and MTS steering winds. However, the upwind storm (S_2) at time t_4, is assumed to continue in x-direction. Usually, S_2 remains a non-supercell storm. Both S_1 and S_2 approach the location P(x,y,0) at time t_5. Stronger gust fronts (e.g. with more than 25 m/s) were observed closer to thunderstorm activities (Wallace and Hobbs, 1977). By intuition from Wallace and Hobbs (1977), Harrison (1986) and Stewart (1998), the increase in the magnitude of torque is dependent on the increase in the applied force and the proximity to the location P(x,y,0) in Figure 3.1c.The location P(x,y,0) and its vicinity in Figure 3.1c is represented in Figures 3.2a and 3.2b. Probably, the sudden ripple effect results from each of gust fronts of S_1 and S_2. Firstly, the development of exponentially strong wind shear and vorticity (i.e. the rotational flow of fluids) in the local environment is assumed from the sustained directional effect of the gust fronts of S_1 (in blue colour) and S_2 (in red colour) in Figure 3.2a. The additional factor to such rotational flow of fluids could be contributed by the gust front of S_1 that is considered stronger than gust front of S_2. This assumption was earlier presented by Dryden and Hill (1926). Secondly, the gust front of S_1 is assumed to be colder and denser than that of S_2. As a result, the gust front of S_1 is assumed to undercut that of S_2 (see Figure 3.2b) and therefore causing the formation of occluded front, as also demonstrated in Figures 2.1 and 2.8. Thirdly, According to Duba (2015), inviscid fluids are expected to remain relatively stable at the introduction of rotational effect such that the governing equations become three-dimensional. Such three-dimensional equation is discussed to estimate the rate of change of the vorticity advection in Equation 2 in Section 2.5.2. Fourthly, the momentum of the assumed rotational flow at location P(x,y,0) is typically lifted into z-

direction; rotational flow is sometimes ingested into S_1 when it is within tens of metres towards location P(x.y,0).

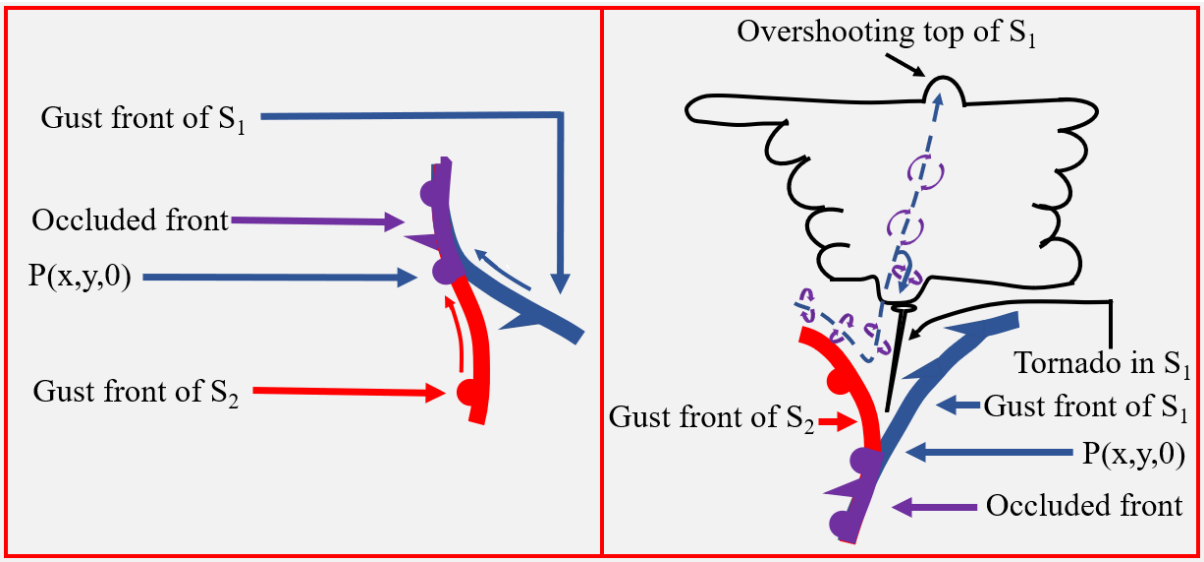


Figure 15.16: Interaction of the gust fronts of S_1 and S_2 from time t_5 as expanded from location P(x,y,0) and its vicinity in Figure 3.1c. Figure 3.2a represent the horizontal view of gust fronts as cold fronts shown in Figures 2.1 and 2.8. Marked difference in the velocities of the gust fronts of S_1 (in blue colour) and S_2 (in red colour) together with their directional effect typically initiate strong wind shear and vorticity (the rotational flow of fluids). Figure 3.2b is the vertical cross-section at P(x,y,0) and shows the colder and denser gust front of S_1 rapidly undercuts the gust front of S_2, with lifting of rotational flow into S_1. Gravity of heavier and denser air usually drops the base of the S_1 with potential for tornadogenesis.

This lifting causes vorticity stretching and tilting, as depicted by Marquis *et al.* (2012). The tilt depicted at location P(x,y,0) in Figure 3.2b gives rise to a helical environmental (i.e. environments with large shear vectors that veers with height in the lowest kilometres) changes (Davies-Jones, 1990). Fifthly, the heavier density of cold air is typically evidenced with the formation of a mesocyclone, a usual precursor for the eminent tornadogenesis (Doswell III, 2001; Trapp, 2018). The mesocyclone is depicted with an oval shape beneath the purple arrow in Figure 3.1c and a drop of cloud base in Figure 3.2b. Tornadogenesis results when the funnel cloud extends from a cumulonimbus cloud towards the ground (D'Abreton, 1991; Smith, 2013). It thus seems feasible for tornadogenesis to develop from two interacting strong gust fronts. The development of tornadoes and their respective hypothesis are discussed using two case studies (Sections 5.3.1 to 5.3.2) and are further supported through schematic models presented in Section 5.3.3.

Alternatively, with conditions presented in Figure 2.3 and by Sun and Sun (2015), the gust front of S_2 could be inferred to significantly strengthen on the lee side of another significant topography. In such cases, rapid development of the new storm typically occurs. In such environments, the new storm could produce a tornado if it is simultaneously acted upon by the strong gust front of S_1 in the y-direction. In other environments, the rotational effect in three-dimensions could be achieved when the gust front of the approaching downwind storm (S_1) interacts with a relatively narrow concave valley. However, the magnitude of rotation in this dissertation remains indeterminate in line with the mathematical limitations stated in Section 3.3.

3.4.1.4 Severe storms relating to 500 hPa vorticity advection

Prevailing discrete thunderstorms of the CTT with temperatures of -40°C or colder were studied in linkage with the MTS troughs or COLs. Axis orientations of these MTS troughs or COLs with their associated negative magnitudes of the 500 hPa vorticity advection (also 500 hPa vertical vorticity) were compared over a passage of time. This comparison was made to determine whether a change in the behaviour of severe thunderstorms exists between trough axes that are oriented north-west to south-east as opposed to those that are oriented north-east to south-west. Severe thunderstorm characteristics are compared from one axis orientation of the MTS troughs (or COLs) to another and are illustrated in 4.3.2. Synergy of the 500 hPa vorticity advection with deep lee lows is exemplified in 4.3.2.2b as was previously studied by Kirchoffer (1986), among others.

3.5 Tornadic storms in relation to the El-Niño Southern Oscillation

The base period of this dissertation was extended to 63 years (1958 to 2021; see Section 5.6). The extension of the base period was necessary for testing whether the relationship between the high frequency of tornadic storms over South Africa and ENSO exists. The second aim was to determine if there were winter tornadoes in the period preceding the base period and if these events may have a relationship with the ENSO. Niño indices in the Niño 3.4 region, as introduced in Section 3.2.9, were used together with the tornadic

storms recorded in the severe weather log. Secondly, the extension of the base period was to establish if there were winter tornadoes in the years preceding 2016 and also to see if landspouts and tornadoes are possible on the western regions of South Africa.

Chapter 4: Severe thunderstorms across South Africa

4.1 Overview of severe storms across South Africa

Severe thunderstorms, which occurred over South Africa during the period June 2016 to June 2021 (1 856 days), are discussed in this chapter. The study of severe thunderstorms in this chapter aims to address research Objective 1. These storms represent 12.61% of the days in the study period and are listed in the Appendix. Close to 58% of these severe storm events occurred during the months of November, December, and January (hereafter, NDJ), 26% in February, March and April (hereafter, FMA), 2% in May, June and July (hereafter, MJJ) and 14% in August, September and October (hereafter, ASO). Based on the data in the Appendix, a summary of seasonal relationships among severe storms with MTS circulations is shown in Figures 13 and 14; their characteristics are discussed in subsequent case studies. Of these severe storms, approximately 47% (i.e. 111 days of the total 234 days) were associated with anticyclonic circulations (i.e. MTS ridges). This suggests that the bulk of severe thunderstorms are linked to the MTS anticyclonic circulations (i.e. subtropical MTS high pressure), resultant from the effects of subsidence. Taljaard (1958), Zunckel *et al.* (1996) and other researchers maintain MTS circulations to control the climate of South Africa. Although not shown in the Appendix, the occurrence of organised severe thunderstorms in South Africa is typically linked with ample warm moisture-laden environments near the landmass. These environments are usually associated with an intense heat low or the development of a mesocyclonic system near the surface. Intense heat lows are known to create a deep layer of vertical wind shear (Baidu *et al.*, 2022). The remaining 53% of the severe storm days were associated with MTS cyclonic circulations (i.e. MTS troughs and COLs). In this dissertation, the link between severe convective storms with MTS anticyclonic circulations is compared to MTS cyclonic circulations. That is the characteristics of severe storms are linked with the short-wave, well-developed and steep MTS troughs together with the COLs. As shown in Figure 4.1, a significant 48% of severe storm days (i.e. in 66 days) were associated with MTS anticyclonic flows (i.e. geopotential height maximum) during the NDJ period.

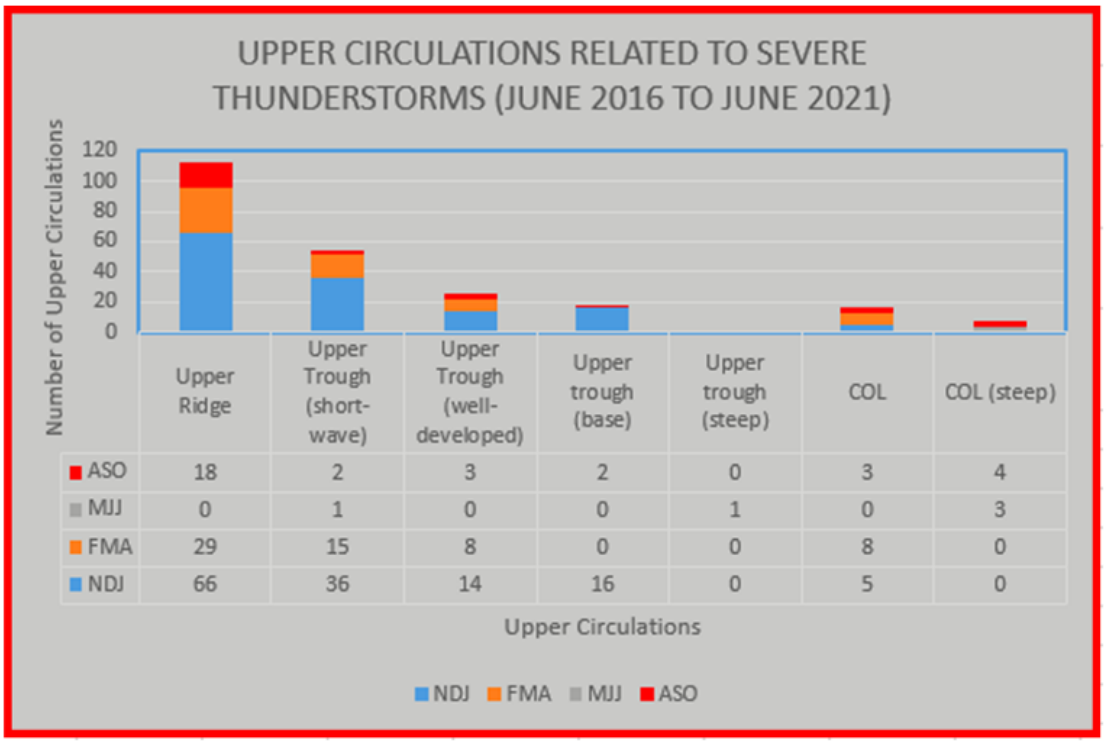


Figure 8.1: Summary of MTS weather circulations associated with severe thunderstorms for the period June 2016 to June 2021. (Source: author after the analysis of data in the Appendix).

The 48% and 56% of severe storm days were linked with MTS anticyclonic circulations in FMA and ASO, respectively. This means, MTS ridges are the first mode to which severe thunderstorms develop, although their effect is near absent during May, June and July (hereafter, MJJ). The link of severe thunderstorms in association with MTS circulations are summarised in Figure 4.1 and is discussed in further detail in Sections 4.2 and 4.3. The second mode to which severe thunderstorms were linked was found to be short-wave MTS troughs, which made up 26%, 25% and 20% of MTS circulations during the months of NDJ, FMA and MJJ, respectively. A further 6% was contributed during the months of ASO.

4.1.1 Forecast decision-making in association with MTS circulations

The South African Weather Service (SAWS) is the sole authoritative voice and issuer of weather alerts to the public in South Africa (SAWS, 2001). Segmentation of MTS weather circulations is classified and graphically represented according to whether severe thunderstorm forecasts were issued between 2 and 24 hours or not. The decision-

making for potential severe thunderstorms in association with MTS ridges were found to occur in approximately 50% of cases in which forecasts were issued versus cases for which no forecasts were issued. MTS anticyclonic circulations with their slack gradients are often linked with light and variable winds near the surface (Landman *et al.*, 2021). With such light airflows, calculations of vertical wind speed shear (e.g. by using winds at UM 4 km) in association with the MTS anticyclonic circulations produce minimal values in comparison to the MTS cyclonic circulations. Further, the directional wind shear is also minimal in association with MTS anticyclonic circulations. Such calculations produce even poorer results with ERA5 at 2.5° x 2.5° grid. Minimal values of speed and directional wind shear in the vertical produce significantly fewer numerical values of vorticity advection. For example, a case study by Lekoloane *et al.* (2021) calculated a minimum vorticity advection of -0.75×10^{-2} s^{-1} in association with the MTS ridge. This value was one order of magnitude smaller than the dynamical definition of a mesoscale. Further, quantities of the SRH in the lower troposphere associated with MTS anticyclonic circulations often have significantly less skill for predicting severe thunderstorms, irrespective of whether the circulation is cyclonic or otherwise. Hourly temporal resolutions along with the spatial resolutions for both the UM and ERA5 also play a significant role in calculating low quantities. Compounded to the low quantities of vertical wind shear, vorticity advection and SRH appear to be the topographic schemes of both the UM and ERA5, which average the terrain heights. As a result, the effect of terrain networks (e.g. concave-shaped mountains) in the development of severe thunderstorms is reduced. However, as presented in Section 2.4.2, the application of conceptual models for NWP winds in interaction with actual topography could improve the forecast for the potential of severe thunderstorms. Relative to the MTS ridges, the decision-making for issuing alerts for potential severe thunderstorms in association with short-wave MTS troughs was determined to be better at approximately 61%. A few of these short-wave MTS troughs were found along the periphery of the MTS ridges. Short-wave MTS troughs often develop to the east of well-developed MTS troughs (i.e. within these ridges), as also noted by Chikoore *et al.* (2021).

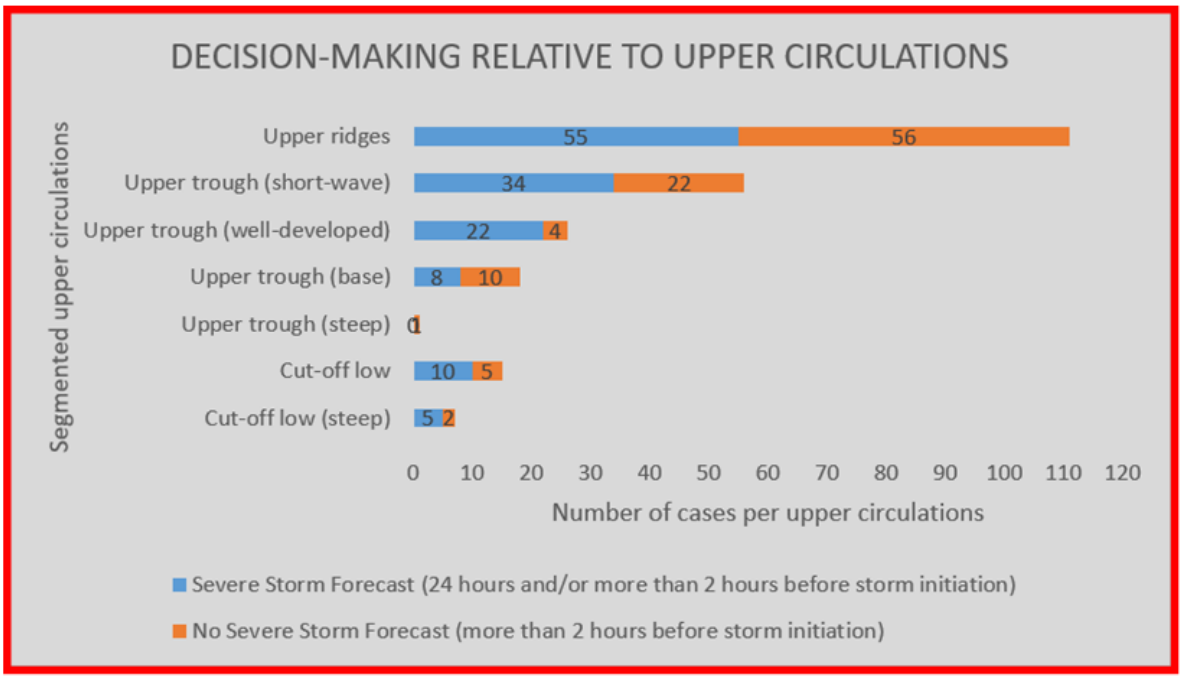


Figure 9.2: Rate of decision-making in reference to MTS circulations over South Africa for the duration June 2016 to June 2021. (Source: author after the analysis of data in the Appendix).

According to Flack *et al.* (2018), short-wave MTS troughs (or perturbations) usually develop irregularly with short-lived lifespan. Data in the Appendix also show that well-developed MTS troughs (i.e. with their axes oriented south-east to north-west) numerically far exceed steep MTS troughs (i.e. with their axes oriented south-west to north-east). In this dissertation, well-developed MTS troughs are dealt with in two segments: the central area of potential organised thunderstorms (i.e. area between bases of MTS troughs and ridges) and their bases. Decision-making regarding severe thunderstorms in association with bases of MTS troughs was determined to be worse at nearly 44%, as summarised in Figure 4.2. Overall, the decision-making improved to between 67% and 85% for potential severe thunderstorms generated in association with central areas of the well-developed MTS troughs and COLs, respectively. Therefore, between 15% and 33% represent cases for which no severe thunderstorm forecasts were issued in relation to strong MTS cyclonic circulations. No forecasts of severe thunderstorm linked to the sole steep MTS trough were sent to the public.

4.2 Effect of topography and gust fronts on severe thunderstorms

The forecasting of isolated severe thunderstorms under the influence of MTS ridges, as presented in Section 4.1.1, is analysed in this section. The objective is to reduce the conundrum of forecasting severe thunderstorms associated with MTS ridges since they contribute to a high percentage of no alerts for short to very short-range forecasts (i.e. between 2 and 36 hours), as indicated in Figure 4.2. To achieve this objective, two case studies were chosen and are discussed in Sections 4.2.1 and 4.2.2 to exemplify severe thunderstorms referenced to the central region and periphery of the MTS ridges. A sensitivity test was conducted on these two case studies to compare the effect of averaged topography scheme of the UM and ERA5 model against adjustable very high-resolution maps of topographic barriers.

4.2.1 Case studies: isolated severe storms under weak MTS ridge

4.2.1.1 Case A: Flash floods and small hail at Sun City on 15 December 2018

A heat low was located over the central interior of South Africa by both the UM and ERA5 reanalysis at 13:00 UTC on 15 December 2018, as seen in Figures 4.3a and 4.3b. Around this time, ERA5 was at a central pressure of 1 490 gpm, 50 gpm less than the UM, which was at 1 540 gpm. Associated horizontal wind strength was light and variable in the north-east of the North West and Gauteng provinces within the highlighted subregion (25°E and 29°E and -27°S and -25.5°S). The approximate coordinates of Sun City are at -25.347 (latitude) and 27.100 (longitude). The UM suggested minimal instability variables with 850 hPa K-index of between 30 and 36, CAPE amounts ranging between 0 and 400 $J.kg^{-1}$ and 500 hPa Lifted Index (LI) of 0°C and -2°C. ERA5 calculated 26 to 32 for K-index and 0 to 500 $J.kg^{-1}$ for CAPE but LI was not calculated. At 500 hPa level in Figures 4.4a and 4.4b, both the UM and ERA5 placed an MTS high over the north-central areas of South Africa with UM suggesting the central pressure at 5 920 gpm, exceeding the ERA5 value by 120 gpm. The vertical wind profile suggested light to moderate speeds with minimal directional shear.

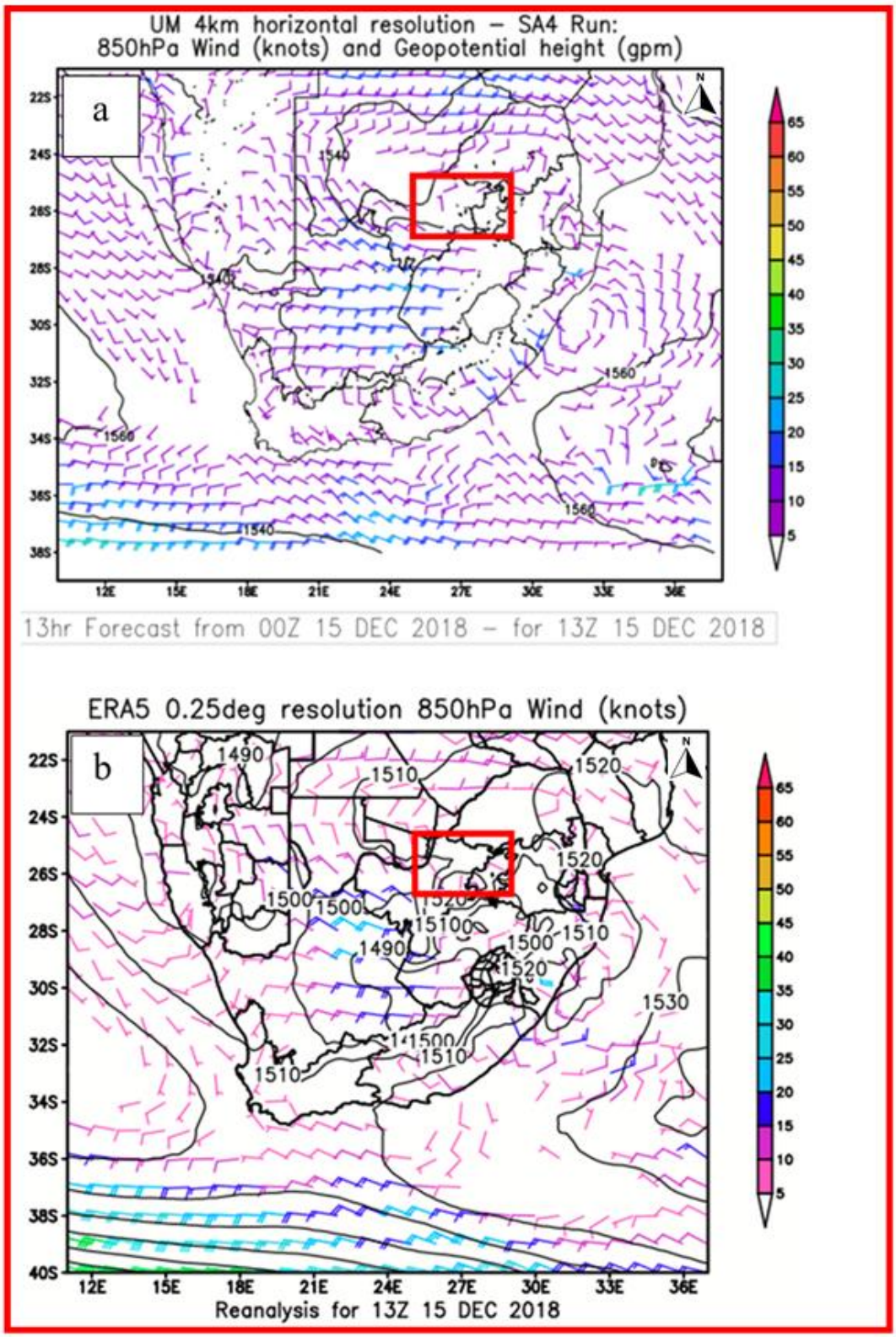


Figure 10.3: Comparison of surface circulations and wind flow (barbs) at 13:00 UTC on 15 December 2018. The UM and ERA5 model outputs are respectively shown in 4.3a and 4.3b with more focus in the subregion highlighted in red.

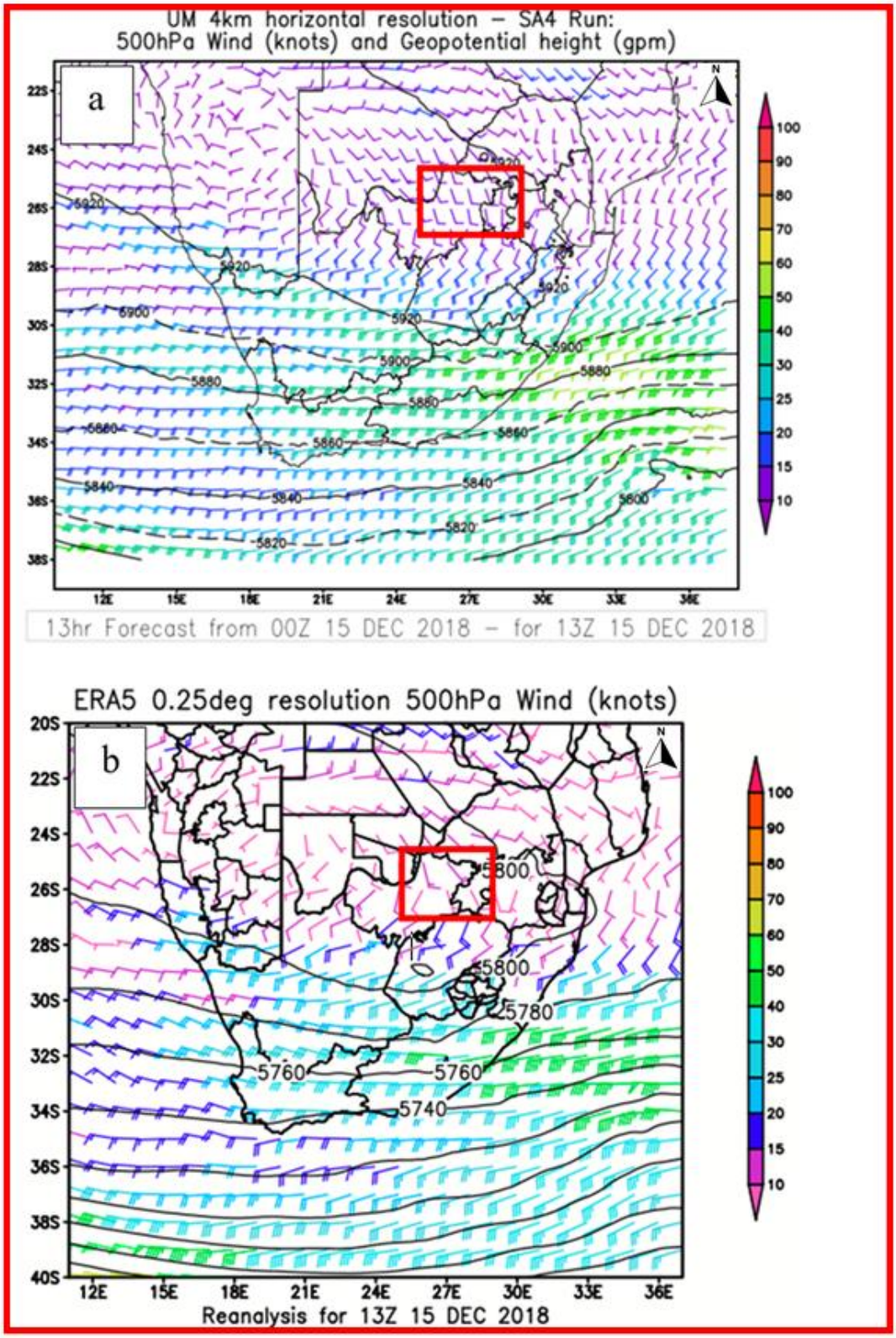


Figure 11.12 Comparison of MTS circulations and wind flow (barbs) at 13:00 UTC on 15 December 2018. The UM and ERA5 model outputs are respectively shown in 4.4a and 4.4b with more focus in the subregion highlighted in red.

Such instability, wind profile and daytime heating have the potential to generate non-severe afternoon thunderstorms, as the SAWS forecasted for on 15 December 2018. This forecast is affirmed by Van Delden (2001) and Mandal (2017), among others. Moreover, Kerns and Chen (2015) found that a core of subsidence warming could optimise instability for severe thunderstorms (the role of subsidence warming is often underrated). As supported by Johns and Doswell III (1992), optimum or extreme instability (e.g. sample of CAPE amounts discussed in Section 5.2.1) is one key requirement for the initiation of severe convective storms. Instability may be little or non-existent in the lower troposphere but exists in the middle and upper troposphere (Mandal, 2017). However, no single standard is used to cover the special characteristics of the severe convective weather (Wang *et al.*, 2016). Mandal (2017) and Lin *et al.* (2021), among others, emphasise that localised vertical wind shear in the lower troposphere is another key ingredient for severe thunderstorms. Localised vertical wind shear is also discussed in Sections 5.2.1, 5.2.2, 5.2.3 and 5.2.4. A larger temperature lapse rate of 7°C/km or more in the mid-level (e.g., 700 to 500 hPa) usually above a level of free convection is considered steep and often leads to localised mid-level vertical wind shear and potential initiation of extreme thunderstorms (Craven and Brooks, 2004; Houston and Niyogi, 2007; Takemi, 2014). The lapse rate of temperature that approaches the dry adiabatic (i.e. 9.8°C/km) between 700 and 500 hPa layer is often associated with an increased downburst and rainfall rate (Houze, 1993). The steepest of the lapse rates in South Africa are usually found in November when surface temperatures are near their maxima, generally contributing to the development of the severest storms associated with large hailstorms, strong gusty winds and tornadoes (Kessler, 1982; Olivier, 1990; Vermeulen, 2014; Simpson and Dyson, 2018). As discussed in Section 5.2.1, vertical wind shear, particularly in South Africa, is usually favoured in areas affected by strong outflow (i.e. downburst, gust front or even localised gale force winds) from active thunderstorms at high ELEV regions in the landscape (e.g. Tyson and Preston-Whyte, 1972; WMO, 1978; Sun and Sun, 2015; Figure 2.3) or the flow of low-level wind into curved mountains.

Actual observations

A temporal split of thunderstorms occurred in the North West province some distance to the north of Magaliesburg town at 13:00 UTC, as shown in Figures 4.5a and by arrows in 4.5d. Thirty minutes later (see Figure 4.5b), storms that moved along the Magaliesburg mountain range towards Hartebeespoort Dam (red arrow to the right in Figure 4.5d) soon dissipated and were not studied further. In contrast, storms that propagated to the left along the mountain range and were to the south of Rustenburg (see Figure 4.5b) remained fairly intense with the increase of CTTs from -62℃ to -53℃. This CTT increase could have resulted from an encounter with the uneven slopes of the mountain range, as shown by the blue arrows in Figure 4.5d. In accordance with Jury (1984), such left-moving thunderstorms in the southern hemisphere are often linked with an increase in Coriolis force, including the interaction of cyclonic fluids with significant topography. The north-westwards propagation of the primary storm was in part influenced by the south-easterly wind flow in the mid-level (Figures 16a and 16b). A chain of events results in accordance with that discussed in the caption of Figure 2.3. Firstly, the gust front of the storm to the south of Rustenburg probably compressed on an encounter with a broader portion of the mountain range. Secondly, the enhanced strong gust front caused the development of a storm to the south of Ga-Luka. Cooling of the CTTs typically signaled the growth of vertical height (Baidu *et al.*, 2022). Thirdly, the interaction of a strong gust front of the storm from south of Ga-Luka with lower heights of mountain range caused the rapid intensification of the small-sized storm at Sun City (hereafter, primary storm) with CTT cooling from between -38℃ and -42℃ to between -48℃ and -52℃**.** Sun City rests near volcanic rock formation (Swart and Horn, 2012). Its location is to the south of the circular significant topography in Figure 4.5d. The CTTs that drop by about 10℃ or more in a short time signify the intensity or severity of storms (e.g. De Coning *et al.*, 2015). The contribution of the surface obstruction to storm intensification and by implication the development of optimum, localised, vertical wind shear in the lower troposphere is also supported by Pettitt and Root (1969). Further, the intensification from the airmass connection is supported by several previous studies (Terblanche, 1985; D'Abreton, 1991; Cox, 2000; Doswell III, 2001 and Sano and Tsuboki, 2006). Times in Figures 4.5a and 4.5e show the primary storm in the Sun City region persisted nearly 60 minutes.

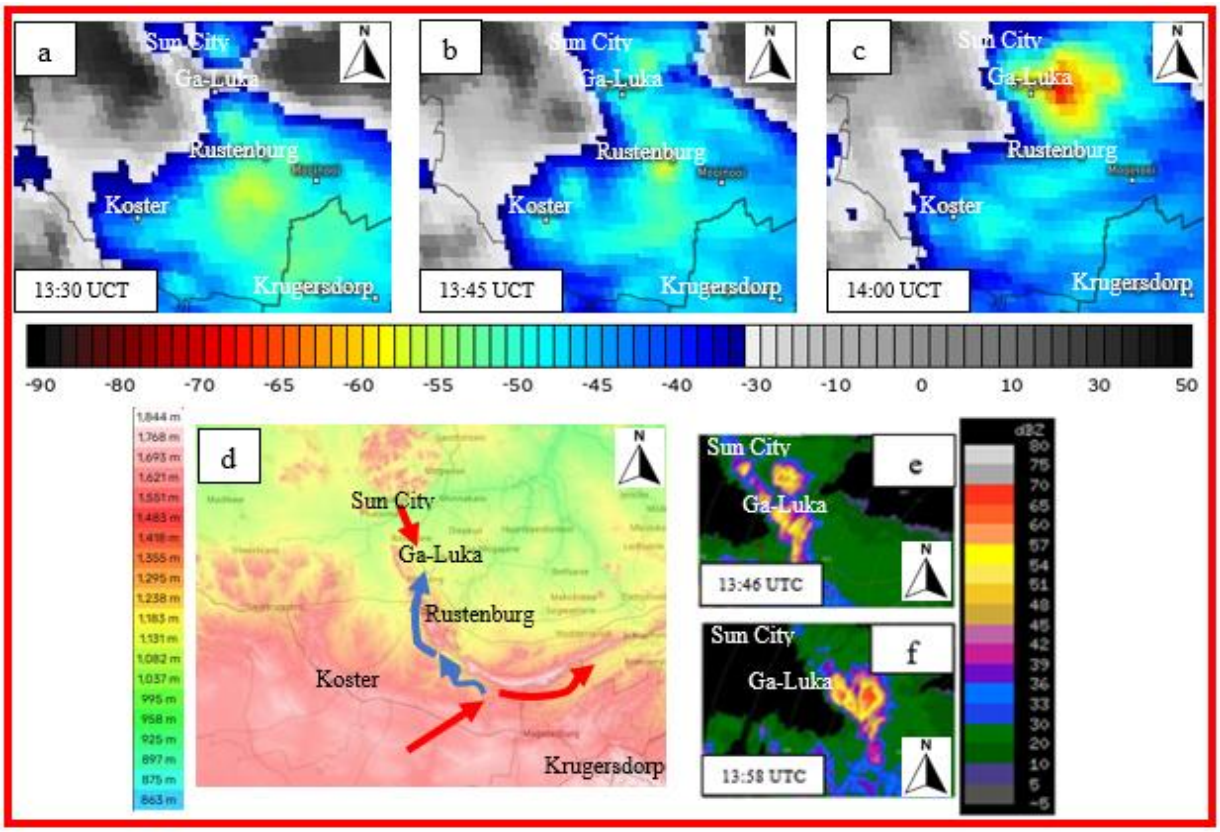


Figure 13.4: Thunderstorm movements between 13:00 UTC and 14:00 on 15 December 2018. The general northward movement of storms along the Magaliesberg mountain range in 4.5a to 4.5c are demonstrated with blue arrows in 4.5d. Small-scale stationary storm to the north of Ga-Luka (at Sun City) persisted for nearly an hour as the times on 4.5a and 4.5e show. The ultimate merger took place a few minutes leading 14:00 UTC. Map scales are 1:4500000 and 1:7200000 for the top and bottom rows, respectively. (Sources: 4.5a to 4.5c – EUMETSAT; 4.5e and 4.5f – SAWS).

Therefore, an unexpected large amount of small hail and flash-flooding occurred (Figures 4.6a and 4.6b) as a result of this small-sized storm. These severe storm events damaged vehicles and disrupted patrons in almost 200 hotel rooms at the Sun City Resort. Minutes before 14:00 UTC, the storm to the south of Ga-Luka began to cross to the right through the shallower section of the mountain range and thus directing the gust front away from the primary storm. A south-eastwards movement of the primary storm from Sun City culminated with the mergence of the storm near Ga-Luka (see Figures 4.5c and 4.5f). Rapid intensification near Ga-Luka (Figure 4.5c) was reflected with very cold CTTs that dropped from -53°C to just below -70°C. Complementary values of RADAR reflectivity also increased to near 70 dBZ. These meteorological tools

suggested the potential for strong winds, hailstones, including heavy rain and flash-flooding.



Figure 14.15: Storm impacts at Sun City Resort. Large quantity of small-sized hailstones with flash-flooding underneath is shown in 4.6a. Flooded resort is shown in part in 4.6b.

A merger that results in severe convective storms aligns with studies by Bluestein and Weisman (2000). Moreover, the north-eastwards trajectory of the merged storms (not shown) confirms that the steering effect of light to moderate mid-level winds is limited and could be cancelled-off. The impact of these storms coincided with the festive season and led to restricted economic activities at this resort, lasting about two weeks with slow recovery thereafter. The residual losses accumulated into tens of millions of Rands.

4.3 Severe thunderstorms related to MTS cyclonic flows

This section uses four cases of severe thunderstorms to investigate the MTS cyclonic circulations from short-wave MTS troughs, well-developed MTS troughs and COLs. The effect of the orientation of the trough axis from south-east to north-west (i.e. trough axis with a bearing between 315° and 360° as in Figures 4.7, 4.11 and 4.15) are compared against their counterpart oriented from south-west to north-east (i.e. trough axis with a bearing between 0° and 45° as shown in Figures 4.17 and 4.19b).

4.3.1 Case studies on short-wave MTS troughs

A 23% of severe thunderstorms in Appendix was associated with short-wave MTS troughs (MTS perturbations). This has been found to be the second biggest contributor in all MTS circulations. Severe thunderstorms could be thought of when extreme instabilities are considered with surface features (i.e. topography and vegetation), as will be discussed in detail in the case studies of Richmond and Ulundi tornadic storms in Sections 5.3.1 and 5.3.2, respectively. Decision-making for the forecasts of severe thunderstorms linked with the short-wave MTS troughs appears to be relatively good in comparison to those linked with the MTS ridge.

4.3.2 Strong MTS waves

4.3.2.1 Well-developed MTS troughs

This section expands on the last paragraph of Section 4.1 and is further discussed in Sub-sections 5.2.2 and 5.2.4. The section deals with well-developed MTS troughs (also known as, large amplitude wave or mid-latitude systems). Orientation of the axes of these MTS troughs range from the south-east to the north-west (i.e. trough axis with a bearing between 315° and 360°), as exemplified in Figures 4.7a and 4.7b. Similar trough axes of well-developed MTS troughs in Figure 4.1 represent 11% of MTS weather circulations in all four seasons to which severe thunderstorms were associated. Of all MTS circulations linked with severe thunderstorms, well-developed MTS troughs represented approximately 10% in NDJ, 13% in FMA, 0% in MJJ and 9% in ASO periods, respectively. An increased occurrence of such MTS troughs during autumn confirms the findings by Tyson and Preston-Whyte (2000) and Dyson (2014). A double jet streak structure in wet events enhances MTS divergence, which contributes to widespread uplift and organised storms on the central region of the MTS trough (i.e. between bases of MTS troughs and ridges) (Barclay *et al.*, 1993; Majodina and Jury, 1996; Mpanza and Dyson, 2015). Intense low surface pressure systems resulting from well-developed MTS troughs (i.e. less frequent mid-latitude circulations) often generate optimal low-level vertical wind shear with the subsequent development of severe thunderstorms. For such MTS trough axes, the decision-making derived from the NWP

model seems very good, as reflected in Figure 4.2. Related to other severe thunderstorms in the NDJ period, as much as 13% of MTS circulations was made up of bases of the MTS trough axes, which were usually orientated south-to-north (i.e. with a bearing of near 360°) (not shown). The development of storms associated with bases of well-developed troughs is often underrated by the NWP model, but an attempt to correct such an error is beyond the scope of this dissertation. According to Ndarana and Waugh (2010), the highest concentration of cold air is typically hosted within well-developed MTS troughs, particularly within the bases of MTS troughs. Cold air aloft promotes potential instability and often triggers the likelihood of thunderstorms (e.g. severe thunderstorms) on a high-energy air near the landmass (Cohuet *et al.*, 2011).

4.3.2.1.a Case B: Organised storm over central South Africa - 24 January 2020

The UM and ERA5 placed the trough axis of a well-defined 500 hPa MTS trough along the west coast of South Africa at 12:00 UTC on 24 January 2020 (Figures 4.7a and 4.7b). Both these models extended the base of the 500 hPa trough to as far north as 25°S over southern Namibia. The UM suggested a longer band of 500 hPa strong winds to be in the region of 35 to 45 knots over the west-central South Africa compared to the ERA5. The UM proposed 500 hPa temperatures to be as cold as -10°C to -6°C and were confined to the central regions of South Africa (not shown). Such cold temperatures also spread to the western region of South Africa and southern Namibia. The observations of the coldest temperature in the equatorward sectors of the MTS troughs (or COLs) are affirmed by Ndarana and Waugh (2010). Van Loon (1972) and the discussion in Section 4.3.2.1 on the occurrence of well-defined MTS troughs over South Africa, consider this as unseasonal in January since a few of the large amplitude waves reach as far north as 30° latitude in mid-summer. Associated with the well-defined MTS trough, the arrival of cold temperatures aloft relative to high-energy air in the lower troposphere promotes the potential instability and thunderstorms (e.g. severe thunderstorms) (Cohuet *et al.*, 2011). Both the NWP and reanalysis (i.e. ERA5) situated the 850 hPa low over the west-central interior of South Africa. Figures 4.8a and 4.8b show the central pressure was 1 480 gpm and 1 450 gpm as output of UM and ERA, respectively. Such deep surface troughs often cause strong surface moisture

convergence, uplift and vorticity advection, following association with the jet stream (i.e. core of strongest winds) and enhanced upper-level divergence at 200 hPa (Cotton and Anthes, 1989; Hart *et al.*, 2010; Lee *et al.*, 2019; Kaluza *et al.*, 2021). It is likely that an imbedded MTS perturbation with the steep topography near the border of the Free State and Eastern Cape provinces at 11:30 UTC (Figure 4.9b) played a role in the intensification of storms that moved into the Eastern Cape. The southward shift of such storms from the southern Free State and Northern Cape to the Eastern Cape seem to serve as evidence of the presence of the strong steering winds in the mid-level layer. Storms that are steered in one direction in tandem with 700 hPa geostrophic winds are supported by Kelley *et al.* (2019). The effect of thermodynamic processes (e.g. colder temperatures aloft) could be deduced from discrete storms on the south-eastern areas of the Northern Cape. Newly developed thunderstorm cells that developed along the southern Drakensberg area (i.e. between Nieu Bethesda and Middleburg in the Eastern Cape) dropped CTTs to between -50°C and -62°C between 10:00 UTC and 10:15 UTC (not shown). Such a short period (i.e. 15 minutes) of cooling of CTTs (e.g. by -12°C) signified a rapid, but momentary, storm intensification. The storm intensification seems to have occurred as demonstrated in Figure 2.3, which is due to the enhanced downslope gust front also discussed in Sections 4.3.2.2b and 5.3.2. After travelling about 215 km to the south-east (near Hogsback), a portion of the storm at the rear flank experienced another drop of CTTs from -59°C to -72°C between 13:15 UTC and 13:30 UTC but less (colder) than -80°C for the next 45 minutes. Sustained storm intensity was suggestive of a very strong rotating updraft with the potential for large hailstones, strong winds, damage to property and uprooting of trees. Further enhancement and evolution of the storm over the south-eastern inland areas of the Eastern Cape seemed to have occurred due to strong and persistent gust fronts from the dissipation process of the intense upwind storm near the border of the Northern Cape and Eastern Cape provinces.

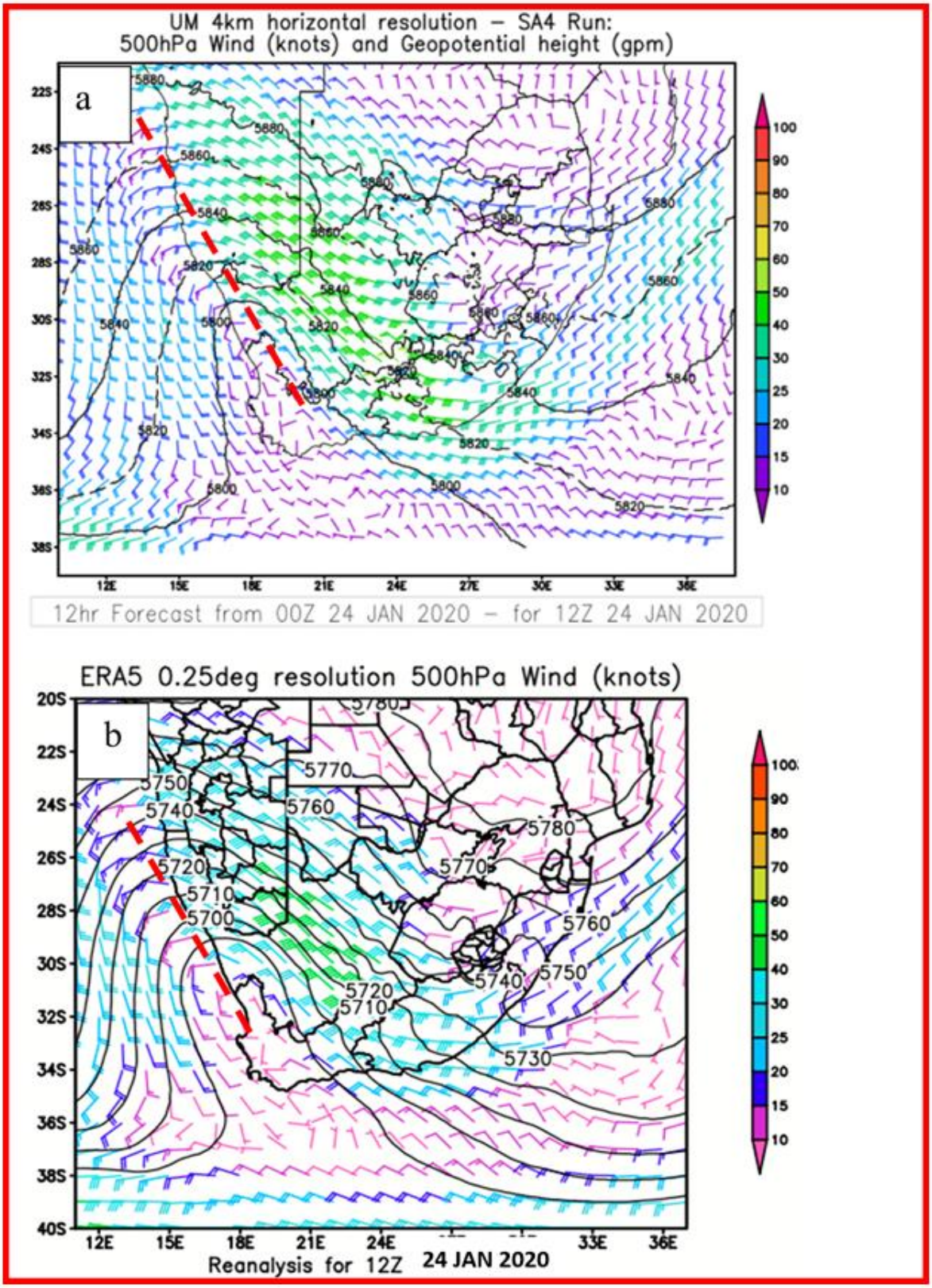


Figure 16.17: The 500 hPa comparison of circulations and winds at 12:00 UTC on 24 Jan 2020. Outputs of UM and ERA5 models are respectively shown in 4.7a and 4.7b. The dashed lines represent the trough axis.

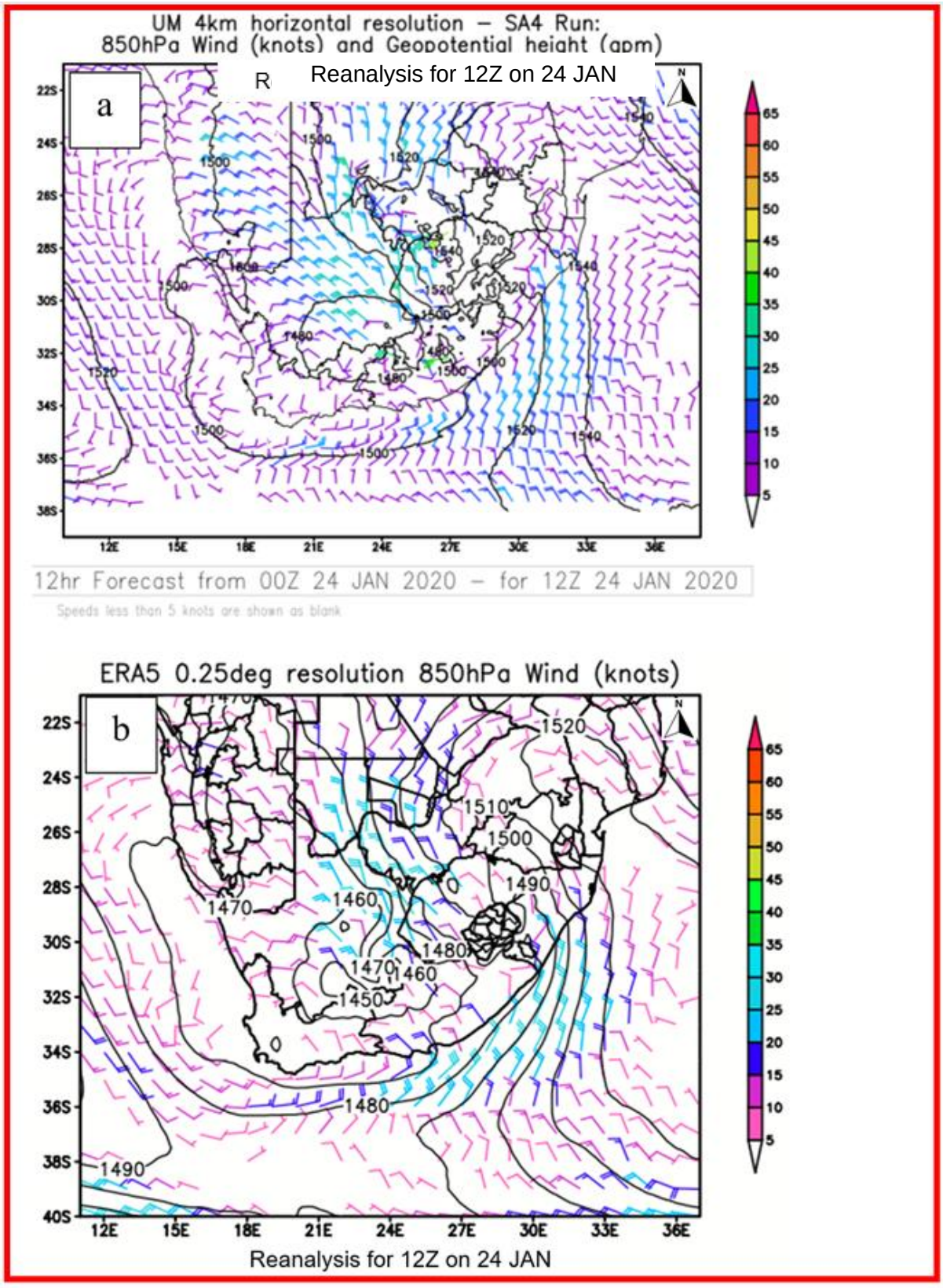


Figure 18.19: The 850 hPa comparison of circulations and winds at 12:00 UTC on 24 Jan 2020. Outputs of UM and ERA5 models are respectively shown in 4.8a and 4.8b with deep surface trough on the west-central region of South Africa.

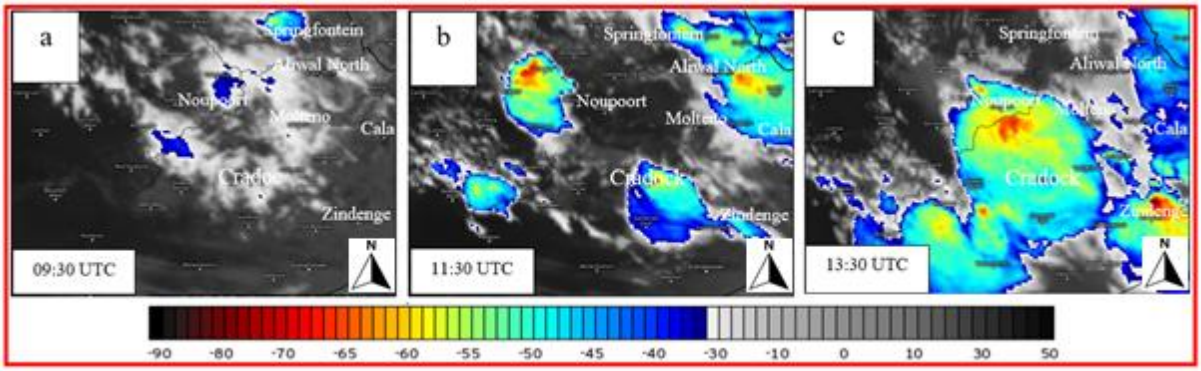


Figure 20.21: Convective cloud pattern linked with a baroclinic well-defined MTS trough in Figures 4.7a. Storms were still developing in Figure 4.9a, intensifying in 4.9b and 4.9c. Map scale is 1:7600000 all three subregions. (Source of images: EUMETSAT).

Such argument is supported by the WMO (1978) and Sun and Sun (2015), and is demonstrated with wind observations in Figures 5.7a to 5.7c and 5.7e. Further, Huang *et al*. (2017) noted that the leading edge of the storm (i.e. gust front) could reach far distances (e.g. 80 km away). Among others, Colby Jr. and Walker (2004), and Ackerman and Knox (2012) support that cold (elevated) thunderstorms could result from rapid development of new thunderstorm cells or the rapid intensification of the existing thunderstorm. In some cases, intense storms could produce gust fronts as fast as 20 to 30 $m.s^{-1}$ (Goliger and Retief, 2007).

4.3.2.2 Cut-off low pressure systems

Development mechanisms of thunderstorms (e.g. severe thunderstorms) associated with COLs fundamentally align with those of well-developed MTS troughs, as discussed in the preceding section. Figure 4.1 summarises the Appendix and shows that COLs contributed 3% of MTS circulations associated with severe convective storms during the NDJ period. The trough axes of these COLs were orientated from south-east to north-west (i.e. trough axis with a bearing between 315° and 360°). As summarised in Figure 4.1, the contribution of COLs to severe thunderstorms increases in these periods as opposed to the NDJ period, despite severe storm incidents being fewer in number in the FMA and ASO periods (3 and 4 COLs) separately. Of all these COLs, steep ones were identified during the months of ASO. Figure 4.1 further shows that severe convective storms during the winter season (e.g. in the MJJ period) most often develop

in association with COLs. An estimated 11 COLs occur per annum over South Africa (Taljaard, 1985; Singleton and Reason, 2007; Molekwa, 2013). In contrast, severe thunderstorms associated with COLs occurred over 21 days in the five years of study. It could be deduced that COLs were fewer in the study period in part because of the dominance of strong MTS highs during the El-Niño phases in 2016 and 2019. On the other hand, some COLs (e.g. on 14 May 2017; 12 March 2019; 21 to 26 June 2019) could not produce extreme weather events and were excluded from this study. Such dry MTS cyclonic circulations are associated with less magnitude of thermodynamic changes, precipitable water (e.g. 15 mm or less) with rainfall intensity over a limited spatial distribution (Barclay, 1993; Mpanza and Dyson, 2015). In similar fashion as in Subsection 4.3.2.1, the COL-related divergence aloft usually leads to the rise of warm air *en masse* in the lower levels, typically leading to deep surface low (e.g. of central pressures less than 1 490 gpm). Such deep surface lows over South Africa often have curvature vorticity, which have been observed to have better skill for spatio-temporal approximation of the SRH in the lowest 3 km. Skill of the SRH is much lower when severe storms are linked with MTS anticyclonic circulations. In Figure 4.1, severe thunderstorms linked with steep COLs have trough axes tilted in a south-west to north-east direction (or trough axes with the bearing between 0° and 45°), as found during MJJ, but more so during ASO. Only 3% of severe thunderstorm-producing MTS circulations seen in Figure 4.1 were represented by such steep COLs. In part, steep COLs seem to occur when an MTS ridge in the east blocks their eastward propagation (DMSLP Report, 2007). In addition, the development of steep COLs could be attributed to the development, approach or amplification of another MTS trough approaching in the west. Accepted as weakening in the northern hemisphere, COLs with south-west-to-north-east orientation over South Africa sometimes produce discrete severe thunderstorms. Steep COLs are often associated with strong vorticity advection and are known to preserve angular momentum (Cotton and Anthes, 1989; Rae, 2014). As such, some steep MTS troughs and COLs favour the occurrence of large hailstorms, strong gusty (*potentially damaging*) winds, or even tornadoes; the severest of these isolated extreme thunderstorms seem to be favourable along the north-eastern periphery of COLs. As discussed in Section 4.1.1, the probability of detecting severe thunderstorms

in association with COLs was determined to be at 71% for short to very short-range forecasts. COLs have been linked with localised flooding over the south-eastern regions of South Africa (Molekwa, 2013; Jacobs, 2017). The tendency for flooding over the south-eastern region of South Africa may be the result of the influx of very moist and unstable air surface winds from the Agulhas Current (Archer *et al.*, 2010). Extreme thunderstorms sometimes occur along the ridge section of the COLs against the subsidence effect.

4.3.2.2a Case C: Severe storms ageostrophic to MTS winds - 13 February 2018

The UM positioned a weak 500 hPa COL just off the west coast of South Africa with moderate to strong winds and a tropical cloud band (not shown) over the extreme western region. Table 2 shows that some light to moderate showers potentially deposited moisture in this region where it cleared post-sunrise. CAPE data on UM were erased but the ERA5 suggested CAPE amounts to be in the region of 200 $J.kg^{-1}$ to 600 $J.kg^{-1}$ at 06:00 UTC, as circled in red in Figure 4.10a. Typically, the western regions of South Africa are climatologically arid and experience highly irregular precipitation (Botai *et al.*, 2018). In the planetary boundary layer, soil moisture is known to regulate atmospheric variables (e.g. humidity, radiation and temperature) and is of significance over the semi-arid regions (Engelbrecht *et al.*, 2022). At Clanwilliam and surrounding vicinity, the surface temperatures were very high, in the region of 35℃ to 38℃ (Table 2). Such surface heating acted on the humid environment (i.e. temperature with humidity in Table 2) and potentially played a role in increasing the CAPE amounts to between 600 $J.kg^{-1}$and 1 200 $J.kg^{-1}$ at 12:00 UTC (Figure 4.10b). In regions far away from the moisture source, substantial CAPE amounts often result from clear skies which promote unimpeded solar radiation energy acting on moisture (Tyson, 1988). Steyn and Bruintjes (1990) and others state that moist unstable conditions with surface heating and topography have the tendency to trigger the thunderstorm initiation. As Figure 4.11a shows at 12:00 UTC, the associated north-westerly winds at 500 hPa were in the region of 15 to 20 knots over the extreme north-western region of the Western Cape onto the extreme south-western region of the Northern Cape. However, a core of stronger winds (e.g. 25 to 35 knots) was present off the west coast. Figure 4.11b shows

the ERA5 output at 500 hPa with a deeper central low at 120 hPa less compared to the UM. Both the NWP (UM) and reanalysis (ERA5) propagated the COL marginally to the east. Consequentially, the UM dropped temperatures at 500 hPa from between -10°C and -8°C at 06:00 UTC to between -12°C to -10°C at 12:00 UTC (shown).

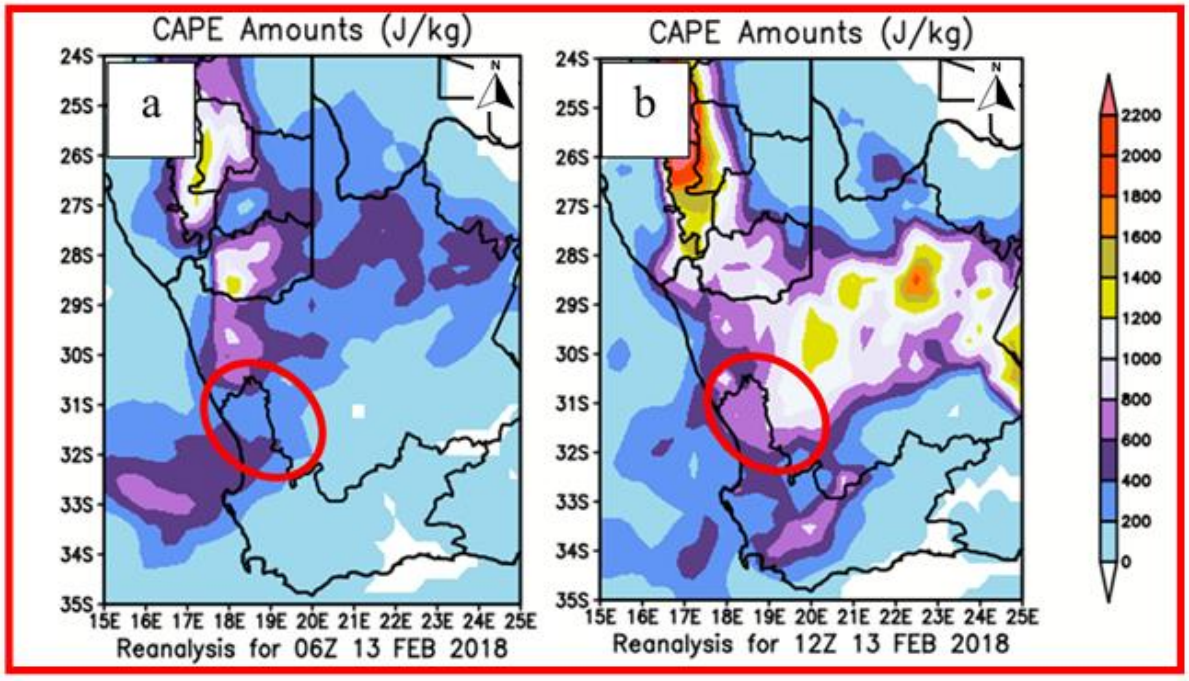


Figure 5.22: Increase of CAPE amounts related to solar heating as shown by the ERA5 reanalysis model between 06:00 UTC and 12:00 UTC on 13 February 2018 in 4.10a and 4.10b respectively.

The ERA5 had an insignificant temperature drop at 500 hPa which remained between -10°C and -8°C at 12:00 UTC compared to 06:00 UTC (not shown). Colder air aloft the moist and hot conditions often leads to potential instability and thunderstorm developments. At 12:00 UTC (Figures 4.12a and 4.12b), both UM and ERA5 located the 850 hPa trough axis nearly along the west coast of South Africa in reference to the associated baroclinic to the weak COL aloft. ERA5 was 30 hPa less with marginally stronger winds in the south along the west coast of South Africa in comparison with UM.

Actual observations

At around 12:00 UTC, a thunderstorm developed rapidly in the valley just to the west of Niewwoudtville, in the Western Cape province (Figure 25a) and at the start of the red arrow in Figure 4.13d. This storm will be referred to as the primary storm. Such storm development is supported by Ndarana and Waugh (2010) and Cohuet *et al.* (2011). The primary storm propagated northward along the steep topography (Figures 4.13b and 4.13d). That is, the effect of a north-westerly steering wind in the middle layer (Figure 4.11) was cancelled, in similar manner as that discussion of actual observations of the control case study (i.e. Figure 4.5) in Section 4.2.1.1. More than two hours later, the storm intensified in the concave valley in the vicinity of Loeriesfontein, probably producing strong winds, hail, including heavy rain and flash-flooding. The primary storm then assumed slower propagation in a north-eastward trajectory in line with the shape of the valley. That is, the primary storm underwent back-building (i.e. a propagation against the mean steering winds) probably because of the interaction of the cyclonic fluids with this mountain range. This argument aligns with Jury (1984) and Houston and Wilhelmson (2006). In another valley, the steering flow directed some small-sized storms south-eastward to the concave-shaped Hantam Mountains (not shown but demonstrated in yellow dashed arrow in Figure 4.13d). The Hantam Mountains are found to the north of Calvinia in the Northern Cape province, where the ELEV rises to over 1 300 m. and is associated with steep gradients. At this concave-shaped mountain range, the storms merged, intensified, and were deflected north-westward against the steering flow, and then merged with the primary storm. Merging of these storms led to notably colder CTTs at less than -80°C (Figure 4.13b). Such cold CTTs signify larger height (vertical depth) of the storm as noted by Steyn and Bruintjes (1990). Gust fronts of a chain of small-sized storms in the upwind and significant topography also played a role in prolonging the primary storm. Five hours after the initiation of the primary storm (Figure 4.13c), CTTs were approximated to -90°C and exhibited further intensification. Such excessively cold CTTs are often associated with the likelihood of hail the remnants of which were seen on the ground the following morning, as depicted in Figure 4.14.

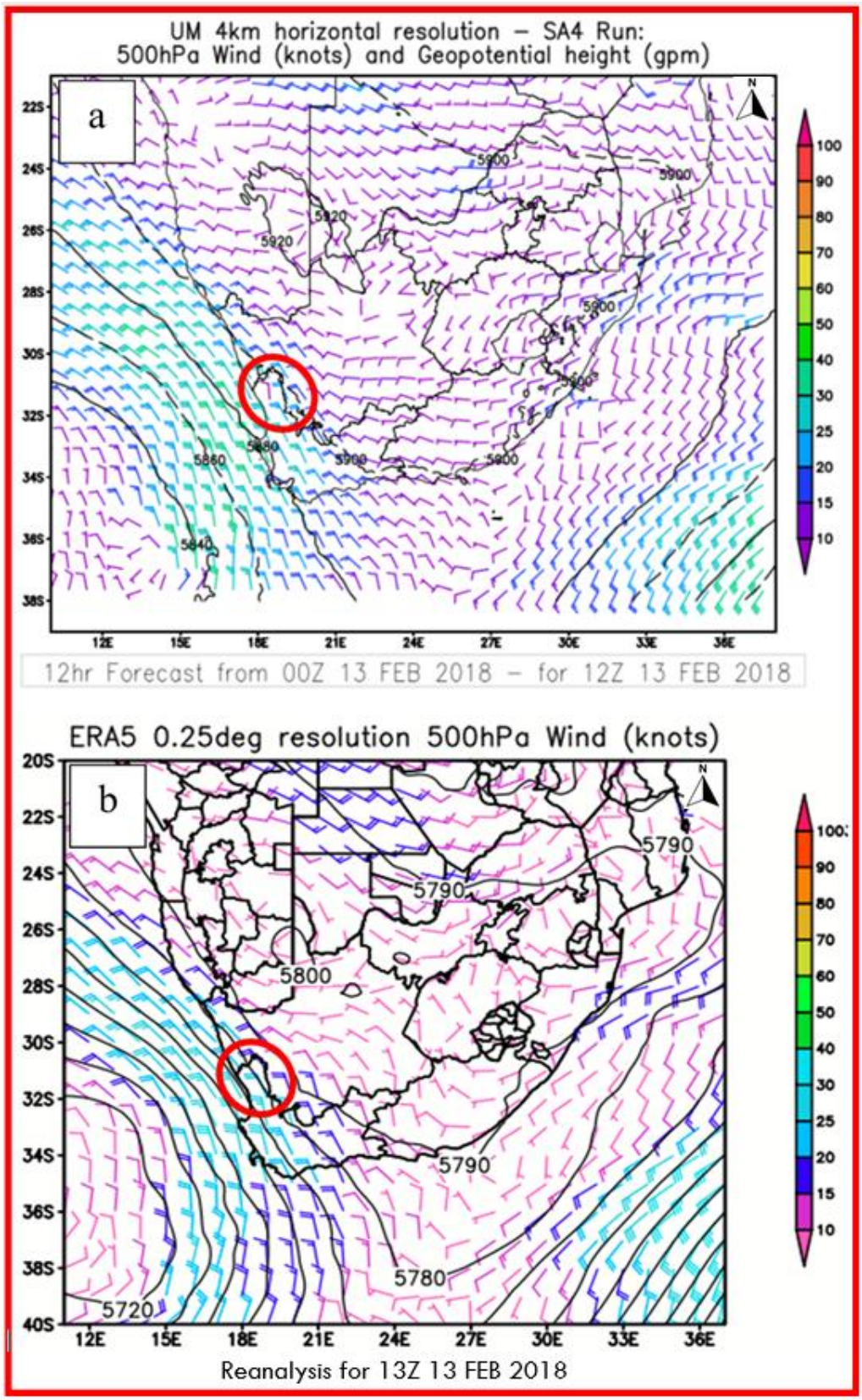


Figure 23.24: The 500 hPa pressure pattern (black contours) and the winds (barbs) at 13:00 UTC on 13 February 2018. Outputs of the UM and ERA5 models are respectively shown in 4.11a and 4.11b. The subregion of interest is highlighted in a red circle.

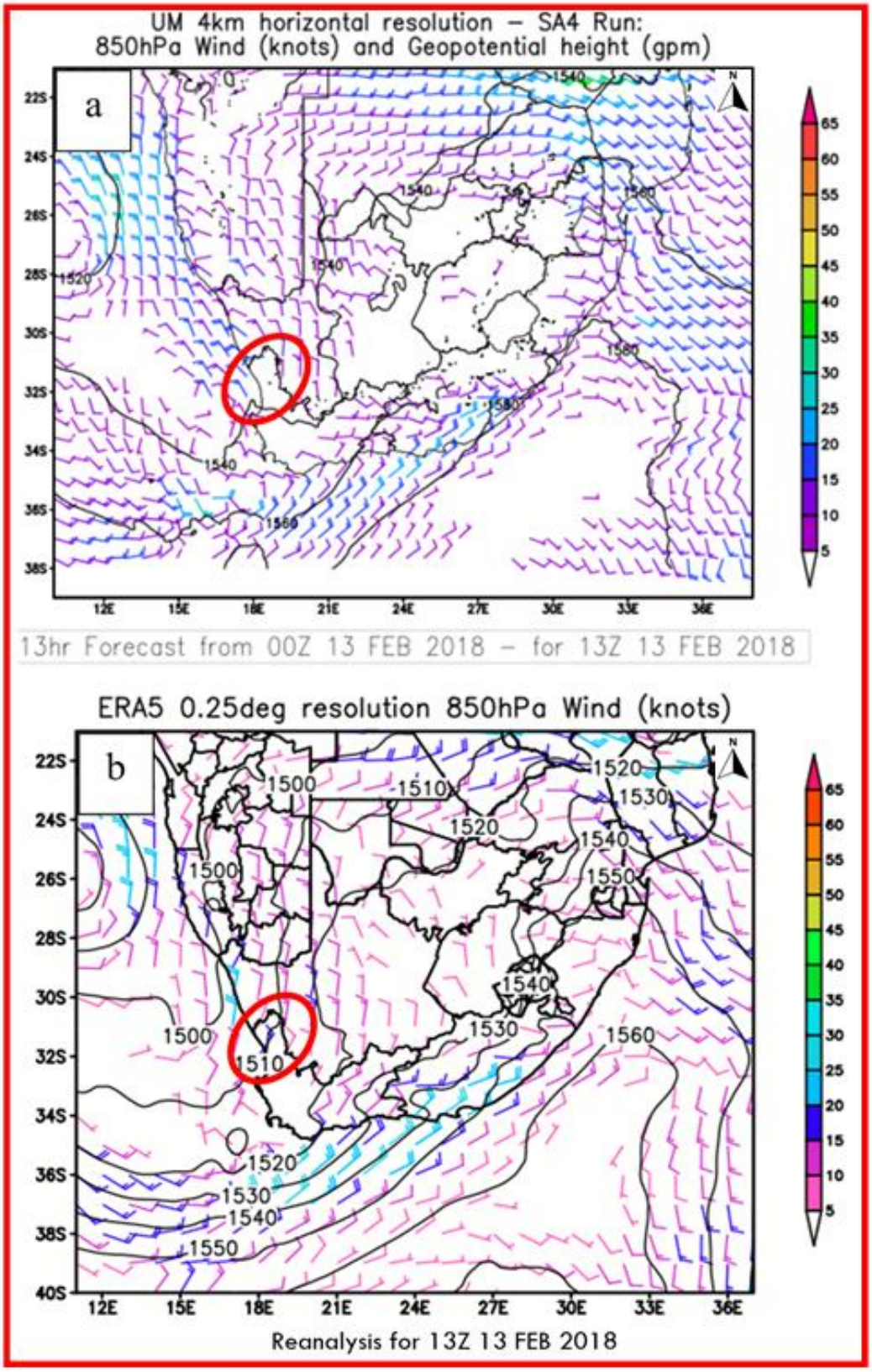


Figure 25.26: The 850 hPa pressure pattern (black contours) and the winds (barbs) at 13:00 UTC on 13 February 2018. Outputs of the UM and ERA5 models are respectively shown in 4.12b a and 4.12b. The subregion of interest is highlighted in a red circle.

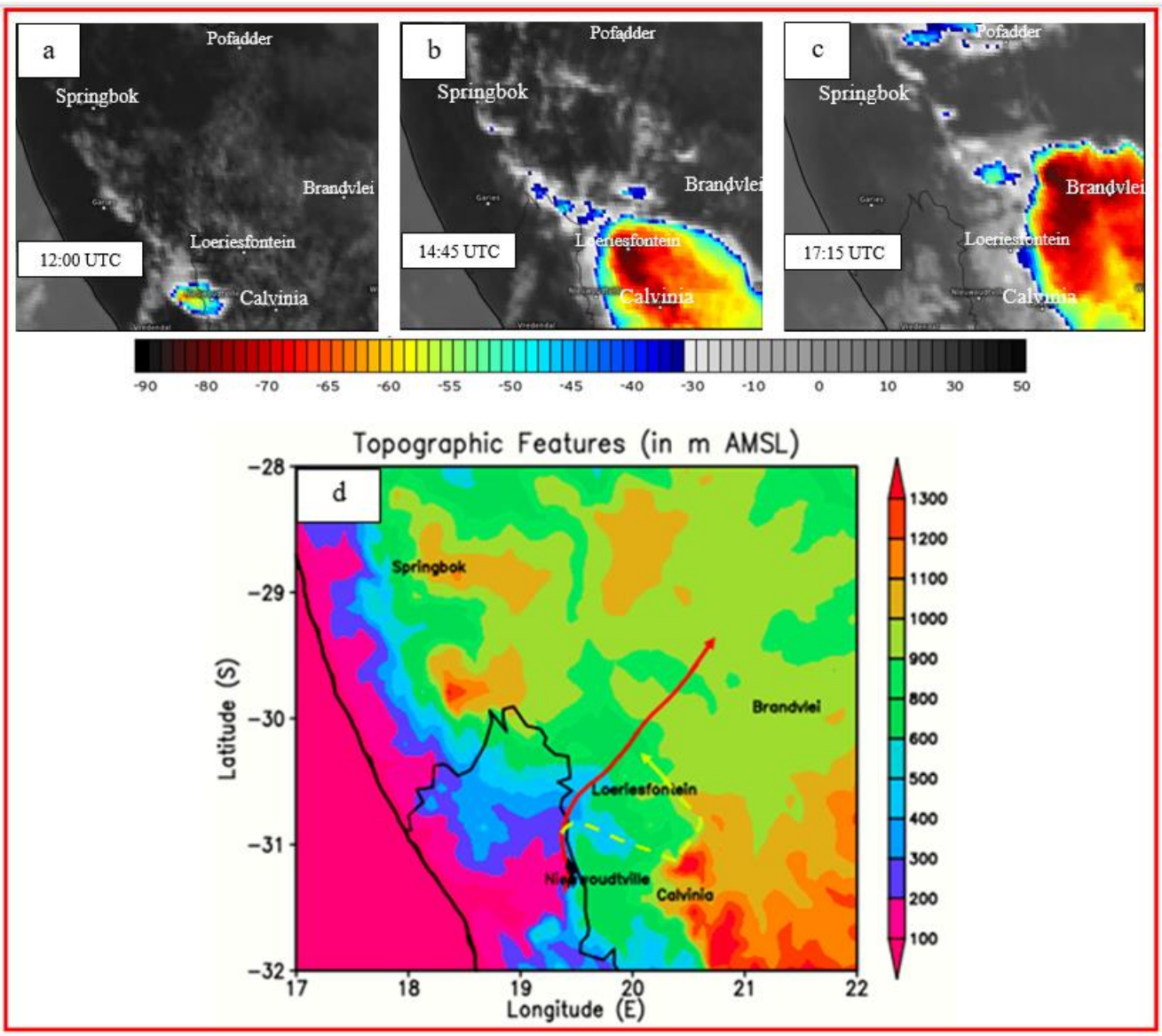


Figure 27.28: Thunderstorm initiation, movement and intensification. 4.13a and 4.13b represent the initiation of thunderstorms in the valley, shows the south-eastward movement to the curved mountain to the north of Calvinia where it intensified. Figures 4.13c and 4.13d show the unusual northwards movement in the afternoon and evening hours of 13 February 2018. Map scale is 1:4964912 for all three subregions. (Source of images: 4.13a to 4.13c – EUMETSAT; 25d - author output topography data on GrADS).

According to Kemp (2018), some areas through which this severe thunderstorm moved were left with island-like surfaces that resulted from heavy rain and flooding along with minor hailstorms (Figure 4.14). The UM model suggested the potential for thunderstorm development over the western region of South Africa but with no change in storm direction. Consequently, a severe storm alert was issued for the south-east of the Hantam Mountains in the Witzenberg, Breede Valley and Laingsburg

municipalities. This decision could have resulted from 1) failure to assess that the light to moderate north-westerly winds could steer the storms into the concave mountain from which intensification could result; 2) the change in direction of the primary storm because of the steep topography; and 3) cold outflow of small-sized storms with ultimate mergers that could further intensify the primary storm, thereby prolonging its lifespan.



Figure 29.6: Aftermath of severe thunderstorms during the early evening of 13 February 2018 at Brandvlei. Bare surfaces, which were reported to have resulted from heavy rain and flooding, with remnants of hailstones during the morning of 14 February 2018. (Photo source: Beeld newspaper)

Longer lead-times for such rare storms could be achieved by creating and using conceptual models. The storm movement with northbound trajectory in the western region of South Africa was last seen on 19 October 1998 between 11:00 UTC and 17:00 UTC, suggesting that trajectories are rare in this region. Comparatively, the frequency of thunderstorms (e.g. severe storms) that move towards the south-west (i.e. opposite to light steering winds) is higher in eastern region of South Africa. Compared to the western region of South Africa, the eastern region is characterised by a horizontally longer escarpment with more pronounced ELEV (e.g. Thaba Cheu local municipality in Mpumalanga).

4.3.2.2b Case D: Downburst at New Bethesda - 2 September 2020

This case study confines the COL properties to directional and strong vertical wind shear together with the shift of the trough axis orientation. The case study deals with Objective 2. Shown in Figure 4.15a at 06:00 UTC on 1 September 2020, the UM suggested a COL at 500 hPa level with the central low at 5 560 gpm and the trough axis orientation at near south-to-north orientation (i.e. dashed red line). In comparison with ERA5 reanalysis, Figure 4.15b shows that the central low at 500 hPa over southern Namibia was 100 gpm deeper (i.e. 5 460 gpm) with marginally stronger winds over the south-eastern sector (area of interest circled in red). Figures 4.16a and 4.16b show that the associated pressure and wind analyses at 850 hPa had a relative similar position as the central lows: central low was at 1 480 gpm with UM but 1 460 gpm with ERA5. As with 500 hPa wind analysis, ERA5 showed stronger wind and pronounced shear in the south-eastern sector compared with the UM. The observation of stronger wind with pronounced vertical wind shear aligns with research by Majodina and Jury (1996). Shown on UM at 18:00 UTC, COL in Figure 4.17a appeared to have moved eastwards while its trough axis shifted to a south-west/north-east orientation (i.e. between 0° and 45°) with tighter pressure gradients and increased wind strengths. Among others, Ndarana and Waugh (2010) noted the high concentration of cold air on the equatorward sector of the MTS troughs or within the COLs. During the shift of the orientation of the trough axis to the bearing between 0° and 45°, dry cold air is typically spread from the equatorward sector to the south-east (de Villiers, 1997). These events led to cloud thinning as seen in Figures 4.20a, 4.20b and 4.20c, in alignment with Knippertz (2004).

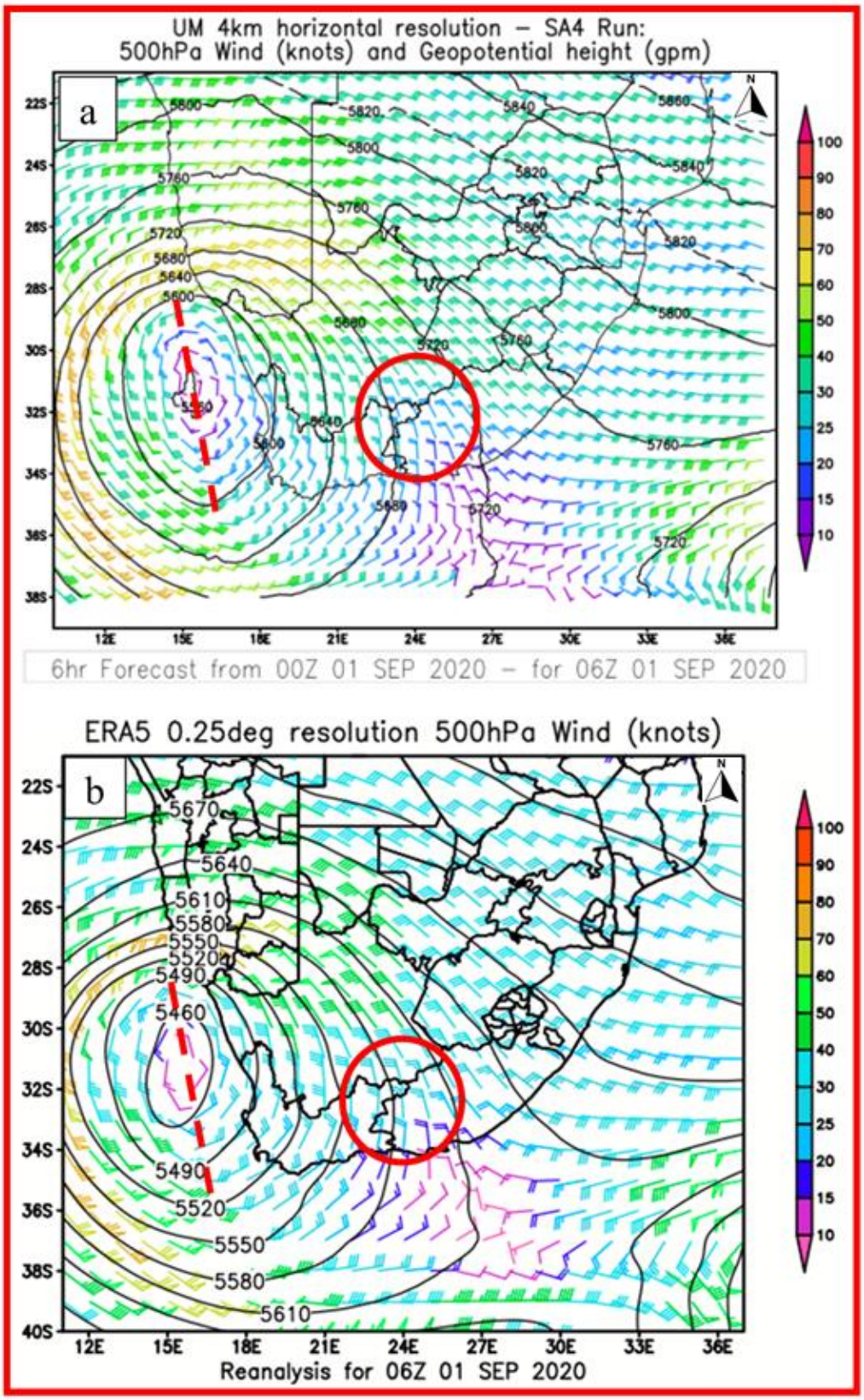


Figure 30.31: Comparison pressure analysis (black contours) and wind (barbs)s at 500 hPa at 0600 UTC on 01 September 2020 using UM and ERA 5 models in 4.15a and 4.15b, respectively.

South-west/north-east trough axis orientations associated with COLs (or MTS troughs) seem to be favoured in part, when the MTS ridge in the east block their eastward propagation (DMSLP Report, 2007). It also appears that steep COLs (or MTS troughs) occur during the amplification of another MTS trough to the west or when a weak MTS trough to the west advances rapidly to the east. A comparison with ERA5 reanalysis in Figure 4.17b seems to have maintained central low 5 460 gpm. In Figure 4.18a, the UM analysis at 850 hPa appeared to have moved the surface low south-south-eastward to the southern region of the west coast of South Africa with the central low at 1 460 hPa. Later at 02:00 UTC on 2 September 2020, a significant SRH was calculated to be in the region of -200 to -250 m^{-2}/s^{-2} (not shown) over the extreme eastern regions of the Western Cape and adjacent areas of the Northern Cape. The SRH dropped to between -250 and -350 m^{-2}/s^{-2} later at 04:00 UTC. Large values of the SRH (negative in southern hemisphere but positive in northern hemisphere) are known to increase the potential for rotational thunderstorms (McNulty, 1995; De Coning and Adam, 2000). With similar movement and position, ERA5 dropped the low to 1 420 hPa as shown in Figure 4.18b. Positional shift of COLs with its properties agrees with Muofhe *et al.* (2020) who found that strong COLs are usually not located precisely, particularly in reference to marked topographical differences. Associated with the steep COL on the evening of 1 September 2020 into the early morning of 2 September 2020, the strong mid-level winds in the region of 25 to 35 knots steered the storm over the significant topography to the lee side. However, storms typically deflect and defy light to moderate steering winds (i.e. 0 to 15 knots) when in contact with significant topography. Moreover, Figure 31b shows that vorticity advection at 500 hPa increased substantially to the east of this COL at 00:00 UTC on 2 September 2020 compared to 24 hours earlier (see Figure 31a). Such vorticity advection aligns with Röhner (2016) and Rammopo and Ndarana (2019), among others. Substantial vorticity advection minimum is contributed to by both the strong horizontal wind shear and curvature (Bates, 1990).

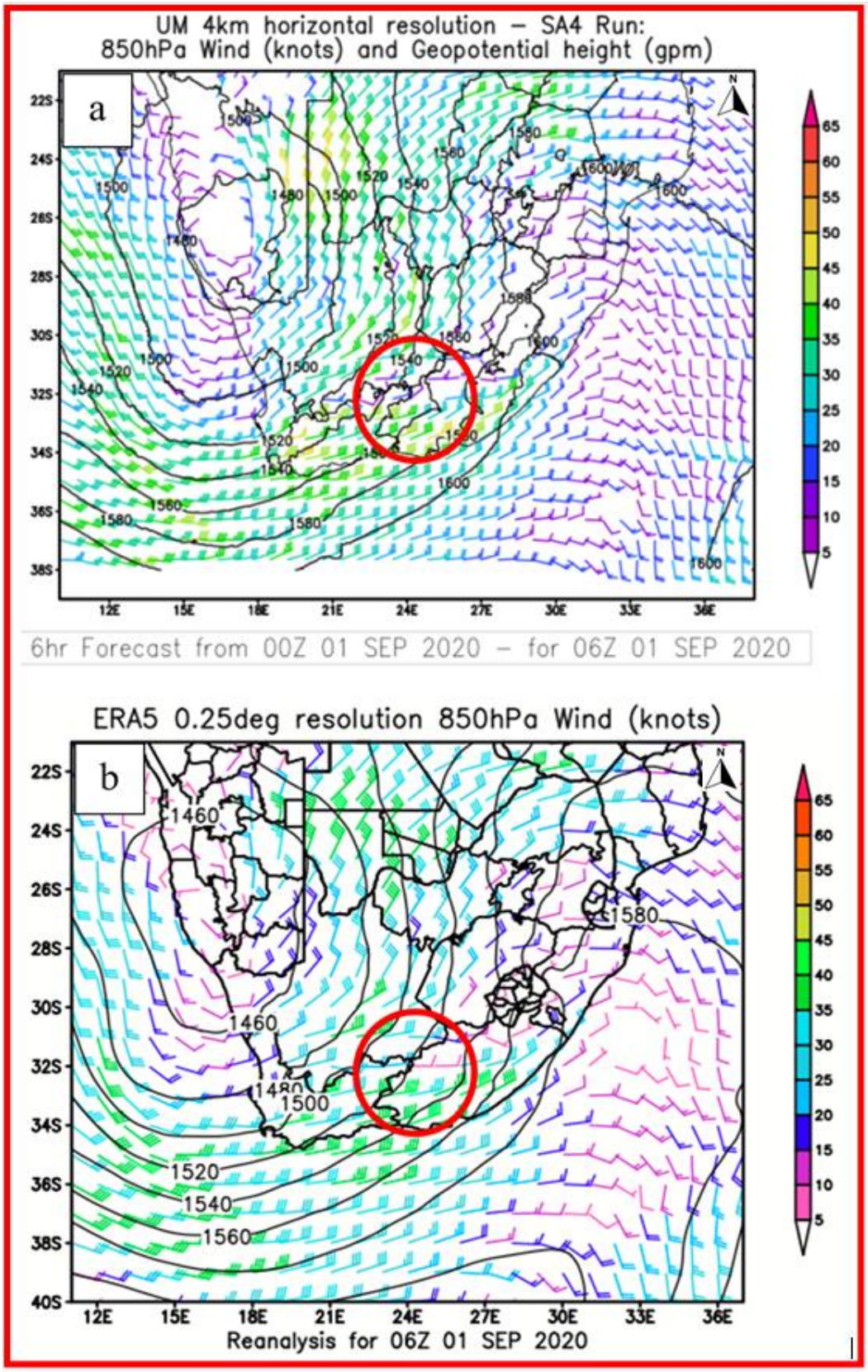


Figure 32.33: Comparison pressure analysis (black contours) and wind (barbs)s at 850 hPa at 0600 UTC on 01 September 2020 using UM and ERA5 models in 4.16a and 4.16b, respectively.

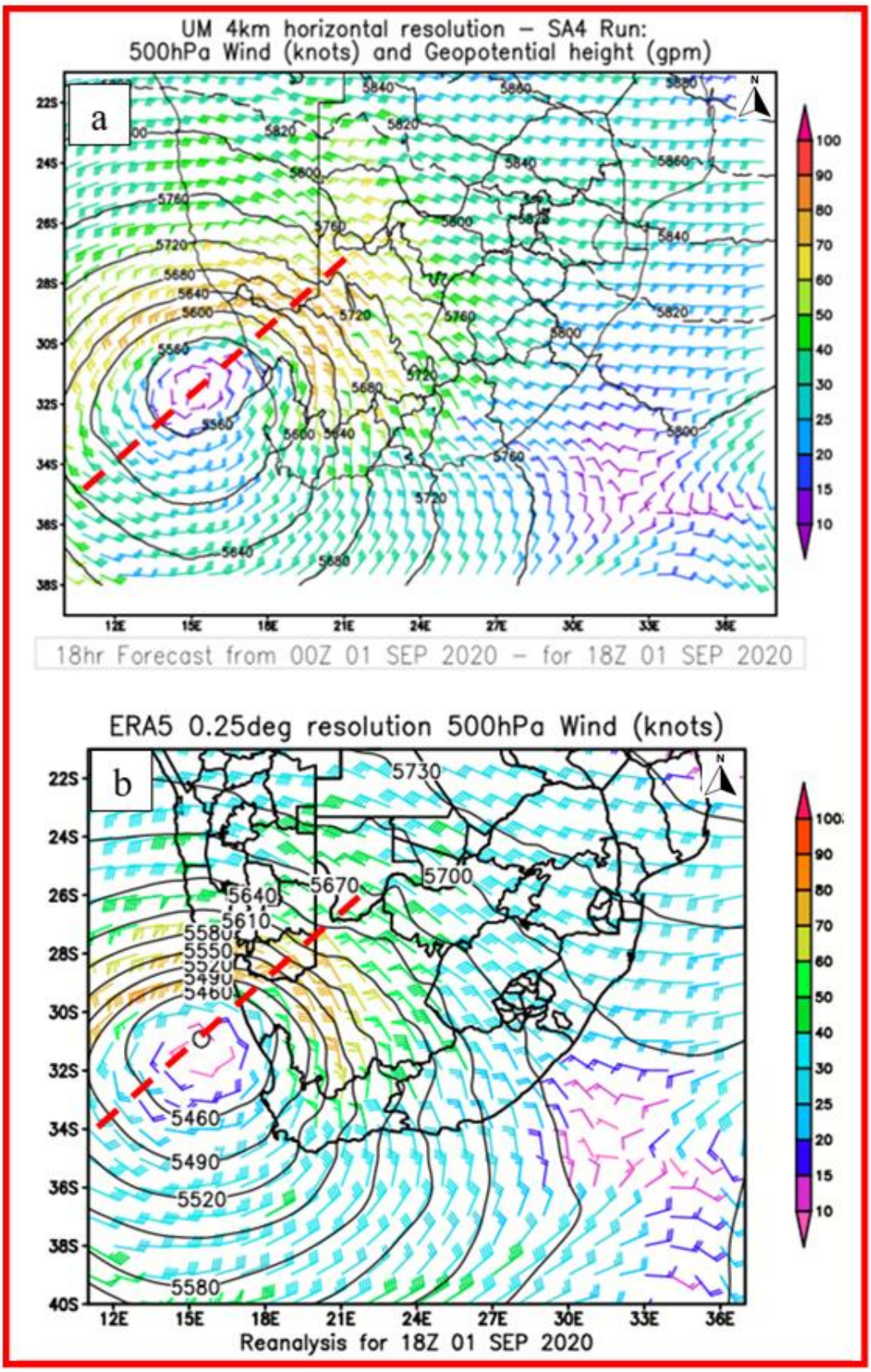


Figure 34.35: Positions of 500 hPa low with associated winds at 18:00 UTC on 02 September 2020. Outputs of the UM and ERA5 models are shown in 4.17a and 4.17b. Area of interest is indicated in red.

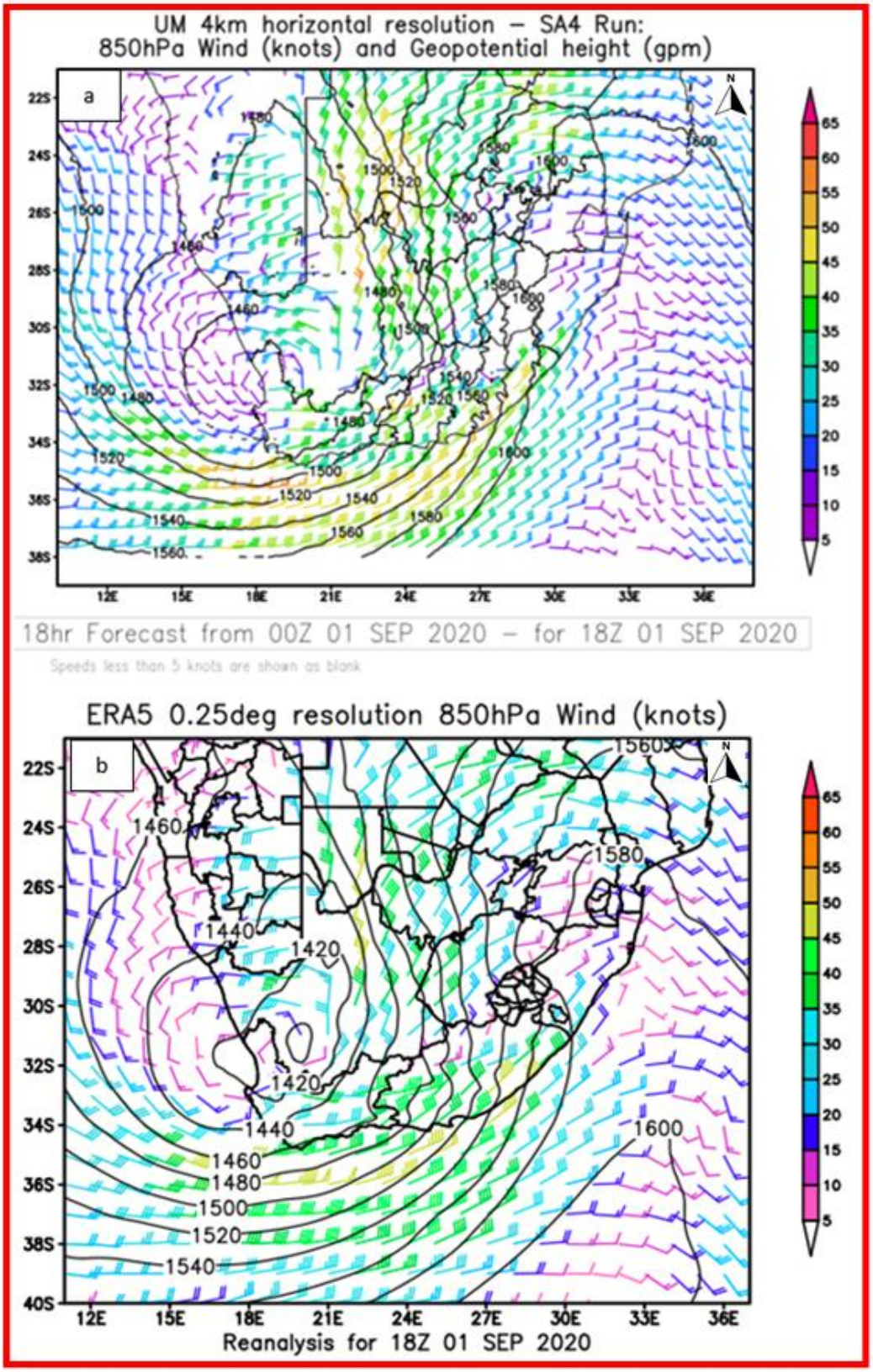


Figure 36.37: Positions of 850 hPa low with associated winds at 18:00 UTC on 01 September 2020. Outputs of the UM and ERA5 models are shown in 4.18a and 4.18b, respectively. Area of interest is circled in red.

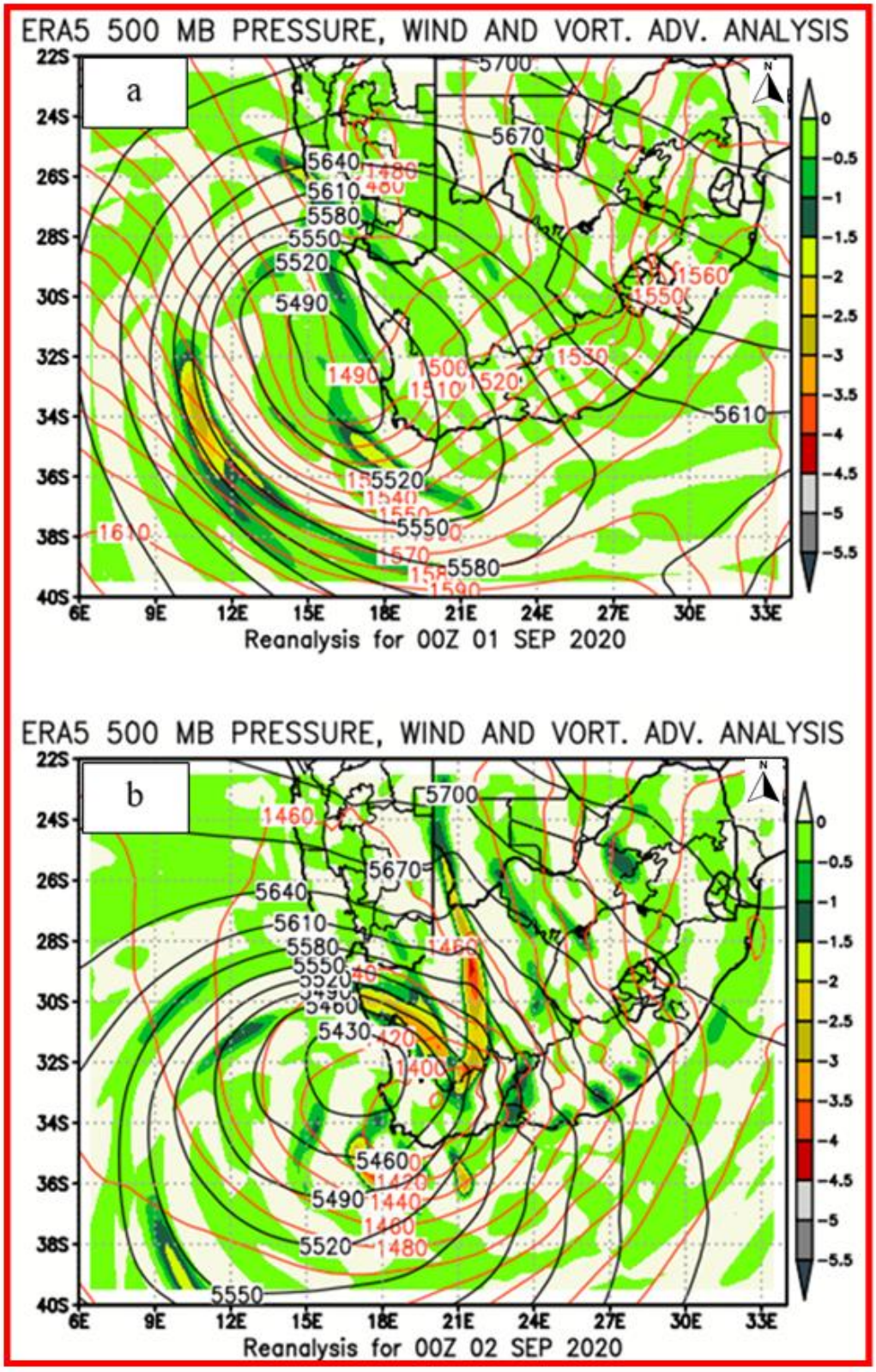


Figure 38.39: Comparison of 500 hPa pressure analysis and amounts of vorticity advection (VORT. ADV.) (shaded) at 00:00 UTC on 1 and 2 September 2020. The Vort. Adv. is calculated at x 10^{-5} s^{-1}. Amounts of VORT. ADV. are shown in 4.19a with significant increase of these amounts in 4.19b.

The synergy between MTS vorticity advection with surface circulations and features are discussed in Section 2.5.1. Rotating storms occurred in the region of 100 to 150 km to the east in reference to where the ERA5 suggested the minimum vorticity advection to be at 500 hPa (Figure 4.19b) (i.e. over the extreme eastern regions of the Western Cape and adjacent areas of the Northern Cape). Even the lowest SRH values of the UM were placed at a similar distance to the west. Observations from around 21:30 UTC on 1 September 2020 to at least 00:30 UTC on 2 September 2020 showed cloud thinning (Figure 4.20). This observation is consistent with the finding by Knippertz (2004). Intense storms (circled in red) tracked south-south-eastwards from the south-eastern region of the Northern Cape province to the north-western region of the Eastern Cape province at 00:00 UTC (Figures 4.20a, 4.20b and 4.20c). The circled storm at about 00:00 UTC probably had its outflow on the windward side of the mountain momentarily compressed and then rapidly released across Nieu Bethesda, which is on the lee side (triangle in Figure 4.21).

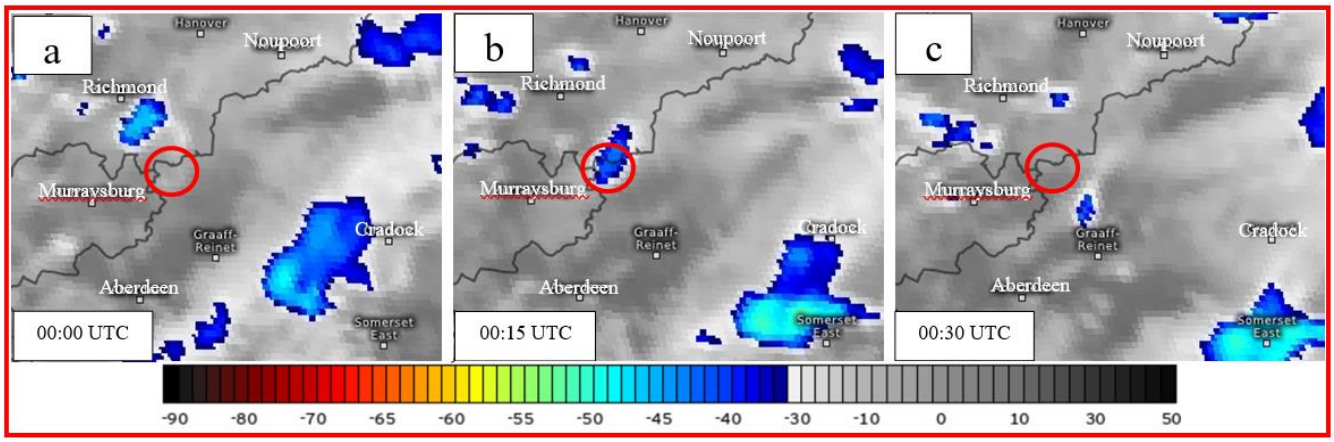


Figure 40.41: Isolated cold convective clouds associated with steep COL and cloud thinning on 2 September 2020. Shallow convective cloud that moved over Niewe Bethesda (in the red circle) are shown in 4.20a, 4.20b and 4.20c. Map scale is 1:3075000 for all three subregions. (Source of images: EUMETSAT)

To this effect, comparatively warmer air rapidly ascended to form a new and rapidly intensifying thunderstorm cell. This argument is derived from Tyson and Preston-Whyte (1972) and WMO (1978). As a result, heavy rain occurred with heavy winds which damaged trees as shown in Figures 4.21a and 4.21b.

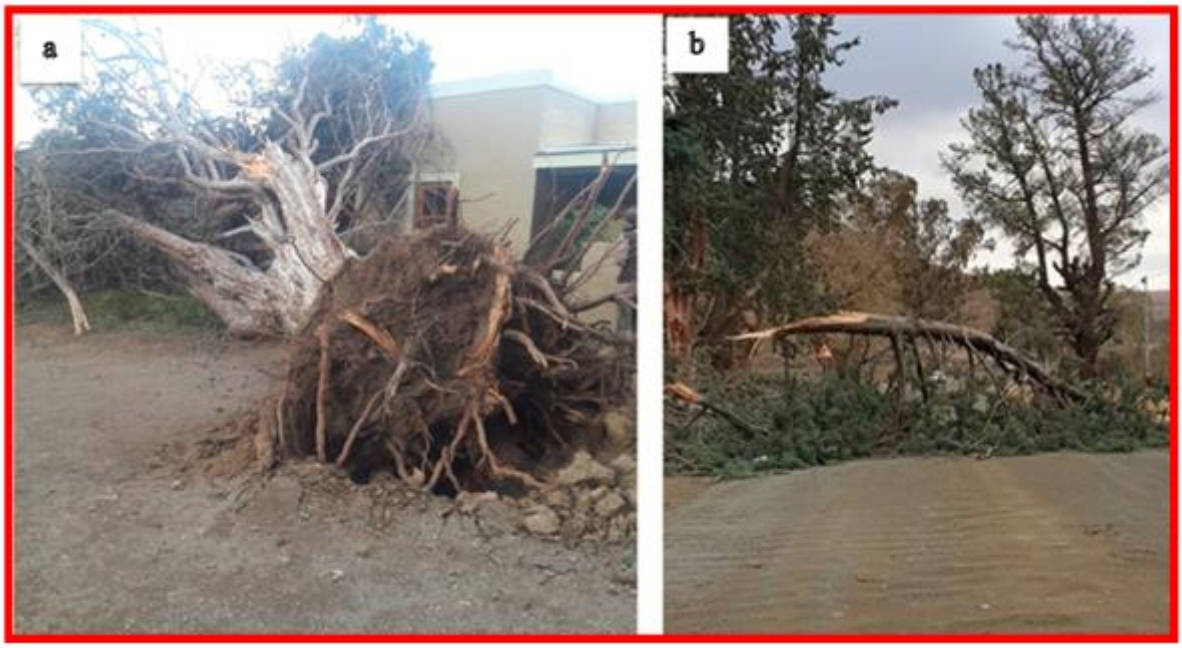


Figure 42.43: Impacts of strong gusty winds at Niue Bethesda on the early morning of 2 September 2020. Uprooted tree and broken stem in 4.21a and 4.21b are respectively shown as a sample of other storm-impacted trees.

Chapter 5: Tornadoes across South Africa

5.1 Introduction

The aim of this chapter is to characterise tornadoes, which occurred across South Africa, according to the mechanisms of their development. The chapter deals with Objective 3 and assesses the inherent challenges in the NWP models in terms of representing tornadic environments. It also explores the three main mechanisms in which the gust fronts of upwind thunderstorms contribute to the development of tornadoes. The first concerns the gust fronts that connect with the inflow sector of the downwind thunderstorm and the second with the rapid development of new thunderstorm cells on the lee side of significant topography. The third mechanism results from the strong gust front of the upwind thunderstorm, which is forced to accelerate and rise between two aretes to the pyramidal peak where tornadogenesis is less typical and was not discussed in detail. Schematic models of the mechanisms of tornadogenesis are shown in Section 5.3.3.

5.2 Systematic analysis of tornadoes in South Africa

5.2.1 Summer season tornadoes

Approximately 41% of total tornadic storms listed in both Tables 3 and 4 were associated with cold CTTs of at least -65°C or colder during the peak summer season (i.e. November to January). These bitterly cold CTTs were associated with MTS ridges contributing a significant 35% of the MTS synoptic weather systems. During peak summer seasons, there was a total of 22 tornadoes. Very few summer tornadoes (i.e. ~18%) were linked with low CAPE (i.e. 0 to less than 500 $J.kg^{-1}$) and the majority of these tornadoes seem to occur mainly on the lee side of the Drakensberg mountain range, as exemplified by tornadoes that occurred at Utrecht, Dannhauser and Bergville. Such peak summer tornadoes seem to develop from localised gale force winds resulting from intense upwind thunderstorms in a similar manner as expressed by the WMO (1978). Close to 27% of peak summer tornadoes were related to extreme CAPE of more

than 1 500 J.kg^{-1} and of these extreme CAPE tornadoes, 27% were linked with steep mid-level lapse rates of greater than 7°C/km between 700 and 500 hPa. In contrast, Table 5 shows that such steep mid-latitude lapse rates were also related to a landspout that occurred in low CAPE, during spring. Dry adiabatic lapse rates (~9.8°C/km) often increase downbursts (i.e. an area of strong winds produced by downdraft over an area from less than 1 km to 10 km in the horizontal dimension) and intense rainfall (Houze, 1993). The rainfall accumulation of at least 1 millimetre per minute could be regarded as intense rainfall even when its onset and cessation is within half an hour. A vacuum created by this core of strong vertical wind is typically filled by adjacent winds with unequal speeds and opposing direction (i.e. vertical wind shearing). However, the majority of summer tornadoes (i.e. approximately 55%) were associated with moderate CAPE, with amounts ranging from 500 to 1 500 J.kg^{-1}. Moderate to extreme CAPE typically results from the easterly component of the low-level synoptic flow, which transports warm and unstable air towards the interior regions from warm sources such as the Mozambique Channel and the Agulhas Current (Rouault *et al*., 2002; Morris *et al*., 2017; Simpson and Dyson, 2018). Other sources of very warm and unstable moisture include the continental tropical lows (Webster, 2019) or passage of tropical cloud bands (D'Abreton, 1991). Nearly 68% of tornadoes listed in Tables 3 and 4 during peak summer season was associated with light to moderate wind shear ranging from 3 to 20 knots, whereas the remaining 32% had fresh wind (>20 knots) at least at one level aloft. It could be concluded that peak summer tornadoes often occur in moderate to extreme CAPE in association with light to moderate wind shear (i.e. South African summer tornadoes occur in HCLS) environments. Storms with CCT range as bitterly cold given that -65°C or colder often have large aerial extents (i.e. have deep convection or are high-topped) and typically produce severe thunderstorm events (De Coning *et al*., 2015). Such bitterly cold cloud tops are typically associated with multicellular or supercellular storms, as exemplified with storms in both Tables 3 and 4. Intensification of discrete storms resulting in very cold cloud tops often suggest the interaction with significant topography (see Figures 5.2a to 5.2c, 5.3a to 5.3c and 5.3e, 5.5a to 5.5d, 5.7a to 5.7c and 40e, 44a to 44c and 44e). This finding reinforces the discussions of Barnes (2001) who earlier observed that tornadic storms in Australia often occur without the

obvious MTS synoptic-scale support (i.e. without well-developed or steep MTS troughs or COLs). The minimal contribution of MTS air support is further affirmed by Evans (1992), who stated that thunderstorms typically become severe in areas of broken topography in the subtropics. According to Mulugeta and Simelane (2016), light to moderate surface flow must be persistent to promote the initiation of rotating thunderstorms (e.g. supercell). The figures cited in this subsection suggest that light to moderate surface winds should flow onto surface features (i.e. significant concave topography, a narrow gap or valley between significant topographic features) to develop optimum localised low-level vertical wind shear. Undulating or steep topographic features are thought of as generators of differential heating and localised vertical wind shear in the lowest layer of the troposphere (Tshehla, 2008; Rae, 2014) and are further regarded as the initiator of forced moist convection and deep storms (Bopape, 2013). According to Schimid *et al.* (1997), localised orographic effects promote the release of convection and thunderstorm initiation in high CAPE environments. The shear component is used to determine low-level vorticities and is discussed in detail in Sections 2.5.1 and 4.1. In reference to Table 3, nearly 59% of the tornadic storms occurred when the LI at 500 hPa was at least -6°C or lower (i.e. colder) while about 40% of the remaining storms occurred when the LI was higher (i.e. warmer) than -6°C. The LI values of -6°C or lower are indicative of extreme instability with the potential for tornadogenesis; the LI measures the difference between the temperature of the parcel and the environmental temperature at 500 hPa, after the parcel is lifted from the condensation level (De Coning *et al.*, 1999). During the summer season, the second significant batch of tornadoes in Tables 3 and 4 were associated with MTS cyclonic short-waves, which contribute 15% of the MTS synoptic weather circulations. The MTS cyclonic short-waves are discussed in detail in Section 4.3.1. Further, well-developed MTS troughs (i.e. with trough axis orientated between 335° and 360°) and COLs (with trough axis orientated between 0° and 45°) each contributed 6% towards summer tornadoes across South Africa. However, steep MTS troughs (i.e. with trough axis between 0° and 45°), contributed 3% of summer tornadoes. The link of MTS waves with low percentage of summer tornadoes could be supported by the repeat finding by Gallego *et al.* (2005): MTS waves are largely kept to the south of 30° latitude during

summer season. There is limited contribution of MTS cyclonic circulations in the development of severe thunderstorms during summer months. This contradicts the finding by Holton (1979) who states that the mid-latitude atmosphere is often dynamically driven from above. Approximately 44% of South African tornadoes were associated with the $SRH_{0\text{-}3km}$ (i.e. SRH integrated between 0 and 3 km) with a maximum of -100 $m^2.s^{-2}$ or less in association with COLs (Table 3). These values were calculated with the UM data. However, tornadic storms linked with the influence of the MTS ridge and short-wave trough were left out due to poor skill of the $SRH_{0\text{-}3km}$. This means, calculations of the $SRH_{0\text{-}3km}$ at the sites of tornadoes under MTS ridges were either uniform or provided marginal differences in relation to the surroundings within a radius of 200 km. These differences remained unchanged throughout the forecast period or became distinct too late (i.e. at 4 hours or more thereafter). The source of poor SRH skill potentially results from the underestimation of vertical vorticity due to (1) the height used (i.e. 3 km AGL of boundary layer) in the integration, and (2) the averaged topography scheme and low grid resolution of the NWP models (i.e. ERA5 and UM). It was shown earlier that most storms in South Africa become severe due to the interaction with significant topography. Therefore, SRH skill to predict severe thunderstorms over South Africa could potentially improve with calculations at lower heights (e.g. at 1 km or 0.5 km AGL) because most storm $SRH_{0\text{-}1km}$ values of at least 100 $m^2.s^{-2}$ often create a conducive environment for tornadogenesis (Rasmussen and Blanchard, 1998).

5.2.2 Autumn season tornadoes

As in Table 3, the population of tornadoes during the autumn season (February to April) is conclusively made up of very few events: two tornadic events in the 5-year study period (June 2016 to June 2021). Autumn season tornadoes contributed 6% of the overall tornadoes and such limited occurrence makes statistical analysis inconclusive. These tornadoes were associated with bitterly cold CTTs of at least -65°C or lower (i.e. colder) with the LI of at least -6°C. It remains a subject for further research that severe thunderstorms could have CTT ranging between -35°C and -65°C. One tornado was associated with a well-developed MTS trough (i.e. with trough axis orientated between

335° and 360°) with moderate CAPE with amounts ranging from 500 to 1 500 J.kg^{-1}, whereas the other was linked with a steep MTS trough (i.e. with trough axis orientated between 0° and 45°) and extreme CAPE of greater than 1 500 J.kg^{-1} (Table 3). There is typically an increase of extra-tropical influences (e.g. MTS troughs and COLs) during the autumn season (Dyson, 2014; Barnes, 2021). Comparing the summer and autumn season tornadoes over South Africa (i.e. Section 5.2.1 vis-à-vis Section 5.2.2) shows that the contribution of MTS cyclonic circulations (i.e. MTS mid-latitude circulations) is significantly less. However, the majority of tornadoes over the USA are linked with frontal occlusions and to a lesser extent the frontal boundaries (i.e. mid-latitude systems) (Cotton *et al.*, 2011). This is potentially because fronts rotating around the parent low imparts an extra velocity component (Hunter, 1987). Frontal vortices over South Africa are very rare (Tucker, 1971; White, 2000). Therefore, the contrast of discussions in Subsections 5.2.1 with 5.2.2 and the subsequent Subsections 5.2.3 and 5.2.4 show that the majority of tornadoes that develop over South Africa do so from different sources compared to those that develop over the USA. According to data read-off from ERA5, very low SRH amounts (i.e. -50 to -100 m^2.s^{-2}) at Delmas on 26 July 2016 seem to suggest better low-level vorticity in terms of timing and approximation of location in association with strong MTS cyclonic circulations (i.e. mid-latitude circulations); vertical cross section with deep opposing vorticities seem to be a proxy of potential tornadogenesis.

5.2.3 Spring season tornadoes

With six events, spring season (i.e. August to October) tornadoes accounted for 12% of the total population of tornadoes in a 5-year base period (June 2016 to June 2021) (Table 3). These few tornadic events result in inconclusive statistical analysis when limited within a season over the 5-year study period. However, the current tornadic events during spring were represented by 67% of CTTs of at least -65°C or lower (i.e. colder). Such bitterly cold cloud tops are regarded as high-topped clouds (De Coning *et al.*, 2015). The remaining 33% of the CTTs in spring were in the range between -35°C and 64°C. Spring season tornadoes were associated with COLs and steep MTS troughs at about 67% and 17% respectively, and these mid-latitude systems were characterised by

trough axis between 0° and 45°. Of these spring season tornadic events, one (or 17%) was associated with MTS ridge in which case significant topography (e.g. escarpment) could have played a central role in generating localised vertical wind shear, as discussed in Subsection 4.1.1. A total of 67% represented both the LI of at most -6℃ or lower (i.e. colder) and low CAPE (i.e. 0 to 500 $J.kg^{-1}$). The remaining 33% accounted for both the LI greater than -6℃ or lower (i.e. colder) and moderate CAPE (i.e. 500 to 1 500 $J.kg^{-1}$).

5.2.4 Winter season tornadoes

A total of four winter season tornadoes (i.e. May to July) were reported in the two successive days during the 5-year study period (i.e. June 2016 to June 2021) (Table 3). Of the 34 tornadoes listed in Tables 3 and 4, winter tornadoes contributed 12% of very cold CTTs ranging between -35℃ and -65℃. It appears that tornadic events with CTTs that are warmer than -40˚C are more favourable beneath a cold pool associated with COLs and such clouds are often lowly topped in comparison with bitterly cold CTTs discussed in the preceding Subsection 5.2.1. The significantly reduced cloud tops could be consequential from forced (topography-induced) moist convection and heavy density very cold air aloft. Winter tornadoes were linked with 50% of the LI at 500 hPa were greater than -6℃ (relatively warmer) and the other 50% of LI were at most -6℃ or lower (relatively colder). The data in Table 3.1 suggest that winter tornadoes develop in association with steep MTS troughs and COLs with trough axis orientated between 0° and 45° and occasionally produce more than one tornado in a single day. An exception to the association of tornadogenesis with steep COLs may be the rare retrogression of COLs. An example of such rare COLs was associated with a tornado touchdown over Tabankulu on 1 November 2000 when this system moved from the extreme south-western Indian Ocean back into the Eastern Cape province. CAPE was characterised by 75% of low amounts ranging from 0 to 500 $J.kg^{-1}$ and directional with moderate wind shear in the vertical (i.e. wind vertical profile in Table 3). Convective storms which produced tornadoes typically occur in relation to sub-zero CTTs. However, winter tornadoes were found in association with relatively warmer CTTs (i.e. lower-topped convective clouds) compared to summer tornadoes. The reduced vertical

extent of convective storms in winter seems to be, in part, the effect of less surface buoyancy (i.e. numerically less CAPE amounts). Occasional advection of cold surface temperatures occurs across South Africa in winter seasons (Lengoasa, 1988). Cold surface temperatures may be the cause of numerically less CAPE amounts. The other potential cause of reduced vertical extent of the severe convective storms may be moderate to strong vertical wind shear as shown on the vertical profile of wind in Table 3. This argument is supported, in part, by Sansom (1966) who noted that a considerable vertical wind shear causes inclined updraft. Circulations such as steep MTS troughs and COLs are accepted to preserve angular momentum leading to rotating storms which typically produce large hailstones (Rae, 2014). In essence, severe thunderstorms over South Africa seem to occur in environments with low-CAPE and high-Shear (LCHS environments) during winter**.** Enhanced MTS -level westerly flow (e.g. in association steep MTS trough) is linked with and enhanced vertical wind shear (e.g. with localised moderate to strong strengths) (Majodina and Jury, 1996).

5.2.5 Landspouts

All nine landspouts listed in Table 5 occurred at LI amounts of 500 hPa greater than -6°C, and 67% of these events were associated with CTTs between -35°C and -65°C. The remaining 33% of overall landspouts were linked with CTTs at -65°C or marginally lower (i.e. colder) and these bitterly cold cloud tops occurred during the peak summer (i.e. November to January). Landspouts with CTTs at the minimum of -65°C or lower contributed 50% of peak South African summer; the other 50% was for CTTs greater (warmer) than -65°C. All three landspouts that were recorded in autumn (i.e. February to April) and spring (i.e. August to October) had CTTs greater (i.e. warmer) than -65°C. Approximately 56% of overall landspouts occurred with low CAPE (0 to 500 $J.kg^{-1}$). Almost 40% of low CAPE landspouts were found during the summer and another during autumn, whereas the remaining 20% were determined in spring. In summer alone, 33.3% of landspouts were found in low CAPE. This finding is supported by Monteverdi and Quadros (1994) who stated that environments that are not characterised by high values of CAPE and vertical shear (i.e. LSLC) can still support severe weather

(e.g. severe thunderstorm) and tornadoes although they receive less attention. Such weak tornadoes are few and require a coalescence of mesocyclones rather than through the influence of the mesocyclone or multiple mesocyclones (Wakimoto and Wilson, 1989; Brady and Szoke, 1989). The development of non-supercell storms (e.g. landspouts) is typically linked with a low-level convergence leading to strong convection that has no significant mid-level rotation (Doswell III, 2001), in which case, according to Wakimoto and Wilson (1989) and Brady and Szoke (1989), vertical incipient circulation moves from the boundary layer to the cloud base. Tropospheric conditions that govern small-scale weather events (e.g. landspouts) are more important in the short-term (i.e. 0 to 6 hours) range (Steyn, 1988; Olivier, 1990). The other 33.3% were found in moderate CAPE of greater than 500 up to 1 500 $J.kg^{-1}$ and extreme CAPE of greater than 1 500 $J.kg^{-1}$. A 67% of the overall landspouts showed was biased towards the linkage with the short-wave MTS cyclonic circulations but 56% was confined to peak summer. A 33% accounted for the remainder of the grand total of landspouts in summer, autumn and spring.

5.2.6 Summary of overall South African tornadoes

This section contains discussions of South African tornadoes linked with the MTS synoptic weather circulations (mainly 500 hPa) for the period June 2016 to June 2021. An overall graphic representation of tornadoes in Tables 3, 4 and 5 is shown in Figure 5.1 with their linkage to the estimated wind shear and CAPE amounts.

Tornadoes (particularly supercell tornadoes represented by the red bars in Figure 5.1) that are linked with MTS ridges or short-wave MTS troughs are shown to be more favourable in the LSHC environments. Their CAPE amounts were discussed to range from moderate to extreme CAPE categories (see Section 5.2.1). Such environments are more typical during La-Niña seasons that succeed moderate to strong El-Niño seasons, as discussed in Section 5.6. Significant supercell tornadoes were also associated with steep COLs. Discussions of Figure 31b argue that such steep COLs typically generate large amounts of negative vorticity advection. Shearing of wind speeds in the vertical attributed to steep COLs is typically in excess of 20 knots; their associated CAPE

amounts are often less than 500 J.kg^{-1}. Thus, COL-attributed tornadoes are most favourable in HSLC environments. Tables 3 and 4 show that the occurrence of a few individual supercell storms in a single day each produced a tornado when these storms were linked with steep COLs. On rare occasions, the development of tornadoes was associated with steep MTS troughs.

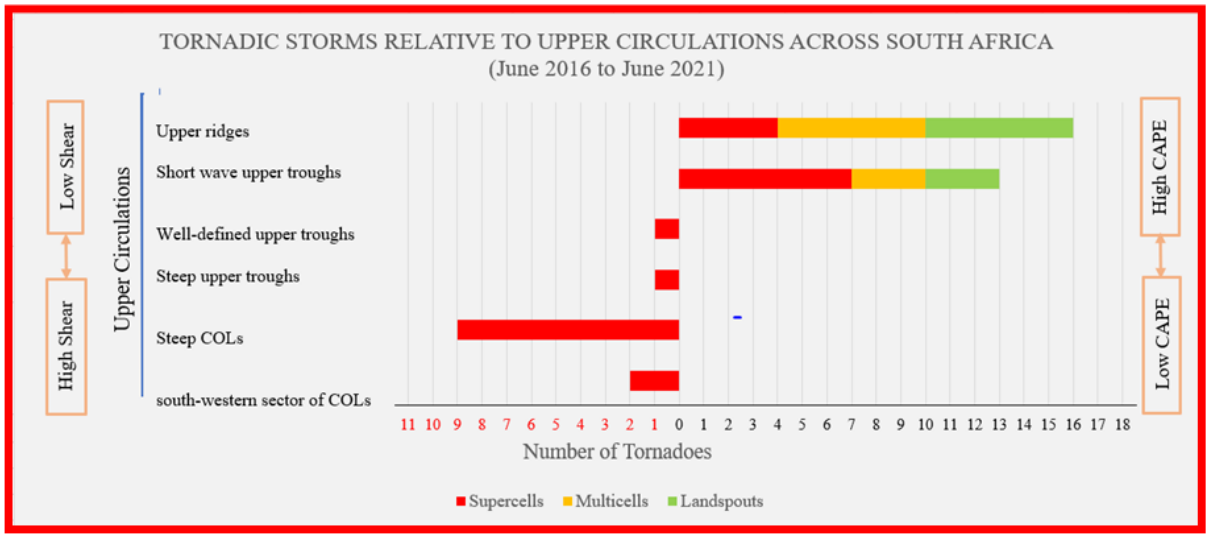


Figure 44.1: Tornado occurrences in association with MTS circulations in the idealised LSHC and HSLC environments. (Source: author after analysis of data from Caelum).

The population of tornadic storms in South Africa were represented by a few multicell tornadoes, as marked with bars in amber colour. Multicell tornadoes in Figure 5.1 were also found to be favourable in LSHC environments. Notably, fewer cases of landspouts (in green bars) were found to contrast their high rate of occurrence in previous literature. The explanation to this contrast is subject for further investigation.

5.3 Tornadogenesis in South Africa

The satellite images seem to suggest the potential for tornadogenesis over South Africa to improve when supercell storms have a linkage with intense upwind thunderstorms or when the rapid-developing downwind thunderstorm results from intense storms moving across complex significant terrain. These observations are highlighted and discussed in Subsections 5.3.1 and 5.3.2. Nearly 70% of tornadoes in South Africa were linked with MTS ridges and perturbations, as discussed in Subsection 5.2.1, the development

mechanism seems to be biased towards surface features (e.g. topography and/or vegetation).

5.3.1 Tornadogenesis effected after thunderstorm deviation

5.3.1.1 The Richmond tornado – 17 March 2020

Discussions of Figures 5.2a to 5.2c could be referenced to the discussions of Figures 3.1a and 3.1c. The inference could be made that a thunderstorm that developed near Kurland (Figure 5.2a) and its illustrated gust front across complex topographic features (Figure 5.2d) were the source for rapid thunderstorm development near Richmond. The atmospheric air in this region was significantly moistened. The storm near Richmond developed probably due to topographic features which generated low-level wind shear with cyclonic vorticity and strong convection, as summarised by Bopape (2013), Lei *et al.* (2017) and De Vos *et al.* (2021). Referring to the discussions of Figure 2.3, the actual observations in 4.2.1.1 and 4.3.2.2b also support this argument. Thunderstorms often occur with gust fronts (i.e. maximum surface wind speeds) over the central and eastern regions of South Africa (Kruger *et al.*, 2010). The secondary thunderstorm to the south-west of Richmond (Figures 5.2b and 5.2c) was intensified and deflected to the left by the topographic features. Consequentially, its gust front became eastward and accelerated with gustiness induced from the complex topography. Cold gust fronts of the storm from the north-west (Kurland) and south-west each generated a vacuum to which non-uniform speed and varying directions converged and rotated, as conceptualised by Dryden and Hill (1926). The optimisation of these wind shear components could be argued to have culminated with the undercutting of the inflow sector, increased vertical wind shear and the strengthening of the storm updraft near Richmond. Such argument aligns with Cox (2000), Barry and Chorley (2003), and Ackerman and Knox (2012). Localised rotational effects from the surface features, such as the tilt of horizontal vorticity into vertical vorticity, are supported by Evans (1992), Engelbrecht and Rautenbach (2000), Ramotubei (2011) and Marquis *et al.* (2012). As a result, enhanced storm rotation near Richmond produced a tornado (see Figure 5.2e).

Atmospheric events such as tornadoes often develop in a matter of minutes (McBean, 2000).

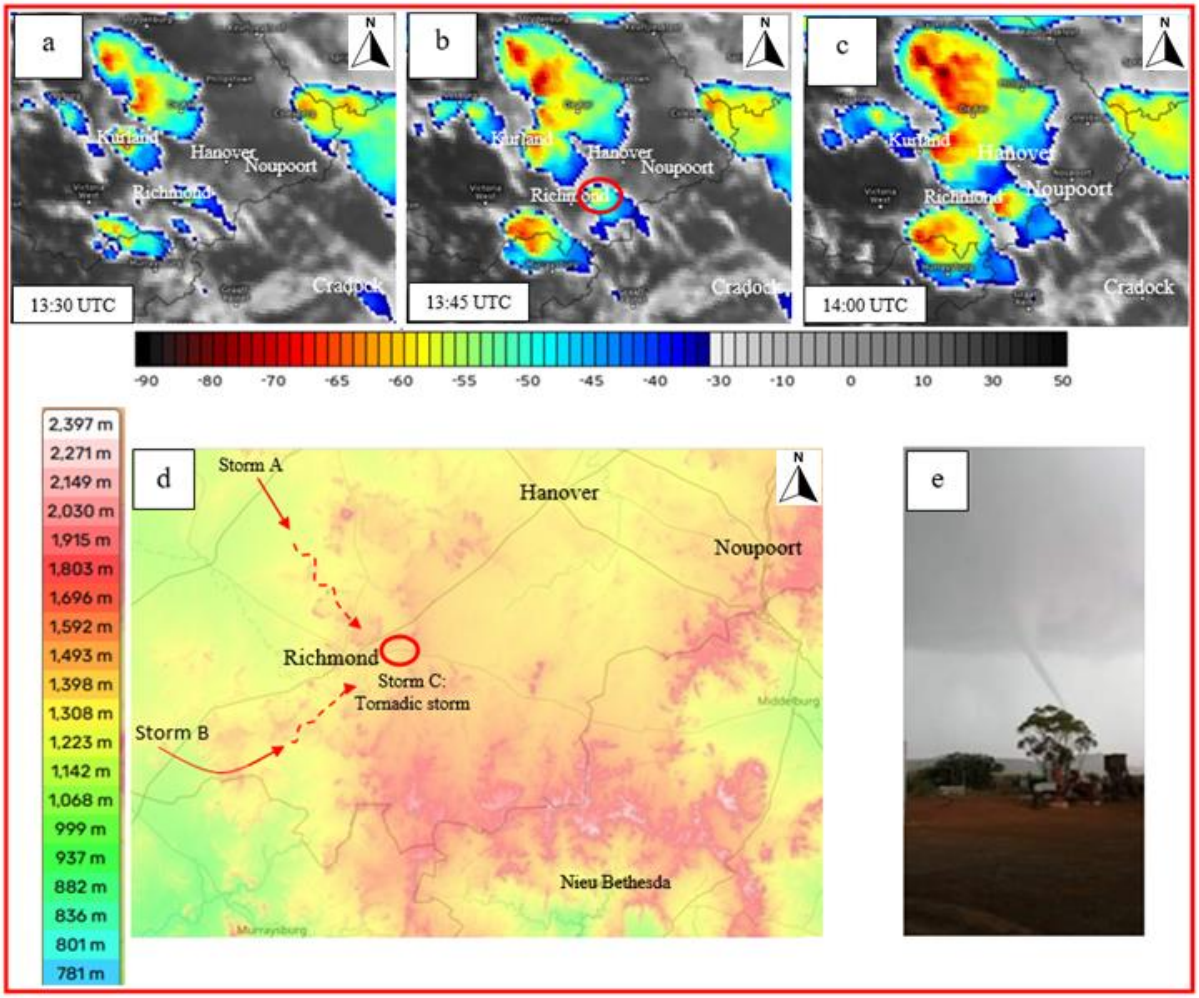


Figure 45.2: Trajectories and partial deflection of thunderstorms with the development of new downwind cell between 11:30 and 12:00 UTC on 17 March 2020. The gust front of the storm near Kurland in the north-west probably led to the development of the storm near Richmond in 5.2a. These storms are respectively labelled Storm A and Storm C in 5.2d. The storm to the south-west of Richmond in 5.2a intensified, deviated to the left and directed its gust front to the east in 5.2b. This storm is labelled Storm B in Figure 5.2d. These slow-moving storms continued to intensify in 5.2c. Optimally strong gust front and localised low-level wind shear could be inferred in the storm near Richmond (red circle in 5.2b) to the effect that the tornadogenesis occurred in Figure 5.2e.

Microscale events, such as the Richmond tornado, require favourable vertical wind shear in the lower troposphere with instability overlap in parameters such as enhanced low-level CAPE, negative but large amount of SRH in the southern hemisphere, as well

as a decreased height of lifting condensation level (Tuschy, 2009). Typically, gust fronts decelerate some distance away from the source thunderstorm or towards the end of storm dissipation (Wallace and Hobbs, 1977).

5.3.1.2 The Vaal Marina tornado – 11 December 2017

This section requires reference to the discussions of Figures 3.1a to 3.1c. The development of thunderstorm occurred to the north-west of Heilbron in Free State province on 11 December 2017 and produced significant quantity of large hail to this town (not shown). Before its rapid intensification, self-organization into a supercell and northward deviation (i.e. deviation to the left with reference to its initial trajectory), the storm (see Figure 5.3a) propagated south-eastward to the network of significant topography demonstrated with a red arrow in Figure 5.3d and by Lekoloane *et al.* (2021). Meanwhile, a weak thunderstorm approached the Vredefort town from the west (hereafter, upwind storm) and moved just to the east of this town, as shown in Figure 5.3b and by the blue in Figure 5.3d. A new supercell position in Figure 5.3b displays a north-eastward trajectory with slow movement across the gust front of the upwind storm. Further supercell intensification occurred due to the resulting interaction with the gust front of the upwind storm. In effect, CTTs rapidly cooled to -60°C but to -70°C in some portions of the supercell storm (not shown). Meanwhile RADAR reflectivity exceeded 70 dBZ (not shown). These estimates strongly suggested the occurrence of strong damaging winds and large hailstones as well as heavy rain and flash-flooding to susceptible areas between 14:45 UTC and 15:15 UTC. In such conditions, it could be argued that much higher frequency of lightning strikes occurred, in similar manner as in Figure 2.9. The upwind storm in Figure 5.5b moved across the fairly flat land surface (along blue line in Figure 5.3d). It required close proximity to the supercell so that its strong gust front could increase near-surface wind shear, as conceptualised by Wallace and Hobbs (1977). The interaction of the gust front of nearby upwind storm with the supercell at 15:15 UTC in Figure 5.3c almost coincided with the RADAR reflectivity at 15:16 UTC in Figure 5.3e. The low-level 3 km RADAR scan in Figure 5.3e also shows a hook echo feature (i.e. an area of reduced reflectivity on RADAR data viewer)

developed and soon after which a tornado developed. A little more than fifteen minutes earlier, the formation of this hook echo began (not shown), as with the tornadic storms studied by Sadowski (1969). Observational analysis of the similar thunderstorm behaviours in Table 3 and 4 suggests an increase in significant rotational effect (optimal vertical wind shear near the surface) that typically leads to development of tornadic storms.

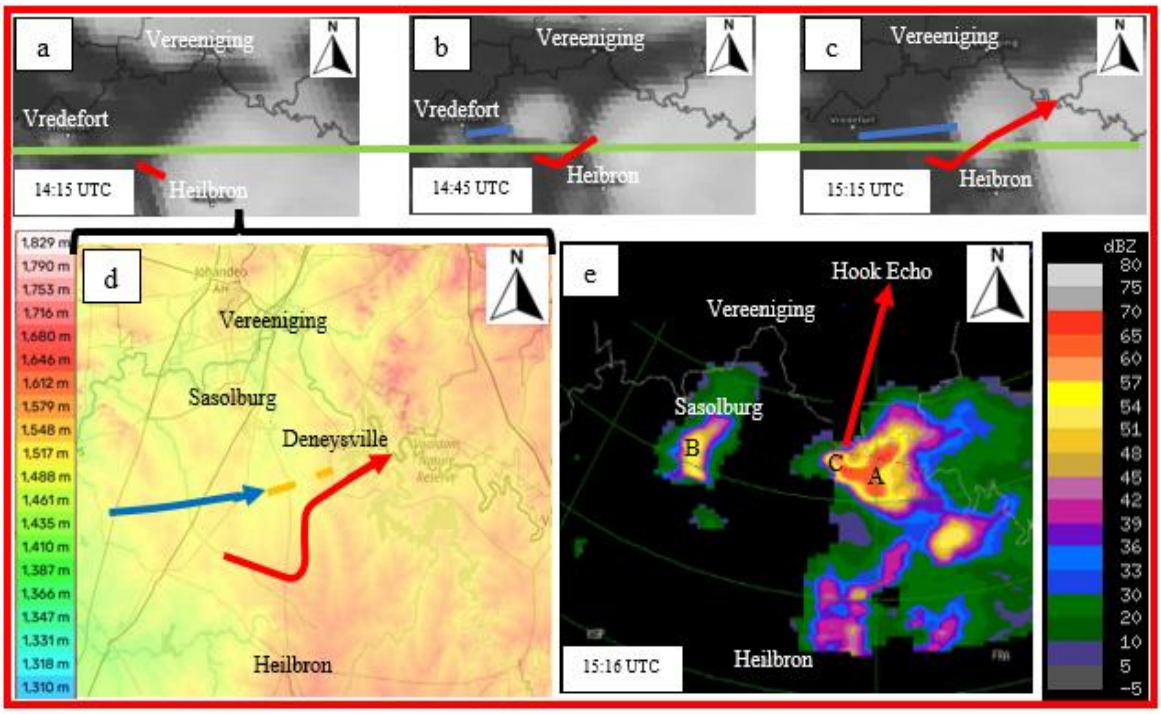


Figure 46.3: The tornadic storm on 11 December 2017 at 15:15 UTC. The ordinary storm (5.3a) typically intensifies into supercell storm (5.3b) on an encounter with curved ELEV (5.3c). The likelihood of tornadogenesis (5.3d) improves due to the gust front of the storm in the upwind. The ERA5 on 5.3e showed no localised vertical wind shearing near the ground surface with a possibility of ordinary storms. Map scales are 1:3500000 and 1:1289474 for the top and bottom rows, respectively. (Sources: 5.3a to 5.3c – EUMETSAT; 36e – SAWS).

Tornadoes that develop in this manner are modelled in Figure 5.13a and are termed tornadogenesis Type A1. They often occur without significant MTS synoptic systems and aligns with Barnes (2001). Their overall contribution nears a 32% of the reported 28 supercell storms recorded in Table 3 and their regional distribution is presented in Section 5.5 and shown in Figure 5.17.

ERA5 reanalysis: Assessment of winds and relative vorticity dipole

Winds at 850 hPa (near the land surface) were modelled to be nearly uniform with strong north-north-westerly flow at largely 20 kts at Richmond and the surrounds (Figure 5.4a). These conditions occurred at 13:00 UTC on 17 March 2020. Earlier on 11 December 2017, the 850 winds were moderate north-westerly at 10 knots, reaching 15 knots at times, as shown in Figure 5.4b. Backing of stronger winds in the middle layer (i.e. 700 to 500 hPa) occurred in both cases with almost due west to west-south-westerly from 600 hPa in Figure 5.4a but from 700 hPa in Figure 5.4b. Their strength ranged from 20 to 30 knots and 30 to 40 knots in Figures 5.4a and 5.4b, respectively. Such middle layer winds flow often cause dry air intrusion which is critical for the development of hailstorms. No strong relative vorticity dipole existed in Figure 5.4a since strong positive relative vorticity occurred near the surface but its counterpart was modelled between 750 and 650 hPa. The relative vorticity amounts were between 24 and 25 °E. The ERA5 reanalysis fields incorporate actual weather observations (Bopape *et al.*, 2022). Therefore, dry air intrusion, strong relative vorticity dipole with other instability indices should be used as a guide from the UM or any NWP model to anticipate the tornadic storms.

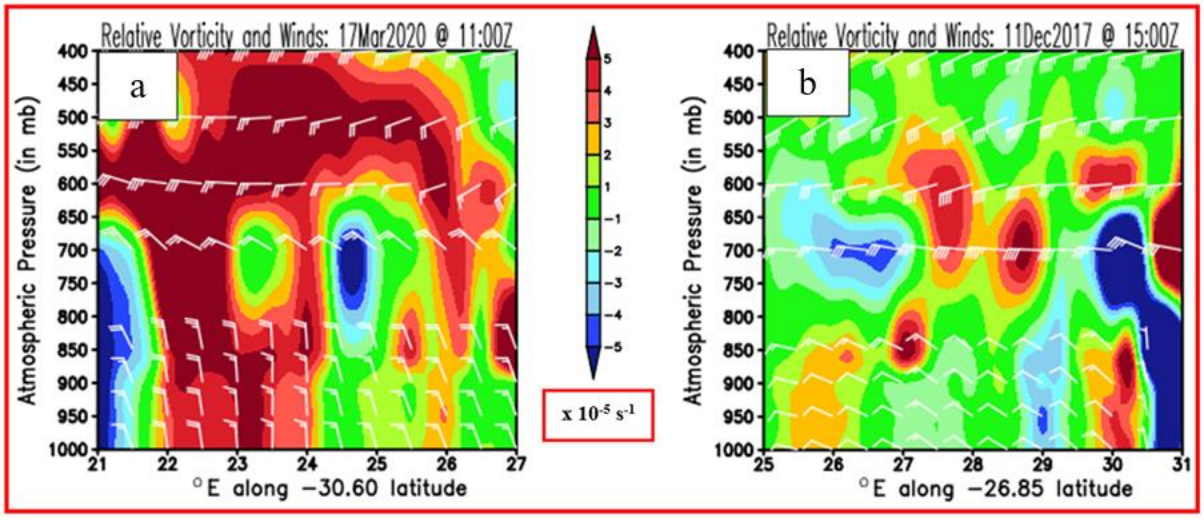


Figure 47.48: Cross-sectional analysis of winds and relative vorticity. Tropospheric conditions are shown at 11:00 UTC on 17 March 2020 for Richmond in the Northern Cape in Figure 5.4a and at 15:00 UTC on 11 December 2017 for Vaal Marina in the Gauteng province in Figure 5.4b.

On contrary, there was no observable, strong relative vorticity dipole in the lower and middle tropospheric layer in Figure 5.4b, hinting no potential tornado development.

This incorrect analysis was, in part, due to the inability to correctly predict the initiation of storms. Filtering out of some of the significant topographic features often dislocates and delays the onset of thunderstorms with the tendency to reduce their intensification and deviation. The failure of the NWP model to predict storm deviations were discussed with observations in Sections 4.2.1.1 and 4.3.2.2a. Additionally, both 1 hour temporal scale and 0.5° x 0.5° of horizontal grid resolution are coarse for microscale events (events that are less than 1 km in size). Microscale events are also not solvable with the UM 4 km, as discussed in Section 2.5.2. There was also no strong relative vorticity dipole in the 700 to 500 hPa layer in both cases. To this effect, Lekoloane *et al.* (2021) calculated the insignificant vorticity advection of -0.75×10^{-2} s^{-1} for the case study in Figure 5.4b.

5.3.2 Tornadogenesis due to topography-enhanced gust front

5.3.2. The Protea Glen tornado – 30 December 2017

This section requires reference to the discussions of Figures 3.1a to 3.1c, as was the case for Sections 5.3.1.1 and 5.3.1.2. The intense thunderstorms occurred on 30 December 2017 and their northwards propagation into the City of Johannesburg metropolitan municipality in Gauteng province are shown in Figures 5.5a to 5.5c. The storm intensification is shown with rapid cooling of CTTs in Figures 5.5b and 5.5c and could reasonably be related to topographic features in Figure 5.5e. The roughness on the range of significant topography along the Lenasia region (see Figure 5.5e) most likely produced enhanced strong downslope gust front on the lee side. An abrupt development of a new thunderstorm occurred as a result. In such cases, and as suggested by Brady and Szoke (1989), strong updrafts grow cumulus clouds into cumulonimbus clouds in a matter of several minutes (e.g. within 30 minutes). Localised gale force winds (e.g. gust front) resulting from an intense, upwind thunderstorm was demonstrated in WMO (1978) and supported by Sun and Sun (2015). Observation of rapidly developing stationary cells with tornadogenesis is supported by Duba (2015), who stated that the inviscid fluids are expected to remain fairly stable at the introduction of rotational effect (e.g. supercell initiation) such that the governing equations become

three-dimensional. The localised gale force wind (enhanced strong gust front) was most probably rotational since the vacuum that resulted attracted the wind flow in opposing directions at non-uniform wind speeds. This argument was conceptualised by Dryden and Hill (1926). Channelling of the assumed rotational gust front on the valley just to the south of Soweto played a role to further enhance the strength of the downslope gust front. Further, the downslope gust front with its vorticity rebounded on the ground surface and developed into upward vorticity, as schematised by Marquis *et al.* (2012).

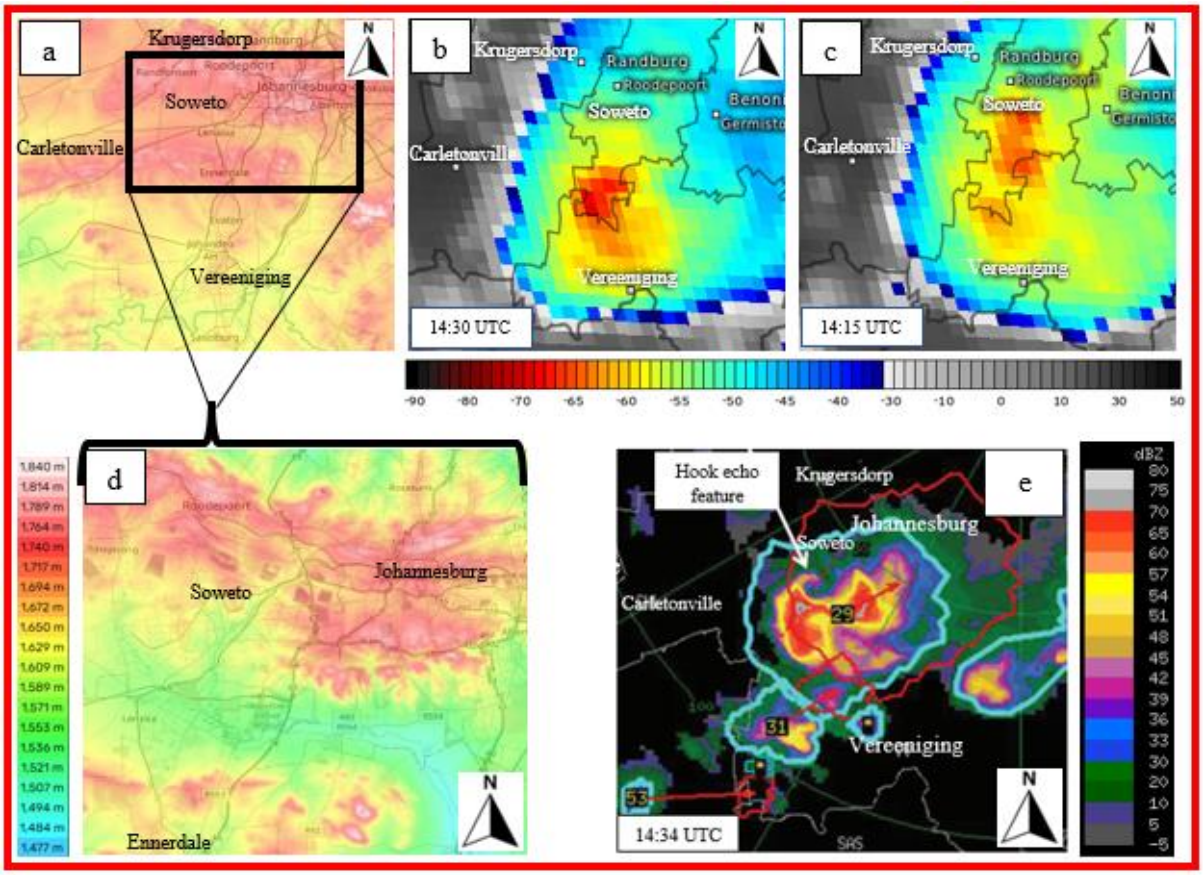


Figure 49.50: Thunderstorm analysis by meteorological tools on 30 December 2017 with consideration of topographic features. Meteological satellite images in 5.5a to 5.5c show storm intensification with cooling of CTTs. RADAR refectivities with hook echoe featurein 5.5d shows bottom-view scan at 3 km, the event that occurred soon after the storm in 5.5b. Storms propagated towards the from the north-west of Vereeniging into the City of Johannesburg Metropolitan Municipality. The intensification of these storms is related to the topograpgical features in 5.5e. Map scales are 1:2444444 for the top row, 1:1850000 for high resolution map in 5.5d, and 1:1700000 for complementary RADAR image in 5.5e. (Sources: 5.5a to 5.5c – EUMETSAT; 5.5d – SAWS).

The RADAR scan in Figure 5.5d shows reflectivity of the supercell storm with secondary storm just to the east at 14:34 UTC at an angle from land surface (3 km scan).

This secondary thunderstorm was on the north side of the valley and propagated westwards where it directed its strong and cold gust front onto the supercell thunderstorm. In effect, a well-defined hook echo feature developed (Figure 5.5d). Storm movement controlled by the high-ELEV features (e.g. mountain ranges) as opposed to mid-level steering winds were discussed with observations in the control case study in Section 4.2.1.1 and supporting case studies in Sections 4.3.2.2a, 5.3.1.1 and 5.3.1.2. Hook echo features are often accepted as precursors for the potential tornadogenesis (Naylor and Gilmore, 2014). The identification of supercell thunderstorms with hook echo feature in Figure 5.5d prompted the issuing of the warning of severe thunderstorm events in Figure 5.6a.

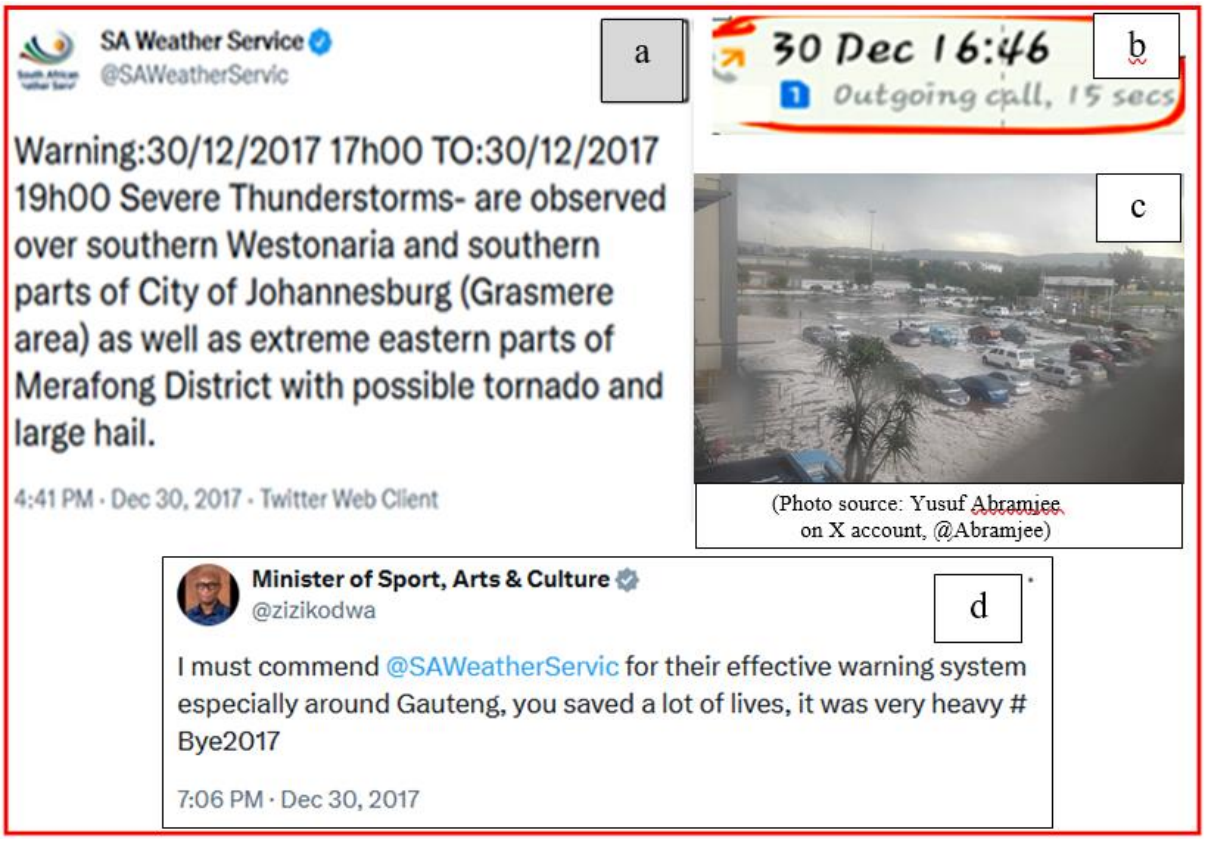


Figure 51.52: Communication that follwed the analysis of meteorological images in Figure 5.6 and subsequent events. A post on X account in Figure 5.6a shows a landmark tornado nowcast. Figure 5.6b is call log of the resident at Protea Glen which coincides with first tornado touchdown and confirm it was about 5 minutes after the tornado warning was issued. Figure 5.6c shows flash-flooding at Trade Route Mall, Lenasia on a photo posted at 17:58 UTC on 30 December 2017. A short summary of extreme events and acknowledgement of the receipt of weather warning was made by the South African politician in Figure 5.6d.

An inclusion of the possibility of a tornado in this warning was a landmark successful attempt by the SAWS, albeit missing the exact location. A call log shown in Figure 5.6b was shared by a resident at Protea Glen, Soweto, who made a call at 14:46 UTC just on the first tornado touchdown. Using the post in Figure 5.6a with call log in Figure 5.6b show that the lead-time of the tornado warning was approximately 5 minutes. Some of the impacts of these storms are reflected in Figure 5.6c after which a South African politician acknowledged the receipt of weather warnings from SAWS, as in in Figure 5.6d. For this event, the UM suggested potential isolated afternoon thunderstorms with no suggestion for the potential extreme storm events.

5.3.2.2 The Mthatha tornado – 7 October 2019

With southwards movement in Figures 5.7a and 5.7b in the eastern regions of the Eastern Cape province of South Africa, the storms were also intense during the interaction with significant topography shown in Figure 5.7c. These events occurred on 7 October 2019. In similar fashion as with the discussion of Figures 5.5b and 5.5d, it could be hypothesised that the enhanced gust front gained rotational effect from uneven topography and vegetation, leading to an abrupt development of a new semi-stationary thunderstorm on the lee side. Topography-enhanced gust fronts contribute approximately 68% of supercell tornadoes listed in Table 3; their regional distribution is shown in Figure 5.17. The discussion in the first paragraph of this section suggests that the intense storm in Figure 5.7b produced strong downslope gust front from the mountain with the ELEV of 700m near Matyeba Village. This mountain is located nearly 30 km to the north-west of Mthatha. Consequentially, a second thunderstorm cell developed rapidly as shown in Figure 5.7b. This storm produced a tornado at Mthatha airport, the strength of which was 252 km/h at approximately 12:30 UTC (see Figure 5.7e). Ratings in Table 1 puts the Mthatha tornado as an EF3 tornado. The extreme velocity winds were reported to have caused property damage, the shaking of well-anchored buildings (i.e. those complying with regulated building standards) as well as posing a threat to human life. Topography-enhanced gust fronts were central in the two tornadic storms discussed in this section: the first was associated with the MTS ridge and the second with steep COL.

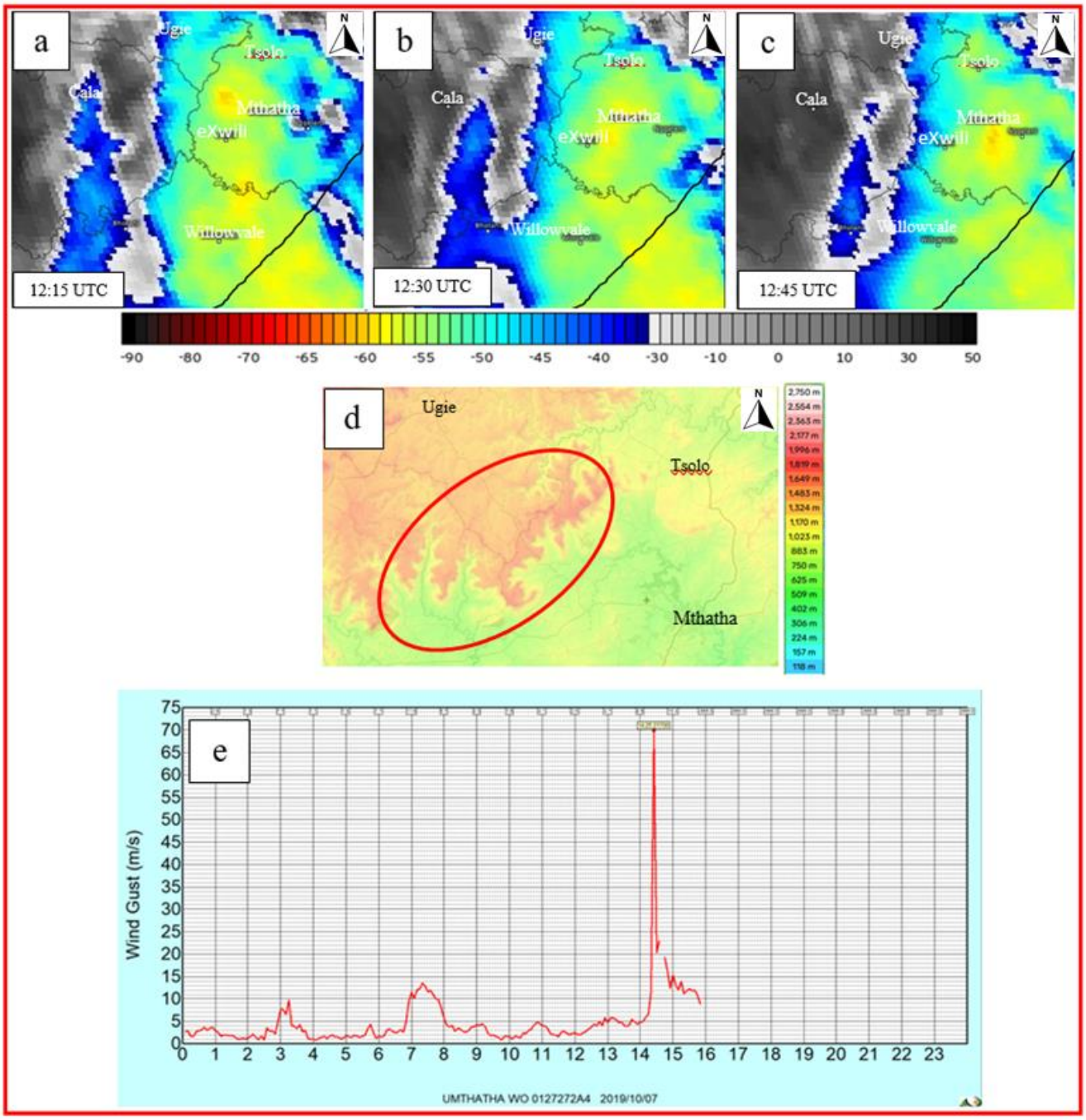


Figure 53.54: A band of thunderstorms along the leading edge of the steep COL. The intense thunderstorm cell that moved over Matyeba mountain (i.e. red circle on parts of 5.7b and 5.7c, led to the tornado strength of 252 km/h and the shaking of well-anchored, solid buildings in Mthatha. (Sources: 5.7a to 5.7c – EUMETSAT; 5.7e – SAWS).

In view of Figure 5.1, tornadogeneses linked with the MTS ridges require LSHC environments but those associated with COLs require HSLC environments. Figure 5.1 also suggests a high likelihood for tornadoes that develop in connection with shortMTS waves (perturbations) and LSHC environments. Numerical analysis with consideration

of the HSLC environment was completed about 04:30 UTC on 7 October 2019 to make a trial forecast for potential occurrence of a tornado among other severe thunderstorm events (evidence not shown). The dry slots (dark areas) in Figures 5.7a, 5.7b and 5.7c are linked with cold MTS wind flow and are understood to induce thermal instability. The curvature of this COL and its preserved angular momentum could be deduced these dry slots. Further, the strong horizontal shear and curvature linked with steep MTS cyclonic flow potentially promoted relatively large quantities of negative vorticity advection. A similar effect of substantial vorticity advection minimum is shown in Figure 31b.

ERA5 reanalysis: Assessment of winds and relative vorticity dipole

The ERA5 model displayed moderate north-westerly winds at 10 to 15 knots in a lower tropospheric layer (i.e. between 700 to 850 hPa), as Figure 5.8a shows. Backing of winds to almost due west in the 700 hPa level and westerly to south-westerly in the remainder of the MTS layer (i.e. 700 to 500 hPa).

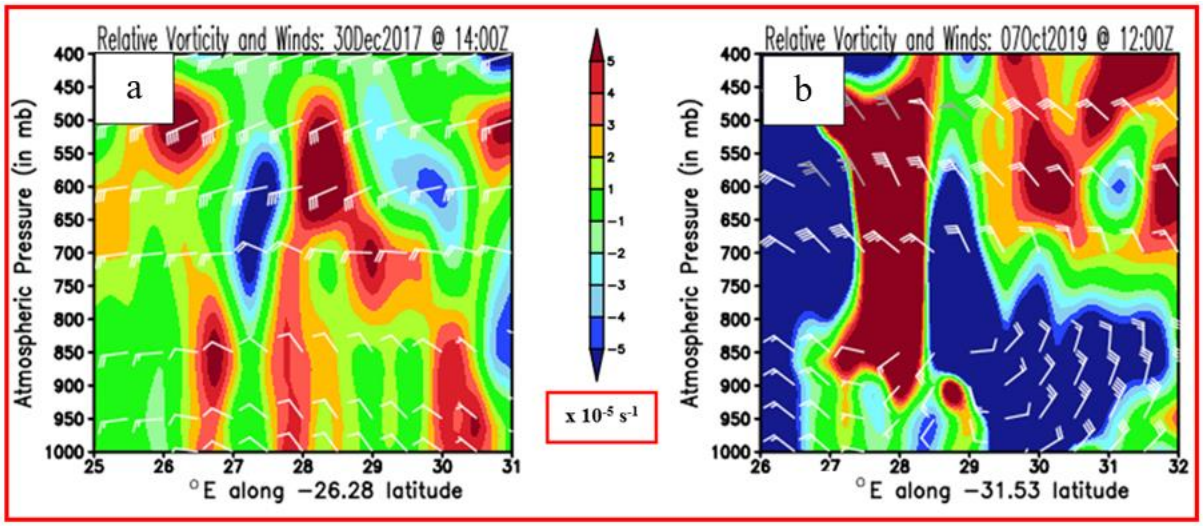


Figure 55.56: Cross-sectional analysis of winds and relative vorticity. Tropospheric conditions are shown for Protea Glen in Gauteng at 14:00 UTC on 30 December 2017 in Figure 5.8a and for Mthatha in the Eastern Cape province at 12:00 UTC on 7 October 2019 in Figure 5.8b.

This suggested potential dry-air intrusion as discussed in the last paragraph of Section 5.3.1.2. Further, strong relative vorticity dipole was shallow between 650 and 500 hPa layer just to the west of 28 °E. This vorticity dipole, its absence in the lower tropospheric

layer where positive relative vorticity dominated did not hint a potential for the tornado development. Challenges to predict such tornadoes were discussed in the last paragraph of Section 5.3.1.2. On contrary, strong relative vorticity dipole existed from lower to mid tropospheric layer, as Figure 5.8b shows. Consideration of such deep layer of strong relative vorticity dipole with other instability indicators could signal the threat of possible tornadogenesis. Veering of strong winds from the middle layer to near the land surface reflected the presence of MTS circulation (steep COL in this case) and deep surface low. At the topographic hook in Figure 5.7d, the moisture-laden (not shown) north-westerly winds of 25 to 35 knots in Figure 5.8b led to rapid storm development (Figure 5.7b). The topography-enhanced strong gust front of this storm into the storm from the west (in Figure 5.7a) led to tornadogenesis, as discussed earlier in this section. Although the cross-sectional analysis in Figure 5.8b was not seen prior the tornadogenesis on the afternoon of 7 October 2019, significantly large amounts of negative vorticity advection at 500 hPa (not shown) were considered to infer the potential for the tornado development. Significant amounts of vorticity advection often result from the steep COLs (or MTS troughs) with acute curvature of strong horizontal winds (Figures 4.19b and 5.1). As discussed briefly in Section 5.2.1, $SRH_{0\text{-}3km}$ (not shown) has better predictive skill for rotational storms linked with COLs. This may be due to the associated strong steering winds that often force thunderstorms to propagate over the significant mountains and thus reducing the potential storm deviations. As Zeitler and Bunkers (2005) put it, the predictive skill of the $SRH_{0\text{-}3km}$ improves when storm motions are predicted well. Additionally, vorticity advection in the middle level has the tendency to extend to near the ground and such a setup is shown in Figure 4.19b.

5.3.2.3 The Ulundi tornado – 23 November 2019

The case study below demonstrates another topography-enhanced gust front which resulted in a tornadogenesis at *eDlebe* (near Ulundi) on 23 November 2019. Short MTS waves (perturbations) were linked to this event in contrast to four case studies of tornadic storms in this dissertation. At 06:00 UTC, both the UM and ERA5 positioned the 850 hPa low over Lesotho and the south-eastern region of South Africa (not shown). In effect, the UM suggested CAPE amounts of between 800 and 1 400 $J.kg^{-1}$ over the

north-eastern midland region of KZN, as shown in Figure 5.9a. The ERA5 calculated CAPE of 400 and 1 000 J.kg^{-1} for the same time and region, as in Figure 5.9b. At 14:00 UTC as seen in Figures 5.9c and 5.9d, each model moved this low to the KZN coast where onshore flow of 5 to 10 knots prevailed with the central pressure at 1 480 gpm for the UM but less by 30 gpm for ERA5. This flow effected additional moisture advection to the central and north-eastern regions of this province. Shown in 42e and 42f, the southern periphery of high and largely zonal winds at 500 hPa persisted over KZN until at least 14:00 UTC with the passing perturbations. Unimpeded solar radiation (satellite images not shown) acting on the advected moisture seem to have caused a substantial increase of CAPE amounts to more than 2 200 J.kg^{-1}, as suggested by the UM and ERA5 in Figures 5.10a and 5.10b. Such abundant moisture input onto KZN could be attributed to the anomalously warm Agulhas Current that is found in the extreme south-western Indian Ocean at about 20 km off the east coast of South Africa (Rouault *et al.*, 2002, Morris *et al.*, 2017). The CAPE amounts that exceeded 1 500 J.kg^{-1} were classified as extreme by Rasmussen and Wilhelmson (1983). Discussions in Section 5.2.1 show cases of extreme CAPE are much fewer in South Africa; moderate CAPE amounts ranging between 500 to 1 500 J.kg^{-1} are frequent. Low-level vertical wind shear could develop from the differential diurnal heating which is typically enhanced with undulating plains (i.e. topographic inhomogeneity) (Tyson *et al.*, 1988; Dyson, 2013). The UM model also modelled the surface-based LI of -4 ^{o}C at 06:00 UTC but dropped to -8 ^{o}C at 12:00 UTC. MTS short-waves with extreme instability and low-level vertical wind shear have the potential to generate severe thunderstorms. This suggested a very deep layer (e.g. tropospheric layer below 500 hPa) of unstable conditions. Korokty (1996) and discussions in Section 5.2.1 classify LI values of -6 ^{o}C or lower as extreme. Very unstable conditions in the mid-upper layer could have resulted from the arrival of cold-upper air associated with mid-upper perturbations. These conditions were suggestive of a very high likelihood of the occurrence of severe thunderstorms.

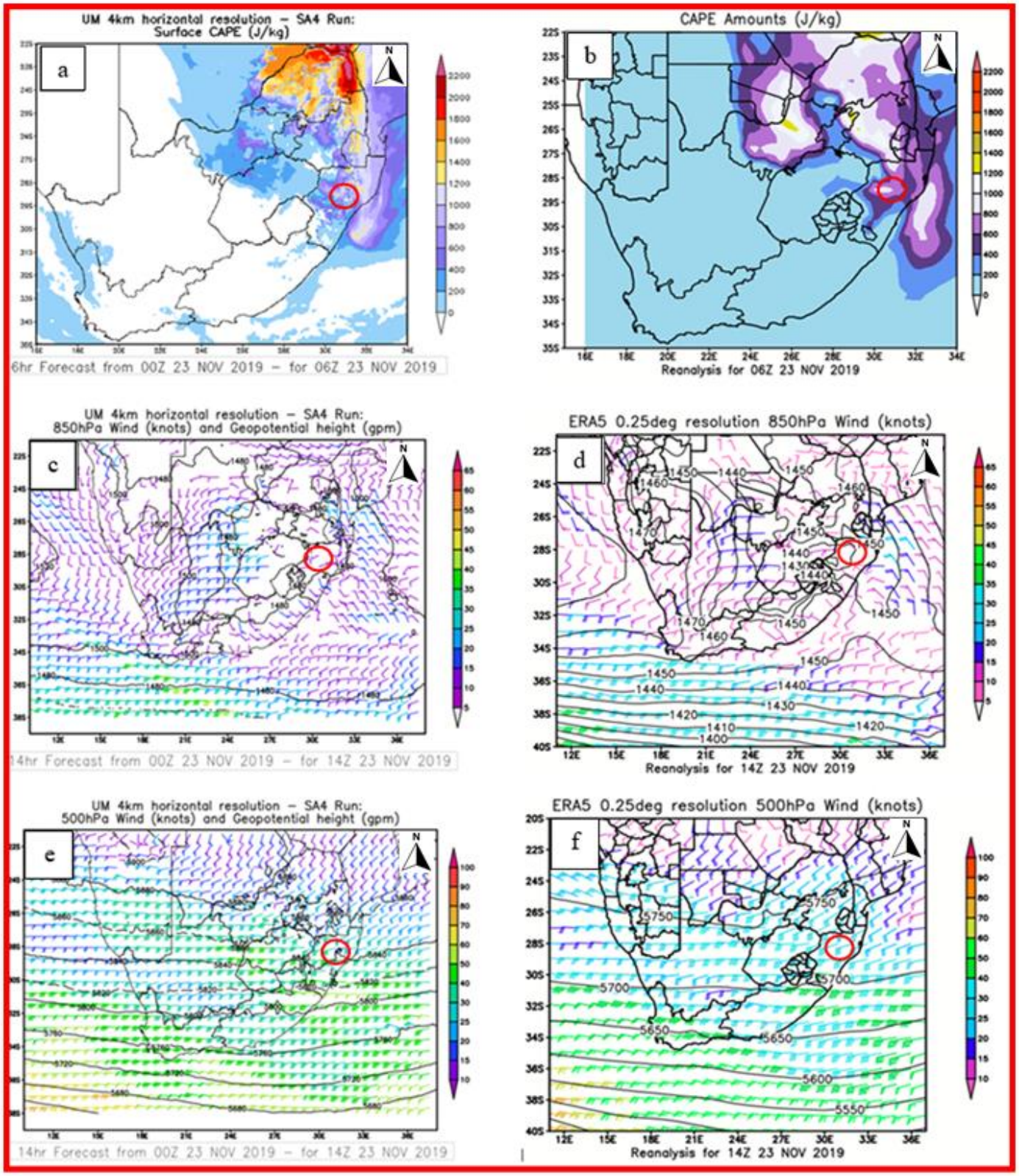


Figure 57.58: Analysis of meteorological conditions. CAPE amounts at 06:00 UTC as calculated by the UM (5.9a) and ERA5 (5.9b). 850 hPa Pressure (contours) and wind (barbs) at 14:00 UTC as calculated by the UM (5.9c) and ERA5 (5.9d). 500 hPa Pressure (contours) and wind (barbs) at 14:00 UTC as calculated by the UM (5.9e) and ERA5 (5.9f).

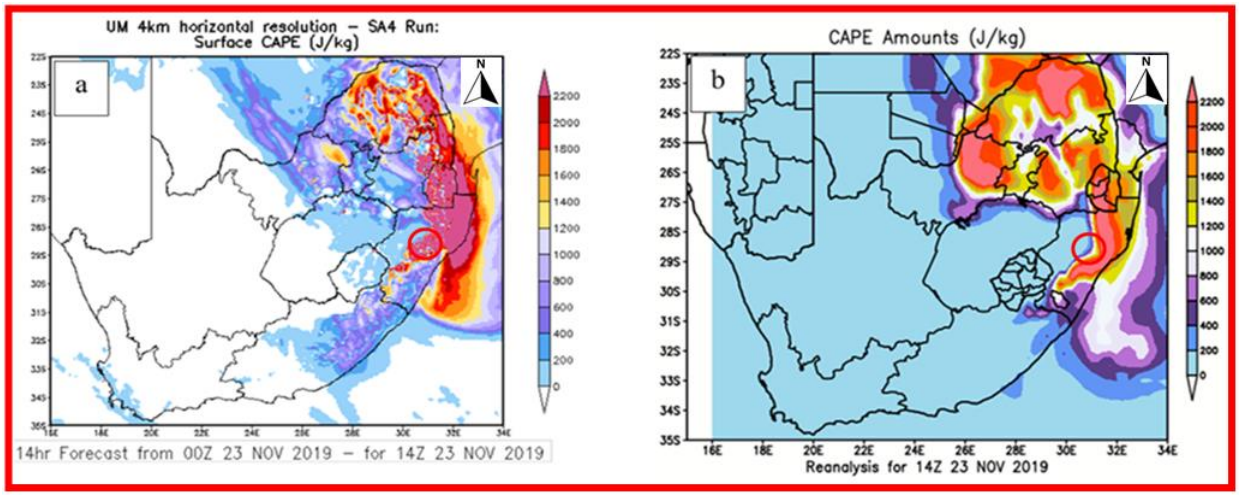


Figure 59.60 : CAPE amounts at 14:00 UTC as calculated by the UM (5.10a) and ERA5 (5.10b)

Actual observations

A few thunderstorms were at a significant distance from the Nkonjeni mountain (hereafter, the mountain) at 14:45 UTC on 23 November 2019 (Figures 5.11a and 5.11d). Peaks of this mountain are as high as 780 m AMSL but 240 m AGL with reference to *eDlebe* village, near Ulundi. Storms propagated south-eastward to the windward side of the mountain where Figure 5.11b shows rapid cooling of CTTs occurred. Cooling of these CTTs probably occurred with severe storm events (e.g. large hail, strong winds as well as heavy rain and flash-flooding) although no ground report was received from communities living on the windward side of the mountain. However, on the lee side of the mountain, a short-lived tornado was photographed at *eDlebe* village in Figure 5.11e with no lives were lost but the damage to property (not shown). Property and infrastructure damage often result from coordinated wind directions at exceptionally strong velocities (Ngubo, 2021). Such tornadoes are referred to as tornadogenesis Type B1 in Section 5.3.3.1. Tornadoes are often produced from small-sized rotational convective clouds on the lee side of the mountain, as discussed in the previous case studies in this chapter. The rotational effect results in part from the rebound of the strong gust front, as shown by Marquis *et al.* (2012). Further, Wilson and Wakimoto (2001), Duba (2015) and Gimeno *et al.* (2016) reinforce this argument. The *eDlebe* tornado was the fourth reported tornadic storm in KZN province in

November 2019 (Mahomed, 2020). No RADAR data were available for this case. The development of this tornado and the other two topography-related tornadoes discussed earlier in this section is a prototype for tornadoes plotted as a black triangle in Figure 5.17.

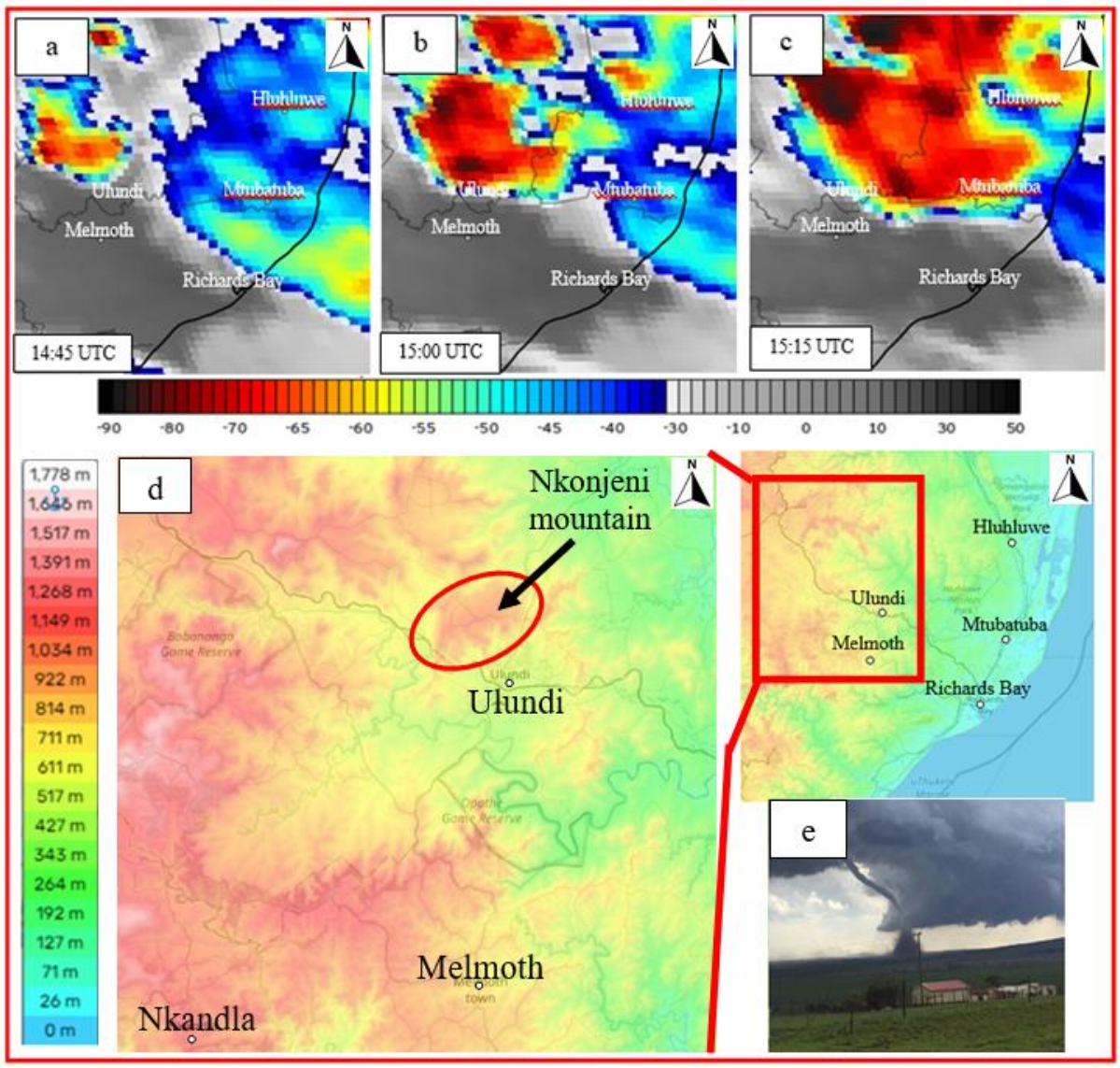


Figure 61.62: Multicell thunderstorms that rapidly intensified to the north of Ulundi on the afternoon of 23 November 2019. Rapid cooling of CTTs just to the west of Ulundi in Figure 5.11b could be inferred to signal potential for large hailstones and very strong downslope on the lee side of the Nkonjeni mountain in Figure 5.11d. Topography-enhanced strong gust front could have rebounded near and forming a new cell at eDlebe where tornado in Figure 5.11e resulted. Map scale is 1:4000000 but 1:700000 for a zoomed image in Figure 5.11d. (Sources: 5.7a to 5.7c – EUMETSAT. Figure 5.11e - unknown photographer)

Prior to the tornado development, thunderstorms developed early in the afternoon (not shown). These storm developments were most probably in response to the convection

that resulted from extreme instability, surface heating and the passage of MTS perturbations.

5.3.3 Simplified representation of tornadoes and landspouts

Prototypes of the tornadogeneses in South Africa were discussed by using case studies in Sections 5.3.1 and 5.3.2, above. This section uses schematic models to further simplify the thunderstorms that typically produce tornadoes and/or landspouts.

5.3.3.1 Schematic model of tornadogenesis in South Africa.

Of significance in tornadogenesis Type A in Figure 5.12 is the primary ingestion of vertical wind shear during the storm interaction with the concave topography, resulting in storm intensification and deflection. A similar effect could occur when the thunderstorm interacts with the significant nearly linear topography at an obtuse angle. Associated contributory factors include the pressure fall and cyclonic intensification, which often cause high frequency of lightning (Williams, 1995; Mahomed, 2020; Figure 2.9). Surface gust fronts often exceed 25 $m.s^{-1}$ in more intense storms (Wallace and Hobbs, 1977). Optimally strong gust front of the upwind thunderstorm often leads to the secondary ingestion of low-level vertical wind shear and potential tornadogenesis in the inflow sector of the deflected thunderstorm. Tornadogenesis Type A in Figure 5.12 is differentiated as Type A1 in 5.12a, Type A2 in 5.12b, Type A3 in 5.12c and Type A4 in 5.12d. Tornadogenesis Type B in Figure 5.13 is favourable in the downwind lee thunderstorm which is often the result of the enhanced strong gust front of the thunderstorm onto the significant topography. For tornadogenesis Type B1 in Figure 5.13a, the newly developed thunderstorms were noted to require the support of optimally strong gust front of the secondary upwind thunderstorm. However, the tornadogenesis Type B2 in Figure 5.13b was observed to require the association with multicell thunderstorms on the significant topography. Alternatively, as with the discussions of Figures 4.19b and 5.8b, tornadogenesis Type B2 requires the synergy between significant thunderstorm and large amounts of negative vorticity advection in the mid-upper level.

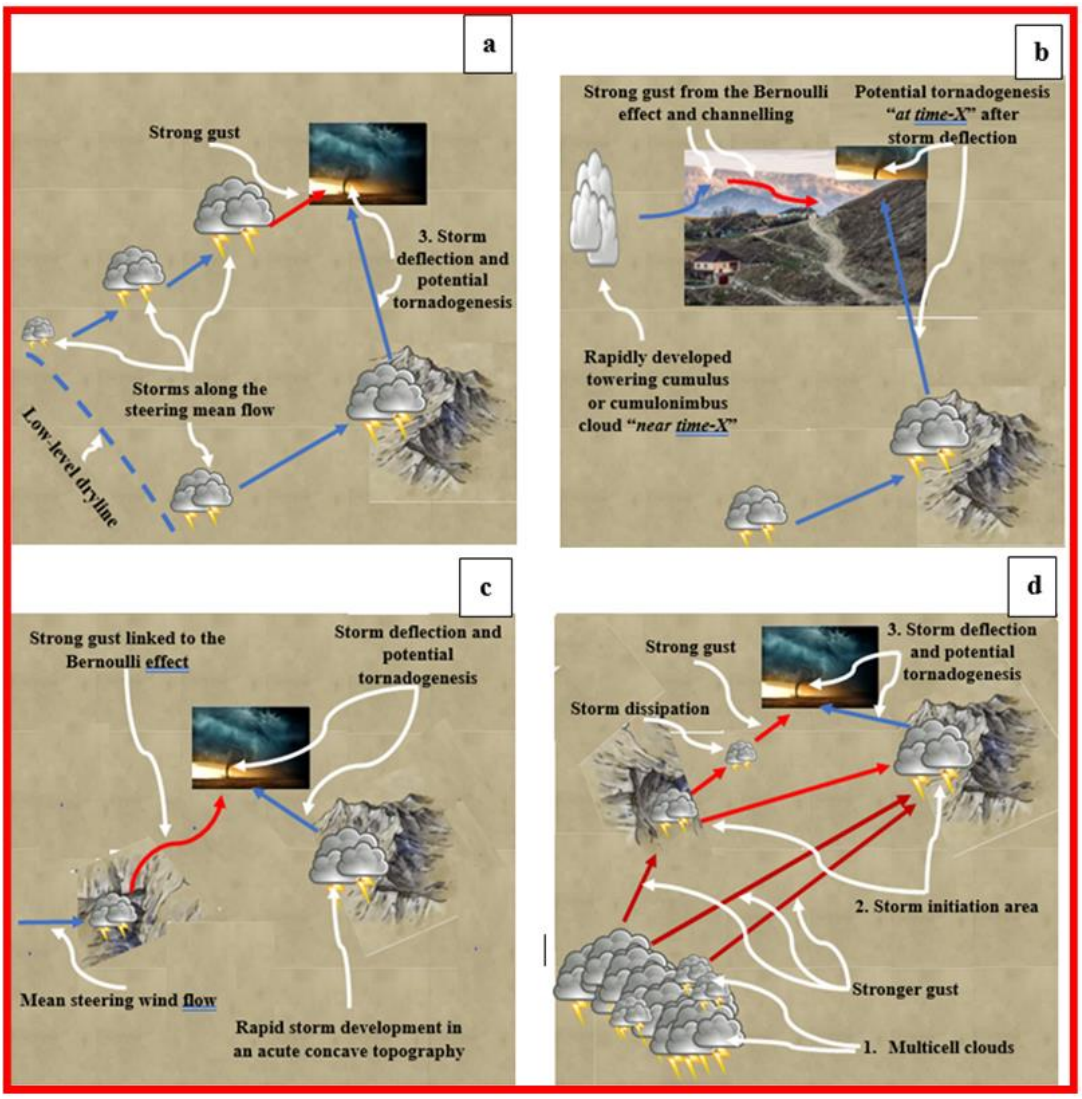


Figure 63.64 Tornadogenesis in the main thunderstorms due to the interaction of its inflow sector with the strong gust front of the upwind thunderstorms. Type A1 in 5.12a shows the tornadogenesis typically occurs in a storm after its deflection and interacts with the gust front of the intensifying upwind storm which is steered by the mean wind flow. Type A2 in 5.12b tornadogenesis after the deflection strong gust front effected from the Bernoulli effect and wind channelling. Type A3 in 5.12c shows the tornadogenesis after the deflection of the rapidly developed storm forming cross wind with the strong gust front generated by the Bernoulli effect. Type A4 in 5.12d shows the tornadogenesis after the deflection of the storm generated from strong multicell gust front forming cross wind with the strong gust front of the dissipating storm. (Mountain drawings and background modified: www.fantasticmaps.com; valley in 5.12b was taken from www.freepik.com).

This alternative contributing mechanism for tornadogenesis Type B2 aligns with Davies and Guyer (2004). Optimisation of the strong gust front of either of these storms most

often undergo the Bernoulli effect, as noted by WMO (1978), Sun and Sun (2015) and others.

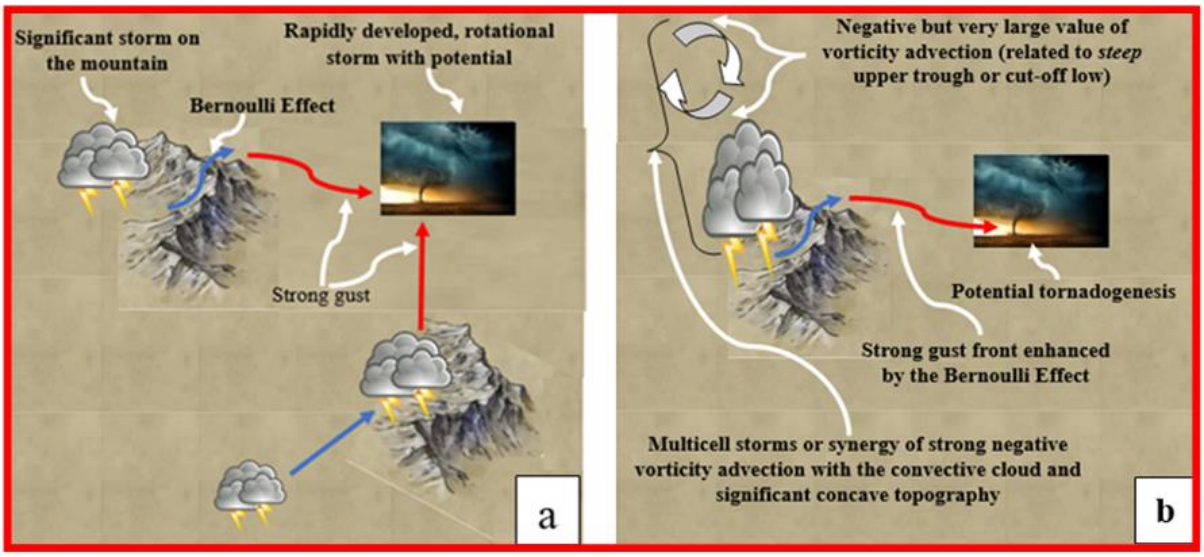


Figure 65.66: Tornadogenesis on the lee thunderstorms generated from the strong gust front enhanced by the Bernoulli effect on the significant concave topography. Type B1 in 5.13a shows the additional effect from the strong gust front of the secondary upwind thunderstorm. Type B2 in 5.13b shows the additional rotational effect from strong negative vorticity advection, which is related to the steep MTS troughs or COLs. (Mountain drawings and background modified: www.fantasticmaps.com).

Optimally strong gust front often tilts vertically on rebound from the land surface, as demonstrated Marquis *et al.* (2012), Xue *et al.* (2019) and Wang *et al.* (2020). Such vertically tilted, strong rotational gust front connecting with the updraft corridor of the low base of newly developed lee thunderstorm or multicell storms increase the potential for the genesis of one or more tornadoes (Fox-Hughes *et al.*, 2018).

5.3.3.2 Schematic model of landspout development in South Africa.

Mechanisms for the development of the landspouts were studied but not reflected in the case studies in this dissertation. Their development mechanisms from the surface to the updraft sector of the convective clouds or storms are demonstrated in Figure 5.14. Such landspouts were previously studied by Bluestein (1985), Wakimoto and Wilson (1989), Grazulis (2003), Monteverdi *et al.* (2015), among others. Sometimes, optimally strong gust fronts of the intense thunderstorm are forced to rise between two aretes to the pyramidal peak shown in Figure 5.14a or tabletop peak in Figure 5.14b.

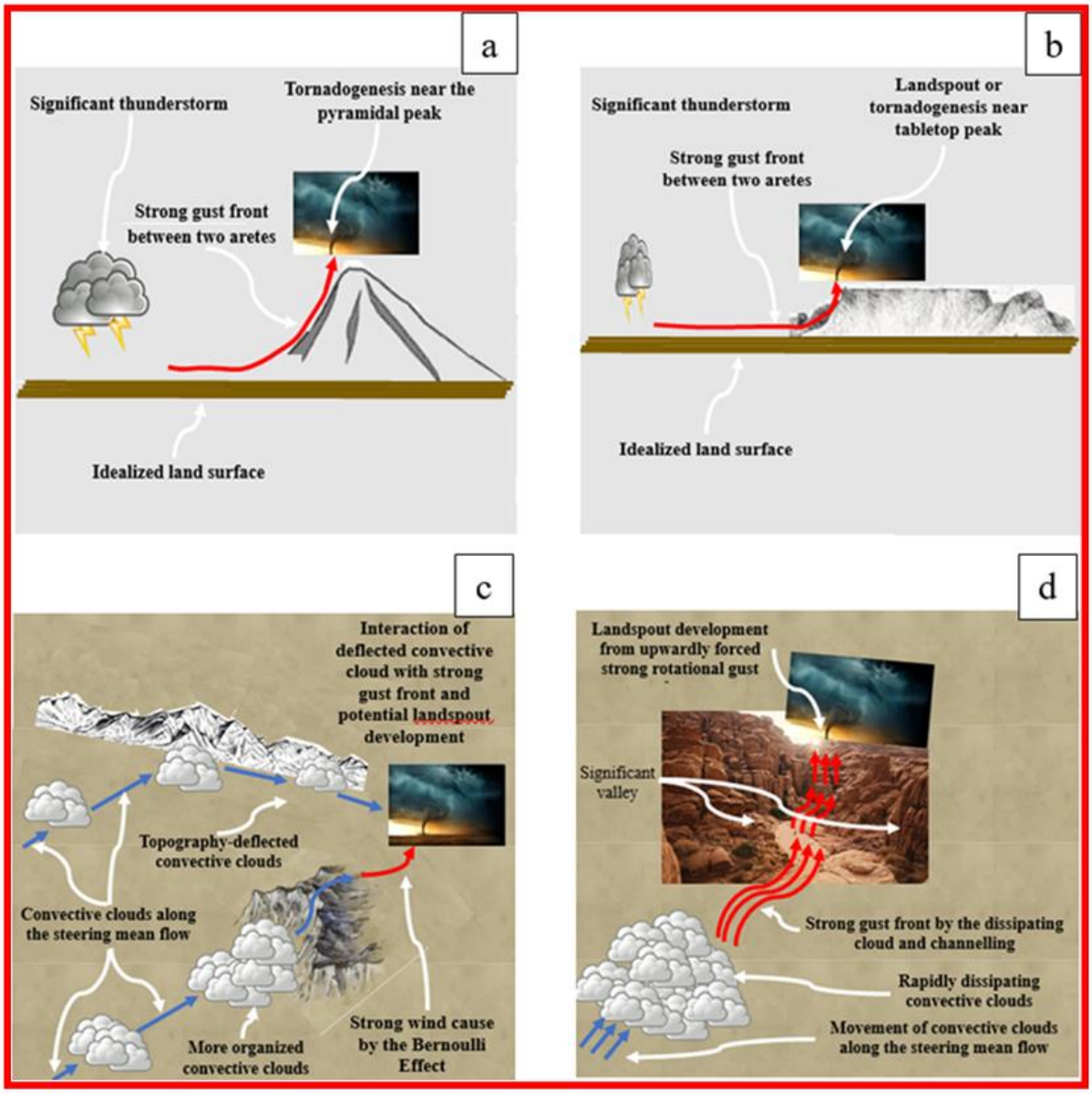


Figure 67.68: Sudden development of the landspout due to the influence of the non-precipitating convective clouds. Landspout development near pyramidal or tabletop peak showing Type A1 and Type A2 in 5.14a and 5.14b due to the strong gust front enhanced in the vortex line between two aretes. Landspout development Type A3 shown in 5.14c due to the interaction of the inflow sector of the deflected storm with the strong gust front of the organised non-precipitating thunderstorms and the Bernoulli effect. Landspout development Type A4 in 5.14d due to the sudden lift of the enhanced strong gust front channelling and rapid dissipation of the organised convective clouds. (Mountain drawings and background modified: www.fantasticmaps.com).

Early rotation shown in Figures 2.4 and 3.2b required a sustaining mechanism before the development of the landspouts near either of these peaks. Alternative development mechanisms of the landspouts are shown in Figure 5.14c and 5.14d and possibly include the effect of the non-precipitating convective clouds. Such events occur in LSLC

environments (Monteverdi and Quadros (1994). As in WMO (1978), Sun and Sun (2015) and others, landspout development Type A3 in Figure 5.14c shows organised convective clouds moving on the mountain while their strong gust front is enhanced by the Bernoulli effect on the lee side. The interaction of such strong gust front with the inflow sector of the deflected non-precipitating convective cloud increases the potential for the sudden development of the landspout. In agreement with Takeda (1966) and Moncrieff and Green (1972), it is reasonable to argue that a proportionally weaker gust front is required to generate optimum vertical shear near the land surface for the landspout development Type A3 in comparison with tornadogeneses Types A and B, above. Alternatively, stronger gust fronts, which may result from multicell thunderstorms, are typically enhanced on the significant topography by the Bernoulli effect. To this effect, downwind multicell storms could produce one or more landspouts. The rapid dissipation of organised convective clouds with their strong gust fronts is shown in Figure 5.14d. Strong gust fronts resulting from the rapid storm dissipation align with Wakimoto *et al.* (2006). Pressure gradient tightens in the valley relative to the distance from one ridge top to another with the stronger gust front (Tshehla and Wright, 2019). Optimally stronger gust fronts that encounter the concave topography may ascend and connect with the updraft corridor of the convective clouds aloft such that sudden landspout development is possible (Fox-Hughes *et al.*, 2018).

5.4 Longevity of tornadoes in South Africa

5.4.1 Short-lived tornadic storms

Most tornadoes were reported to have lasted for less than 15 minutes in the recent 60 consecutive months (i.e. between June 2016 and June 2021), as listed in Tables 3 to 5. Genesis of tornadic storms is simplified with schematic models in Section 5.3.3. The satellite study of parent clouds with adjacent upwind storms strongly suggests that the lifespan of tornadoes is shortened on account of the demise of adjacent storms, disconnections of outflow-inflow relationships and in some cases the disconnection of the parent storm from the wind-channelled surface jet. Further, the weakening of the

adjacent upwind storm relative to landspout-producing storms appear to suggest an even shorter lifespan.

5.4.2 Long-lasting tornadic storms

Nearly 7% of overall tornadoes in Tables 3 and 4 are constituted by South African tornadoes that lasted for more than 15 minutes and is categorised as long-lasting tornadoes in this dissertation. Such tornadoes appear to be possible in austral summer when associated with upwind multicell storms or squall lines, which are known to cause persistent gust front. Shortly after 14:00 UTC on 7 September 2005, a tornado occurred to the south-east of Bloemfontein in the Free State province and was associated with large hailstorms (Rosenfeld *et al.*, 2005). This was a long-lasting tornado that occurred in HSLC environment, as shown in Figure 5.15.

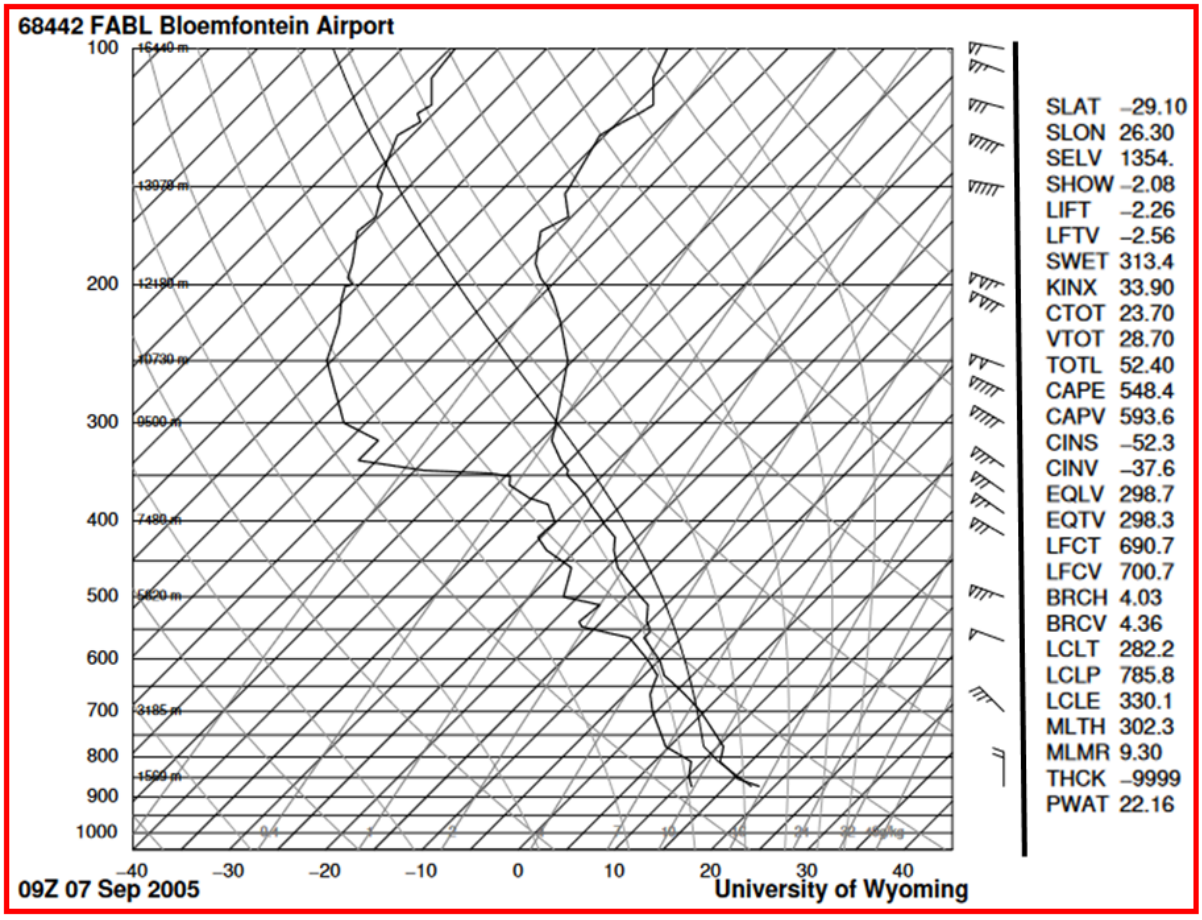


Figure 6970: The vertical profile of variables at Bloemfontein airport on 7 September 2005 at 12:00 UTC. (Source: University of Wyoming with data from the SAWS)

With the dewpoint temperature of about 10°C at 850 hPa, the vertical profile of this day showed a wind speed difference of 55 knots between 500 and 850 hPa. Later that same day, another tornado struck areas near Maseru, Lesotho (Vodacom, 2005). High shear environments in the USA requires the vertical wind speed shear between 500 and 850 hPa to be at least 40 knots although a far lesser strength produces tornadoes in the United Kingdoms (UK) (Mulder and Schultz, 2015; Apsley *et al.*, 2016). Their initiation improves with the 500 hPa storm-relative winds in the region of 8 $m.s^{-1}$ (≈16 knots) and 19 $m.s^{-1}$ (≈38 knots) (Thompson, 1998).

5.5 Distribution of tornadoes across South Africa

5.5.1 Tornado distribution by region

Coordinates of tornadoes listed in Tables 3 and 4 together with landspouts in Table 6 were used to plot these phenomena shown in Figures 5.16 and 5.17. Most of these tornadoes were found to be favourable over the central and eastern interior regions of South Africa in relation to the gust fronts and significant topographic variations found in eastern interior regions. Of the total reported, 34 tornadoes and nine landspouts, 21% occurred across the Mpumalanga province, of which 12% occurred over south-western areas and 7% along the escarpment. The frequency of tornadic events is high near the town of Standerton, probably because the outflow of the upwind thunderstorms gains extra velocities and horizontal vorticity at the topographical gap to the west of this town. Convective clouds near Standerton seem to tilt the strong horizontal vorticity into vertical vorticity, thus increasing the probability for tornadogenesis. Over 19% of tornadoes reported across South Africa occurred over the central Gauteng region (i.e. along the Gauteng Highveld). Tornadoes that develop from rebounding and rotating gust fronts are presented with those for which the gust fronts of the approaching storms connect existing parent storms in Figure 5.16; a ratio of 2:1 was determined for these tornadoes. Thunderstorm gust fronts often occur over the central and eastern regions of South Africa (Kruger *et al.*, 2010) and according to Koletsis *et al.* (2010), such a core of strong wind typically increases the velocities at the exit of major sloping topographical gaps**.** Current tornado distribution confirms the presentation by

D'Abreton (1991) and Goliger *et al.* (1997) with the tornado spread from 1984 to 1990 and from 1905 to 1996, respectively. The province of KZN experienced 14% of the total tornadoes reported across South Africa with 7% of occurrence on the great escarpment, and another 7% over the undulating plains in the midland areas. The occurrence of tornadic storms in KZN province may be the consequence of unstable low-level moisture resulting from the warm Agulhas Current (Rouault *et al.*, 2002). Comparable to the findings by Goliger *et al.* (1997), most of the tornadoes in the Eastern Cape (14% of the total tornadoes across South Africa) are found on the south-eastern interior – the highest frequency (i.e. with four tornadoes) was found near the town of Mthatha.

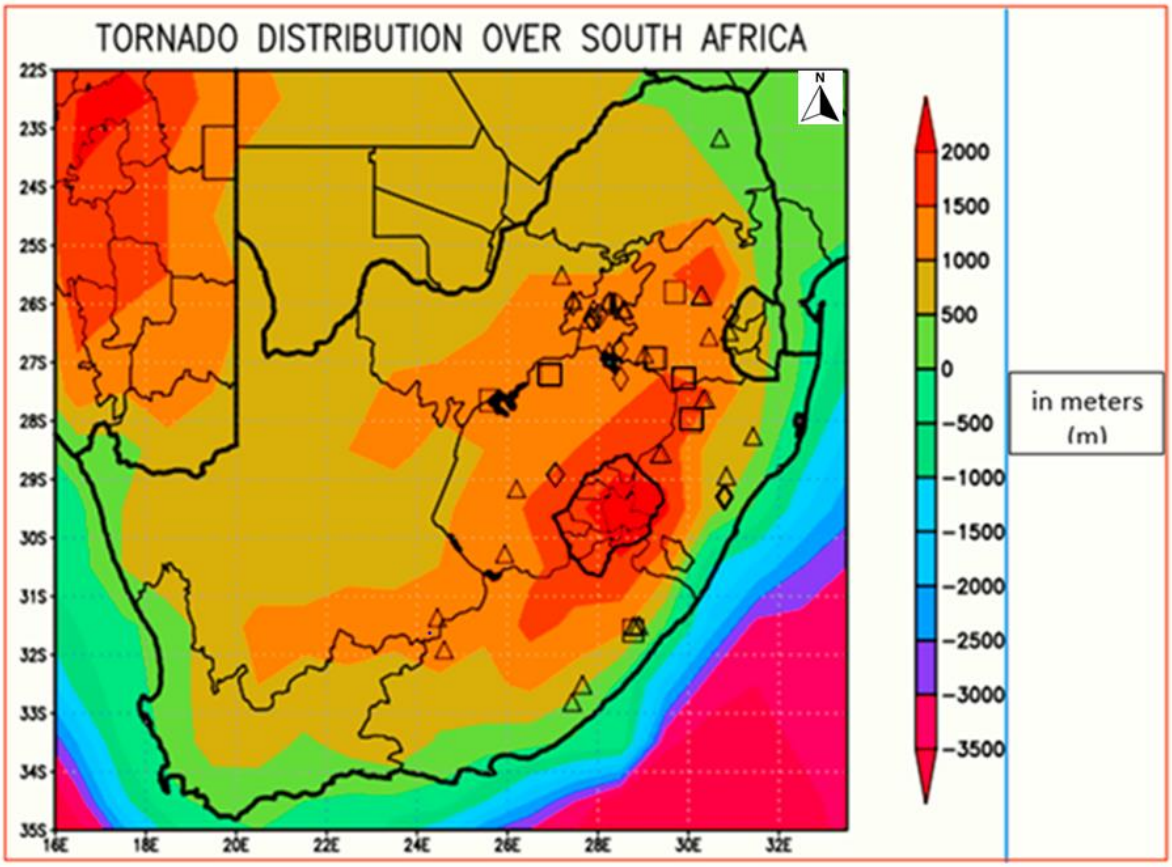


Figure 7172: The distribution of tornadoes (triangles and squares) and landspouts (diamond shape) across South Africa.

Figure 5.16 demonstrates the overall low frequency of tornadoes over the central areas of South Africa and their almost non-occurrence over the western regions. This low to non-existent frequency of tornado occurrence over the western part of South Africa may

be due to at least two factors: the generally flat landscape (i.e. the plateau) and limited reach of moist unstable surface air.

5.5.1.1 Distribution of tornadic supercell storms

Tornado development over South Africa was discussed broadly in Section 5.3. Tornadic supercell storms are rated from an EF2 threshold with extreme wind velocities from 178 km/h or stronger (Rae, 2014). Almost 68% of the total 28 tornadic supercell storms (i.e. closed triangles on Figure 5.17) were produced on the leeward side of significant topography due to the enhanced downburst of intense upwind thunderstorms. Their occurrences appear to be affected by moderate to strong wind flows (i.e. more than 15 knots as suggested by the NWP models) in the middle troposphere, which have a tendency to steer intense thunderstorms over such topography (i.e. steep mountains).

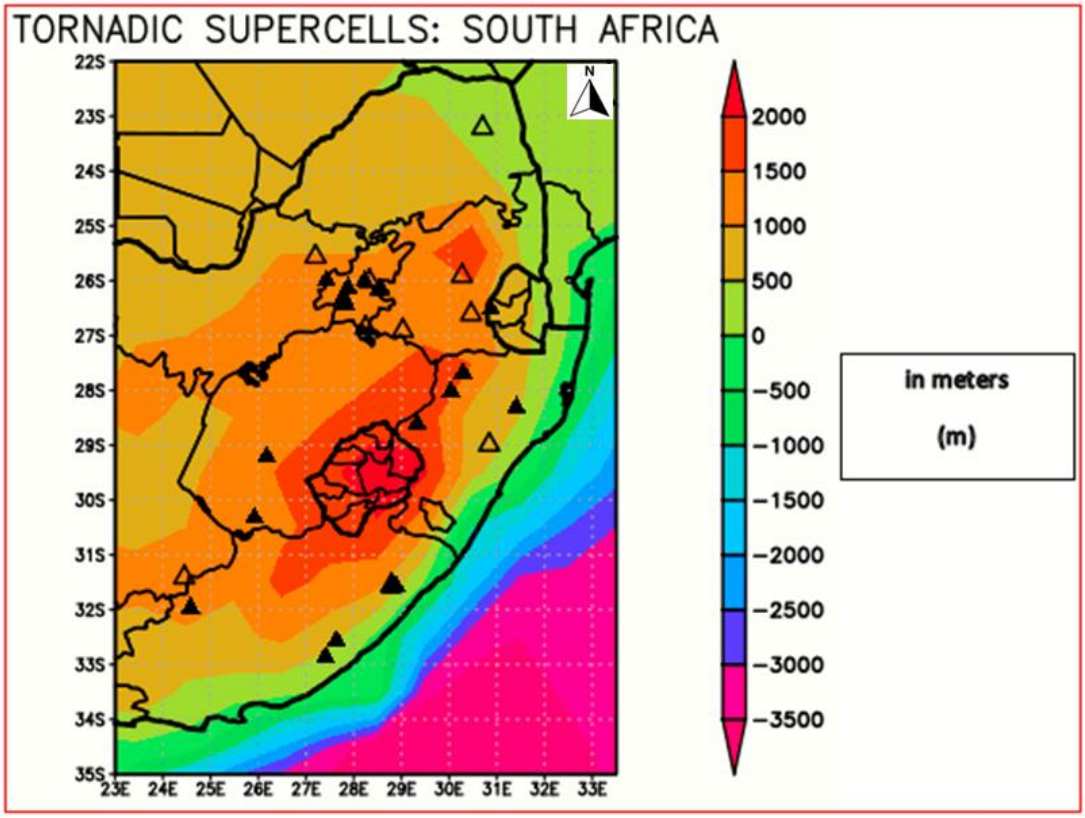


Figure 7374: Distribution of tornadic supercell storms across South Africa (June 2016 to June 2021). Matured tornadic supercell storms in interaction with the gust front of adjacent upwind storm (open triangle), with typical semi-stationary tornadic supercell rapidly developing due to the enhanced downburst of the intense upwind storms on the significant topography.

This observation is derived from analysing the movement of storms with reference to moderate to strong MTS wind flows, particularly resulting from steep COLs (or MTS troughs), as in Figure 5.1. Axes of these COLs (or MTS troughs) run through 0° to 45°. The other cohort of tornadic supercells (i.e. nearly 32%) occur when their inflow sector connects with extra velocities associated with the gust front of the adjacent upwind storms. Tornadoes with similar characteristics as these are discussed in detail in Section 5.3.1.

5.5.2 Tornado distribution by seasons

The highest tornado occurrence over South Africa was found from late spring (i.e. October) to mid-summer (i.e. up to January) and constituted approximately 62% of tornadoes listed in Tables 3 and 4. At about 38%, the highest frequency of tornadoes over South Africa is found in the month of November, followed by 29% in December, 24% in October and 10% in January (Figure 5.18). Cumulative CAPE amounts were separately calculated from numerical models (i.e. UM and ERA5) and each came close to 15 000 $J.kg^{-1}$ for the months of October and November (Figure 5.19). As corroborated by Williams *et al.* (1984), Kessler (1982) and many other investigators, low-level easterlies are established over southern Africa (e.g. South Africa) in the month of November when surface temperatures are near their maxima. Over South Africa, subsequent low-level moist and extremely unstable conditions in association with well-defined westerly flow aloft have the tendency to produce frequent and severe thunderstorms; such severe storms are initiated when cold, dry westerly air moves over warm, moist air in the lower troposphere. In November, occasional tornadic storms produce other severe storm events such as large hailstorms with strong gusty winds (Williams *et al.*, 1984; Olivier, 1990; Vermeulen, 2014; Simpson and Dyson, 2018). Fewer tornadic storms occur in an environment that is linked with steep lapse rates (e.g. lapse rate of 7°C/km or more) in the middle troposphere. A 5-year cumulative CAPE amounts in October and November nearly equals the total for summer, autumn and early spring seasons.

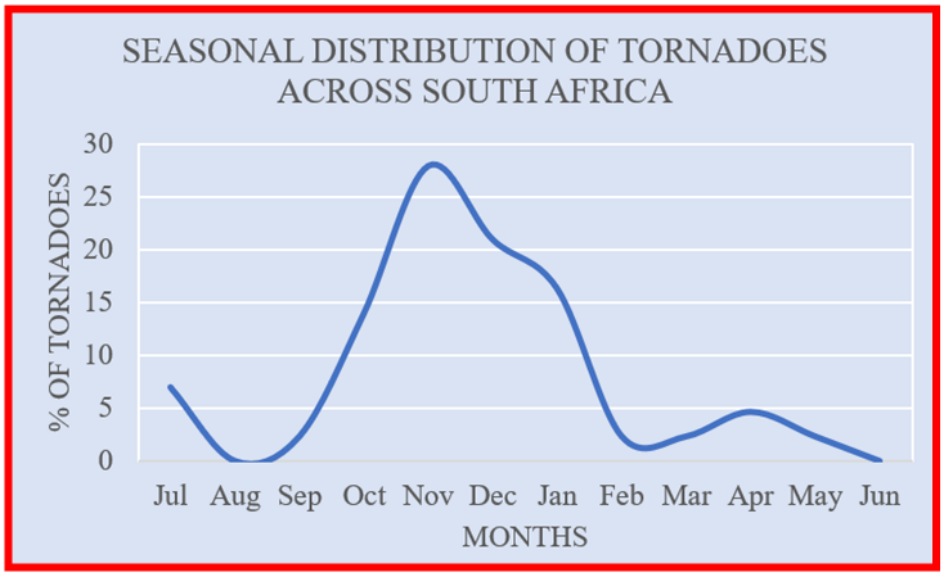


Figure 75.76: Seasonal distribution of tornadoes across South Africa.

As discussed in Section 5.2.1, the highest frequency of severe storms (e.g. tornadoes) is significantly influenced by moderate to extreme CAPE amounts.

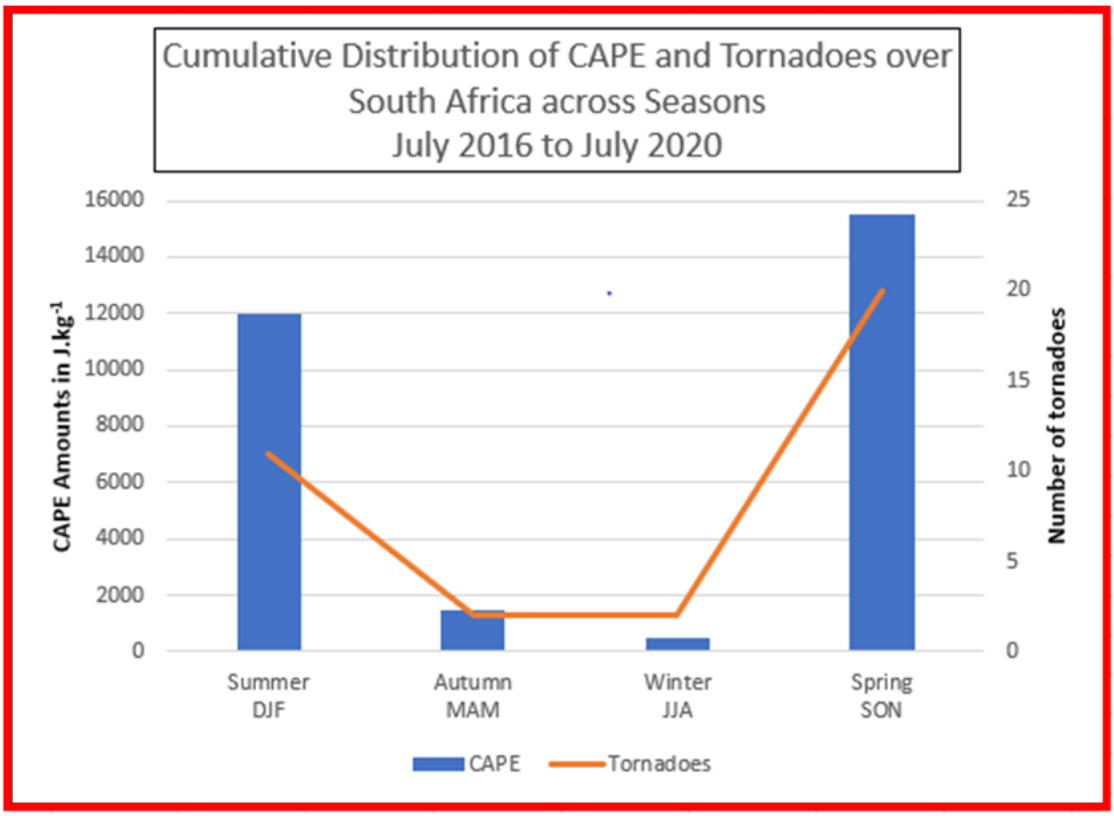


Figure 7778: Seasonal distribution of CAPE across South Africa.

CAPE amounts should not be used as the sole determinant of severe thunderstorms (Holley *et al.*, 2014). In other seasons, the occurrence of tornadoes and their distributions are very isolated. To a far lesser extent, 5% of tornadoes occur in the late morning and early afternoon on account of very extreme unstable low-level moist conditions. Invisible counterparts of tornadoes occur at night (Ashley *et al.*, 2008) and typically carry a much higher risk to cause fatalities compared to those occurring during the day (Mason *et al.*, 2018). Approximately 71% of the 34 South African tornadoes listed in Tables 3.1 and 3.2 occurred between 14:00 and 17:00 UTC (or between 16:00 and 19:00 SAST) and are accepted to be almost all cyclonic. Bias of tornadoes to the late afternoon and early evening was reported by De Coning and Adam (2000). This bias may be, according to Clark and Webb (2013), because of optimum or excessive diurnal heating which act on surface buoyancy (SB-CAPE), thereby increasing it rapidly and thus generating an optimal depth of turbulent mixing and topography-induced vertical wind shear. Tables 3 to 4 also show that the remaining 29% of tornadoes occurred outside 14:00 and 17:00 UTC and, of these tornadoes, 90% occurred earlier between 09:00 and 14:00 UTC (11:00 to 16:00 SAST). Late morning and early afternoon tornadoes seemed more favourable in association with high vertical wind shear of at least 25 knots (Tables 3 and 4). One tornado (i.e. 10% of tornadoes occurred outside 14:00 to 17:00 UTC) occurred during overnight hours in associated with a HSLC environment. Tornadoes that occur at night are invisible (Ashley *et al.*, 2008) and typically carry, according to Mason *et al.* (2018), a much higher risk to cause fatalities compared to those that occur during the day. Such HSLC tornadoes are discussed by Sherburn and Parker (2014). Other studies of strong dynamic systems and tornadoes include case studies by Kimambo (2018), Wood (1998, 2000) as well as De Coning and Adam (2000).

5.5.3 Distribution of anticyclone tornadoes

Anticyclonic tornadoes were very rare across South Africa and this is reflected as a weak sole event in the 5-year period of study. An anticyclonic tornado was video recorded by at least one motorist near Kempton Park, in Gauteng province, on the afternoon of 9 January 2018. The corresponding top view satellite images (not

included) showed overcast conditions over the central and southern regions of Gauteng such that movements of individual storms were obscured. Therefore, using satellite images to draw the inference on trajectories of storm gust fronts were impossible. However, the 3 km scan of Irene RADAR exhibited a hook echo feature at 14:16 UTC some distance to the south, as circled with a red oval in Figure 5.20a. The hook echo feature probably developed when the cold gust front of the storm to the north-east of Kempton Park moved westwards to the rear sector of the thunderstorm that was tracking south-eastwards (parent storm). Maintaining the 3 km scan for the same time, the analysis of radial winds displays the fairly weak low-level anticyclonic rotation (inbound-outbound maxima), as highlighted by the yellow oval in Figure 5.20b. Light green pixels represent the inbound flow and pink pixels represent the outbound flow. It is probably these connections that led to anticyclonic tornado between 14:30 and 15:00 UTC.

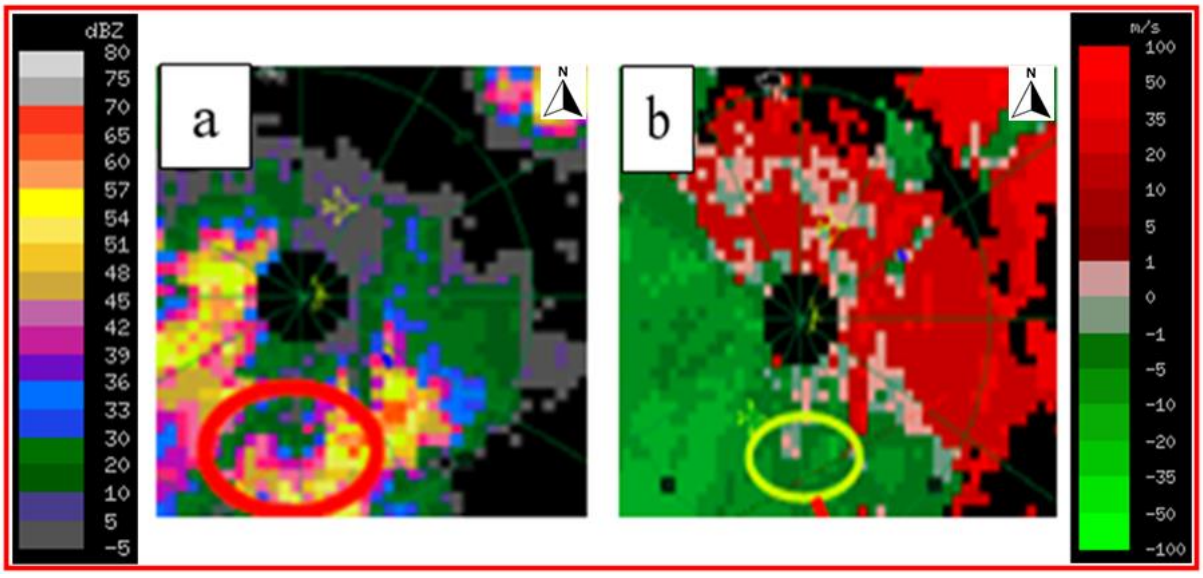


Figure 7980: Analysis of storm features using images of meteorological RADAR at Irene (Pretoria) as at 14:16 UTC on 8 January 2018. Red oval in 5.20a highlights the reduced reflectivity (hook echo) in response to the cold gust front of a larger thunderstorm moving in an opposite direction. Lime yellow oval in 5.20b highlights weak circulating radial winds (i.e. inbound-outbound maxima) where the pink colour shows low-level wind moving away from the RADAR while the light green colour shows low-level wind moving towards the RADAR. Map scales is 1:100000. (Source of images: SAWS)

Ge *et al.* (2013) propose that the radial winds should be assessed to determine whether a tornado would be cyclonic or otherwise. Such assessment is supported by Fujita

(1965) and Markowski (2001) and should be conducted at the rear sector of the parent storm. The anticyclonic tornado soon lifted back into parent storm when its rear sector disconnected from the gust front of the thunderstorm that was tracking westwards. As discussed in Sections 4.2.1.1.a and 5.4.1, storms that are steered by light to moderate winds could move along the significant topography. In the context of the northern hemisphere, the majority of tornadoes have anticlockwise rotations and clockwise rotations are rare (Tyrrell, 2009).

5.6 Spread of tornadoes relative to El-Niño/Southern Oscillation

5.6.1 Frequencies of tornadic storms

Tornadoes and landspouts were reported in the eastern region of South Africa (i.e. to the east of 24°E) during the base period, June 2016 and June 2021. These events represent 18.8% of the population of such events reported between 1958 and 2021. Section 5.5 discussed the regional pattern of tornadic occurrences. The long-term average of four tornadoes per year was determined from 229 tornadic events recorded over a 64-year period (1958 to 2022), as shown in the graphs in Figure 5.21. Considering ENSO on the label b in these figures, high frequencies of tornadic storms (i.e. more than 4 tornadoes) coincided with La-Niña seasons, which were preceded by the end of moderate to strong El-Niño seasons. Such high frequencies of tornadic storms were found in spring and summer seasons. Development framework of individual tornadoes was discussed in Section 5.3. The frequencies of tornadic storms during the South African summer were largely below the long-term average with no clear association to ENSO. Reports of winter tornadoes (in the MJJ months) were largely non-existent across the eastern parts of South Africa. This scarcity may be correlated with dry conditions, which typically result from the dominance of the descending component of the Hadley cell circulation (e.g. concurrence of surface and MTS anticyclonic circulations). Hadley cell circulation was briefly discussed in Section 1.2 and Subsection 2.6.1. In contrast, several winter tornadoes were reported in 1983, 1994, 2012, 2016 and 2019. These winter tornadoes seemed favourable in the neutral ENSO phase in association with some steep COLs. They occurred behind the main cloud bands

that formed on the leading edge of these steep COLs. Discussions in Section 4.3.2.2b showed that such COLs are typically associated with large values of negative vorticity advection at 500 hPa. Most of the landspouts developed in the spring season over the south-western region of South Africa: the Mediterranean climate region. Often, seasons with average to slightly above-average tornado frequencies (at least 5 tornadoes) were observed when the peak of El-Niño occurred in late spring or early summer, as reflected in a in the graphs in Figure 5.21. Nearly 37% (13 times) of the overall tornadoes which occurred between October and March during the period 1958 to 2022 as seen in these graphs were above the long-term average. Such high tornado frequency was recorded during the summer of 1986-1987 by D'Abreton (1991). Figure 5.21 also shows that three out of 13 occasions account for a double or more of average tornado frequencies (i.e. 8 or more) during the most recent two and a half decades. However, the frequency of tornadic storms was below the long-term average during La Niña in the South African summer, which followed the end of moderate to strong El-Niño in early 1973. The IOD event of 1973 and 1974 was recorded as insignificant (e.g. Rao *et al*., 2002; Ashok *et al*., 2003; Fan *et al*., 2016). The insignificant (i.e. near-zero) IOD together with the interaction of synoptic and mesoscale circulations might have restricted the spread of moist conditions on the eastern areas of South Africa together with the thunderstorm dynamics.

5.6.2 Indirect causal effects for high frequencies of tornadic storms

Recorded high frequencies of tornadic storms in Figure 5.21 occurred in La-Niña seasons that were preceded by the moderate to strong El-Niño. Derived from De Villiers and Van Heerden (2007), these high tornado frequencies may be correlated with the updraft corridor that ingest loose soil and other minute particles into the thunderstorms. Thunderstorms were noted to have a longer lifespan when they were naturally ingested with high concentration of dust (Yair *et al.*, 2022). Earlier, Olivier (1990) reported the occurrence of high frequency of severe thunderstorms across South Africa at the end of a drought season.

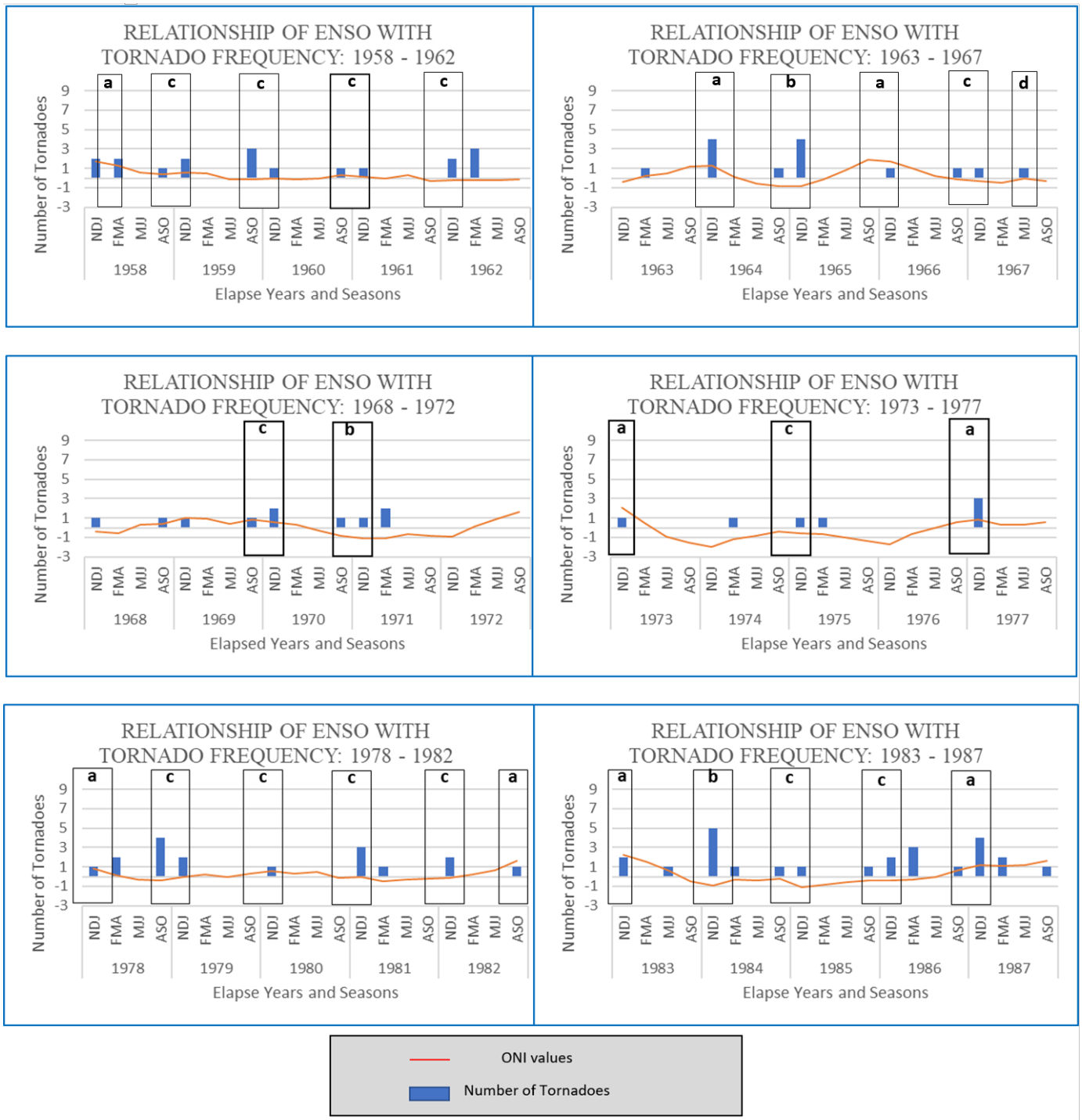


Figure 81.82: Relationship of ENSO phases with tornado frequencies.

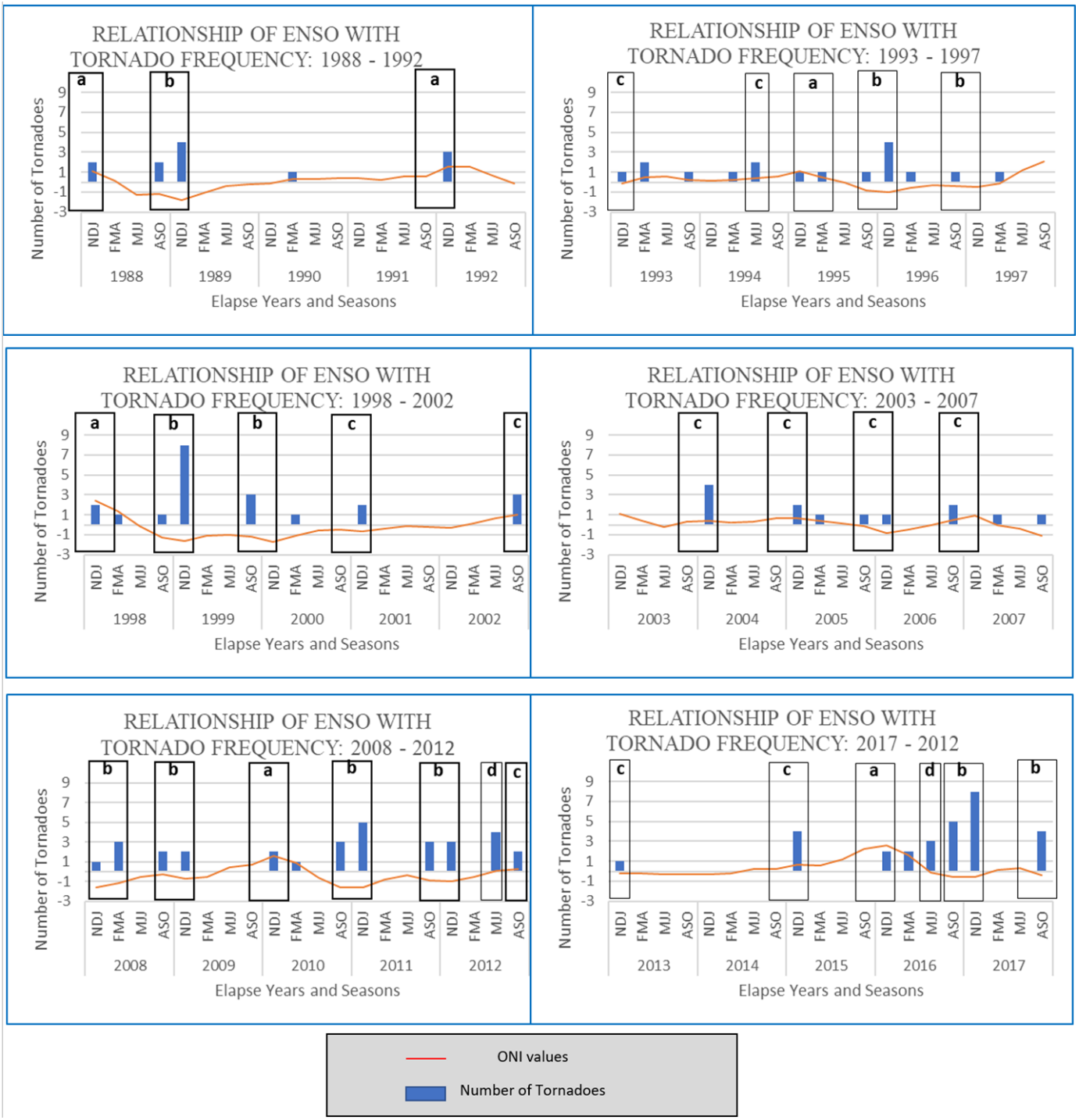


Figure 83.84: Relationship of ENSO phases with tornado frequencies (continued).

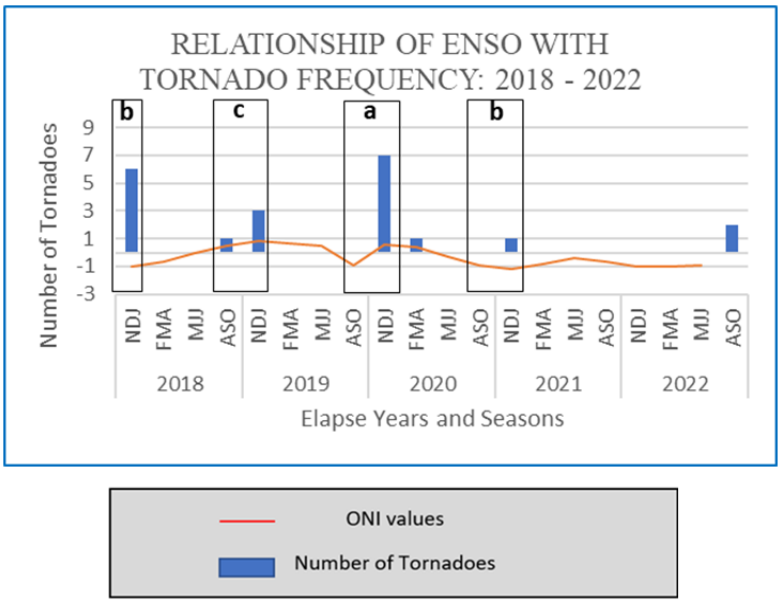


Figure 85.86: Relationship of ENSO phases with tornado frequencies (continued).

During their long lifespan, such severe thunderstorms produced a small fraction of tornadic storms particularly when they interacted with topographical features, as discussions in Sections 5.3.1 and 5.3.2 show. Dry conditions, loose soil and minute particles of drought-sensitive vegetation are prevalent when the El-Niño season co-occur with the positive IOD (Chikoore *et al.*, 2021; Chivangulula *et al.*, 2023). An increased rate of tornadic storms over South Africa during the past four decades as seen in Figure 5.21 seem to confirm lag correlation with frequent El-Niño events. Trenberth (1997) noted the dominance of El-Niño events in the years after 1979. The El-Niño events during 1997and 1998, and 2015 and 20216 seem to suggest an increased intensity. The former event was associated with high tornado frequency for the South African summer of 1998 and 1999 (De Coning and Adam, 2000; Table 3.4) and the latter event was associated with 12 tornadoes. The most active single year was 2016 with 20 tornadoes of which 60% occurred around the trough (i.e. peak) of the La-Niña event (i.e. during October to December of 2016 – the period which coincided with weak La-Niña), following the strongest El-Niño event recorded within six and a half decades.

The remaining 40% were spread during the transition from this El-Niño to La-Niña events: three tornadoes were reported during the steep decline of the very strong El-Niño between November 2015 and February 2016 with five tornadoes through a neutral phase in autumn and winter. Neutral or La-Niña phenomena that succeed strong to very strong El-Niño events appear to have a residual effect in the sense that high tornado frequency in one summer is usually followed by yet another high tornado activity in the next summer. Potential for such residual effect is most probable during October to March and is reflected in Table 3.4 with nine occasions in association preceding strong to very strong El-Niño events. However, low tornado frequencies over South Africa appear to link with neutral states as well as weaker El-Niño and La-Niña seasons. Below-average tornadoes also appear to have a weak correlation with an increase of mid-latitude circulations during the autumn and spring season. As discussed in Subsections 4.3.2 to 4.3.4, the weak correlation of tornadoes over South Africa in relation with mid-latitude circulations may be because only a few of these circulations became steep (i.e. with trough axis between 0° and 45°). Most of these events were below average (i.e. less than four tornadoes) but the most tornado activity (i.e. ten tornadoes) was recorded during 2017 and 2018. Tornado-producing conditions prevailed during the neutral state in the summer season of 2019 to the effect that four tornadoes were produced in KZN province within 30 days of November 2019 after the end of an El-Niño period in late winter of 2019.

Chapter 6: Conclusions and recommendations

6.1 Overview summary

The study of the contribution of either the gust fronts or topographic features was done to pursue Objective 1. The influence of topographic features in the development of extreme weather (e.g. severe thunderstorms) has been observed across the globe for much longer than the millennium. A range of reasons were and are still provided to explain these extreme weather events. However, meteorologists often link such severe thunderstorms to the development of the mesoscale circulations in the setting of synoptic circulations. The scope of this dissertation excluded the cluster of thunderstorms such as tropical cyclones, cloud bands associated with TTTs, COLs and MTS troughs due the difficulty to make inferential isolation of their gust fronts. Criteria were developed for the restriction of subjectivity in the manual identification of the isolated severe thunderstorms and set out in Section 3.4.1. These storms were identified during the base period between June 2016 and June 2021 and are listed in the Appendix. The vast majority of these storms underwent a rapid drop in CTTs colder than -50°C. Stratified sampling was used for case studies in Chapter 4 to reflect the significant contribution of topographic features. These case studies could be used as prototypes for the potential development of severe thunderstorms in the future. A detailed summary of the contribution of topographic features to severe thunderstorms is set out in Section 6.2 below. Gust fronts of upwind thunderstorms were inferred to have played a role in the development and/or maintenance of some of the isolated severe thunderstorms. Listed in the Appendix, severe thunderstorms were associated with MTS meteorological circulations. A summary of this association is displayed in Figure 4.1. Under a variety of tropospheric meteorological conditions, the analysis of the decision-making for the potential development of these storms is shown in Figure 4.2. Aligning with the climate of South Africa, the top bar of Figure 4.2 demonstrates that most severe thunderstorms in South Africa are linked with the MTS ridges. This top bar further suggests tentativeness in the decision-making since it shows an almost 50% split of warnings of severe thunderstorms in the two categories: within 2 hours and between 2

and 36 hours. Albeit in very few cases as seen in Figure 4.2, there was an almost 50% split into the said two categories for severe thunderstorms, which were linked to the bases (northmost sections) of the MTS troughs. Research in this dissertation sought to find significant bias in favour of warnings between 2 and 36 hours or beyond, as opposed to within 2 hours of the initiation of severe thunderstorms. The outputs of this research could be used by the forecasting desk, which will help towards protecting moveable property and preventing economic loss. Safety of human life, livestock and disaster management planning remain centralised, which is helpful considering the increasing incidents of severe thunderstorms. Figure 4.2 shows that the decision-making is comparatively good but could still be improved for severe thunderstorms that are linked with strong MTS circulations. Such circulations are COLs, well-developed MTS troughs and their irregular perturbations to the east. Early decision for issuing warnings of imminent severe thunderstorms, which are related to strong MTS circulations, could be because the NWP (e.g. UM 4km) often show clearer the required vertical wind shear in the lower troposphere. A significant increase in the amount of negative vorticity advection was shown to be associated with the steepening of a COL in Figure 31. Such events were shown to be very few in Figures 4.2 and 4.3. The organization of the long-lived and occasionally severe thunderstorm was in synergy with these large amounts of vorticity advection. This storm was used in pursuit of Objective 2. As an extension of both Objectives 1 and 2, Objective 3 sought to formulate a theoretical basis for nowcasting the potential for tornadoes over South Africa. A detailed summary of Objective 3 is provided in Section 6.5.

6.2 Effect of topographic features to gust fronts and severe storms

Topographic features remain almost unchanged yet their consequences in the development of severe thunderstorms require the strong appreciation of varying meteorological conditions. Such conditions include, but are not limited to, the availability of warm moisture with favourable surface heating and subsequent substantial CAPE. Thermal afternoon thunderstorms and their gust fronts are typical due to the combinations of these conditions. On encountering topographic features, gust fronts of ordinary thunderstorms were inferred to undergo the Bernoulli effect such that

vertical wind shear is initiated. It is accepted in meteorology that an optimal degree of vertical wind shear is required for the release of CAPE in the development of severe thunderstorms. The severe thunderstorms discussed in the case studies in Chapter 4 underwent a rapid drop in CTTs signifying their severity. The study in reference to the high-resolution topographical maps revealed two distinct cases from which vertical wind shear developed. One case is for the initial thunderstorm movement that forms an obtuse angle after the deflection to the left along the significant and nearly linear topography. In some cases, near linear topography may cause localised wind circulations with incremental storm intensification. Such storms are associated with the increase of Coriolis force and probably the surface-based vorticity advection, which are clockwise in the southern hemisphere. The other case is for storm movement into the significant concave topography which then deviate to the left along the declining arete. Before the deviation, the movement of these storms were often steered in the middle level at moderate to strong mean winds (e.g. 10 to 20 knots). Moderate to strong mean steering winds are most often associated with the MTS ridges but they are also possible with weak COLs (e.g. Case C) or MTS troughs. Often, such thunderstorms undergo rapid intensification with severe events such as strong winds, heavy rain and flash-flooding. They usually have a temporal longer span. Digital solutions (e.g. Machine Learning algorithms) would most likely outdo the human forecaster on nowcasting. However, the improvement of the lead-time for the forecast of potential severe thunderstorms in South Africa could be achieved through meteorological conditions with a reasonable appreciation of the locations of topographic features. This means a significant bias could be achieved in favour of warnings between 2 and 36 hours or beyond, as opposed to within 2 hours of the initiation of severe thunderstorms. On the other hand, the deviation of thunderstorms to the right undergoes less Coriolis force which usually leads to their demise. Such right-moving storms often develop on the right side of the significant convex-shaped topography. In essence, the hypothesis of the effect of topographical features in the development (demise) of severe thunderstorms was tested and confirmed.

6.3 Effect of gust fronts of upwind storms on severe storms

The gust front of an ordinary upwind storm could generate optimal vertical wind shear in the inflow sector of the downwind thunderstorm. Therefore, the thunderstorm that already underwent rapid drop in CTTs is likely to be maintained or to drop further when its inflow sector interacts with the gust front of the upwind of ordinary thunderstorms. The original trajectory of the upwind thunderstorm is maintained by the moderate to strong mean steering winds, mainly association with the MTS ridge as suggested in Figures 4.2 and 4.3. The outflow-inflow interaction in the deflected storm often results in the prolonged (i.e. maintenance of) severe storm events, as demonstrated in aspects of Case A and Sections 4.2.1.1, 4.3.2.2a, 5.3.1 and 5.3.2. In other cases, the outflow-inflow and storm intensification occurred when the upwind storm nearly caught up with the downwind storm. Downwind thunderstorms usually become severe in either of these cases. Other aspects of Case A show that the storm severity was influenced by the merger of the upwind storm with the downwind storm.

6.4 Synergy of storms with large 500 hPa vorticity advection

Characteristics and events of the discrete severe thunderstorms were tested against the synergy of the low-level circulations with the negative vorticity advection at 500 hPa for different axis orientations of a COL. Although different axis orientations of the MTS troughs were not used in this dissertation, they often produce similar events as under the governance of the COLs. Investigative avenues that were taken were in pursuit of Objective 2. Understanding the modification in the characteristics of the discrete severe thunderstorms under different trough orientations is important for the operational forecasting and issuing of appropriate and timely warnings. Pockets of numerically smaller amounts of 500 hPa vorticity advection were shown in Figure 31b of Section 4.3.2.2b in association with the axis of the COL which was orientated south-east to north-west. Similar orientation and amounts of the 500 hPa vorticity advection also associated with the well-developed MTS trough. In such environments, thunderstorms are known to be characterised with heavy showers and flash-flooding. Significant increase in the amounts of the negative vorticity advection at 500 hPa were noted when

the COL steepened. That means, a significant increase in the amounts of the negative vorticity advection at 500 hPa were linked with the trough axis which leans south-west to north-east. This significant increase in vorticity advection is interpreted to signify the additional potential spinning effect. Steepening COLs are also known to advance (surge) the cold air to the east, giving effect to the thinning of the cloud band and resultant reduction of showers. A few isolated thunderstorms often develop in the cold zones behind the cloud bands associated with steep COLs (or steep MTS troughs). However, the near-surface trough seen in Section 4.3.2.2b deepened causing the strengthening of the low-level vertical wind shear and prolonged thunderstorms. Sections 5.4.2 and the discussion of Figure 4.20 in Section 4.3.2.2b show that thunderstorms that developed in an environment with strong low-level wind shear are usually long-lived. The Bernoulli effect on the gust front of the thunderstorm which moved across the significant topography (e.g. southern escarpment) rapidly produced a severe lee thunderstorm. CTTs associated with this thunderstorm ranged between -40°C to -50°C and the wind destruction was also reported.

6.5 Development of landspouts and tornadoes

Disaster management practitioners and a tiny minority of users of Facebook and X benefited from the tornado warning in December 2017. This direct tornado warning was made available to users at 16:42 on 30 December 2017, 4 to 5 minutes before the genesis and touchdown on the outskirts of Protea Glen, Soweto. In context, the warning was the only one of 228 rotational phenomena (landspouts and tornadoes) recorded since 1958 and 2021. The landmark lead-time is regarded as a great success in scientific decision-making, although hardly useful to the users. Tornadoes are known to be the worst of the events produced from the thunderstorms, but relatively warm cumuliform clouds may also produce some of the rotating tornado counterparts: landspouts. Therefore, for Objective 3 of this dissertation it was necessary to study the association of the topographic features and satellite-based cloud formations for the notable increase of the achieved 4 minutes. Systematic study of the 34 tornadoes was conducted and the results are summarised with schematic models in Section 5.3.3. Photographic evidence of the tornadoes and/or the assessed damages thereof was considered in the analysis in some

cases. Meteorological RADAR images were also used to affirm two of the case studies. Of significant importance regarding the South African tornadoes is the inferred centrality of the optimally strong gust front of the upwind thunderstorm. The potential for the tornadogenesis is heightened in the deflected downwind thunderstorm that move across the optimally strong gust fronts. Such tornadogenesis occurs when the optimally strong gust front connects with the inflow sector (updraft sector) of the deflected downwind thunderstorm. Often, the strength of the gust front is optimised by the Bernoulli effect from the topographic features (terrain barriers). In some cases, the potential for the tornado occurrence in the deflected thunderstorm is heightened when its inflow sector interacts with the strong gust optimised by the valley channelling. Such gust fronts may be possible from the towering cumulus or weak thunderstorms with CTTs in the region of -35 and -50°C but more typically from the significant upwind thunderstorms with CTTs colder than -50°C. Inferred, favourable strong gust front generated by these significant windward storms (or multicell storms) with the addition of Bernoulli effects on the significant topography could contribute to the tornadogenesis in the lee storms. Synergy of the Bernoulli effect on encounter with topographic features, thunderstorms and strong cyclonic flow (i.e. spinning effect) generated from large amounts of negative vorticity advection at 500 hPa (or higher, pressure surfaces) was studied. The results recorded in Section 5.3.2 and the discussions of Figures 4.9 to 4.14 in Section 4.3.2.2b suggest the potential for sudden tornadogenesis on the lee storms. Evaluative research, as briefly seen in the associated discussion of Figure 5.7, was used to suggest the predictiveness of the potential of the tornadogenesis from the newly developed conceptual framework. Such a tornadic event was associated with the large amounts of negative vorticity advection at 500 hPa (or higher, pressure surface). Similar efforts could be used for the benefit of disaster management, protection of human lives and livestock, the insurance industry or the prevention of economic losses in broader scope. Thunderstorms (e.g. severe storms) could develop from the high cloud bases of convection convective systems, independent of the topographic features and strong gust fronts. Case studies for the severe thunderstorms, which were linked with the 500 hPa LI of -6°C or colder as well as the ample moisture and steep temperature lapse rates (i.e. of 7°C/km or more) in the 700 to 500 hPa layer, were excluded in this

dissertation in line with its scope. Their cloud bases are occasionally high with the tendency to produce small hailstorms with microbursts but in rare occasions they produce weak tornadoes. The systematic study of the bottom-up development of nine landspouts was also conducted with their schematic model in Section 5.3.3.2. Their developments seem to require gust fronts that are optimally strengthened between two aretes to the pyramidal or table-top peak of the mountain. Some gust fronts could be optimally strengthened by the valley-channelling with the potential development of landspouts where the valley has a roughly concave shape. Except for relatively warm clouds (e.g. with CTTs in the region of -35℃ to -50℃), other landspouts developed from cloud movements that were similar to those of tornadoes. Arguments in this section, together with the other referenced sections, sought to reduce the knowledge gap regarding the development of tornadoes and landspouts. Referencing the tornadic convective clouds to topographic features could assist the South African Weather Service to use refined verification of reports of landspouts and tornadoes.

Plots of Niño indices and tornadoes in a time series are arranged in seasons in Figure 5.21 in Section 5.6 for the period 1958 to 2021. These plots highlight the high frequency of tornadoes during/after the end of moderate to strong ENSO El-Niño phases. The observations were supported (negated) when drought (precipitation) over southern Africa (e.g. South Africa) was associated with the El-Niño event. Residual effect to the second year is possible after the end of the strong El-Niño events. Whether an El-Niño event would result in dry (humid) conditions required the literature assessment of the correlation with another climate indicator, namely IOD. The literature suggests that moderate to strong El-Niño events with positive IOD would result in significant drought and lack of soil moisture. Numerical models by which seasonal forecasts are produced reasonably predict the polarity of IOD and ENSO phases. Therefore, the end of El-Niño phases that are preceded by major droughts could be used to predict the potential high frequency of tornadoes. Such outlook forecast could serve as an input for the planning strategy of the disaster management. The high frequency of tornadoes may be associated with the onset of warm moist conditions and favourable wind shearing in the lower troposphere in an environment with ample loose soil (dust) particles. Among other

cloud condensation nuclei, optimum amount of the loose soil enables the development and maintenance of some of the convective clouds. A summary of the scenarios that could lead to the individual occurrence of tornadoes and landspouts was made in the preceding paragraph of this section: relative movements of convective clouds and storms across topographic features were shown to contribute to the development of tornadoes and landspouts.

6.6 Recommendations

Estimates or actual measurements of the gust fronts were not available for almost all events used in the case studies in Chapters 4 and 5. However, gust fronts that were measured at the in-situ data collection point could be used along with the thunderstorm characteristics (e.g. their sizes, movements and CTTs), including the topographic features where they pass. These aspects could be used to train and develop the cost-effective Machine Learning algorithm for the direction and estimates of the strength of the storm gust fronts. These estimates should be stored and archived for use in the refinement of the algorithm in the future. The algorithm should also calculate the speed of the individual thunderstorms to make a short-term prediction (e.g. 30 minutes) of whether the storm will deviate or move over the significant topography. A combination of these efforts will potentially improve the manual monitoring of the thunderstorms with the potential to nowcast tornadoes and landspouts. The success of this envisaged project could assist the operational forecaster with the lead-time and the inclusion of the potential development of tornadoes. Speed of thunderstorms could also be used in the reanalyses to evaluate the steering winds suggested by the NWP.

Table 2: Influence of temperature on humid environment on 13 February 2018

Metadata			Weather Data			
Place	Latitude	Longitude	Time (UTC)	Air Temperature (℃)	Humidity (%)	Rain (mm)
Cape Agulhas	-34.83	20.01	00:05	20.7	82.4	0.0
			06:00	20.3	92.5	0.0
			12:00	22.1	82.3	0.0
			18:00	21.3	86.2	0.2
Tygerhoek	-34.15	19.10	00:05	19.3	89.4	0.0
			06:00	19.8	84.6	0.0
			12:00	30.2	49.0	0.0
			18:00	20.3	85.8	0.0
Worcester	-33.66	19.42	00:05	21.4	78.8	0.0
			06:00	19.7	83.7	0.0
			12:00	31.4	42.9	0.0
			18:00	27.7	59.9	0.0
Ceres	-33.38	19.32	00:05	22.8	70.1	0.0
			06:00	22.1	60.5	0.0
			12:00	32.5	33.9	0.0
			18:00	25.6	52.6	0.0
Laingsburg	-33.19	20.86	00:05	22.4	61.7	0.0
			06:00	22.4	66.1	0.0
			12:00	29.8	38.4	0.0
			18:00	26.4	61.2	0.0

Table 2 (continued): Influence of temperature on humid environment on 13 February 2018

Metadata			Weather Data			
Place	Latitude	Longitude	Time (UTC)	Air Temperature (℃)	Humidity (%)	Rain (mm)
Excelsior	-32.96	19.43	00:05	19.7	71.3	0.0
			06:00	19.4	72.6	0.0
			12:00	28.6	38.6	0.0
			18:00	19.1	80.7	0.0
Clanwilliam	-32.18	18.89	00:05	25.8	65.3	0.0
			06:00	29.9	36.9	0.0
			12:00	37.8	25.2	0.0
			18:00	32.0	46.4	0.0
Brandvlei	-30.46	20.48	00:05	20.7	83.6	0.8
			06:00	20.4	84.8	0.0
			12:00	28.5	53.0	0.0
			18:00	20.5	84.9	1.6
Springbok	-29.67	17.88	00:05	25.6	38.3	0.0
			06:00	22.00	60.6	0.0
			12:00	30.5	33.1	0.0
			18:00	25.2	40.5	0.0

Table 3: Tornadic supercell with upwind thunderstorm

	Location	Latitude / Longitude	Date	Time of Event	Cloud-top Temperatures (°C)	500 to 700 hPa circulations	Tropospheric Instability	Vertical Profile				
								Time (UTC)	Level (hPa)	Moisture (%)	Speed (knot)	Direction (°)
Tornadic Supercell with Adjacent Upwind Thunderstorm	Vaal Marina / Mamello	-26.85, 28.25	11/12/2017	17:00 – 17:15	Supercell: -68 to -72 Adjacent storm: -60	MTS ridge	12:00 UTC K-index: 28 CAPE: 1 400 J.kg^{-1} 500 hPa LI: -4°C to -7°C	16:00	500 600 700 850 10m	40 30 25	20 20 15 5 10	250 260 280 315 310
	Panbult (east of Ermelo)	-26.60, 30.46	03/01/2020	18:15 – 19:00	Supercell: -78 to -85 Adjacent storm: -68 to -50	MTS ridge	12:00 UTC K-index: 31 CAPE: 900 J.kg^{-1} 500 hPa LI: -4°C to -7°C	16:00	500 600 700 850 10m	53 50 80	5 5 5 3 3	230 140 135 225 10
	New Hanover	-28.98, 30.84	12/11/2019	16:30 – 17:00	Supercell: -65 to -75 Adjacent storm: -40 to -44	MTS trough (well-developed)	12:00 UTC K-index: 32 CAPE: 1 800 J.kg^{-1} 500 hPa LI: -4°C to -6°C	14:00	500 600 700 850 10m	60 70 65	10 15 10 5 5	270 270 315 360 30
	Standerton	-26.90, 29.03	12/11/2016	17:30 – 18:00	Supercell: -73 to -75 Adjacent storm: -66 to -60	MTS trough (short-wave)	12:00 UTC K-index: 26 CAPE: 800 J.kg^{-1} 500 hPa LI: -4°C to -6°C	15:00	500 600 700 850 10m	55 90 48	45 40 30 10 10	270 275 280 310 315
	Rustenburg	-25.55, 27.20	01/11/2018	13:15 – 13:45	Supercell: -66 to -69 Adjacent storm: -61 to -57	MTS trough (well-developed)	12:00 UTC K-index: 32 CAPE: 700 J.kg^{-1} 500 hPa LI: -4°C to -7°C	10:00	500 600 700 850 10m	80 80 70	20 20 2 3 3	270 280 270 180 280

Table 3 (continued): Tornadic supercell with upwind thunderstorm

	Location	Latitude / Longitude	Date	Time of Event	Cloud-top Temperatures (°C)	500 to 700 hPa circulations	Tropospheric Instability	Vertical Profile				
								Time (UTC)	Level (hPa)	Moisture (%)	Speed (knot)	Direction (°)
Tornadic Supercell with Adjacent Upwind Thunderstorm	Richmond	-31.60, 24.05	17/03/2020	1500 – 15:30	Supercell: -70 to -75 Adjacent storm: -51 to -49	MTS trough (short-wave)	12:00 UTC K-index: 36 CAPE: 1 200 J.kg^{-1} 500 hPa LI: -4°C to -7°C	13:00	500 600 700 850 10m	 70 70 60	20 15 15 10 10	270 350 310 335 270
	Giyani	-23.20 30.70	28/11/2018	16:15 – 16:45	Supercell: -72 to -80 Adjacent storm: -68 to -57	MTS trough (steep)	12:00 UTC K-index: 40 CAPE: 1 200 J.kg^{-1} 500 hPa LI: -4°C to -7°C	14:00	500 600 700 850 10m	 50 45 55	5 5 10 0 5	265 265 275 0 315
	Belfast	-25.90, 30.27	26/10/2016	13:45 – 14:15	Supercell: -62 to -67 Adjacent storm: -64 to -62	MTS ridge	12:00 UTC K-index: 24 CAPE: 1 400 J.kg^{-1} 500 hPa LI: -4°C to -7°C	12:00	500 600 700 850 10m	 30 70 50	10 5 5 3 5	230 225 275 275 0
	Kempton Park	-26.00, 28.33	09/01/2018	16:15 – 16:45	Supercell: -62 to -66 Adjacent storm: -57 to -53	MTS trough (short-wave)	12:00 UTC K-index: 28 CAPE: 900 J.kg^{-1} 500 hPa LI: -4°C to -7°C SRH_{0-3km} at 15:00 UTC: -200 to-300 m^2.s^{-2}	14:00	500 600 700 850 10m	 30 50 50	10 15 10 3 5	180 230 270 330 315

Table 4: Tornadic storm influenced by intense storm across significant topography

	Location	Latitude / Longitude	Date	Time of Event	Cloud-top Temperatures (°C)	500 to 700 hPa circulations	Tropospheric Instability	Vertical Profile				
								Time (UTC)	Level	Moisture (%)	Speed (knot)	Direction (˚)
Intense storm with significant topography to the upwind of the newly-developed supercell	Mthatha	-28.79, 31.55	07/04/2018	17:30 – 18:00	Supercell: -60 to -68 Adjacent storm: -64 to -58	MTS trough (well-developed)	12:00 UTC K-index: 30 CAPE: 1 600 J.kg^{-1} 500 hPa LI: -7°C	15:00	500 600 700 850 10m	 80 75 85	10 5 5 5 5	300 270 250 315 280
	Mthatha	-28.90 31.53,	07/10/2019	16:30 – 17:00	Supercell: -50 to -55	MTS trough (steep)	12:00 UTC CAPE: 1 000 J.kg^{-1} 500 hPa LI: -4°C	15:00	500 600 700 850 10m	 75 80 95	10 30 10 5 15	280 315 290 330 260
	Utrecht	-27.67, 30.31	23/11/2019	15:00 – 15:30	Supercell: -44 to -53 Intense Upwind storm: -60 to -52	MTS ridge	12:00 UTC CAPE: 300 J.kg^{-1} 500 hPa LI: -5°C	12:00	500 600 700 850 10m	 65 55 30	15 15 10 5 10	260 260 270 315 265
	Dannhauser	-28.01, 30.06	13/12/2019	1645 – 17:15	Supercell: -50 to -55 Adjacent storm: -60 to -58	MTS ridge	12:00 UTC CAPE: 300 J.kg^{-1} 500 hPa LI: -5°C	14:00	500 600 700 850 10m	 60 90 75	15 15 10 5 5	265 260 300 50 45
	Nieu Bethesda	-31.55, 24.60	02/09/2020	01:15 – 01:45	Supercell: -47 to -50	North-east of steep COL	12:00 UTC K-index: 18 CAPE: 20 J.kg^{-1} 500 hPa LI: -3°C	00:00	500 600 700 850 10m	 80 90 85	30 40 35 10 10	320 320 355 30 15

Table 4 (continued): Tornadic storm influenced by intense storm across significant topography

	Location	Latitude / Longitude	Date	Time of Event	Cloud-top Temperatures (°C)	500 to 700 hPa circulations	Tropospheric Instability	Vertical Profile				
								Time (UTC)	Level	Moisture (%)	Speed (knot)	Direction (˚)
Intense storm with significant topography to the upwind of the newly-developed supercell	Bergville	-28.60, 29.35	14/11/2019	11:45 – 12:15	Supercell: -40 to -44	In the south-west of COL	12:00 UTC K-index: 24 CAPE: 500 J.kg^{-1} 500 hPa LI -8°C SRH_{0-3km} between 09:00 and 13:00 UCT: -150 to -300 m^2.s^{-2}	10:00	500 600 700 850 10m	 50 60 80	10 15 10 3 5	265 185 275 265 270
	Bhunywa	-26.51, 30.90	04/12/2018	13:15 – 13:45	Supercell: -65 to -74	MTS ridge	12:00 UTC 700 to 500 hPa lapse rate: 9°C/km CAPE: 2 200 J.kg^{-1} 500 hPa LI: -9°C	12:00	500 600 700 850 10m	 70 50 80	50 45 25 0 5	275 270 280 0 70
	Ulundi	-28.30, 31.43	22/11/2019	19:00 – 19:30	Supercell: -67 to -73	MTS ridge	12:00 UTC CAPE: 1 700 J.kg^{-1} 500 hPa LI: -6°C	12:00	500 600 700 850 10m	 50 65 80	10 15 15 5 5	260 265 270 45 0
	Butterworth / Nqamakwe	-32.55, 27.66	27/12/2018	13:45 – 14:15	Supercell: -71 to -75 Upwind storm: -59 to -49	MTS trough (short wave)	12:00 UTC K-index: 31 CAPE: 1 200 J.kg^{-1} 500 hPa LI: -11°C	11:00	500 600 700 850 10m	 80 60 80	30 25 20 5 5	280 280 285 30 350

Table 4 (continued): Tornadic storm influenced by intense storm across significant topography

	Location	Latitude / Longitude	Date	Time of Event	Cloud-top Temperatures (°C)	500 to 700 hPa circulations	Tropospheric Instability	Vertical Profile				
								Time (UTC)	Level	Moisture (%)	Speed (knot)	Direction (˚)
Intense storm with significant topography to the upwind of the newly-developed supercell	Waterbron (near Bloemfontein)	-29.20, 26.20	08/05/2019	16:30 – 17:00	Supercell: -56 to -60	MTS trough (steep)	12:00 UTC K-index: 26 CAPE: 300 J.kg^{-1} 500 hPa LI: -4°C	15:00	500 600 700 850 10m	75 80 70	20 15 20 10 10	275 280 275 320 315
	Magaliesburg	-25.98, 27.45	25/07/2016	14:00 – 14:30	Supercell: -53 to -58	North-east of steep COL	12:00 UTC K-index: 25 CAPE: 180 J.kg^{-1} 500 hPa LI: -7°C	12:00	500 600 700 850 10m	65 60 65	20 20 25 10 10	320 255 360 45 45
	Roodepoort	-26.12, 27.90	09/10/2017	15:15 – 15:45	Supercell: -62 to -71	North-east of steep COL	12:00 UTC K-index: 18 CAPE: 20 J.kg^{-1} 500 hPa LI: -3°C	23:00	500 600 700 850 10m	40 55 25	30 25 10 5 5	280 315 320 360 310
	Protea Glen	-26.30, 27.80	30/12/2017	16:30 – 17:00	Tornadic supercell: -69 to -72 Upwind supercell and topography: -75 to -70	MTS ridge	12:00 UTC K-index: 33 CAPE: 1 200 J.kg^{-1} 500 hPa LI: -7°C	14:00	500 600 700 850 10m	30 50 50	15 15 10 3 10	260 230 275 315 315
	Tembisa	-25.99, 28.25	26/07/2016	1500 – 15:30	Supercell: -39 to -42	North-east of steep COL	12:00 UTC K-index: 36 CAPE: 1 200 J.kg^{-1} 500 hPa LI: -7°C	13:00	500 600 700 850 10m	30 60 70	30 25 20 3 5	315 315 320 355 320

Table 4 (continued): Tornadic storm influenced by intense storm across significant topography

	Location	Latitude / Longitude	Date	Time of Event	Cloud-top Temperatures (°C)	500 to 700 hPa circulations	Tropospheric Instability	Vertical Profile				
								Time (UTC)	Level	Moisture (%)	Speed (knot)	Direction (˚)
Intense storm with significant topography to the upwind of the newly developed supercell	Delmas	-26.15, 28.55	09/10/2017	16:30 – 17:00	Supercell: -63 to -70	North-east of steep COL	12:00 UTC K-index: 18 CAPE: 0 J.kg^{-1} 500 hPa LI: -10°C $SRH_{0\text{-}3km}$ at 15:00 UTC: -50 to -100 m^2.s^{-2}	15:00	500 600 700 850 10m	 60 40 60	60 50 40 20 15	45 310 315 10 315
	Delmas	-26.13, 28.59	26/07/2016	15:30 – 16:00	Supercell: -39 to -38	North-east of steep COL	12:00 UTC K-index: 25 CAPE: 100 J.kg^{-1} 500 hPa LI: -5°C	13:00	500 600 700 850 10m	 25 70 70	25 30 70 3 70	315 315 320 10 0
	Bethulie	-30.31, 25.94	09/10/2017	16:30 – 17:00	Supercell: -35 to -41	In the south-west of COL	12:00 UTC K-index: 22 CAPE: 400 J.kg^{-1} 500 hPa LI: -3°C	12:00	500 600 700 850 10m	 60 40 15	20 40 35 0 15	325 260 265 0 320
	Bisho	-32.55, 27.66	02/12/2017	14:30 – 15:00	Supercell: -48 to -55 Intense Upwind storm: -53 to -47	In the south-west of COL	12:00 UTC K-index: 30 CAPE: 2 700 J.kg^{-1} 500 hPa LI: -11°C $SRH_{0\text{-}3km}$ between 18:00 and 21:00 UCT: -200 to -300 m^2.s^{-2}	10:00	500 600 700 850 10m	 60 55 50	45 20 15 20 5	45 270 275 275 225

Table 5: Tornadic multicell with enhanced gust front from upwind multicell

	Location	Latitude / Longitude	Date	Time of Event (UTC)	Cloud-top Temperatures (°C)	500 to 700 hPa circulations	Tropospheric Instability	Vertical Profile				
								Time (UTC)	Level	Moisture (%)	Speed (knot)	Direction (°)
Tornadic Multicell with Adjacent Upwind Thunderstorm	Ennerdale	-26.41, 27.84	14/11/2016	15:15 – 15:45	Supercell: -52 to -56	MTS ridge	12:00 UTC K-index: 25 CAPE: 1 500 J.kg^{-1} 500 hPa LI: -5°C	13:00	500 600 700 850 10m	 48 79 42	20 15 10 3 5	220 260 270 265 275
	Middleburg	-25.80, 29.70	14/11/2016	16:00 – 17:00	Tornadic multicell: -65 to -68 Upwind multicell: -73 to -67	MTS ridge	12:00 UTC CAPE: 2 200 J.kg^{-1} 500 hPa LI: -4°C	16:00	500 600 700 850 10m	 70 80 95	25 15 15 10 10	285 280 190 105 100
	Volksrust	-27.30, 29.89	09/11/2019	15:00 – 15:30	Tornadic multicell: -58 to -60 Upwind multicell: -65 to -62	MTS ridge	12:00 UTC CAPE: 700 J.kg^{-1} 500 hPa LI: -2°C	15:00	500 600 700 850 10m	 70 60 50	30 25 20 15 15	270 265 270 105 45
	Standerton	-26.93, 29.24	11/12/2017	15:30 – 15:45	Tornadic multicell: -58 to -63 Upwind multicell: -60 to -56	MTS ridge	12:00 UTC CAPE: 1 300 J.kg^{-1} 500 hPa LI: -5°C	15:00	500 600 700 850 10m	 40 70 50	60 55 40 20 15	30 265 270 300 315
	Standerton	-26.93, 29.29	10/12/2016	16:15 – 16:45	Tornadic multicell: -66 to -69 Upwind multicell: -60 to -58	MTS trough (short-wave)	12:00 UTC CAPE: 900 J.kg^{-1} 500 hPa LI: -5°C	14:00	500 600 700 850 10m	 70 60 40	40 25 20 20 10	275 270 280 90 80

Table 5 (continued): Tornadic multicell with enhanced gust front from upwind multicell

	Location	Latitude / Longitude	Date	Time of Event (UTC)	Cloud-top Temperatures (°C)	500 to 700 hPa circulations	Tropospheric Instability	Vertical Profile				
								Time (UTC)	Level	Moisture (%)	Speed (knot)	Direction (˚)
Tornadic Multicell with Adjacent Upwind Thunderstorm	Viljoenskroon	-27.23, 26.95	11/11/2016	17:00 – 17:30	Tornadic multicell: -67 to -72 Upwind multicell: -70 to -61	MTS trough (short wave)	12:00 UTC CAPE: 2 200 J.kg^{-1} 500 hPa LI: -9°C 700 to 500 hPa lapse rate: 9°C/km	15:00	500 600 700 850 10m	 40 70 50	40 45 30 20 15	275 270 280 220 315
	Bloemhof	-27.65, 25.61	04/01/2020	16:45 – 17:15	Tornadic multicell: -44 to -53 Adjacent storm: -60 to -52	MTS ridge	12:00 UTC CAPE: 300 J.kg^{-1} 500 hPa LI: -5°C	14:00	500 600 700 850 10m	 75 67 73	10 5 5 5 5	280 270 275 175 225

Table 6: Landspouts (Weak EF0 and EF1) Tornadoes

	Location	Latitude / Longitude	Date	Time of Event (UTC)	Cloud-top Temperatures (°C)	500 to 700 hPa circulations	Tropospheric Instability	Vertical Profile				
								Time (UTC)	Level	Moisture (%)	Speed	Direction (˚)
Adjacent Thunderstorm to the upwind of supercell storm	Near Oshoek	-26.22, 30.95	05/01/2019	14:15 – 14:45	Single cell: -27 to -37	Short-wave	12:00 UTC CAPE: 1 600 J.kg^{-1} 500 hPa LI: -4°C	14:00	500 600 700 850 10m	 70 80 75	20 10 10 5 5	265 240 260 10 360
	Protea Glen	-26.28, 27.90	30/10/2016	15:00 – 15:30	Tornadic single cell: -41 to -55	MTS ridge	12:00 UTC 700 to 500 hPa lapse rate: 9°C/km CAPE: 0 J.kg-1 500 hPa LI: 0°C	15:00	500 600 700 850 10m	 55 30 5	10 10 10 5 5	265 270 270 270 270
	Johannesburg	-26.20, 28.03	02/01/2020	13:15 – 13:45	Tornadic single cell: -56 to -59	Short-wave	12:00 UTC SRH_{0_3km} at 18:00 UTC: -200 to -300 m^2.s^{-1} CAPE: 800 J.kg^{-1} 500 hPa LI: -3°C	13:00	500 600 700 850 10m	 45 75 40	5 10 5 3 5	265 225 260 5 275
	Excelsior	-28.93, 27.06	13/12/2019	11:15 – 11:45	Tornadic single cell: -55 to -62	MTS ridge	12:00 UTC CAPE: 300 J.kg^{-1} 500 hPa LI: --3 °C	11:00	500 600 700 850 10m	 85 87 75	20 10 5 5 5	265 272 315 355 315
	Waterfall Valley (Woodmead)	-26.26, 27.86	09/02/2020	15:30 - 15:45	Tornadic single cell: -26 to -43	MTS ridge	12:00 UTC CAPE: 400 J.kg^{-1} 500 hPa LI: --3°C	15:00	500 600 700 850 10m	 60 90 60	5 5 5 3 5	275 270 220 185 185

Table 6 (continued): Landspouts (Weak EF0 and EF1) Tornadoes

	Location	Latitude / Longitude	Date	Time of Event (UTC)	Cloud-top Temperatures (°C)	500 to 700 hPa circulations	Tropospheric Instability	Vertical Profile				
								Time (UTC)	Level	Moisture (%)	Speed	Direction (˚)
Adjacent Thunderstorm to the upwind of supercell storm	Magaliesburg	-25.99, 27.45	13/04/2019	12:30 – 13:00	Line of convective clouds: 2 to	Short-wave	12:00 UTC CAPE: 0 J.kg^{-1} 500 hPa LI: --3°C	12:00	500 600 700 850 10m	 30 75 47	5 5 3 3 3	90 60 10 355 315
	New Hanover	-29.30, 30.80	07/01/2020	15:15 – 15:45	Tornadic single cell: -54 to -57 Upwind multicell: -58 to –66	Short-wave	12:00 UTC CAPE: 1 600 J.kg^{-1} 500 hPa LI: -5°C	15:00	500 600 700 850 10m	 15 20 45	10 5 5 5 5	355 355 330 45 80
	Grootvlei	-26.77, 28.48	16/11/2016	14:30 – 15:00	Tornadic single cell: -62 to -66	Short-wave	12:00 UTC CAPE: 1 000 J.kg^{-1} 500 hPa LI: -5°C	14:00	500 600 700 850 10m	 40 62 67	5 5 5 5 5	265 255 275 360 360
	Frankfort	-27.28, 28.50	30/11/2020	10:15 – 10:45	Tornadic single cell: -55 to -65	Short-wave	12:00 UTC CAPE: 400 J.kg^{-1} 500 hPa LI: -3°C	10:00	500 600 700 850 10m	 50 70 45	20 15 10 5 5	280 275 280 315 340

Appendix

Year and month of severe storm occurrence	Day	Start	End	Associated MTS weather circulations
2016 June	25	12:45	13:00	Cut-off low (steep)
	26	12:00	14:45	Cut-off low (steep)
		14:45	16:00	
2016 October	1	12:45	14:45	MTS trough (base)
	16	17:00	19:45	MTS trough (base)
	18	16:15	21:15	MTS ridge
	20	13:45	19:00	MTS trough (short-wave)
	21	13:00	16:00	MTS trough (short-wave)
	22	12:45	15:30	MTS trough (short-wave)
	26	11:00	12:30	MTS ridge
	27	12:00	16:45	MTS ridge
	30	14:30	14:45	MTS ridge
2016 November	10	13:00	15:45	MTS trough (short-wave)
		13:45	16:00	MTS trough (short-wave)
	12	12:00	13:45	MTS trough (base)
		12:45	17:45	
	13	13:15	15:00	MTS trough (base)
	14	13:30	15:00	MTS ridge
	15	12:00	14:45	MTS trough (short-wave)
	17	14:00	16:00	MTS trough (well-developed
	23	12:30	15:15	MTS trough (short-wave)
2016 December	1	11:15	18:45	MTS trough (base)
	6	12:45	13:45	MTS ridge
	7	12:00	13:45	MTS ridge
	9	13:30	14:45	MTS trough (short-wave)
	10	14:45	16:00	MTS trough (base)
	12	10:30	16:15	MTS ridge
	14	14:00	14:45	MTS ridge
	16	13:15	14:45	MTS ridge
		12:00	15:15	
	18	12:15	16:00	MTS ridge
		13:30	15:15	
	19	14:15	18:15	MTS ridge
	24	11:45	16:15	MTS trough (base)
	28	11:00	17:30	MTS trough (short-wave)
2017 January	1	14:00	16:00	MTS ridge
	2	14:45	17:30	MTS ridge
	6	16:30	20:15	MTS ridge
	19	13:15	15:00	MTS trough (short-wave)
	20	13:30	19:00	MTS trough (base)
	30	13:00	14:45	MTS trough (short-wave)
	31	16:15	18:15	MTS ridge

Year and month of severe storm occurrence	Day	Start	End	Associated MTS weather circulations
2017 February	7	13:45	16:00	MTS ridge
	8	14:00	18:15	MTS ridge
	15	14:15	18:00	MTS ridge
	16	19:15	20:45	MTS ridge
2017 March	7	13:45	15:15	MTS ridge
	8	14:30	19:30	MTS ridge
2017 April	6	12:00	17:00	MTS ridge
	7	11:45	16:45	MTS trough (well-developed
2017 October	8	12:45	16:00	MTS trough (well-developed)
	9	12:00	15:30	Cut-off low (steep)
		11:30	13:00	
	10	09:00	11:30	Cut-off low
2017 November	9	12:00	15:00	Cut-off low
	10	16:30	20:30	MTS trough (base)
2017 December	2	12:00	15:00	MTS trough (short-wave)
	3	15:00	17:15	MTS trough (short-wave)
	4	13:00	16:00	MTS trough (short-wave)
	5	14:00	17:15	MTS trough (short-wave)
	10	13:45	16:45	MTS trough (short-wave)
	11	12:45	17:15	MTS trough (short-wave)
		15:00	16:00	
	12	13:15	16:45	MTS trough (short-wave)
		14:45	16:45	
	23	13:30	17:00	MTS ridge
	24	16:45	20:00	MTS ridge
	29	13:30	18:30	MTS trough (short-wave)
	30	14:00	18:00	MTS trough (short-wave)
		14:30	17:30	
	31	14:45	18:00	MTS trough (short-wave)
2018 January	1	13:15	19:00	MTS trough (base)
	4	13:15	17:00	MTS trough (short-wave)
	8	12:45	18:45	MTS trough (short-wave)
	9	14:00	15:15	MTS trough (short-wave)
	12	13:30	17:00	MTS ridge
	13	16:00	17:15	MTS ridge
	14	13:45	16:00	MTS ridge
	15	14:45	17:00	MTS ridge
	24	12:45	15:15	MTS trough (short-wave)
	25	13:00	15:30	MTS ridge
	26	16:00	21:00	MTS trough (short-wave)

Appendix (Continue)

Year and month of severe storm occurrence	Day	Start	End	Associated MTS weather circulations
2018 February	1	16:30	18:15	MTS trough (short-wave)
	2	12:00	14:30	MTS ridge
	12	12:00	14:15	MTS ridge
		13:00	15:30	
		17:00	21:30	
	13	12:00	21:45	Cut-off low
2018 March	14	12:00	14:30	MTS trough (short-wave)
	27	12:45	15:30	MTS trough (short-wave)
		13:00	16:00	
	28	14:00	16:30	MTS ridge
2018 April	4	14:00	16:00	MTS trough (well-developed)
	5	16:45	17:00	MTS trough (well-developed)
		14:00	16:45	
	7			MTS trough (short-wave)
2018 May	27	14:45	18:45	MTS trough (base)
2018 September	5	12:15	14:00	MTS trough (well-developed)
	9	15:00	14:30	MTS ridge
	21	12:00	14:15	MTS ridge
	22	11:45	17:30	MTS ridge
	27	13:00	16:00	MTS ridge
	28	14:15	17:45	MTS ridge
	29	14:30	20:00	MTS ridge
2018 October	13	12:00	15:00	Cut-off low
	14	14:45	18:15	Cut-off low (steep)
	19	13:30	15:00	MTS ridge
	20	14:00	17:45	MTS ridge
2018 November	1	11:00	13:00	MTS trough
	20	12:15	16:00	MTS trough (well-developed)
	21	12:00	14:30	Cut-off lo
	27	11:00	13:15	MTS trough (well-developed)
	28	11:15	18:15	MTS trough (base)
2018 December	1	14:00	16:00	MTS ridge
	3	13:45	15:00	MTS ridge
	4	10:00	14:00	MTS ridge
		11:15	13:15	
	7	11:30	13:15	MTS ridge
	8	13:00	15:45	MTS trough (well-developed)
	13	11:45	16:30	MTS ridge
	15	13:45	18:00	MTS ridge
	26	09:15	13:00	MTS ridge

Year and month of severe storm occurrence	Day	Start	End	Associated MTS weather circulations
2018 December	27	12:00	14:45	MTS trough (short-wave)
		11:15	13:00	
	28	05:30	14:30	MTS ridge
	29	12:15	17:45	MTS ridge
2019 January	4	12:00	13:30	MTS ridge
	5	12:30	15:15	MTS trough (base)
	7	11:30	13:45	MTS ridge
	8	13:15	17:00	MTS trough (base)
	9	14:00	18:00	MTS ridge
		18:00	20:15	
	23	12:30	15:00	MTS ridge
	24	14:15	18:45	MTS ridge
	29	07:00	18:45	MTS ridge
		12:00	17:15	
	30	13:00	15:15	MTS ridge
2019 February	1	13:00	15:00	MTS trough (well-developed)
	2	13:00	15:00	Cut-off low
		14:00	18:00	
	9	15:30	18:30	MTS ridge
	20	14:45	16:45	MTS ridge
	23	15:00	21:45	MTS ridge
2019 March	3	10:45	16:00	MTS ridge
	4	17:45	21:45	MTS ridge
		19:15	24:00	
	5	00:00	01:00	MTS ridge
	13	18:15	19:30	MTS trough (short-wave)
	17	14:15	16:30	MTS ridge
	18	16:15	19:00	MTS ridge
	19	22:00	22:30	MTS ridge
	20	13:45	17:30	MTS ridge
	24	13:00	21:45	MTS ridge
		13:00	16:30	
	25	13:45	16:45	MTS ridge
2019 April	22	11:30	17:15	Cut-off low
	23	17:00	20:00	Cut-off low
	24	14:00	21:45	Cut-off low
2019 May	8	13:15	18:15	MTS trough (steep)
2019 October	7	10:30	14:00	Cut-off low (steep)
	9	10:30	12:45	MTS ridge
	10	11:00	13:30	MTS ridge

Appendix (Continue)

Year and month of severe storm occurrence	Day	Start	End	Associated MTS weather circulations
2019 November	9	12:00	19:00	MTS ridge
		12:00	15:00	MTS ridge
	10	11:00	13:45	MTS ridge
		13:00	19:00	
		13:00	19:00	
	11	14:45	16:45	MTS trough (well-developed)
	12	12:15	16:30	MTS trough (well-developed)
	13	12:45	15:00	MTS trough (well-developed)
	14	09:45	14:30	Cut-off low
	17	13:45	15:30	MTS trough (base)
	18	11:00	15:00	MTS trough (base)
	19	13:00	15:00	MTS trough (short-wave)
	20	13:00	17:15	MTS trough (short-wave)
	21	12:00	20:30	MTS ridge
	22	12:00	15:30	MTS ridge
		12:30	16:15	
		19:30	20:15	
	23	14:15	14:45	MTS ridge
	24	12:00	14:00	MTS ridge
	25	12:00	16:45	MTS ridge
	27	13:30	15:00	MTS ridge
	28	12:30	15:45	MTS ridge
2019 December	2	13:15	16:00	MTS ridge
	3	17:15	20:15	MTS ridge
	12	13:30	15:00	MTS ridge
	13	14:00	17:00	MTS ridge
	29	12:00	15:15	MTS ridge
	30	10:45	13:45	MTS ridge
2020 January	2	12:45	14:00	MTS ridge
		14:15	18:00	
		17:45	18:00	
	3	13:15	17:30	MTS ridge
		14:15	19:00	
		15:30	17:30	
	5	13:30	17:00	MTS ridge
	7	14:45	17:30	MTS trough (short-wave)
	22	14:00	15:30	MTS ridge
	24	12:30	15:45	Cut-off low
	25	16:15	18:30	MTS trough (short-wave)
	29	13:00	16:00	MTS ridge
2020 February	19	17:15	19:30	MTS ridge
	20	10:45	13:45	MTS ridge
		12:15	16:00	
		13:45	17:45	
	21	15:15	14:15	MTS ridge

Year and month of severe storm occurrence	Day	Start	End	Associated MTS weather circulations
2020 March	10	13:00	18:45	MTS trough (short-wave)
	12	11:15	15:45	Cut-off low
	16	13:45	15:00	MTS ridge
2020 April	9	13:30	17:00	MTS trough (short-wave)
	10	11:00	16:45	MTS trough (short-wave)
		13:00	19:15	
	13	14:15	16:30	MTS trough (short-wave)
	14	11:15	15:15	MTS trough (well-developed)
	15	13:15	15:15	Cut-off low
	16	13:15	16:15	MTS trough (short-wave)
	23	13:30	15:45	Cut-off low
	24	12:15	16:15	MTS ridge
2020 September	1	20:00	24:00	Cut-off low
	2	00:00	02:00	
2020 October	9	13:30	17:00	MTS trough (well-developed)
	10	14:15	17:45	Cut-off low
	21	12:15	14:30	MTS ridge
	22	14:15	17:30	MTS ridge
	24	17:45	18:00	MTS ridge
	25	13:00	15:00	MTS ridge
2020 November	17	13:45	18:00	MTS trough (well-developed)
	18	12:15	16:00	MTS trough (well-developed)
	24	12:30	16:15	MTS trough (short-wave)
		16:30	21:30	
	25	16:30	17:30	MTS trough (short-wave)
2020 December	10	17:00	20:00	MTS ridge
	11	20:00	23:00	MTS trough (short-wave)
	12	08:15	12:00	MTS trough (well-developed)
		09:00	15:00	
		09:30	11:00	
		12:30	16:00	
	21	13:00	17:45	MTS trough (short-wave)
		15:15	22:00	
		15:15	22:00	
	22	22:00	24:00	MTS trough (short-wave)
		00:00	01:15	
	23	09:00	10:15	MTS ridge
		11:15	22:00	
	24	22:00	24:00	MTS ridge
		00:00	07:00	
	28	11:45	14:45	MTS ridge
	29	10:00	15:30	MTS trough (short-wave)

Appendix (Continue)

Year and month of severe storm occurrence	Day	Start	End	Associated MTS weather circulations
2021 January	1	00:00	01:30	MTS ridge
		00:30	07:30	
		20:00	22:00	
	2	00:00	05:30	MTS ridge
	3	13:15	14:45	MTS ridge
	6	15:45	24:00	MTS ridge
	7	00:00	03:00	MTS ridge
		19:00	20:15	
	15	13:15	16:15	MTS trough (well-developed)
	16	19:00	22:00	MTS trough (well-developed)
	20	16:00	20:00	MTS ridge
	21	11:00	14:00	MTS ridge
	22	13:00	15:00	MTS ridge
	23	16:30	19:00	MTS ridge
	24	12:00	21:45	MTS ridge
	27	14:00	20:15	MTS ridge
	31	00:00	06:00	MTS trough (well-developed)
		17:30	19:00	
	1	00:00	01:00	MTS trough (well-developed)
	2	11:30	16:30	MTS trough (well-developed)
	4	12:45	21:45	MTS ridge
		15:15	21:45	
	5	00:00	04:00	MTS trough (short-wave)
	14	11:45	15:30	MTS ridge
	23	14:00	17:30	MTS ridge
		17:00	21:00	
	9	15:45	20:00	MTS ridge
	17	13:45	17:00	MTS trough (short-wave)
	21	12:00	14:45	MTS trough (short-wave)
2021 June	1	15:00	16:00	MTS ridge

References

Ackerman, S. A., and Knox, J. (2012). Meteorology: Understanding the atmosphere (3rd ed). Jones & Bartlett Learning. London (UK), p. 351.

Adamson, P. T. (1981). Southern African storm rainfall. Department of Environment Affairs. Branch of Scientific Services, TR 102, Pretoria, 8

Adedoyin, J. A., and Mphale, K. (2014). Climate variability: Its impacts and mechanism within the Kalahari transect of southern Africa. 120-135. Retrieved from https://www.researchgate.net/publication/228590836

Ahrens, C. D., and Henson, R. (2018). Essentials of meteorology: An invitation to the atmosphere (8th ed.). Cengage Learning, p. 66, 978-1-305-62845-8

AIC. (2000). The effects of thunderstorms and associated turbulence on aircraft operations. Dar es Salaam, Tanzania, p. 6 and 8.

Alcock, P. G. (2013). Snow in, or on the outskirts of Pietermaritzburg (1851–2013). Natalia, 43(2013), 73-83.

Alexander, L. S., Sills, D. M. L., and Taylor, P. A. (2018). Initiation of convective storms at low-level mesoscale boundaries in southwestern Ontario. Weather and Forecasting, 583-598. doi:10.1175/waf-d-17-0086.1

Alfahmi, F., Boer, R., Hidayat, R., Perdinan, and Sopaheluwakan, A. (2019). The impact of concave coastline on rainfall offshore distribution over Indonesian maritime continent. Scientific World Journal, #11 pages. doi:10.1155/2019/6839012

Anders, A. M., Roe, G. H., Hallet, B., Montgomery, D. R., Finnegan, N. J., and Putkonen, J. (2006). Spatial patterns of precipitation and topography in the Himalaya. Geological Society of America Special Papers, 39-53.

Apaydin, H., Anli, A. S., and Ozturk, F. (2011). Evaluation of topographical and geographical effects on some climatic parameters in the Central Anatolia Region of Turkey. International Journal of Climatology, 31(9), 1264 - 1279. doi:10.1002/joc.2154

Apsley, M., Mulder, K. J. and Schultz, D. M. (2016). Reexamining the United Kingdom's greatest tornado outbreak: forecasting the limited extent of tornadoes along a cold front. Weather and Forecasting, 31, 853-875.

Arnold, D. L. (2008). Severe deep moist convective storms: forecasting and mitigation. Geography Compass, 2(1), 30-66. doi:10.1111/j.1749-8198.2007.00069.x

Ashley, W. S., Krmenec, A. J., and Schwantes, R. (2008). Vulnerability due to nocturnal tornadoes. Weather and Forecasting, **23**, 795–807, https://doi.org/10.1175/2008waf2222132.1

Ashok, K., Guan, Z., and Yamagata, T. (2003). Influence of the Indian Ocean dipole on the Australian winter rainfall, Geophysical Research Letters, 30(15), 1821, doi:10.1029/2003gl017926.

Baidu, M., Schwendike, J., Marsham, J.H. & Bain, C. (2022). Effects of vertical wind shear on intensities of mesoscale convective systems over West and Central Africa. Atmospheric Science Letters, 23, 1-9. doi:10.1002/asl.1094

Barclay, J. J., Jury M. R., and Landman, W. (1993). Climatological and structural differences between wet and dry troughs over southern Africa in the early summer. Meteorology and Atmospheric Physics, 51, 41-54.

Barnes, G. M. (2001). Severe local storms in the tropics. In: Severe convective storms. (C. A. Doswell III, Ed.). Meteorological Monographs, American Meteorological Society, A comprehensive discussion of severe weather in the tropics, 28, 359-432.

Barnes, M. A., Ndarana, T., and Landman, W. A. (2021). Cut-off lows in the southern hemisphere and their extension to the surface. 1-39. Retrieved from https://repository.up.ac.za/bitstream/handle/2263/86956/Barnes_CutOff_2021.pdf?sequence=1

Barretta, B. S., Marin, J. C., Jacques-Coper, M. (2020). A multiscale analysis of the tornadoes of 30–31 May 2019 in south-central Chile. Atmospheric Research, 14 pages. Retrieved from https://doi.org/10.1016/j.atmosres.2019.104811

Barry, R. G. (1992). Mountain weather and climate (Second edition). Routledge (London and New York), 402.

Barry, R. G. and Chorley, R. J. (2003). Atmosphere, weather and climate (5th ed.). Taylor & Francis Group, London and New York, p. 117, 198

Barry, R. G., and Carleton, A. M. (2001). Synoptic and dynamic climatology. Routledge: Taylor & Francis Group, London and New York, p. 488

Bates, G. T. (1990). A case study of the effect of topography on cyclone development in the western United States. Monthly Weather Review, 118, 1808-1825

Benhin, J. K. (2006). Climate change and South African agriculture: Impacts and adaptation options. Centre for Environmental Economics and Policy in Africa. Pretoria: University of Pretoria.

Betten, D. P., Biggerstaff, M. I., and Ziegler, C. L. (2018). Three-dimensional storm structure and low-level boundaries at different stages of cyclic mesocyclone evolution in a high-precipitation tornadic supercell. Advavnced Meteorology, 1–24. doi:10.1155/2018/9432670

Bhavika, B. (2007). The influence of terrain elevation on lightning density in South Africa. University of Johannesburg, Johannesburg, pp. 67 and 78.

Biggerstaff, M. I., and Houze, R. A. Jr. (1991). Midlevel vorticity structure of the 10–11 June 1985 squall line. Monthly Weather Review, 3066–3079. doi:10.1175/1520-0493(1991)119<3066:MVSOTJ>2.0.CO;2

Blamey, R. C., and Reason, C. J. C. (2009). Numerical simulation of a mesoscale convective system over the east coast of South Africa. Tellus, 61A, 17-34.

Blamey, R. C., Middleton, C., Lennard, C., and Reason, C. J. C. (2016). A climatology of potential convective environments across South Africa. Climate Dynamics, 49, 2161-2178. doi:10.1007/s00382-016-3434-7

Blamey, R., and Reason, C. J. C. (2007). Relationships between Antarctic sea-ice and South African winter rainfall. Climate Research, 33, 183-193. doi:10.3354/cr033183

Blanchard, D. O. (1998). Assessing the vertical distribution of convective available potential energy. Weather and Forecasting, 13, 870-877.

Bluestein, H. B. (1985). The formation of a "landspout" in a "broken-line" squall line in Oklahoma. Preprints. 14th Conference on Severe Local Storms. American Meteorological Society, Indiapolis, 267-270.

Bluestein, H. B. (2013). Severe convective storms and tornadoes: observations and dynamics. Oklahoma: Springer-Praxis, Books in Environmental Sciences, Springer, Oklahoma, p. 213. doi.org/10.1007/978-3-642-05381-8

Bluestein, H. B. (2017). Tornadoes and Their Parent Convective Storms. Oxford Handbooks Online. doi:10.1093/oxfordhb/9780190699420.013.15

Bluestein, H. B., and Parker, S. (1993). Modes of isolated, severe convective-storm formation along the dryline. Monthly Weather Review, 121, 1354–1372

Bluestein, H. B., and Weisman, M. L. (2000). The interaction of numerically simulated supercells initiated along lines. Monthly Weather Review, 128, 3128-3149.

Bluestein, H. B., Lindsey, D. T., Bikos, D., Reif, D. W., Wienhoff, Z. B. (2019). The relationship between overshooting tops in a tornadic supercell and its radar-observed evolution. Monthly Weather Review, 147(11), 4151-4176. doi:10.1175/MWR-D-19-0159.1

Bopape, M.-J. M. (2013). Simulations of moist convection using the quasi-elastic equations. Pretoria: University of Pretoria.

Bopape, M.-J. M., Engelbrecht, F. A., Maisha, R., Chikoore, H., Ndarana, T., Lekoloane, L., Thatcher, M., Mulovhedzi, P. T., Rambuwani, G. T., and Barnes, M. A. (2022). Rainfall simulations of high-impact weather in South Africa with the Conformal Cubic Atmospheric Model (CCAM). Atmosphere, 13, 1987. https://doi.org/10.3390/atmos13121987.

Borque, P., Vidal, L., Rugna, M., Lang, T. J., Nicora, M. G., & Nesbitt, S. W. (2020). Distinctive signals in 1-min observations of overshooting tops and lightning activity in a severe supercell thunderstorm. Journal of Geophysical Research: Atmospheres, 125, #19 pages. doi:10.1029/2020jd032856

Bosart, L. F., Seimon A., Lapenta, K. D., and Dickson, M. J. (2006). Supercell tornadogenesis over complex terrain: The Great Barrington, Massachusetts, tornado on 29 May 1995. Weather and Forecasting, 21, 897-922.

Botai, C., Botai, O. J., and Adeola, A. M. (2018). Spatial distribution of temporal precipitation contrasts in South Africa. South African Journal of Science, 114(7/8). doi:10.17159/sajs.2018/20170391

Botes, Z. A. (2014). Flooding in KwaZulu-Nata: Modelling, history and future aspects. Pietermaritzburg: University of KwaZulu-Natal.

Boyer, C. H., and Dahl, J. M. (2020). The Mechanisms Responsible for Large Near-Surface Vertical Vorticity within Simulated Supercells and Quasi-Linear Storms. Monthly Weather Review, 4281–4297. doi:10.1175/mwr-d-20-0082.1

Brady, R. H., and Szoke, E. J. (1989). Nonmesoscale tornado development in northeast Colorado: Similarities to waterspout formation. Weather and Forecasting, 117, 843--856. doi:10.1175/1520-0493

Brimelow, J. (2018). Hail and hailstorms. Oxford Research Encyclopedia, 1-58. doi:10.1093/acrefore/9780190228620.013.666

Brooks, H. (2004). On the environments of tornadic and nontornadic mesocyclones. Weather and Forecasting, 9, 606–618.

Brown, M. C., Nowotarski, C. J., Dean A. R., Smith, B. T., Thompson, R. L. and Peters, J. M. (2021). The early evening transition in south-eastern U.S. tornado environments. Weather and Forecasting, 1431-1452. doi:10.1175/waf-d-20-0191.1

Bunkers, M. J. Hjelmfelt, M. R., and Smith, P. L. (2006). An observational examination of long-lived supercells. Part I: Characteristics, evolution, and demise. Weather and forecasting, 21, 673-688.

Byers, H. R., and Rodebush, H. R. (1948). Causes of thunderstorms of the Florida Peninsula. Journal of Meteorology, 5, 275-280.

Caplan, S. J., Bedard, A. J., and Decker, M. T. (1990). The 700–500 mb lapse rate as an index of microburst probability: An application for the thermodynamic profilers. Journal of Applied Meteorology, 29(8), 680-687. doi:10.1175/1520-0450(1990)029<0680:tmlraa>2.0.co;2

Caruso, J. M., and Davies, J. M. (2006). Tornadoes in nonmesocyclone environments with preexisting vertical vorticity along convergence boundaries. Electronic Journal of Operational Meteorology, 1-36.

Changnon, S. A. (1999). Impacts of 1997-98 El Niño-generated weather in the United States. 80(99), 1819-1828. doi:10.1175/1520-0477(1999)080<1819:ioenog>2.0.co;2

Chavas, D. R., and Dawson II, D. T. (2020). An idealized physical model for the severe convective storm environmental sounding. Journal of the Atmospheric Sciences, 78, 653-670.

Chikoore, H., Bopape, M.-J. M., Ndarana, T., Muofhe, T. P., Gijben, M., Munyai, R. B., Manyanya, T. C., Maisha, R. (2021). Synoptic structure of a sub-daily extreme precipitation and flood event in Thohoyandou, north-eastern South Africa. Weather and Climate Extremes, 33(2021), #17 pages. doi:https://doi.org/10.1016/j.wace.2021.100327

Chivangulula, F. M., Amraoui, M., and Pereira M. G. (2023). The drought regime in southern Africa: A systematic review. Climate, 11(7), 1-23. doi.org/10.3390/cli11070147

Chuang, M.-T., Chiang, P.-C., Chan, C.-C., Wang, C.-F., Chang, E.-E. and Lee, C.-T. (2008). The effects of synoptical weather pattern and complex terrain on the formation of aesorol events in the Greater Taipei area. 399(1-3), 128-146. doi:10.1016/j.scitotenv.2008.01.051

Cintineo, J. L., Pavolonis, M. J., Sieglaff, J. M., and Lindsey, D. T. (2014). An empirical model for assessing the severe weather potential of developing convection. Weather and Forecasting, 639-653. doi:10.1175/waf-d-13-00113.1

Clark, T. J., 1988: The Lubbock tornado: an elevated mixed layer case study. MSc thesis, Department of Geosciences, Texas Tech University, p. 192.

Clark, M. R., and Webb, J. D. C. (2013). A severe hailstorm across the English Midlands on 28 June 2012. Weather, 68(11), 1-8

Coffer, B. E., Parker, M. D., Thompson, R. L., Smith, B. T. and Jewell, R. E. (2019). Using near-ground storm relative helicity in supercell tornado forecasting. Weather and Forecasting, Volume 34(Number 5), 1417-1435. Retrieved from https://doi.org/10.1175/waf-d-19-0115.1

Cohuet, J. B., Romero, R., Santaner, V. H., Ducrocq, V. and Ramis, C. (2011). Initiation of a severe thunderstorm over the Mediterranean Sea. Atmospheric Research, 100(4), 603-620. doi:10.1016/j.atmosres.2010.11.002

Colby Jr., F. P., and Walker, B. E. (2004). Tornadoes from elevated convection. University of Massachusetts Lowell, Lowell, MA 01854, 7A.8. 1-18.

Corlett, R. T. (2013). Where are the Subtropics? Biotropica, 45(3), 273-275. doi:10.1111/btp.12028

Cotton, W. R., and Anthes, R. A. (1989). Storms and cloud dynamics. Academic Press, San Diego, p. 220.

Cotton, W. R., Bryan, G. H., and Van den Heerver, S. C. (2011). Storm and cloud dynamics: The dynamics of clouds and precipitating mesoscale systems (2nd ed.). Academic Press, International Geophysics, 99, p. 313, 9780120885428.

Cox, J. D. (2000). Weather for dummies. Wiley Publishing, Inc., Indianapolis, Indiana, 204-205, 978-0-7645-5243-4

Craven, J. P. and Brooks, H. E. (2004). Baseline climatology of sounding derived parameters associated with deep, moist convection. National Weather Digest, 28, 13–24.

D'Abreton, P. (1991). A synoptic characterization of some South African tornadoes. South African Journal of Science, 87, 56-61.

Davies, J. M., and Guyer, J. L. (2004). A preliminary climatology of tornado events with closed cold core 500 mb lows in the central and eastern United States. Preprints, 22d Conf. on Severe Local Storms, Hyannis, MA, American Meteorological Society, CD-ROM, 7B.4.

Davies-Jones, R. P., Burgess, D. W., and Foster, M. (1990). Test of helicity as a tornado forecast parameter. 16th Conference on Severe Local Storms. American Meteorological Society, Kananaskis Park, Canada. 588-592.

De Boer, A. M., Collier, A. B., and Rodrigo Caballero, R. (2013). Processes driving thunderstorms over the Agulhas Current. Journal of Geophysical Research: Atmospheres, 118, 2220-2228. doi:10.1002/jgrd.50238

De Coning, E., Adam, B. F., Goliger, A. M., and Van Wyk, T. (1999). An F3 tornado in Heidelberg, South Africa on 21 October 1999. #8 pages.

De Coning, E., and Adam. B. F. (2000). The tornadic thunderstorm events during the 1998-1999 South African summer. Water SA, 26(3), 361-376.

De Coning, E., Gijben, M., Maseko, B., and Van Hemert, L. (2015). Using satellite data to identify and track intense thunderstorms in South and southern Africa. South African Journal Science, 111(7/8). Retrieved from http://dx.doi.org/10.17159/sajs.2015/20140402

De Oliveira, M. I., De Santa-Maria, F., Maria, S., Nascimento, E. L., Ferreira, V., Lopes, M. M., and Figueiredo, E. L. D. (2016). A left-moving, cyclonic supercell in southern Brazil: radar data analysis and atmospheric environment. 28th Conference on Severe Local Storms. doi:https://ams.confex.com/ams/28SLS/webprogram/Paper300453.html

De Villiers, M. P. (1997). The Rosettenville Storm (1996-10-23). Pretoria: South African Weather Bureau.

De Villiers, M. P. and Van Heerden, J. (2007). Dust storms and dust at Abu Dhabi International Airport. #5 pages.

De Vos, M., Vichi, M. and Rautenbach, C. (2021). Simulating the coastal ocean circulation near the Cape Peninsula using a coupled numerical model. Journal of Marince Science Engeneering, 9, 1-30. doi:10.3390/jmse9040359

Dean, R. A., and Schneider, S. R. (2008). Forecast challenges at the NWS Storm Prediction Center relating to the frequency of favorable severe storm environments. 24th Conference on Severe Local Storms, Savannah, GA, Amer. Meteor. Soc., 9A.2, https://ams.confex.com/ams/24SLS/webprogram/Paper141743.html.

Dedekind, Z., Engelbrecht, F. A. and Van der Merwe, J. (2016). Model simulations of rainfall over southern Africa and its eastern escarpment. Water SA, 42(1), 129-143.

Dieppois, B., Rouault, M., and New M. (2015). The impact of ENSO on southern African rainfall in CMIP5 ocean atmosphere coupled climate models. Climate Dynamics, 45, 2425-2442. doi:10.1007/s00382-015-2480-x

DMSLP. (2007). Severe weather compound disaster: June 2007 cut-off lows and their consequences in the West Coast, South Africa. Cape Town: Provincial Disaster Management Centre, Western Cape.

Doswell III, C. A., Brooks, H. E., and Maddox, R. A. (1995). Flash flood forecasting: An ingredients-based methodology. #34 pages.

Doswell III, C. A., Caracena, F. and Magnano, M. (1985). Temporal evolution of 700-500-mb lapse rate as a forecasting tool - A case study. 14th Conference on Severe Local Storms (pp. 398-401). Indianapolis: American Meteorological Society.

Dryden, H.L. & Hill, G.C. (1926). Wind Pressures on Structures. Scientific Papers of the Bureau of Standards. No. S523. 20, 697-732.

Duba, C. T. (2015). Wind-wave interactions, density stratification and double diffusive convection rotating flows. Pietermaritzburg: University of KwaZulu-Natal. Retrieved from http://hdl.handle.net/10413/13494

Dube, L. and Jury, M. (2000). The nature of climate variability and impacts of drought over KwaZulu-Natal, South Africa. South African Geographical Journal, 82(2), 44-53.

Durán-Quesada, A. M., Reboita, M., and Gimeno, L. (2012). Precipitation in tropical America and the associated sources of moisture: a short review. Hydrological Sciences Journal, 57(4), 612–624.

Dyson, L. L. (2013). Atmospheric thermodynamics and circulation associated with heavy rainfall over the Gauteng Province, South Africa. Pretoria: University of Pretoria.

Dyson, L. L. (2014). A heavy rainfall sounding climatology over Gauteng, South Africa, using self-organising maps. #30 pages.

Dyson, L. L., Van Heerden J., and Summer, P. D. (2015). A baseline climatology of sounding-derived parameters associated with heavy rainfall over Gauteng, South Africa. International Journal of Climatology, 35(1), 114-127. Retrieved from https://doi.org/10.1002/joc.3967

Eastlund, B, J. and Jenkins, L. M. (2000). Concept for disrupting tornado formation with space solar power. doi:10.1061/40479(204)129

Edwards, R. and Thompson, R. L. (2000). RUC-2 supercell proximity soundings, Part II: An independent assessment of supercell forecast parameters. 20th AMS Conference on Severe Local Storms. Orlando: Preprints.

Engelbrecht, E. H. Landman, W. A., Landman, S. (2022). The Impact of High-Resolution Soil Moisture States on Short-Term Numerical Weather Prediction of Convective Initiation over South Africa. #29 pages

Engelbrecht F. A., Rautenbach C. J. de W, McGregor J. L. and Katzfey J. J. (2002). January and July climate simulations over the SADC region using the limited-area model DARLAM. Water SA, 28, 361-374.

Engelbrecht, C. J. (2015). Meteorological analysis of four severe weather events in the Western Cape, Agricultural Research Council, Institute for Soil, Climate and Weather, Pretoria.

Engelbrecht, F. A., and Rautenbach, C. J. de W. (2000). Perspective for nested climate modelling over southern Africa. South African Academy for Science and Arts, 19(2), 47-51.

Engelbrecht, F. A., Landman, W. A., Engelbrecht, C. J., Landman, S., Bopape, M. M., Roux, B., McGregor, J. L., and Thatcher, M. (2011). Multi-scale climate modelling over southern Africa using a variable-resolution global model. Water SA, 37(5), 647-658. doi:0.4314/wsa.v37i5.2

Engelbrecht, F., and Landman, W. (2010). A brief description of South Africa's present-day climate. South African Risk and Vulnerability Atlas (SARVA), p. p. 1.

Engelbrecht, F., Adegoke, J., Bopape, M.-J., Naidoo, M., Garland, R., Thacher, M., McGregor, J., Katzfey, J. Werner, M., Ichoku, C., and Gatebe, C. (2015). Projections of rapidly rising surface temeratures over Africa under low mitigation. Environmental Research Letters. :10.1088/1748-9326/10/8/085004

Ernest, J., and Matson, M. (1983). A Mediterranean tropical storm? Weather, 38, 332-337.

Esau, I. a. (2012). Wind climate in Kongsfjorden, Svalbard, and attribution of leading wind driving mechanisms through turbulence-resolving simulations. Advances in Meteorology, 2012, #16 pages. doi:10.1155/2012/568454

Estie, K. E. (1984). Forecasting the formation and movement of coastal lows. Paper presented at the Coastal Low Workshop, Simonstown, 17-27.

Evans, J. L. (1992). Comment on “Can existing climate models be usedto study anthropogenic changes in tropical cyclone climate?”. Geophysical Research Letters, 19, 1523-1524.

Fan, L., Shin, S. I., Liu, Z., Liu, Q. (2016). Sensitivity of Asian Summer Monsoon precipitation to tropical sea surface temperature anomalies. Climate Dynamics, 47(7), 2501–2514.

Favre, A., Hewitson, B., Lennard, C., and Cerezo-Mota, R. (2013). Cut-off Lows in the South Africa region and their contribution to precipitation November 2013. Climate Dynamics, 41(9-10), 2331-2351. doi:10.1007/s00382-012-1579-6

Feldman, M., Gabella, M., Hering, A., and Berne, A. (2022). Hailstorms and rainstorms versus supercells - a regional analysis of convective storm types in the Alpine region. Climate Dynamics, 1-15. doi:10.21203/rs.3.rs-1666457/v1

Fitchett, J. (2018). Recent emergence of CAT5 tropical cyclones in the South Indian Ocean. South African Journal of Science, 114, #6 pages. doi:10.17159/sajs.2018/4426

Flack, D. L. A., Gray, S. L., Plant, R. S., Lean, H. W., and Craig, G. C. (2018). Convective-scale perturbation growth across the spectrum of convective regimes. Monthly Weather Review, 146, 387–405. doi:10.1175/MWR-D-17-0024.1

Fox-Hughes, P., Barnes-Keoghan, I., and Porter., A. (2018). Observations of a tornado at an automatic weather station in northern Tasmania. Journal of Southern Hemisphere Earth Systems Science, 68, 215-230. doi:10.22499/3.6801.012

Freiman, M. T. and Tyson, P. D. (2000). The thermodynamic structure of the atmosphere over South Africa: Implications for water vapour transport. Water SA, 26(2), 153-158.

Fujita, T. T. (1965). Formation and steering mechanisms of tornado cyclones and associated hook echoes. Monthly Weather Review, 93, 67-78.

Gao, J., Ge, G., and Xue, M. (2013). Impact of a diagnostic pressure equation constraint on tornadic supercell thunderstorm forecasts initialized using #DVAR radar assimilation. Advances in Meteorology, 2013. Retrieved from http://dx.doi/10.1155/2013/947874

Garstang, M., Kelbe, B. E., Emmitt, G. D., and London, W. B. (1987). Generation of convective storms over the escarpment of northeastern South Africa. Monthly Weather Review, 429-443.

Gbambie, A. S. B., and Steyn, D. G. (2012). Sea breezes at Cotonou and thier interaction with the West African moonsoon. *International Journal of Climatology* , #11 pages. doi:10.1002/joc.3637

Ge, X. Y., Li, T., and Peng, M. (2013). Effects of vertical shears and midlevel dry air on tropical cyclone developments. Journal Atmospheric Science, 70, 3859-3875.

Gialletti, A, and Alvar-Beltrán, J. (2023). SDG 17: Partnerships for the goals. In: United in Science 2023. ResearchGate. Retrieved from https://www.researchgate.net/publication/373993402

Gijben, M. (2012). The lightning climatology of South Africa. South African Journal of Science, 108(3/4), #10 pages. doi:10.4102/sajs.v108i3/4.740

Gijben, M., and De Coning, E. (2017). Using satellite and lightning data to track rapidly developing thunderstorms in data sparse regions. Atmosphere, 8(4), #15 pages. doi:10.3390/atmos8040067

Gill, A. (1982). Atmosphere-Ocean Dynamics. Academic Press, New York, p. 96.

Gill, T. (2008). Initial steps in the development of a comprehensive lightning climatology of South Africa. Johannesburg: University of the Witwatersrand.

Gimeno, L., Dominguez, F., Nieto, R., Trigo, R., Drumond, A., Reason, C. J., Taschetto, A. S., Ramos, A. M., Kumar, R., and Marengo, J. (2016). Major mechanisms of atmospheric moisture transport and their role in extreme precipitation events. Review of Environment and Resources, 41, 117– 141.

Godoy, A. A., Possia, N. E., Campetella, C. M., amd Skabar, Y. G. (2011). A cut-off low in southern South America: dynamic and thermodynamic processes. Revista Brasileira de Meteorologia, 26(4), 503-514. doi:10.1590/S0102-77862011000400001

Goliger, A. and Retief, J. V. (2007). Severe wind phenomena in Southern Africa and the related damage. Journal of Wind Engineering and Industrial Aerodynamics, 95(9-11). doi:10.1016/j.jweia.2007.01.029

Goliger, A. M., Milford, R. V., Adam, F., Edwards, M. (1997). Inkanyamba—tornadoes in South Africa. Pretoria, South Africa: Joint publication of the CSIR and the SA Weather Bureau. 10.

Grab, S., Linde, J., and De Lemos, H. (2017). Some attributes of snow occurrence and snowmelt/sublimation rates in the Lesotho Highlands: environmental implications. WaterSA, 43(2). doi:10.4314/wsa.v43i2.16

Gray, W. M. (1968). Global view of the origin of tropical disturbances and storms. Monthly Weather Review, 96(10), 669-700.

Grazulis, T. P. (2003). The tornado: Nature's ultimate windstorm. University of Oklahoma Press and Edith Gaylord Harper, Oklahoma, p. 70

Gultepe, I., Heymsfield, A. J. Field, P. R. and Axisa, D. (2017). Ice-phase precipitation. Meteorological Monographs, 6, #6 pages. doi:10.1175/amsmonographs-d-16-0013-1

Gutierrez, R. E. (2019). Environmental and radar characteristics of gargantuan-hail-producing storms. M.S. thesis, Department of Meteorology and Atmospheric Science, The Pennsylvania State University, p. 68. https://etda.libraries.psu.edu/catalog/17162rzg85.

Haberlie, A. M., Ashley, W. S., Battisto, C. M., and Gensini, V. A. (2022). Thunderstorm activity under intermediate and extreme climate change scenarios. Geophysical Research Letters, #11 pages. doi:10.1029/2022gl098779

Hand, W. H., and Cappelluti, G. (2011). A global hail climatology using the UK Met Office convection diagnosis procedure (CDP) and model analyses. Meteorological Applications, 18, 446–458. doi:10.1002/met.236

Harrison, M. S. (1984). A generalized classification of South African rain-bearing synoptic systems. Journal of Climatology, 4, 547-560. doi:10.1002/joc.3370040510

Harrison, M. S. (1986). A synoptic climatology of South African rainfall variations. PhD thesis, University of the Witwatersrand, Johannesburg.

Hart, N. C. (2012). Synoptic-scale rainfall patterns over southern Africa: scale-interactions with large-scale modes of variability. Cape Town: University of Cape Town.

Hart, N. C. G., Reason, C. J. C., and Fauchereau, N. (2010). Tropical-extratropical interactions over southern Africa: Three cases of heavy summer season rainfall. Monthly Weather Review, 138, 2608-2623. doi:10.1175/2010mwr3070.1

Hart, N. C. G., Reason, C. J. C., and Fauchereau, N. (2013). Cloud bands over southern Africa: Seasonality, contribution to rainfall variability and modulation by the MJO. Climate Dynamics, 41(5-6), doi: doi:10.1007/s00382-012-1589-4

Hersbach, H., Bell, B., Berrisford, P., Hirahara, S., Horányi, A.,Muñoz-Sabater, J., Nicolas, J., Peubey, C., Radu, R., Schepers, D., Simmons, A., Soci, C., Abdalla, S., Abellan, X., Balsamo, G., Bechtold, P., Biavati, G., Bidlot, J., Bonavita, M., De Chiara, G.,Dahlgren, P., Dee, D., Diamantakis, M., Dragani, R., Flemming,J., Forbes, R., Fuentes, M., Geer, A., Haimberger, L., Healy, S., Hogan, R.J., Hólm, E., Janisková, M., Keeley, S., Laloyaux, P., Lopez, P., Lupu, C., Radnoti, G., De Rosnay, P., Rozum, I., Vam-borg, F., Villaume, S. and Thépaut, J.-N. (2020). The ERA5 global reanalysis. Quarterly Journal of the Royal Meteorological Society,146, 1999–2049. https://doi.org/10.1002/qj.3803.

Heydenrych, C. M. (1987). A climatology of the coastal low in the SW Cape. Cape Town: University of Cape Town.

Hlalele, B. M. (2015). From fulminology to human safety: A case of N8 road South Africa. International Journal of Emergency Mental Health and Human Resilience, Volume 18(Number 1), 737-741.

Holley, D. M., Dorling, S. R., Steele, C. J., Earl, N. (2014). A climatology of convective available potential energy in Great Britain. International Journal of Climatology, 34(14), 3811-3824. doi:10.1002/joc.3976

Holton, J. (2004). An introduction to dynamic meteorology (4th ed), Elsevier Academic Press, Amsterdam, 88, p. 55, ISBN: 0-12-354015-1

Holton, J. R. (1972). An introduction to dynamic meteorology. Academic Press. New York; London, pp. 55 and 66.

Holton, J. R. (1979). An introduction to dynamic meteorology (2nd Ed). Academic Press. New York; London, p. 33.

Houston, A. L., and Niyogi, D. (2007). The sensitivity of convective initiation to the lapse rate of the active cloud-bearing layer. Monthly Weather Review, 135, 3013-3032.

Houston, A. L., and Wilhelmson, R. B. (2006). Observational analysis of the 27 May 1997 Central Texas tornadic event. Part I: Prestorm environment and storm maintenance/propagation. Monthly Weather Review, 135, 701-726.

Houze Jr., R. A. (1993). Cloud Dynamics. Academic Press, Inc., International Geophysics, California, p. 326, 0-12-356881-1

Houze, Jr. R. A. (2014). Cloud dynamics (2nd ed.). International Geophysics, Academic Press, 104, p. 103, 9780123742667

Houze, R. A., Schmid W., Fovell R. G., and Scheiesser H.-H. (1993). Hailstorms in Switzerland: left movers, right movers and false hook. Monthly Weather Review, 121, 3345-3370.

How to draw, shade, and colour a mountain range. [Online]. Available: http://www.fantasticmaps.com/2015/01/how-to-draw-shade-and-colour-a-mountain-range/ [10 March 2024].

Huang, M. J., Chen, M. Y., Pan, N., Feng, J. Q., and Yue, H. Y. (2017). Multi-source data analyses of processes of a squall line and the gale weather with heavy hails before squall line. Journal of Geoscience and Environmental Protection, 5, 27-40. doi:10.4236/gep.2017.58004

Hunter, I. T. (1987). The weather of the Agulhas Bank and the Cape South Coast. MSc dissertation, University of Cape Town, Cape Town.

Hyndman, D. W., and Hydman, D. W. (2014). Natural Hazards and Disasters. Nature. Brooks/Cole, Cengage Learning, p. 82, ISBN: 9780357701898

Jacobs, T. L. (2017). A meteorological analysis of extreme flood events in the southern parts of the Eastern Cape, South Africa. Grahamstown (Makhanda): Rhodes University.

Jay, S. (2009). Wind shear - poses challenges and dangers at the most critical stages of flight. Vaisala: Application Note, 1-6.

Jayaratne, E. R., and Ramachadran, V. (1998). A five-year study of lightning activity using a CGR3 flash counter in Gaborone, Botswana. Meteorol Atmos Phys (edit), Volume 66, 235-241. doi:10.1007/bf01026636.

Jayaratne, E.R. and Keleshov, Y. (2006). The relationship between lightning activity and surface wet-bulb temperature and its variation with latitude in Australia. Met. Atmos. Phys., 91, 17-24.

Johns, R. H., and Doswell III, C. A. (1992). Severe local storms forecasting. Weather and Forecasting, Volume 7(Number 4), 588-612.

Johns, R. H., Davies, J. M., and Leftwich, P. W. (1993). Some wind and instability parameters associated with strong and violent Tornadoes: 2. Variations in the combinations of wind and instability parameters (Vol. 79). (C. B.-J. Church, Ed.) Geophysical Monograph Series. doi:10.1029/gm079p0583

Johnson, A. (2002). A study of various thermodynamic and wind variables associated with tornadic supercells exhibiting atypical motion. Volume 26, 16 pages. Retrieved from https://digitalcommons.unl/usdeptcommercepub/32

Joubert, L. S. (2008). Boiling point: People in a changing climate. Johannesburg: Wits University Press.

Jung, E. and Kirtman, B. P. (2016). Can we predict seasonal changes in high impact weather in the United States? Environmental Research Letters, 11, #8 pages. doi:10.1088/1748-9326/11/7/07/074018

Jury, M. (1984). Wind Shear and Differential Upwelling Along the SW Tip of Africa. University of Cape Town. Cape Town, pp. 2 and 11.

Kaluza, T., Kunkel, D., and Hoor, P. (2021). On the occurrence of strong vertical wind shear in the tropopause region: a 10-year ERA5 northern hemispheric study. Weather Climate Dynamics, 2(3), 631-651. doi:10.5194/wcd-2-631-2021

Kaufmann, L., Marcolli, C., Hofer, J., Pinti, V., Hoyle, C. R. and Peter, T. (2016). Ice nucleation efficiency of natural dust samples in the immersion mode. Atmospheric Chemistry and Physics, 16(17), 11177-11206. doi:10.5194/acp-16-11177-2016

Kemp, C. (2018, Feb 15). Stof in Boesmanland het doodgerëen. Beeld, p. 12.

Kerns, B. W., and Chen, S. S. (2015). Subsidence warming as an underappreciated ingredient in tropical cyclogenesis. Part I: Aircraft observations. Journal of the Atmospheric Sciences, 4237-4260. doi:10.1175/jas-d-14-0366.1

Keshishian, L. G., and Bosart, L. F. (1987). A case study of extended East Coast frontogenesis. Monthly Weather Review, 100-117.

Kelley, D. I., Bistinas, I., Whitley, R., Burton, C., Marthews, T. R., and Dong, N. (2019). How contemporary bioclimatic and human controls change global fire regimes, Nature Climate Change, 9, 690–696, https://doi.org/10.1038/s41558-019-0540-7

Kessler, E. (1982). Thunderstorm morphology and dynamics. US Department of Commerce, USA.

Kimambo, O. N. (2018). Tornadoes in South Africa: An overview with a case study. Preprints, 1-13. doi:10.20944/preprints201811.0547.v2

King, J. R., Parker, M. D., Sherburn, K. D., and Lackmann, G. M. (2017). Rapid evolution of cool season, low-CAPE severe thunderstorm environments. Weather Forecasting, 32, 763–779. doi:10.1175/waf-d-16-0141.1

Kirchoffer, P. J. (1986). Analyzed potential vorticity fields for explosive and non-explosive cyclogenesis events during FGGE 1986. Thesis collection, California. Retrieved from http://hdl.handle.net/10945/21668

Klein, S. A., Soden, B. J., and Lau, N.-C. (1999). Remote sea surface temperature variations during ENSO: Evidence for a tropical atmospheric bridge. Journal of Climate, 917-932. doi:10.1175/1520-0442(1999)012<0917:RSSTVD>2.0.CO;2

Klemp, J. B. (1987). Dynamics of tornadic thunderstorms. Annual Review of Fluid Mechanics, 19, 369-402.

Knapp, D. I. (1994). Using cloud-to-ground lightning data to identify tornadic thunderstorm signatures and nowcast severe weather. National Weather Digest, 19, 35-42.

Knippertz, P. (2004). A simple identification scheme for upper-level troughs and its application to winter precipitation variability in Northwest Africa. Journal Climate, 17, 1411-1418.

Koletsis, I., Giannaros, T. M., Lagouvardos, K., and KotroniI, V. (2016). Observational and numerical study of the Vardaris wind regime in northern Greece. Atmospheric Research, 171, 107–120. doi:10.1016/j.atmosres.2015.12.011

Koletsis, I., Langouvrados, K., Kotroni, V., and Bartzokas, A. (2010). The interaction of northern wind flow with the complex topography of Crete Island-Part 2: Numerical study. Natural Hazards and Earth System Sciences, 10(6), 1115-1127. doi:10.5194/nhess-10-1115-2010

Kossin, J. P., Emanuel, K. A., Vecchi, G. A. (2014). The poleward migration of the location of tropical cyclone maximum intensity 2014. Nature, 509(7500), 349-52. doi:10.1038/nature13278

Kruger, A C, Goliger, A M, Retief, J. V., and Sekele, S. (2010). Strong wind climatic zones in South Africa. Wind & Structures Journal, 13(1), 37-55.

Kruger, A. C.,Pillay, D. L., and Van Staden, M., . (2016). Indicative hazards profile for strong winds in South Africa. South African Journal of Science, 112(1/2), 1-11. Retrieved from http://dx.doi.org/10.17159/sajs.2016/20150094

Landman, S., Engelbrecht, F. A., Engelbrecht, C. J., Dyson, L. L., and Landman, W. A. (2012). A short-range weather prediction system for South Africa based on a multi-model approach. Water SA, 38(5), 765-774. doi:10.4314/wsa.v38i5.16

Landman, W. A., and Tennant, W. (2000). Statistical downscaling of monthly forecast. International Journal of Climatology, 20(13), 1521-1532. doi:10.1002/1097-0088(20001115)20:13<1521:aid-joc558>3.0.co;2-n

Landman, W. A., Nkabinde, D., and Barnes, M. (2021). Synoptic-scale circulation and vorticity in mid-latitudes. Dynamic meteorology course. University of Pretoria.

Lee, B. D., Finley C. A., and Karstens, C. D. (2012). The Bowdle, South Dakota, cyclic tornadic supercell of 22 May 2010: Surface analysis of rear-flank downdraft evolution and multiple internal surges. Monthly Weather Review, Volume 140, 3419-3441. doi:10.1175/mwr-d-11-00351

Lee, B. D., Jewett, B. F., and Wilhelmsom, R. B. (2006). The 19 April 1996 Illinois tornado outbreak. Part II: Cell mergers and associated tornado incidence. Weather and Forecasting, 449-464.

Lee, S. H., Williams, P. D., and Frame, T. H. A. (2019). Increased shear in the North Atlantic upper-level jet stream over the past four decades. Nature Research, 572(7771), 1-4. doi: 10.1038/s41586-019-1465-z

Lee, S.-K., Wittenberg, A. T., Enfield, D. B., Weaver, S. J., Wang, C., & Atlas, R. (2016). US regional tornado outbreaks and their links to spring ENSO phases and North Atlantic SST variability. Environmental Research Letters, 11.

Lei, L., Chan, P. W. and Tse, S. M. (2017). Observation and simulation of mountain wave trains in a tropical cyclone situation. Quarterly Journal of Meteorology, Hydrology and Geophysics, 68(2), 253-26o. Retrieved from https://doi.org/10.54302/mausam.v68i2

Lekoloane, L. E., Bopape, M.-J. M., Rambuwani, T. G., Ndarana, T., Landman, S., Mofokeng, P., Gijben, M., and Mohale, N. (2021). A dynamic and thermodynamic analysis of the 11 December 2017 tornadic supercell in the Highveld of South Africa. Weather and Climate Dynamics, 2(2), 373-393. doi:10.5194/wcd-2-373-2021

Lengoasa, J. R. (1988). Surface temperature fields and circulation variations over southern Africa. 41-47. doi:10.1080/03736245.1991.9713547

Lengoasa, J. R., Lindsay, J. A. and Van Nierop, A. M. (1993). The influence of a synoptic-scale disturbance on topographically induced boundary layer circulations over the central Namib Desert. 18(2), 71-78.

Lennard, C. (2014). Simulating an extreme wind event in a topographically complex region. Boundary-Layer Meteorology, 153, 237–250.

Lepore, C. Tippett, M. K., and Allen, J. T. (2017). ENSO-based probabilistic forecasts of March-May U. S. tornado and hail activity. Geophysical Research Letters, 9093-9101. doi:10.1002/2017gl074781

Letsie, M. M., and Grab, S. W. (2015). Assessment of social vulnerability to natural hazards in the Mountain Kingdom of Lesotho. Mountain Research and Development, 35(2), 115-125, http://dx.doi.org/10.1659/mrd-journal-d14-00087-1

Liesker, C. G., Dyson, L. L., and Becker, E. H. (2024). Characteristics of warm season left-moving supercells over the Highveld South Africa. Atmospheric Research, 300. doi:10.1016/j.atmosres.2024.107234

Lin, D., Sorathia, K., Wang, W., Merkin, V., Bao, S., and Pham, K. (2021). The role of diffuse electron precipitation in the formation of subauroral polarization streams. Journal of Geophysical Research: Space Physics, 126(12). doi:10.1029/2021JA029792

Ludlam, F. H. 1963. Severe local storms, a review. Meteorological Monographs, American Meteorological Society, 5(27), 1.

Lynch, S. D. (2004). Development of a raster database of annual, monthly and daily rainfall for southern Africa. Pietermaritzburg: Water Research Commission.

Mahomed, M. (2020). Detection and early warning of lightning and extreme storm events in KwaZulu-Natal. Phd thesis, Pietermaritzburg: University of KwaZulu-Natal.

Maisha, T. R. (2014). The influence of topography and model grid resolution on extreme weather forecasts over South Africa. Pretoria: University of Pretoria. doi:http://hdl.handle.net/2263/43159

Majodina, M. (2002). La Niña and its impacts in South Africa during 1998-2000: In: Glantz, M. H. (ed.) (2002). La Niña and its impacts: Facts and speculation.

Majodina, M., and Jury, M. R. (1996). Composite winter cyclones south of Africa. South African Journal of Marine Science, 17(1), 241-252.

Malala, R. (2007, unpublished). The impact of weather on aviation accidents. #6 pages. Retrieved from https://www-cdn.eumetsat.int/files/2020-04/pdf_conf_p48_s2a_07_malala_v.pdf

Mandal, T. K. (2017). Loss of crop yields in India due to surface ozone: an estimation based on a network of observations. Environ. Sci. Pollut. Res., 24, 20972–20981. doi:10.1007/s11356-017-9729-3

Markowski, P. M. (2001). Hook echoes and rear-flank downdrafts: A review. Monthly Weather Review, 130, 852-876.

Markowski, P. M., Straka, J. M., Rasmussen, E. N., and Blanchard, D. O. (1998). Variability of storm-relative helicity during VORTEX. Monthly Weather Review, 2959-2971.

Markowski, P., and Richardson, Y. (2010). Convection initiation. Mesoscale Meteorology in Midlatitudes, 185–199.

Marquis, J., Richardson, Y., Markowski, P., Dowell, D., and Wurman, J. (2012). Tornado maintenance investigated with high-resolution dual-Doppler and EnKF analysis. Monthly Weather Review, 140, 5017-5043.

Martín, F., Riosalido, R., and De Esteban, L. (1997). The Sigüenza tornado: A case study based on convective ingredients concept and conceptual models. Meteorological Applications, 4(3), 191-206. doi:10.1017/S1350482797000479

Mason, R.L., Ellis, N.K., Winchester, B., and Schexnayder, S. (2018). Tornado warnings at night: Who gets the message? Weather, Climate, and Society, 10, 561-568.

Mass, C. F., Ovens, D., Westrick, K., and Colle, B. A. (2002). Does increasing horizontal resolution produce more skillful forecasts? The result of two years of real-time numerical weather prediction over the Pacific North-West. 407-430.

Mathaba, T., Mpholo, M., and Letuma, M. (2012). Velocity and power density analysis of the wind at Letseng-la-terae in Lesotho. Renewable Energy, 210-217. doi:10.1016/j.renene.2012.04.003

McBean, G. (2000). Forecasting in the 21st Century. 9th IMO Lecture. Geneva.

McBride, C. M., Kruger, A. C. and Dyson, L. (2022). Changes in extreme daily rainfall characteristics in South Africa: 1921–2020. Weather and Climate Extremes, 1-11. doi:10.1016/j.wace.2022.100517

McCaul, E. W. (1991). Buoyancy and characteristics of hurricane-tornado environment. Monthly Weather Review, 119, 1954-1978.

McNulty, R. P. (1995). Severe and convective weather: A central region challenge. Weather and Forecasting, 10, 187-202. Retrieved from http://journals.ametsoc.org/doi/pdf/10.1175/1520-0434(1995)010<0187:SACWAC>2.0.CO;2

Miller, R. C. (1959). Tornado-producing synoptic patterns. Bulletin of the American Meteorological Society, 40(9), 465–472. https://doi.org/10.1175/1520-0477-40.9.465

Mitra, C., Shepherd, J. M., and Jordan, T. (2012). On the relationship between the premonsoonal rainfall climatology and urban land cover dynamics in Kolcata city, India. International Journal of Climatology, 32(9), 1443-1454. doi:10.1002/joc.2366

Moeletsi, M. E., Walker, S., and Landman, W. A. (2011). ENSO and implications on rainfall characteristics with reference to maize production in the Free State Province of South Africa. Physics and Chemistry of the Earth, 36(14-15), 715-726. doi:10.1016/j.pce.2011.07.043

Molekwa, S. (2013). Cut-off lows over South Africa and their contribution to the total rainfall of the Eastern Cape Province. Pretoria: University of Pretoria.

Moller, A. R. (2001). Severe local storms forecasting. In: Doswell III, 2001 (ed). Severe convective storms (Vol. 28). American Meteorological Society.

Moller, A. R., Doswell III C. A., Foster M. P., and Woodall G. R. (1994). The operational recognition of supercell thunderstorm environments and storm structures. Weather Forecast, 9(3), 327-347. doi:10.1175/1520-0434

Moncrieff, M. W., and Green, J. S. A. (1972). The propagation and transfer properties of steady convective overturning in shear. Quarterly Journal of the Royal Meteorological Society, 98, 336-352, doi:10.1256/smsqj.41606

Monteverdi, J. M., and Quadros, J. (1994). Convective and rotational parameters associated with three tornado episodes in northern and central California. Weather and Forecasting, 9, 285-300.

Monteverdi, J. P., Edwards, R., and Stumpf, G. J. (2015). An Analysis of the 7 July 2004 Rockwell Pass, California, Tornado: Highest-Elevation Tornado Documented in the United States. Monthly Weather Review, 143(2), 419-432. doi:10.1175/mwr-d-13-00316.1

Moon, J., Lee, W. K., Song, C., Lee, S. G., Heo, S. B., Shvidenko, A., Kraxner, F., Lamchin, M., Lee, E. J., Zhu, Y., Kim, D., and Cui, G. (2017). An introduction to mid-latitude ecotone: Sustainability and environmental challenges. Siberian Journal of Forest Science, 41–53. doi:10.15372/sjfs20170603

Morris, T., Hermes, J., Beal, L., Du Plessis, M., Duncombe Rae, C., Gulekana M, Lamont, T., Speich, S., Roberts, M., and Ansorge, I. J. (2017). The importance of monitoring the Greater Agulhas Current and its inter-ocean exchanges using large mooring array. South African Journal of Science, #7 pages; 113(7/8). http://dx.doi.org/10.17159/sajs.2017/20160330

Mountain dirt winding road with rural houses on the hillside. Morning view of a mountain valley. [Online]. Available: https://www.freepik.com/premium-photo/mountain-dirt-winding-road-with-rural-houses-hillside-morning-view-mountain-valley-with-serpentine-road-matlas-gorge-dagestan_15946113.htm. [10 March 2024]

Mpanza, T. (2016, November 30). In April 2016 a supercell thunderstorm occurred over the Free State with a short-lived tornado. Retrieved from Eumetsat: https://www.eumetsat.int/supercell-thunderstorm-south-africa

Mpanza, T., and Dyson, L. (2015). Comparison of the January 1981 cut-off low and the January 2014 cut-off low. (pp. 27-30). South African Society of Atmospheric Science.

Mukheli, A. (2018). Investigation of factors influencing borehole yields in the Nzhelele - Makhado Area in Limpopo Province, South Africa. University of Venda, Thohoyandou, p. 4.

Mulder, K. J. and Schultz, D. M. (2015). Climatology, storm morphologies, and environments of tornadoes in the British Isles: 1980–2012. Monthly Weather Review, 143(6), 2224–2240. doi:10.1175/mwr-d-14-00299.1

Mulovhedzi, P. T., Rambuwani, G. T., Bopape, M.-J., Maisha, R., Monama, N. (2021). Model inter-comparison for short-range forecasts over the southern African domain. South Africa Journal of Science, 117(9/10), #12 pages. doi:10.17159/sajs.2021/8581

Mulugeta, G., and Simelani, T. (eds). (2016). Natural and human-induced hazards and disasters in Africa. Pretoria: Africa Institude of South Africa.

Muofhe, T. P., Chikoore, H., Bopape, M.-J. M., Nethengwe, N. S., Ndarana, T., and Rambuwani, G. T. (2020). Forecasting Intense cut-off lows in South Africa using the 4.4 km Unified Model. Climate, #20 pages. doi:10.3390/cli8110129

Naylor, J. and Gilmore, M. S. (2014). Vorticity evolution leading to tornadogenesis and tornadogenesis failure in simulated supercells. Journal of Atmospheric Science, 71, 1201-1217.

Ndabambi, M. F. (2002). Forecasting of gale force westerly winds along the Eastern Cape coast between Cape St Francis and Port Elizabeth . Master's Diploma in Technology, Technikon Pretoria, Pretoria.

Ndarana, T., and Waugh, D. W. (2010). The link between cut-off lows and Rossby wave breaking in the southern hemisphere. Quarterly Journal of the Royal Meteorological Society, 136, 869-885. doi:10.1002/qj.627

Ndarana, T., Rammopo, T. S., Chikoore, H., Barnes, M. A., and Bopape, M.-J. (2020). A quasi-geostrophic diagnosis of the zonal flow associated with cut-off lows over South Africa and surrounding oceans. #23 pages.

Nel, W., and Sumner, P. (2008). Rainfall and temperature attributes on the Lesotho Drakensberg escarpment edge, South Africa. doi:10.1111/j.1468-0459.2008.00337.x

Ngubo, N. (2021). Reviewing precautionary thresholds at seaport precincts on account of intense coastal weather conditions in KwaZulu-Natal. MComm dissertation, University of KwaZulu-Natal, Pietermaritzburg, p. 10.

Nielsen, E. R. (2015). Double impact: When both tornadoes and flash floods threat at the same time. Monthly Weather Review, 30, 1673-1693.

Nilo, S. T., Romanom F., Cermak, J., Cimini, D., Ricciardelli, E., Cersosimo, A., Di-Paola, F., Gallucci, D., Gentile, S., Geraldi, E., Larosa, S., Ripepi, E., and Viggiano, M. (2018). Fog detection based on Meteosat Second Generation-Spinning Enhanced Visible and infrared imager high resolution visible channel. Remote Sensing, 10, #20 pages. doi:10.3390/rs10040541

NWS. (2004). NWS Operations Manual. Silver Spring, 9-10, https://www.nws.noaa.gov/directives/010/archive/pd01016005b.pdf

NWS. (2024, January 31). The enhanced Fujita scale (EF Scale). Maryland, United States of America.

Olivier, J. (1990). Hail in the Transvaal: Some geographical and climatological aspects. PhD thesis, Rand Afrikaans University, Johannesburg.

Özdemírm, E. T., Kolay, O., and Yetemen, O. (2019). A case study of rural area hailstorm in Yomra, Trabzon, on August 31, 2017. Journal of Atmospheric and Environmental Science, 4(2), 243-250.

Park, S.-H., and Jung, H.-S. (2016). Spatiotemporal analysis of snow over variations at Mt. Kilimanjaro using multi-temporal Landsat images during 27 years. 37-46. doi:10.1016/j.jastp.2016.03.007

Peng, M. S., Li, S.-W., Chang, S. W., and Williams, R. T. (1995). Flow over mountains: Coriolis force, transient troughs and three dimensionality. Quarterly Journal of the Royal Meteorological Society, 121, 593-613. Retrieved from http://hdl.handle.net/10945/44176

Perez, A. H., Wicker, L. J., and Orville, R. E. (1997). Characteristics of cloud-to-ground lightning associated with violent tornadoes. Weather and Forecasting, 3, 428-437. doi:10.1175/1520-0434(1997)012<0428:coctgl>2.0.co;2

Pettitt, R. B., and Root, R. G. (1969). Vertical wind shear in the boundary layer. 1-30.

Pharoah, R., Fortune, G., Chasi, V. and Holloway, A. (2013). The environment & risk reduction: focus on urban risk. Stellenbosch University: Disaster Mitigation for Sustainable Livelihoods Programme. (DiMP).

Pienaar, N., Dyson, L. L., and Klopper, E. (2015). Atmospheric anomalies during the 2012/13 extreme hail seasons over Gauteng. 31st Annual Conference of South African Society (pp. 149-152). Research Gate. Retrieved from https://www.researchgate.net/publication/324223684

Poolman, E. R. (2014). A probabilistic impact-focussed early warning system for flash floods in support of disaster management in South Africa. Unpublished PhD Thesis, University of Pretoria, Pretoria.

Preston-Whyte, R. A. (1988). The atmosphere and weather of southern Arica. Cape Town: Oxford University Press.

Pretorius, I. (2013). Dynamical downscaling of prevailing synoptic scale winds over the complex terrain of Mariepskop, South Africa. Pretoria: University of Pretoria.

Quagraine, K. A., Hewitston, B., Jack, C., Pinto, I., and Lennard, C. (2019). A methodological approach to access the co-behavior of climate processes southern Africa. Journal of Climate, 2483-2495. doi:10.1175/jcli-d-18-0689.1

Rae, K. and Dyson, L. (2015). Sounding-derived characteristics associated with some supercell storms over the Gauteng Province of South Africa. European Conference on Severe Storms, (pp. 14-18). Wiener Neustadt.

Rae, K. J. (2014). A modified supercell composite parameter for supercell thunderstorms over Gauteng Province, South Africa. Pretoria: University of Pretoria.

Rakov, V. A. and Uman, M. A. (2006). Lightning: physics and effects. New York: Cambridge University Press.

Rammopo, T. S., and Ndarana, T. (2019). The role of non-quasi-geostrophic forcing during cut-off low pressure system onsets over South Africa. Pretoria: University of Pretoria.

Ramotubei, T. S. (2002). Radar radial velocity data assimilation over Hefei using WRF-3DVar system and sensitivity of WRF model to initialization . Nanjing University of Information Science and Technology.

Rao, S. A., Gopalakrishna, V. V., Shetye, S. R., and Yamagata, T. (2002). Why were cool SST anomalies absent in the Bay of Bengal during the1997 Indian Ocean Dipole Event?, Geophysical Research Letters,29(11), 1555,doi:10.1029/2001GL014645.

Rasmussen, E. N., and Blanchard, D. O. (1998). A baseline climatology of sounding-derived supercell and tornado forecast parameters. Weather and Forecasting, 13(4), 1148-1164.

Rasmussen, E. N., and Wilhelmson, R. B. (1983). Relationships between storm characteristics and 1200 GMT hodographs, low-level shear, and stability. 13th Conf. on Severe Local Storms (pp. J5–J8). Tulsa: American Meteorological Society.

Rasmussen, E. N., Richardson, S., Straka, J. M., Markowski, P. M., and Blanchard, D. O. (2000). The association of significant tornado with a baroclinic boundary on 2 June 1995. Monthly Weather Review, 128, 174-191. doi:10.1175/1520-0493(2000)128<0174:taostw>2.0.co;2

Ratna, S. B., Behera, S., Ratnam, J. V., Takahashi, K., and Yamagata, T. (2013). An index for tropical temperate troughs over southern Africa. Climate Dynamics, 41, 421-441. doi:10.1007/s00382-012-1540-8

Ratnam, M., Santhi, Y., Rajeevan, M., and Rao, S. (2013). Diurnal variability of stability indices observed using radiosonde observations over a tropical station: comparison with microwave radiometer measurements. Atmospheric Research, 124, 21-33. doi:10.1016/j.atmosres.2012.12.007

Reboita, M. S., Gan, M. A., da Rocha, R. P., and Ambrizzi, T. (2010). Regimes of precipitation in South America: a bibliographical review. Braz. J. Meteorol., 25, 185-204. doi:10.1590/s0102-77862010000200004

Redelsperger, J.-L., Diongue, A., Diedhiou, A., Ceron, J.-P., Diop, M., Gueremy, J.-F., Lafore, J.-P. (2002). Multi-scale description of a Sahelian synoptic weather system representative of the West African monsoon. Research Article, 128(582), 1229-1257. doi:10.1256/003590002320373274

Reimel, R. K. (2017). An analysis of total lightning characteristics in tornadic storms preparing for the capabilities of the GLM. MSc dissertation, Colorado State University, Colorado, pp. 2-5 and 28.

Riemann-Campe, K. (2010). Can convective precipitation variability be deduced from the variability in CAPE and CIN?: An analysis of global CAPE and CIN variability in present and future climates. Max-Planck-Institut fur meteorologie, Hamburg.

Riphagen, H. A., Bruyere, C. L., Jordan, W., Poolman, E. R. and Gertenbach, J. D. (2002). Experiments with the NCEP Regional Eta Model at the South African Weather Bureau, with emphasis on terrain representation and its effect on precipitation predictions. Monthly Weather Review, 130, 1246-1263.

Röhner, L. (2016). Heavy precipitation events in the western Mediterranean area: physical processes and predictability. PhD thesis.

Rogers, J. W., and Weiss, C. C. (2008). The association of cell mergers with tornado occurrence. 24th Conference on Severe Local Storms. Savannah: American Meteorological Society. Retrieved from https://ams.confex.com/ams/24SLS/webprogram/Paper141784.html

Rosenfeld, N., Young, J. W., Alon, U., Swain, P. S., and Elowitz, M. B. (2005). Gene regulation at the single-cell level. 307(5717), 1962-1965. doi:10.1126/science.1106914

Rotunno, R. (1979). A study in tornado-like vortex dynamics. Research Article, 140–155. doi:10.1175/1520-0469(1979)036<0140:asitlv>2.0.co;2

Rotunno, R. (1981). On the evolution of thunderstorm rotation. Monthly Weather Review, 109, 577-586.

Rouault, M., White, S., Reason, C. J. C., Lutjeharms, J. and Jobard, I. (2002). Ocean–atmosphere interaction in the Agulhas Current region and a South African extreme weather event. Weather Forecast, 17(4), 655–669.

Sadowski, A. (1969). Size of tornado warning area when issued on the basis of radar hook echo. ESSA Tech. Memo. WBTM Fest. 10, p. 26 [NTIS PB 184613].

Saff, E. B. and Snider, A. D. (2003). Fundamentals of complex analysis with applications for engineering and science (3rd ed). Pearson Education, inc., pp. 180-182

Sano, T. and Tsuboki, K. (2006). Structure and evolution of a cumulonimbus cloud developed over a mountain slope with the arrival of sea breeze in summer. Journal of the Meteorological Society of Japan, 84(4), 613-640. doi:10.2151/jmsj.84.613

Sansom, H. W. (1966). The occurrence and distribution of hail in Africa. In: The Meteorological Magazine (July 1966), (1966). 95(1128), 212-218. doi:551.501.45:551.509.335:551.589(41/42)

Satsig (2011). Longitude/Latitude to screen coordinates. [Online]. Available: https://www.physicsforums.com/threads/longitude-latitude-to-screen-coordinates.281447/ [20 March 2024]

SAWS (2001, 03 19). South African Weather Service Act Number 8. Cape Town, 432(22422), p. 8, https://www.weathersa.co.za/Documents/Legislature/South_African_Weather_Service_Act_8_of_2001_09022021083232.pdf

SAWS. (2003, 02 06). SAWS Library Orientation. Retrieved from http://moodle.weathersa.co.za/moodle/enrol/index.php?id=30

Schaefer, J. T., Kelly, D. L., Doswell, III, C. A., Galway, J. G., Williams, R. J., McNulty, R. P., Lemon, L. R., and Lambert, B. D. (1980). Tornadoes, when, where, how often. Weatherwise, 33, 52-59.

Schimid, W., Schiesser, H.-H., and Bauer-Messmer, B. (1997). Supercell storms in Switzerland: Case studies and implications for nowcasting severe winds with Doppler radar. Meteorological Apllications, Volume 4, 49-67.

Schlef, K. E., Moradkhani, H., and Lall, U. (2019). Atmospheric circulation patterns associated with extreme United States floods identified via machine learning. 1-12. Retrieved from https://doi.org/10.1038/s41598-019-43496-w

Schmidlin, T. (2010). Tornadoes (B. Warf ed.). Encyclopaedia of Geography. doi:10.4135/9781412939591.n1149

Schultz, C. J., and Kellenbenz, D. J., and Kaiser, J. W. (2013). Analysis of the 26 August 2007 northern plains tornado outbreak. #37 pages.

Schulze, G. (1986). Climate of South Africa. Part 8: General Survey. p. 330.

Schulze, G. C. (2007). Atmospheric observations and numerical weather prediction. South African Journal of Science, 103, 318.

Seeley, J. T., and Romps, D. M. (2015). Why does tropical convective available potential energy (CAPE) increase with warming? Geophysical Research Letters, 42, 10429–10437. doi:10.1002/2015gl066199

Sherburn, K. D., and Parker, M. D. (2014). Climatology and ingredients of significant severe convection in high shear, low-CAPE environments. Weather Forecasting, 29, 854–877. doi:10.1175/WAF-D-13-00041.1

Simpson, L.-A., and Dyson L. L. (2018). Severe weather over the Highveld of South Africa during November 2016. Water SA, 44(1), 75-85. doi:http://dx.doi.org/10.4314/wsa.v44i1.09

Singleton, A. T. and Reason C. J. C. (2006). Numerical simulations of a severe rainfall event over the Eastern Cape coast of South Africa: sensitivity to sea surface temperature and topography. Tellus, 58(3), 355-367. doi:10.1111/j.1600-0870.2006.00180.x

Singleton, A. T., and Reason, C. J. C. (2007). A numerical model study of an intense cut-off low pressure system over South Africa. Monthly Weather Review, 1128-1150. doi:10.1175/mwr3311.1

Smith, K. (2013). Environmental hazards: assessing risk and reducing disaster (6th ed.). Routledge: Taylor & Francis Group, London and New York, p. 247

Spellman, F. R. (2013). The handbook of meteorology. Toronto: Scarecrow Press, Inc.

Spiridonov, V., and Ćurić, M. (2019). Evaluation of supercell storm triggering factors based on a cloud resolving model simulation. Asia-Pacific Journal of Atmospheric Sciences, 55, 439-458. doi:10.1007/s13143-018-0070-7

Stander, J. H., Dyson, L., and Engelbrecht, C. J. (2016). A snow forecasting decision tree for significant snowfall over the interior of South Africa. South African Journal of Science, 112(9/10).

Starr, K. (2010). Eluding aeolus: Turbulence, gusts, and wind shear. In: NASA's contributions to aeronautics (Vol. 2). (R. P. Hallion, Ed.) Washington DC: National Aeronautics and Space Administration.

Stewart, J. (1998). Multivariable calculus: concepts and contexts. Carlifonia: Brooks/Cole Publishing Company.

Steyn, G. J. (1988). A farming systems study of two rural areas in the Peddie District of Ciskei. University of Fort University of Fort.

Steyn, P. C. L. and Bruintjes, R. T. (1990). Convective cloud characteristics for Bethlehem area. Water SA, 16(2), 115-118.

Sun, W.-Y., and Sun, O. M. (2015). Bernoulli equation and flow over a mountain. Geoscience Letters, #12 pages. doi:10.1186/s40562-015-0024-1

Swart, I. and Horn, A.C. (2012). Evaluation of the environmental and social sustainability policy of a mass tourism resort: A narrative account. HTS Teologiese Studies/Theological Studies, 68(1), 7 pages. http://dx.doi.org/10.4102/hts.v68i1.1264

Swann, A. L. S., Fung, Inez Y., and Chiang J. C. H. (2012). Mid-latitude afforestation shifts general circulation and tropical precipitation. Proceedings of the National Academy of Sciences of the United States of America, 109(3), 712-716. doi:10.1073/pnas.1116706108

Takeda, T. (1966). The downdraft in the convective clouds and raindrops: A numerical computation. Journal of the Meteorological Society of Japan, 44, 1-11.

Takemi, T. (2014). Characteristics of summertime afternoon rainfall and its environmental conditions in and around the Nobi Plain. Environmental Science. doi:10.2151/sola.2014-033

Taljaard, J. J. (1958). South African air-masses: their properties, movement and associated weather. Johannesburg: Witwatersrand. Retrieved from http://hdl.handle.net/10539/28993

Taljaard, J. J. (1996). Atmospheric circulation systems, synoptic climatology and weather systems of South Africa. Part 5: Temperature phenomena in South Africa. p. p. 42.

Taljaard, J. J., Schmitt, W., and Van Loon, H. (1961). Frontal analysis with application to the southern hemisphere. 25-57.

Tennant, W. J., and Hewitson, B. (2002). Intra-seasonal rainfall characteristics and their importance to the seasonal prediction problem. International Journal of Climatology, 22, 1033-1048.

Tennant, W. J., and Van Heerden, J. (1994). The influence of orography and local sea-surface temperature anomalies on the development of the 1987 Natal floods: A general circulation model study. South African Journal of Science, 90, 45-49.

Terblanche, D. E., Steffens, F. E., Fletcher, L. Mittermaier, M. P. and Parsons, R. (2000). Toward the operational application of hygroscopic flares for rainfall enhancement in South Africa. Journal of Applied Meteorology, 39, 1811-1821.

Tessendorf, S. A. (2009). Characteristics of lightning in supercells. In: Betz, H. D., Schumann, U., and Laroche, P. (2009). Lightning: principles, instruments and applications. New York: Springer.

Thompson, R. L. (1998). Eta model storm-relative winds associated with tornadic and non-tornadic supercells. Weather and Forecasting, 13, 125–137.

Thompson, R. L., and Edwards, R. (2000). RUC-2 supercell proximity soundings, Part I: an examination of storm-relative winds normalized to supercell depth. 20th AMS Conference on Severe Local Storms (p. #6 pages). Orlando: Preprints.

Tijssen, L. (2015). Tornado outbreak in Europe. University of Utrecht.

Tladi, M. J. (2018). Well-posedness and long-time dynamics of the rotating Boussinesq and quasigeostrophic equations. Journal of Applied Meteorology and Climatology, 2(9), 379-456. doi:10.26855/jamc.2018.09.003

Trapp, R. J. (2018). Formation and development of convective storms. Oxford Research Encyclopedia of Climate Science.

Trapp, R. J., Stumpf, G. J., and Manross, K. L. (2005). A reassessment of the percentage of tornadic mesocyclones. Weather Forecasting, 20, 680-687. doi:10.1175/WAF864.1

Trenberth, K. E. (1997). The definition of El Niño. 2771-2778. doi:10.1175/1520-0477(1997)078<2771:tdoeno>2.0.co;2

Trenberth, K. E., Caron, J. M., Stepaniak, D. P., Worley, S. (2002). Evolution of El Niño–Southern Oscillation and global atmospheric surface temperatures. Journal of Geophysical Research: Atmospheres, 107(D8), p. AAC 5-1-AAC 5-17. doi:10.1029/2000JD000298

Tshehla, C. E. (2008). Climatology of air mass transport to Cape Point. MSc dissertation, University of KwaZulu-Natal, Durban, p. 4.

Tshehla, C., Wright, C. Y. (2019). Spatial variability of PM_{10}, $PM_{2.5}$ and PM chemical components in an industrialised rural area within a mountainous terrain. South African Journal of Science, 115(9/10) 10 pages. https://doi.org/10.17159/ sajs.2019/6174

Tucker, R. B. (1971). An exceptional late spring cold front in South Africa. 26(12), 506. Retrieved from https://doi.org/10.1002/j.1477-8696.1971.tb04151.x

Tuschy, H. (2009). Examination of severe thunderstorm outbreaks in Central Europe. University of Innsbruck. Retrieved from https://www.uibk.ac.at/acinn/theses/diploma-theses/tuschy_helge_2009_dipl.pdf (accessed 20 February 2021)

Tyrrell, J. G. (2009). A tornado with anticyclonic rotation at Clooncan, Co.Mayo. Proceedings of the Royal Irish Academy, 109B(1), #10 pages.

Tyson, P. D. (1999). Atmospheric circulation changes and palaeoclimates of southern Africa. South African Journal of Science, 95, 194-201.

Tyson, P. D., and Kruger, F. J., and Louw, C. W. (1988). Atmospheric pollution and its implications in the eastern Transvaal Highveld. Pretoria: Council for Scientific and Industrial Research.

Tyson, P. D., and Preston-Whyte, R. A. (1972). Observations of regional topographically-induced wind systems in Natal. Journal of Applied Meteorology, 643-649.

Tyson, P. D., and Preston-Whyte, R. A. (2000). The weather and climate of southern Africa. Oxford University Press.

Van Delden, A. (2001). Observations and modelling of the sea breeze with the return current. Atmospheric Research, 56(1-4), 89-110.

Van den Heever, S. C., D'Abreton, P. C., and Tyson, P. D. (1997). Numerical simulation of tropical-temperate troughs over southern Africa using the CSU RAMS model. South African Journal of Science, 93, 359-365.

Van Heerden, J. (1995). Reviews of the Earth science. South African Journal of Science, 91, 222-233.

Van Heerden, J. and Taljaard, J. J. (1998). Africa and surrounding Waters. In Meteorology of the Southern Hemisphere (Vol. 27(49), p. 141). American Meteorological Society.

Van Heerden, J. H. (1987). Southern Africa's weather patterns: 'an introductory guide', (Second edition ed.). Acacia books, via Africa Limited.

Van Leer, K. W. (2013). Storm mergers and their role in tornado genesis during the 2011 Joplin storm. Urbana, Illinois: University of Illinois.

Van Loon, H. (1972). Wind in the Southern Hemisphere. Meteorology of the southern hemisphere, 59-86.

Vermeulen, J. (2014). Two tornadoes reported in almost as many days - is this normal? Retrieved 06 30, 2022, from https://www.702.co.za/articles/951/after-two-tornados-reported-in-as-many-days-what-s-up-with-the-weather

VODACOM. (2007). Vodacom Group Annual Report 2007. Vodacom. p. 76 Retrieved from https://vodacom.com/pdf/investor/integrated-report/2007/integrated-annual-report.pdf

Wakimoto, R. M., and Wilson, J. W. (1989). Non-supercell Tornadoes. Monthly Weather Review, 1113-1140. doi:1989

Wakimoto, R. M., Murphey, H. V., and Nester, A., Jorgensen, D. P. and Atkins, N. T. (2006). High winds generated by bow echoes. Part I: Overview of the Omaha Bow Echo 5 July 2003 Storm during BAMEX. Monthly Weather Review, 134, 2793-2812.

Wallace, J. M., and Hobbs, P. V. (1977). Atmospheric Science: An introductory survey. Academic Press, Inc. pp. 242, 248.

Wang, C.-C., Ma, S.-K., and Johnson, R. H. (2020). A numerical study on the influences of Sumatra topography and synoptic features on tropical cyclone formation over the Indian Ocean. Monthly Weather Review, 148(7), 2777-2799. doi:10.1175/mwr-d-19-0259.1

Wang, X., Zhou, C., Liu, M., Honary, F., Ni, B., and Zhao, Z. (2016). Parametric instability induced by X-mode wave heating at EISCAT. Journal of Geophysical Research: Space Physics, 121(10), 10536–10548. doi:10.1002/2016JA023070Wright

Washington, H., E., R., and Hodges, K. I. (2019). Tropical lows in southern Africa: Tracks, rainfall contributions, and the role of ENSO. Journal of Geophysical Research-Atmospheres, 124, 11009–11032. doi:10.1175/jcli-d-19-0437.1

Water Research Commission (WRC). (2016). Investigating projected changes in the nature of extreme rainfall over South Africa during the 21st century through an assessment of their associated synoptic environments. Water Research Commission, Cape Town, pp. 41-33.

Water Research Commission WRC. (2019). Ocean impact on southern African climate variability and water resources. Water Research Commission, Pretoria, p. 13.

Webster, E. M. (2019). A synoptic climatology of continental tropical low pressure systems over southern Africa and their contribution to rainfall over South Africa. MSc dissertation, University of Pretoria, Pretoria, pp 11-12.

White, S. A. (2000). The Influence of the Agulhas Current on two South African extreme weather events. Depart. of Oceanography. Cape Town: University of Cape Town.

Wicker, L. J., and Cantrell, L. (1996). The role of vertical buoyancy distributions in miniature supercells. 18th Conf. on Severe Local Storms (pp. 225–229). Preprints.

Williams, E. R. (1995). Meteorological aspects of thunderstorm. In: Handbook of atmospheric electrodynamics (Vol. 1). (H. Volland, Ed.) Florida: CRC Press.

Williams F. R., Renard, R. J., Jung, G. H., Timkins, R. D. and Picard, R. R. (1984). Forecasters handbook for the southern African continent and Atlantic/Indian Ocean Transit. Department of Meteorology. Monterey, California: Naval Postgraduate School.

Williams, E. and Renno, N. (1993). An analysis of the conditional instability of the tropical atmosphere. Monthly Weather Review, Volume 121, 21-36.

Williams, E., Boldi, B., Matlin, A., Weber, M., Hodanish, S., Sharp, D., Goodman, S., Raghavan, R., and Buechler, D. (1999). The behavior of total lightning activity in severe Florida thunderstorms. Atmospheric Research, 51, 245-265.

Wilson, M. B. (2019). An analysis of differential reflectivity arc characteristics in 109 supercell storms. University of Nebraska. Retrieved from https://digitalcommons.unl.edu/geoscidiss/119

Wissmeier, U., and Smith, R. K. (2011). Tropical cyclone convection: the effects of ambient vertical vorticity. Quarterly Journal of the Royal Meteorological Society, 137, 845 – 857. doi:10.1002/qj.819

Witt, A., Burgess, D. W., Seimon, A., Allen, J. T., Snyder, J. C., and Bluestein, H. B. (2018). Rapid-scan radar observations of an Oklahoma tornadic hailstorm producing giant hail. Weather and Forecasting, 33(5), 1263–1282. doi:10.1175/waf-d-18-0

WMO. (1969). Vertical wind shear in the lower layers of the atmosphere. Technical Note No. 93, Geneva.

WMO. (1978). Gravity waves: rotor clouds. https://resources.eumetrain.org/data/4/452/navmenu.php?tab=4&page=2.0.0

Wood, F. (1998, 12 6). Hogsback.co.za. Retrieved from https://hogsback.co.za/magical_hogsback/tornadoes_serpents.htm

Wood, F. (2000). The snake in the sky: Tornadoes in clay and local narrative in the Hogsback-Alice area 2000. Critical Arts, 4(2), 79-95. doi:10.1080/02560040085310101

Woodhams, B. J., Birch, C. E., Marsham, J. H., Lane, T. P., Bain, C. L. and Webster, S. (2019). Identifying key controls on storm formation over the Lake Victoria Basin. Monthly Weather Review, 147, 3365-3390. doi:10.1175/mwr-d-19-0069.1

Wurman, J., Dowell, D., Richardson, Y., Markowski, P., Rasmussen, E., Burgess, D., Wicker, L., and Bluestein, H. B. (2012). The second verification of the origins of rotation in tornadoes experiment: VORTEX2. 93, 1147–1170.

Xue, H., Li, J., Qian, T., and Gu, H. (2019). A 100-m-scale modelling study of a gale event on the lee side of a long narrow mountain. Journal of Applied Meteorology and Climatology, 59(1). doi:10.1175/jamc-d-19-0066.1

Yair, Y. Y., Lynn, B. H., Korzets, M. and Jaffe, M. (2022). The “weekend effect” in lightning activity during winter thunderstorms over the Tel-Aviv, Israel, Metropolitan Area. Atmosphere, 13, #11 pages. doi:10.3390/atmos13101570

Zeitler, J. W., and Bunkers, M. J. (2005). Operational forecasting of supercell motion: review and case studies using multiple datasets. National Weather Digest, 29 (1), 81–97.

Zhang, S. Q., Fu, G., Lu, C. G., and Liu, J. W. (2017). Characteristics of explosive cyclones over the Northern Pacific. Journal of Applied Meteorology and Climatology, 56, 3187–3210. doi:10.1175/jamc-d-16-0330.1

Zinner, T., Forster, C., De Coning, E., and Betz, H.-D. (2013). Validation of the Meteosat storm detection and nowcasting system Cb-TRAM with lightning network data - Europe and South Africa. Atmospheric Measurement Techniques, 6, 1567-1583.

Zunckel, M., Turner, C. R., and Wells, R. B. (1996). Dry deposition of sulphur on the Mpumalanga highveld: a pilot study the inferential method. South Africa Journal of Science, 92, 485-491.